

NASA CR 72486

TRW NO. 09667-6001-R0-00

69 27975.

NASA CR 72486

## FINAL REPORT

## SPACE STORAGE PROPELLANT PERFORMANCE

by  
J.V. Mageean

Prepared For

NATIONAL AERONAUTICS AND SPACE ADMINISTRATION  
Contract NAS-3-11200

**CASE FILE  
COPY**

**TRW**  
SYSTEMS GROUP

ONE SPACE PARK • REDONDO BEACH, CALIFORNIA 90278

## NOTICE

This report was prepared as an account of Government sponsored work. Neither the United States, nor the National Aeronautics and Space Administration (NASA), nor any person acting on behalf of NASA:

- a) Makes any warranty or representation, expressed, or implied, with respect to the accuracy, completeness, or usefulness of the information contained in this report, or that the use of any information, apparatus, method, or process disclosed in this report may not infringe privately owned rights; or
- b) Assumes any liabilities with respect to the use of, or for damages resulting from the use of any information, apparatus, method or process disclosed in this report.

As used above, "person acting on behalf of NASA" includes any employee or contractor of NASA, or employee of such contractor, to the extent that such employee or contractor of NASA or employee of such contractor prepares, disseminates, or provides access to, any information pursuant to his employment or contract with NASA, or his employment with such contractor.

Requests for copies of this report should be referred to

National Aeronautics and Space Administration  
Office of Scientific and Technical Information  
Attention: AFSS-A  
Washington, D. C. 20546

NASA CR 72486

TRW NO. 09667-6001-R0-00

## FINAL REPORT

### SPACE STORAGE PROPELLANT PERFORMANCE

by  
J.V. Mageean

28 MARCH 1969

Prepared For

NATIONAL AERONAUTICS AND SPACE ADMINISTRATION  
Contract NAS-3-11200

NASA LEWIS RESEARCH CENTER  
CLEVELAND, OHIO  
LIQUID ROCKET TECHNOLOGY BRANCH  
LARRY GORDON



ONE SPACE PARK • REDONDO BEACH, CALIFORNIA 90278

## FOREWORD

This report was prepared by the Science and Technology Division of the TRW Systems Group at One Space Park, Redondo Beach, California, under Contract NAS 3-11200. The contract was administered by the Lewis Research Center of the National Aeronautics and Space Administration, Cleveland, Ohio. This report is the final report on the subject contract and summarizes the technical work conducted during the period 25 July 1967 to 21 July 1968. The NASA Project Manager for the contract was Mr. Larry Gordon.

The following personnel at TRW contributed to the technical effort of this program: J. V. Mageean, Program Manager; Dr. H. L. Burge, and S. J. Van Grouw, Technical Advisers; J. J. King, Thermal Analysis; K. C. Mock, Design; and F. E. Robinett, Test Operations.

## ABSTRACT

A combustion performance evaluation program was conducted with the objective of demonstrating high performance with the space storable liquid-liquid propellant combination of 80 percent FLOX and a fuel blend of 55 percent methane and 45 percent ethane. The demonstrated performance goal was 97 percent of shifting equilibrium characteristic velocity with the TRW coaxial injector at an oxidizer/fuel mixture ratio of 5.35. Effects of chamber geometry as well as chamber pressure were investigated. Detailed heat transfer data were collected during the program to provide design data for rocket engine designs utilizing the TRW coaxial injector.

## NOMENCLATURE

A	area	k	thermal conductivity
C	discharge coefficient	l	distance
D	diameter	m	mass
E	modulus of elasticity	t	time
H	enthalpy parameter	w	flow rate, distance
I	specific impulse	x	distance
K	constant	$\alpha$	thermal diffusivity
L	length	$\delta$	thickness
P	pressure	$\gamma$	specific heat ratio
Q	heat rate	$\rho$	density
R	gas constant, radius	$\nu$	Poissons ratio
T	temperature	<u>Subscripts and Superscripts:</u>	
U	velocity	ad	adiabatic
V	velocity	$\delta$	at edge of boundary layer
$R_e$	Reynolds number	c	cold, cross-section, chamber
$P_r$	Prandtl number	f	fuel, fluid
MR	mixture ratio	g	gas
CR	contraction ratio	i	initial
a	constant, axial	l	liquid
b	constant, characteristic dimension	o	stagnation, oxidizer, outside
c	specific heat, constant, characteristic velocity	p	at constant pressure
d	differential	s	surface
g	gravitational constant	w	wall
h	film coefficient	y	yield

## CONTENTS

	Page
1. INTRODUCTION . . . . .	1
2. SUMMARY . . . . .	3
3. HARDWARE DESCRIPTION . . . . .	6
3.1 Test Engine Design Summary . . . . .	6
3.1.1 Injector Design . . . . .	6
3.1.2 Experimental Thrust Chamber Design . .	25
3.1.3 Injector Fabrication . . . . .	33
3.1.4 Chamber Fabrication . . . . .	36
4. TEST EFFORT . . . . .	38
4.1 Test Descriptionp . . . . .	38
4.2 Test Summary . . . . .	40
5. PERFORMANCE EVALUATION SUMMARY . . . . .	75
5.1 General Performance Data Reduction. . . . .	75
5.2 Sawtooth Configuration Performance Summary . .	76
5.3 Canted Slot Configuration Performance Evaluation. . . . .	77
5.4 Straight Slot Configuration Performance Summary . . . . .	78
5.5 Pressure Drops . . . . .	84
5.6 Stability Observations . . . . .	84
5.7 Data Consistency . . . . .	85
5.8 Summary . . . . .	85
6. HEAT TRANSFER DESIGN AND RESULTS . . . . .	86
6.1 Injector Heat Transfer Design . . . . .	86
6.2 Experimental Heat Flux Measurements . . . . .	86
7. COLD FLOW ANALYSES AND RESULTS . . . . .	127
8. SUMMARY OF RESULTS . . . . .	136
8.1 Combustion Performance. . . . .	136
8.2 Heat Transfer . . . . .	137
8.3 Cold Flow Correlation. . . . .	138
8.4 Operational Characteristics . . . . .	138

## CONTENTS (Continued)

	Page
APPENDIX	
A    CALORIMETRIC PLUG DESIGN . . . . .	A-1
B    CALCULATION OF CHARACTERISTIC VELOCITY EFFICIENCY . . . . .	B-1
C    PHYSICAL PROPERTY AND THEORETICAL PERFORMANCE SUMMARY . . . . .	C-1
D    COMPUTER PROGRAMS . . . . .	D-1
E    TEST FACILITIES AND EQUIPMENT . . . . .	E-1
F    DATA ACQUISITION SYSTEM ACCURACY AND METHODS . . . . .	F-1
G    FINAL REPORT DISTRIBUTION LIST (NASA CR-72486) "SPACE STORABLE PROPELLANT PERFORMANCE" . . . . .	. . . . .

## ILLUSTRATIONS

Figure		Page
3-1	Basic Coaxial Injector Design Approach . . . . .	7
3-2	Basic Fuel Assembly of TRW Coaxial Injector . . . . .	7
3-3	Basic Oxidizer System in TRW Coaxial Injector . . . . .	8
3-4	Simple Sheet Impingement for Pintle Sizing . . . . .	15
3-5	Post-Firing View of Single Element Coaxial Injector Using Sawtooth Oxidizer Injection Scheme . . . . .	16
3-6	Preliminary Sawtooth Pintle Configuration . . . . .	16
3-7	Sawtooth Sheet Impingement for Pintle Sizing . . . . .	18
3-8	Irregular Flow Pattern Found to Exist in the Center Element Without Specially Designed Flow Passage . . . . .	19
3-9	Flow Pattern Generated Using the Sawtooth Configuration with Specially Designed Flow Passage to Eliminate Flow Irregularities . . . . .	19
3-10	Closeup of Sawtooth Flow Pattern with Stable Flow . . . . .	20
3-11	Basic Injector Design Showing Original Cruciform Concept . . . . .	20
3-12	Cruciform Assembly . . . . .	21
3-13	Modified Cruciform Showing Multiorifice Radial Flow Passages . . . . .	21
3-14	Injector Element Schematic Diagram . . . . .	22
3-15	Exploded View Showing Ring Concept . . . . .	23
3-16	Coaxial Injector With Canted Slot Ring Element . . . . .	25
3-17	Nominal Thrust Chamber Throat Section, $\epsilon = 2.5$ . . . . .	27
3-18	Thrust Chamber Spool Sections . . . . .	29
3-19	Chamber Thermocouple Plug . . . . .	33
3-20	Injector Assembly . . . . .	34
3-21	Oxidizer Subassembly . . . . .	35
3-22	Injector Assembly in Clean Room . . . . .	37
3-23	Chamber Spool Section . . . . .	37
4-1	Engine Installation on Test Stand . . . . .	38
4-2	Strip Chart Data for Run 070 . . . . .	45
4-3	Post-Firing View of Sawtooth Injector After Test 070 . . . . .	47
4-4	Post-Firing View of Chamber After Test 070 . . . . .	47
4-5	Injector Modification SS-1 . . . . .	51
4-6	Post-Firing View of Injector Element SW-2 . . . . .	51

## ILLUSTRATIONS (Continued)

Figure		Page
4-7	Turbulence Ring After Test 080 . . . . .	53
4-8	Post-Firing View of Thrust Chamber After Test 082 . .	
4-9	Post-Firing View of Injector Modification SS-1A After Test 083 . . . . .	55
4-10	Post-Firing View of Injector Modification SS-2 After Test 084 . . . . .	55
4-11	Post-Firing View of Injector Tip After Test 087. . . . .	57
4-12	Post-Firing View of Chamber Assembly After Test 087 . . . . .	58
4-13	Prefiring View of Canted Slot Injector Modification Before Test 088 . . . . .	59
4-14	Post-Firing View of Injector With Stainless Steel Modification CS-3 After Test 089 . . . . .	60
4-15	Post-Firing View of Injector Ring CS-4 After Test Test 090 . . . . .	61
4-16	Strip Chart Data for Run 093 . . . . .	63
4-17	Post-Firing View of Stainless Steel Injector Ring SS-4 After Test 093 . . . . .	65
4-18	Post-Firing View of Nickel Ring SS-6 After Tests 096 Through 100 . . . . .	67
4-19	View of Chamber Assembly After Tests 096 Through 100 . . . . .	67
4-20	Complete Injector Assembly After Completing Tests 096 Through 100 With Ring SS-6 . . . . .	68
4-21	Post-Firing View of Injector Ring SS-7 with Rounded Entrances After Test 102. . . . .	69
4-22	Post-Firing View of Injector Element SS-9 After Test 104 . . . . .	70
4-23	Post-Firing View of Injector Element SS-8 After Test Test 105. . . . .	70
4-24	Engine Assembly on Test Stand with Insulation Coverings in Place. . . . .	73
4-25	Post-Firing View of Injector Element SS-12 After Completing Test 127 Showing Carbon Deposition on Face of Pintle Tip . . . . .	74
4-26	Post-Firing View of Thrust Chamber After Test 127 Showing Carbon Deposition on Chamber Walls. . . . .	74
5-1a	Average Performance Values of Baseline Test with 90% FLOX and 55% Methane-45% Ethane. Injector Element SS-6 and A Chamber Contraction Ratio of 2.5 . . . . .	81

## ILLUSTRATION (Continued)

Figure		Page
5-1b	Peak Performance Values of Baseline Test with 90% FLOX and 55% Methane—45% Ethane. Injector Element SS-6 and a Chamber Contraction Ratio of 2.5 . . . . .	81
5-2	Peak and Average Performance Values of Baseline Test Using SS-12 Ring Element and 80% FLOX and 55% Methane and 45% Ethane . . . . .	82
5-3	Peak and Average Performance Values of High Contraction Ratio Chamber $\epsilon = 4.5$ Using SS-12 Ring Element with 80% FLOX . . . . .	83
5-4	Peak and Average Performance Values of 15-Inch L* Chamber Using SS-12 Ring Element with 80% FLOX . . . . .	83
5-5	Peak and Average Performance Values of 45-Inch L* Chamber Using SS-12 Ring Element with 80% FLOX . . . . .	84
5-6	Correlations of Thrust Measurements with Chamber Pressure Measurements for Performance . . . . .	85
6-1	Pintle Heat Transfer Analysis Model . . . . .	87
6-2	Transient Pintle Heat Transfer Analysis . . . . .	88
6-3	Pintle Temperature Profile . . . . .	89
6-4	Axial Layout of Thermocouples in Nominal Chamber . . . . .	91
6-5	Thermocouple Key by Axial Section Number in the Chamber Spool . . . . .	92
6-6	Thermocouple Key by Axial Section Number in the Chamber Throat . . . . .	93
6-7	Chamber Heat Flux as a Function of Propellant Momentum Ratio . . . . .	103
6-8	Average Axial Heat Flux Profiles for Runs 101 Through 105 . . . . .	106
6-9	Axial Heat Flux Profiles for Runs 118 Through 121 . . . . .	106
6-10	Heat Flux Composite for the Six Radial Thermocouples Locations for Runs 101, 102, 104, and 105 . . . . .	107
6-11	Radial Heat Flux Distribution for Run 101 . . . . .	109
6-12	Radial Heat Flux Distribution for Run 104 . . . . .	111
6-13	Radial Heat Flux Distribution for Run 105 . . . . .	113
6-14	Heat Flux Composite of Six Radial Thermocouple Locations for Runs 118 Through 121 . . . . .	115
6-15	Radial Heat Flux Distribution for Run 118 . . . . .	117

## ILLUSTRATIONS (Continued)

<b>Figure</b>		<b>Page</b>
6-16	Radial Heat Flux Distribution for Run 119.....	119
6-17	Radial Heat Flux Distribution for Run 120.....	121
6-18	Radial Heat Flux Distribution for Run 121.....	123
6-19	Axial Heat Flux Profiles for Run 118.....	125
6-20	Axial Heat Flux Profiles for Run 119.....	125
6-21	Axial Heat Flux Profiles for Run 120.....	126
6-22	Axial Heat Flux Profiles for Run 121.....	126
7-1	Coaxial Injector Cold Flow Collector.....	129
7-2	Coaxial Injector Cold Flow Collector Head End Assembly .....	130
7-3	Cold Flow Test on Element SS-6.....	133
7-4	Cold Flow Test on Element SS-4.....	133
7-5	Cold Flow Test on Element SS-8.....	134
7-6	Cold Flow Test on Element SS-12 .....	135

## TABLES

Table		Page
4-1a	Test Summary.....	41
4-1b	Test Summary.....	42
4-2	Summary of Injector Configurations.....	43
5-1	Sawtooth Configuration Summary Performance Evaluation.....	77
5-2	Canted Slot Configuration Summary Performance Evaluation.....	78
5-3	Straight Slot Configuration Performance Evaluation ..	79
5-4	C* Performance as a Function of FLOX Concentration .....	82
6-1	Heat Flux Data Summary—Run 101 .....	95
6-2	Heat Flux Data Summary—Run 102 .....	96
6-3	Heat Flux Data Summary—Run 104 .....	97
6-4	Heat Flux Data Summary—Run 105 .....	98
6-5	Heat Flux Data Summary—Run 118 .....	99
6-6	Heat Flux Data Summary—Run 119 .....	100
6-7	Heat Flux Dat Summary—Run 120 .....	101
6-8	Heat Flux Data Summary—Run 121 .....	102

## 1. INTRODUCTION

The Space Storable Propellant Performance contract NAS 3-11200 was a three-task program involving analysis, design and experimental efforts to investigate the applicability of the TRW coaxial injector for obtaining high performance with the space storable propellants. Under this contract, the selected space storable propellant combination was 80 percent FLOX and a 55 percent methane-45 percent ethane blend. The major emphasis of the program was on the demonstration of high characteristic velocity,  $C^*$ , efficiency, performance and injector design criteria. During the first phase of the test program, three coaxial injector geometries were screened for performance. The balance of the test program was conducted with the best performing injector geometry, investigating various chamber geometries as well as off-design conditions for the propellants. Testing was conducted at sea-level conditions for a nominal engine thrust of 3000 lb<sub>f</sub> and a chamber pressure of 100 psia.

A series of tests was conducted on the selected injector configurations to provide the necessary data for establishing the baseline injector performance characteristics. These tests included variations in the FLOX mixture percentage as well as the chamber geometry variations in  $L^*$  and contraction ratio.

Task I consisted of an analysis and design effort to generate the required injector and thrust chamber assemblies. A review of hydraulic data on the coaxial injector was conducted and its application to the FLOX/methane-ethane propellants evaluated.

Task II covered the fabrication of the basic injector assembly with two configuration modifications. These modifications were interchangeable with the basic injector assembly, making a total of three injector geometries for the baseline tests conducted in Task III. In addition to the injector assembly, one 3000 lb<sub>f</sub> thrust chamber with three chamber length spools and one high contraction ratio nozzle were fabricated.

Task III covered the experimental tests. The objective of these tests was the evaluation of the TRW coaxial injector design to obtain high characteristic velocity,  $C^*$ , performance efficiency with the 80 percent FLOX and 55 percent methane-45 percent ethane propellant combination. The performance goal was 97 percent characteristic velocity efficiency in a 30-inch L\* chamber at a nominal chamber pressure of 100 psia and an oxidizer/fuel mixture ratio of 5.35. The propellants were delivered to the injector at liquid nitrogen temperatures. For performance evaluation, the characteristic velocity efficiencies were determined from both chamber pressure and thrust measurements. Instrumentation provisions were made for obtaining combustion chamber heat flux measurements as well as for the installation of flush mounted (high frequency) pressure transducers. Detailed cold flow investigations and analyses were conducted to obtain basic data on the mixing and mass distribution characteristics of the final injector geometry. The cold flows were conducted with propellant simulants.

## 2. SUMMARY

The objective of the work conducted under contract NAS 3-11200 was to develop an understanding of the TRW coaxial injector combustion characteristics when used with the space storable propellants FLOX and a blend of methane and ethane and to demonstrate the feasibility of achieving a performance goal of 97 percent of characteristic velocity,  $C^*$ , efficiency. The engine designed and used under this contract employed a coaxial injector configuration of flexible design with a copper heat sink chamber. The nominal design conditions were 100 psi chamber pressure and a sea-level thrust of 3000 pounds.

The program was divided into three tasks: Task I involved a survey of hydraulic and hypergolic data related to the coaxial injector based on experience at TRW and NASA facilities. Based on the findings of this investigation, an injector design was developed which would have the flexibility of investigating the relative characteristics of three modifications of the coaxial injector. Task II was a fabrication phase in which the injector and chamber assembly were manufactured. Task III was the testing effort in which a series of tests were conducted to screen each of the three injector modifications and evaluate their performance characteristics. In addition, Task III involved some specialized testing for determining more detailed performance characteristics of the best of the three injector modifications.

The engine design formulated during this contract featured extensive mechanical flexibility. The injector allowed complete interchangeability of components with a minimum of effort, in that any component in the injector could be completely removed and replaced without total disassembly of the injector. The chamber was also designed for flexibility. The chamber was made up of spools and throat sections. Each spool was equivalent to approximately 15 inches of  $L^*$ , and the chamber  $L^*$  could be changed in increments of approximately 15 inches. Two throat sections were designed with contraction ratios of 2.5 and 4.5 with the nominal chamber design using a throat with a contraction ratio of 2.5.

The three coaxial injector modifications used under this contract were a sawtooth configuration, a canted slot configuration, and, finally, a straight slot configuration. The sawtooth configuration was a modification of the coaxial injector using two continuous propellant sheets impinging at 90 degrees. The sawtooth modification was a zig-zag arrangement of the oxidizer sheet in order to increase the exposed surface area and reduce the effective sheet thickness. The oxidizer was injected into the chamber in a radial fan while the fuel was injected as an axial cylindrical sheet. The canted slot configuration consisted of oxidizer slots set at an angle to the impingement of the fuel. The purpose of this was to achieve a maximum impingement surface while at the same time allowing a venting area for the combustion process between the fuel and the oxidizer. Finally, the straight slot configuration consisted of primary oxidizer jets backed up with secondary jets. The secondary jet flow rate was 15 to 20 percent of the total oxidizer flow. This injector configuration was similar to the injector employed for the Lunar Module Descent Engine (LMDE).

The sawtooth configuration indicated that good propellant mixing would require venting of the oxidizer fan. Since the sawtooth configuration was designed as a continuous sheet impingement and did not allow for venting, high performance was never achieved in the nominal 30-inch L\* chamber. Canted slot injector configurations that were tested achieved performance levels as high as 90 percent of characteristic velocity efficiency. The straight slot configuration, similar to the LMDE injector, was the most promising coaxial injector design for applications involving FLOX and light hydrocarbon. The configuration demonstrated high performance (excess of 97 percent of C\* efficiency) and excellent durability at an O/F of 5.3.

Tests conducted with the straight slot configuration demonstrated a relatively flat performance characteristic over a wide range of mixture ratios. Performance characteristic of this injector configuration over a mixture ratio from 4 to 6 showed a deviation within this mixture range of less than 2 percent. This injector configuration ran cool with heat fluxes into the chamber wall of  $2.5 \text{ to } 3 \text{ Btu/in}^2/\text{sec}$  within nominal 6-second firings, thus exhibiting design control of the effective propellant

mixture ratio at the chamber walls. The injector design exhibited stable combustion. Throughout the entire test program, there was never a test that exhibited any spontaneously initiated instability mode. The maximum combustion roughness measured in the program was approximately 6 psi (peak-to-peak).

In conclusion, this contract has demonstrated that the coaxial injector design can achieve high performance with the space storable FLOX light hydrocarbon fuel propellant systems. The injector design possesses inherent flexibility at the nominal design conditions, thus providing the necessary propellant control and propellant distribution important for achieving the desired thrust chamber wall environment control.

### 3. HARDWARE DESCRIPTION

#### 3.1 TEST ENGINE DESIGN SUMMARY

The selected nominal design conditions for the test hardware were 3000 lb<sub>f</sub> sea-level thrust with an optimum sea-level expansion nozzle and a chamber pressure of 100 psia. The engine was designed for use with an oxidizer of 80 percent fluorine and 20 percent oxygen and a blended fuel of 55 percent methane and 45 percent ethane. Normal temperature operating conditions for the system were liquid nitrogen temperatures, approximately -300° to -320°F. The optimum propellant mixture ratio for this propellant combination is 5.35.

The injector design was based upon the use of the concept of propellant injection by means of the TRW single element coaxial injector. The injector design was arranged to be highly flexible, permitting a large number of systematic variations of injection parameters to change mixing and distribution characteristics. The approach provided a means of using an injector as a basic building block that could undergo inexpensive modifications.

##### 3.1.1 Injector Design

At the outset of the design effort for the Space Storable Propellant Performance contract, a design goal was established to evolve a design which would incorporate maximum flexibility as well as economy in fabrication. Figure 3-1 shows a layout of the basic injector design.

The injector assembly is composed of two basic subassemblies: the fuel assembly and the oxidizer assembly. The two subassemblies are bolted together using a single common seal. The fuel assembly shown in Figure 3-2 consists of the body, faceplate and fuel annulus. The fuel annulus is bolted to the faceplate and establishes the fuel metering injection orifice. The fuel annulus is a basic interchangeable component and is aligned by precision dowel pins. A set of fuel annuli were produced for this injector, each having a different size precision bore to provide different fuel pressure drops during the testing program.

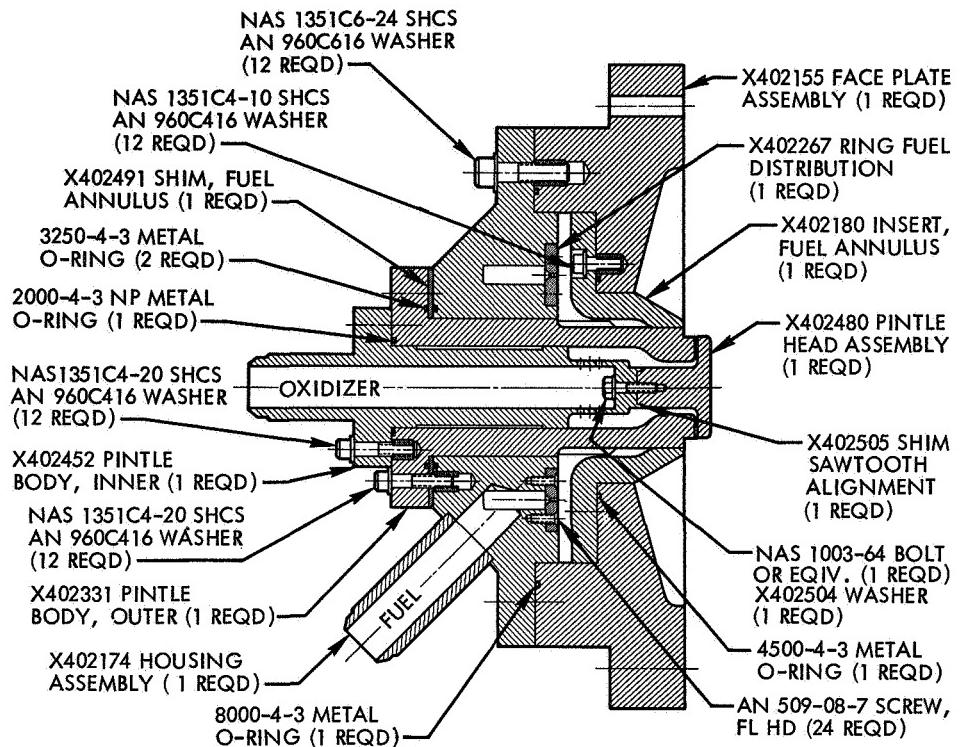


Figure 3-1. Basic Coaxial Injector Design Approach

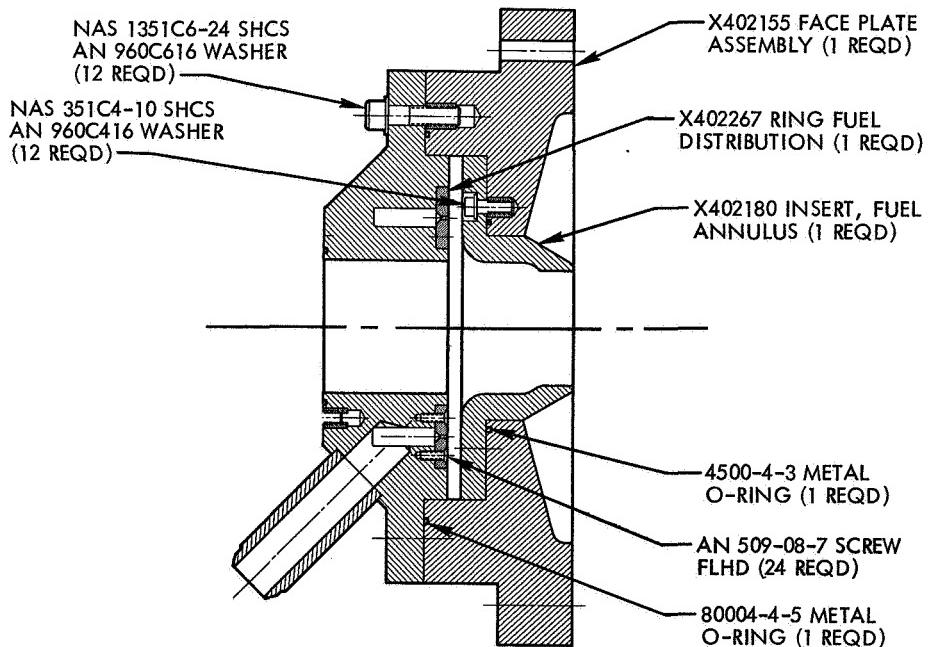


Figure 3-2. Basic Fuel Assembly of TRW Coaxial Injector

The body and faceplate were fabricated of 304 stainless steel and the fuel annulus was fabricated from nickel 200. The nickel 200 is a more durable material when exposed to the flame environment within the combustion chamber of a fluorine engine.

The oxidizer subassembly, shown in Figure 3-3, consisted of an outer and inner pintle body and a pintle tip. The inner pintle body acts as a support for the pintle tip. (Some designs for the oxidizer orifice used at TRW consist of a single unit in which the pintle is integral with the outer pintle body, thereby eliminating the need for inner pintle body. However, this concept was not chosen for this program because it does not lend enough flexibility for changing the oxidizer orifices.)

The outer pintle body and the pintle tip were made of nickel 200 to provide compatibility in the flame zone with the fluorine. The inner pintle body was made from 304 stainless. Since these parts all fit within one another with controlled tolerances, the surfaces in contact with each other were chrome plated for abrasion resistance and lubricity. The inner pintle body contained a support structure which allowed the oxidizer flow to pass down the center of the inner pintle body and radially out into the outer pintle body and then through the oxidizer injection orifice.

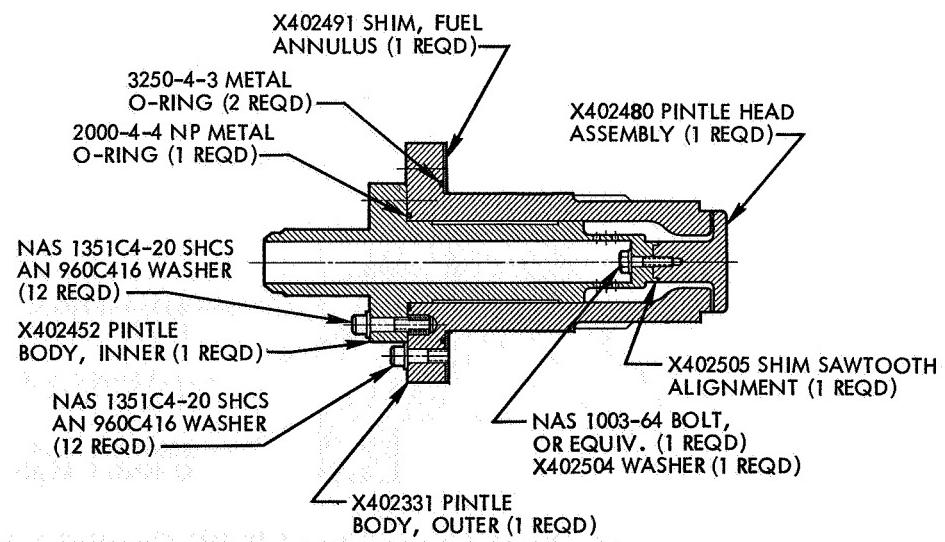


Figure 3-3. Basic Oxidizer System in TRW Coaxial Injector

## Injector Combustion Design Requirements

The geometrical configuration of the TRW coaxial injector is grossly different from the more common flat faced injectors; however, the fundamental processes which must take place in the interval between injection of liquid propellants into the rocket chamber and the completion of combustion are the same for the coaxial injector and other injector concepts. The manner in which these processes occur and their individual effects on the other processes are generally different for the coaxial injector as compared with the flat faced injector. The processes referred to are distribution, atomization, vaporization and, finally, chemical reaction.

The method of obtaining propellant distribution with the coaxial injector is very much different as compared with the highly distributed flat faced injectors. Consideration must be given to the chemical reaction rate and energy release of the propellants in order to clearly define the distribution technique to be used with the coaxial injector. Since TRW had no prior experience with the FLOX, light hydrocarbon propellant combination, the program approach was to design three distribution configurations of the coaxial injector and determine the effects of the chemical reaction on distribution. The elemental sizing of the element geometries is described below.

For the basic impinging jet element analyses where discrete drops of a species can occur, the basic mean volume drop size is taken as that given by Ingebo (Reference 1) with a 60-degree impingement and negligible gas effect:

$$d_{30} = \frac{1}{2.64} \sqrt{\frac{D_j}{U_j}} \quad (3-1)$$

Local gas effects can only result in reduced diameters. The maximum size is taken as:

$$d_{\max} = 3 d_{30} \quad (3-2)$$

The distribution is taken as that of the Nukiyama-Tanasawa (Reference 2) distribution. From these relations, the resulting spray fields can be rapidly evaluated for estimating internal thrust chamber ballistics and combustion effects. For example, the pintle-coaxial flow injector purposely results in a portion of the fuel striking the wall to serve as film coolant. An elemental combustion and droplet ballistic analysis can be carried out by following the vaporization and trajectories of a given size fraction of droplets by treating the fuel and oxidizer separately and assuming local thermodynamic equilibrium reaction between vaporization reactants. The evolved reaction products are assumed to flow one-dimensionally down the chamber. The trajectory of the fuel drops is then determined by the drag equation.

$$m_d \frac{d(\bar{U}_g - \bar{U}_d)}{dt} = \rho \frac{(\bar{U}_g - \bar{U}_d)^2}{2g} C_d A_d \quad (3-3)$$

where  $C_d$  = Drag coefficient and may be taken as nearly unity for initial design calculations.

Note that  $\bar{U}_g - \bar{U}_d$  is a vector quantity of gas velocity with respect to the drop. To proceed further requires the droplet mass and energy balances. These result in the temperature of the droplet as well as the size of the droplet as a function of time. The temperature is obtained from an analysis by Weiber (Reference 3). His final corrected result is

$$\frac{dT_d}{dt} = \frac{864}{C_p l^2 d_d^2} \left\{ k_m (T_g - T) \left( \frac{z}{z-1} \right) \frac{N_{uh}}{3600} - \frac{144 D_v M_l H_v P N_{um}}{R T_M} \ln \left( \frac{P}{P-P_v} \right) \right\} \quad (3-4)$$

$$z = \frac{(144)(3600) D_v M_l C_{P,v} P N_{um}}{k_m R T_m N_{uh}} \ln \left( \frac{P}{P-P_v} \right) \quad (3-5)$$

The vaporization rate is given by

$$\dot{W} = \frac{dW}{dt} = \frac{12\pi D_v d \rho M_f N_{um}}{R T_m} \ln \left( \frac{P}{P-P_v} \right) \quad (3-6)$$

The Nusselt number and mass transfer numbers are taken to be identical forms

$$Nu_h = 2 + 0.6 Pr^{1/3} Re^{11/2} \quad (3-7)$$

$$Nu_m = 2 + 0.6 Sc^{1/3} Re^{11/2} \quad (3-8)$$

No emphasis is placed on incorporating droplet breakup criteria into the calculations, because the indicated breakup times calculated by the method of Reference 4 show times considerably in excess of the 0.0006 second stay time. This series of equations is then used to determine fuel trajectories as well as the percentage of fuel striking the wall for the pintle. Also of interest are the trajectories and burn times with the impinging jet designs. The elements are properly sized when the computations show that the largest drops are consumed.

These methods are used only as guidelines because of the effects of reaction brought on by liquid phase mixing. It is most important here that the momentum ratios be optimized. The guidelines presented by Elverum (Reference 5) and Rupe (Reference 6) are used here to provide a basis for the start of all combustion analysis. These studies indicate a maximum in performance when the liquid phase mixing occurs at essentially the combustion design mixture ratio, resulting in the individual droplets being of mixed constituents at the design mixture ratio. For this to occur to the maximum extent possible requires optimum use of the stream momentums as indicated later. This is particularly true if the impinging streams are highly reactive to the extent that complete liquid phase mixing cannot occur. In this case, the injection and combustor design must incorporate features to promote secondary mixing of the reactants.

### 3.1.1.1 Basic Injector Configurations and Design

As a part of the analysis investigation of the injector design, the effects of geometry, momentum ratios, velocities, impingement angles, pressure drops, etc. were studied. The results of these analyses were used to establish the basic design of the sawtooth injector. By considering the continuity equation and liquid injection at 140°R and the flow area-pressure relationship

$$C_{DA} = \frac{\dot{W}}{[\rho g \Delta P]^{1/2}} \quad (3-9)$$

it is found that the fuel injection area requirements are small. However, the area is a function of the orifice pressure drops selected, and this pressure drop must be optimized with the oxidizer pressure drop for mixing performance.

The hydraulic factor involving momentum ratios is a measure of the inherent propellant energy for atomization and mixing. This ratio is

$$\frac{F_f}{F_o} = \frac{\omega_f V_f}{\omega_o V_o} \quad (3-10)$$

Using the maximum velocities available for equal tank pressure (without distributing devices), this ratio is

$$\frac{F_f}{F_o} = \frac{1}{MR} \left[ \frac{\rho_o}{\rho_f} \right]^{1/2} \quad (3-11)$$

assuming equal  $\Delta P$  values on both propellant sides. Contrasted with hydrazine storables with ratios of 0.6 to 0.7, it is seen that the gross fuel momentum interchange with the oxidizer is much less than the FLOX/LPG propellants with a momentum interchange of 0.3. This is

important to hydraulic atomization and mixing. Therefore, attention must be given to the control of the oxidizer dispersion early in the injection process and the mixing of the fuel in the oxidizer for maximum performance.

To achieve maximum uniformity of mixture ratio and mass distribution, careful control of available fuel and oxidizer momentum is required. Initial maximum mixing can be achieved only by optimum use of the available momentum forces. Using this approach a possible design argument is

$$\frac{F_f}{F_o} \approx 1 \quad (3-12)$$

On the basis of the foregoing design approach, it was established that the optimum velocity ratio for these propellants at the peak equilibrium mixture ratio is

$$\frac{V_o}{V_f} = 0.192 \quad (3-13)$$

So far, the analysis has applied only to a generalized injector. Certain design criteria must be established about the coaxial injector and the integration of the foregoing generalized criteria. Therefore, the following design parameters were established based on a review of hydraulic data on the coaxial injector.

- Minimum hydraulic diameter equal to 0.005 inch
- Maximum hydraulic diameter equal to 0.035 inch
- Minimum injection pressure drop equal to 15 psi
- Maximum injection pressure drop equal to 200 psi

The first criterion was established as a practical limitation, since ultra-thin sheets of fluid flow require excessive amounts of machining and alignment care. The second criterion was established as a result of a simple vaporization limit criteria imposed on the oxidizer to insure that the oxidizer was totally vaporized in the combustion process in the

allotted chamber volume. (The methods of Reference 7 were used for this computation.) The latter two criteria were the result of system dynamic and application considerations. Experience at TRW with the coaxial injector shows that the pressure drop at 100 psia cannot be reduced much below 15 psia without feed system coupled chugging occurring. The 200 psi drop was a practical upper limit for pressure fed systems.

Using these parameters, the injector sizing was established. Figure 3-4 shows a plot of injector pintle diameter as a function of propellant sheet thickness. However, it was noted that at no time can all the design parameters be met, that is, the maximum allowable pintle diameter based on the minimum sheet thickness does not intersect with the oxidizer velocity curve within the constraints of an oxidizer sheet thickness of 0.035 inch. It should be noted that it was assumed that sheet impingement occurs at the same diameter as the injector pintle in this basic design analysis. The injection gaps in the case of Figure 3-4 were calculated on the basis of simple cylindrical sheets in order to meet all the design requirements established.

In order to satisfy the basic design criteria several design approaches were taken. These are discussed below.

#### Sawtooth Configuration

The first injector concept generated on the program was the sawtooth configuration shown in Figure 3-5. This configuration was a variation of the continuous slot coaxial injector which has been used in other injector designs at TRW. It was a concept which, in theory, met the design objectives for an engine operating with a high mixture ratio such as the 3K FLOX engine with a mixture ratio of 5.35. With this concept, sheet thicknesses would be thin enough to allow adequate propellant atomization, and propellant momentum relationships could be designed to provide optimum mixing based on momentum ratios.

Figure 3-6 shows the basic sawtooth gap configuration. This configuration changes the effective diameter for a given gap dimension through a process of geometrical folding. In this manner, a continuous

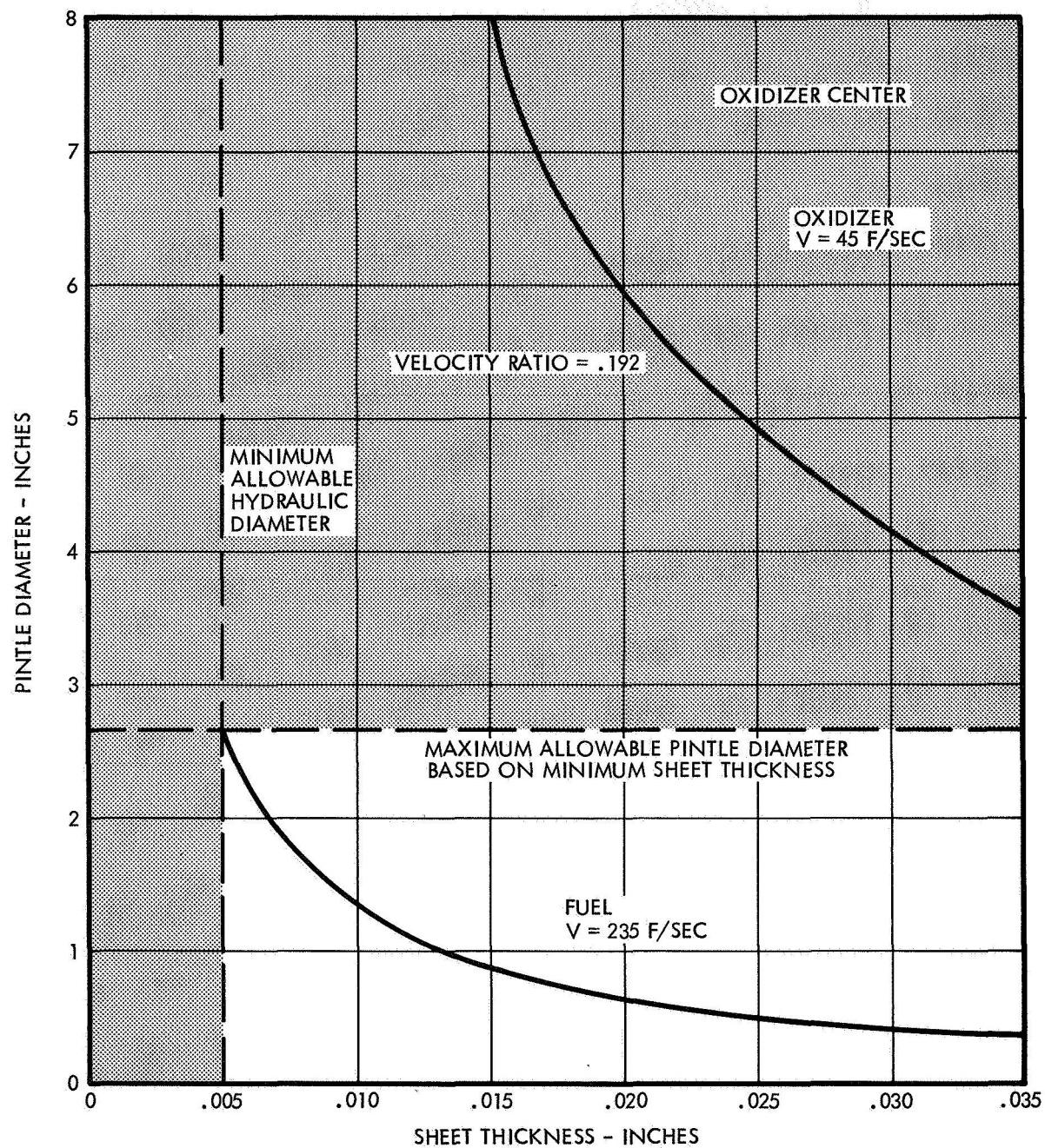


Figure 3-4. Simple Sheet Impingement for Pintle Sizing

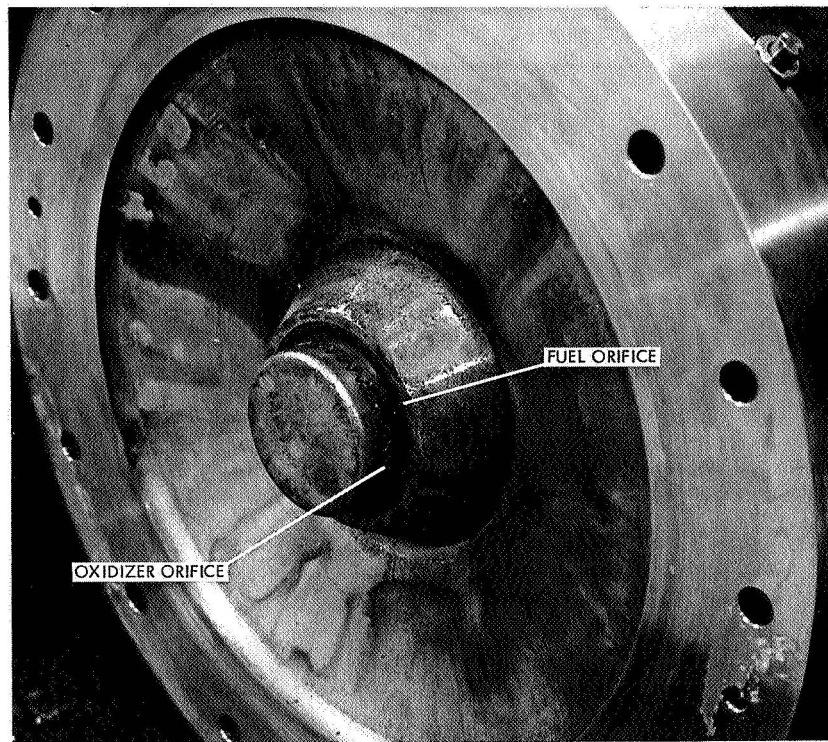


Figure 3-5. Post Firing View of Single Element Coaxial Injector Using Sawtooth Oxidizer Injection Scheme

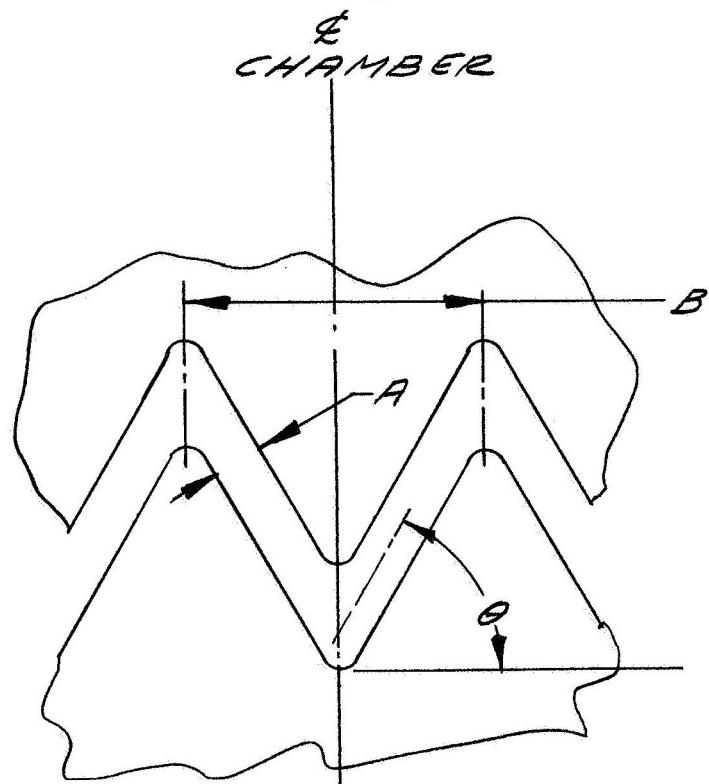


Figure 3-6. Preliminary Sawtooth Pintle Configuration

flat sheet was now transformed into a folded fan. Figure 3-7 shows the sheet gap as a function of pintle diameter for these sawtooth pintle configurations. The figure shows two tooth angles, 45 and 60 degrees. Applying the given design criteria, it was seen that a 60-degree sawtooth provides the greatest flexibility within the design parameters.

Considering off-design conditions to be investigated, an optimum pintle diameter can be established. On the basis of the analysis and curves shown, a pintle diameter of 2 inches was selected to provide maximum design flexibility.

Hydraulic studies were conducted on this design to observe and evaluate the resulting flow pattern. These early hydraulic studies revealed a severe non-uniformity and flow irregularity. Figure 3-8 shows a typical example of this flow irregularity. The irregularity was caused by a fluidic instability resulting from an expanding flow pattern unable to maintain wall attachment. A detailed water flow study was conducted to find the cause of this irregularity and its solution. The flow irregularity was solved by a specially designed hydraulic flow passage contoured as a result of an analysis conducted with the water flow test. The results of this effort were a very even and stable flow pattern shown in Figures 3-9 and 3-10. However, before the flow irregularity problem could be studied, a problem in the basic pintle support structure had to be solved. The technique, shown in Figure 3-11, used a center support structure designed for attachment of the pintle tip while at the same time allowing the oxidizer flow to reach the oxidizer orifice. The original design, Figure 3-12, had five large holes in the support structure set at an angle to allow flow to pass down the center tube and out through the pintle cavity. The pintle cavity was designed with a constricting flow passage to eliminate voids caused by the pintle support. However, the water flow tests showed that voids were in the flow pattern. Five additional holes were drilled into the unit to improve the flow. An additional water flow study was conducted to completely develop the cruciform assembly. The design product of this hydraulic study, shown in Figure 3-13, was extremely encouraging. Not only have the flow characteristics been excellent, but the concept has proven injector flexibility as well as economy in fabrication.

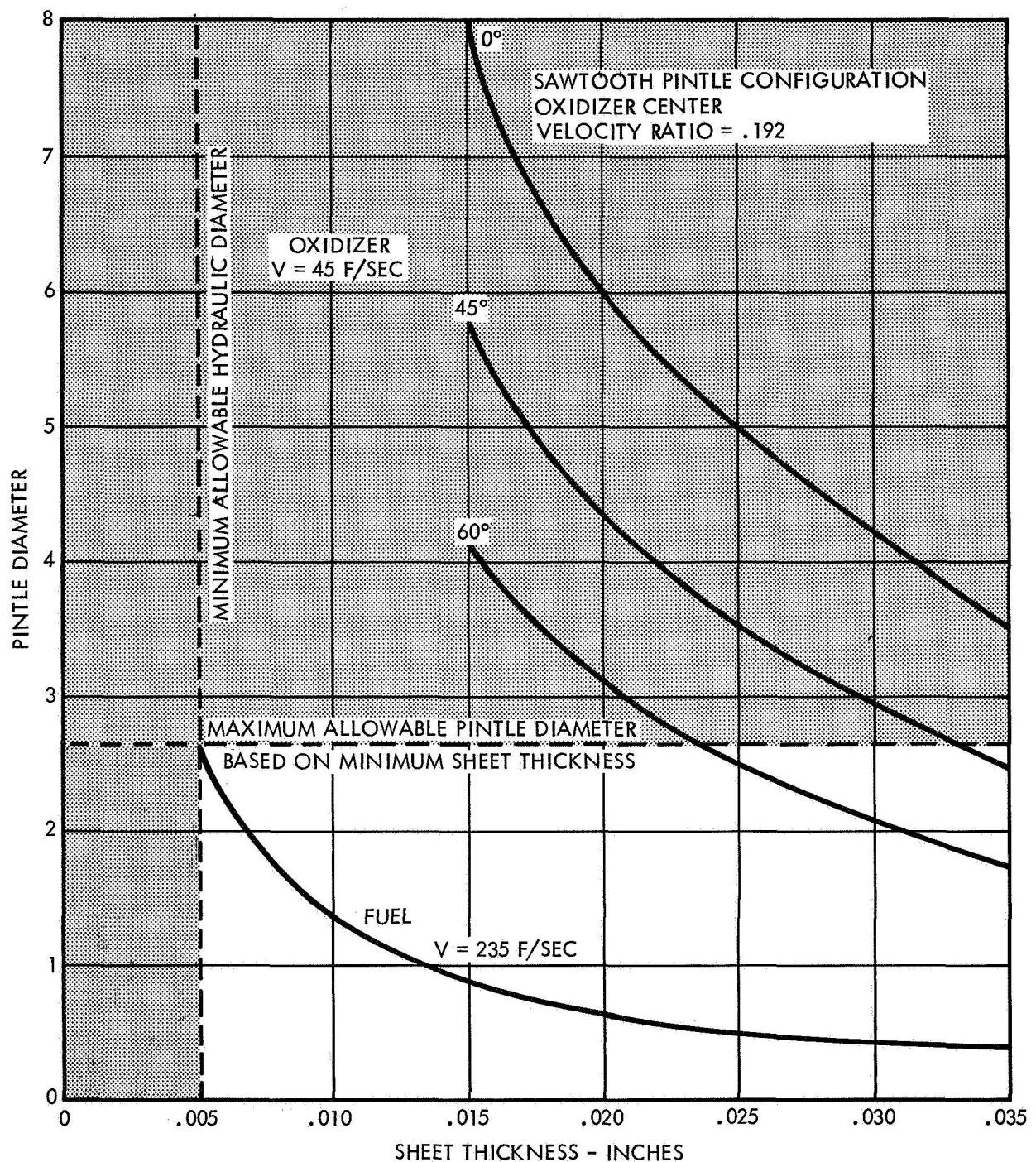


Figure 3-7. Sawtooth Sheet Impingement for Pintle Sizing

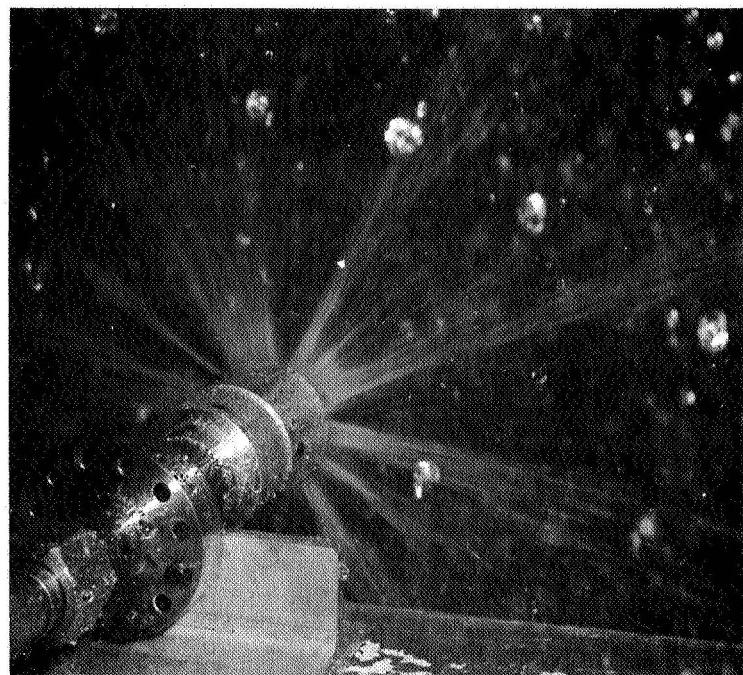


Figure 3-8. Irregular Flow Pattern Found to Exist in the Center Element Without Specially Designed Flow Passage

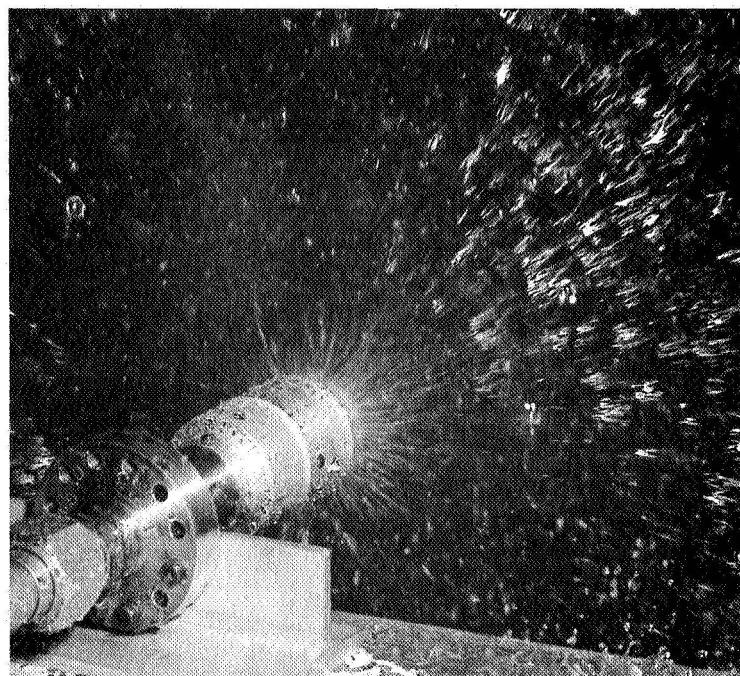


Figure 3-9. Flow Pattern Generated Using the Sawtooth Configuration with Specially Designed Flow Passage to Eliminate Flow Irregularities

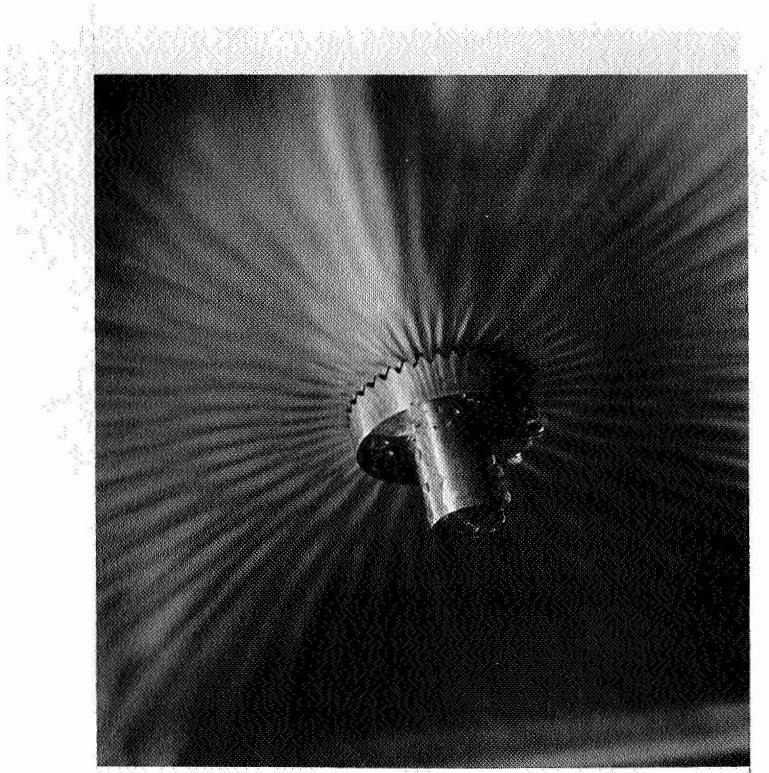


Figure 3-10. Closeup of Sawtooth Flow Pattern with Stable Flow

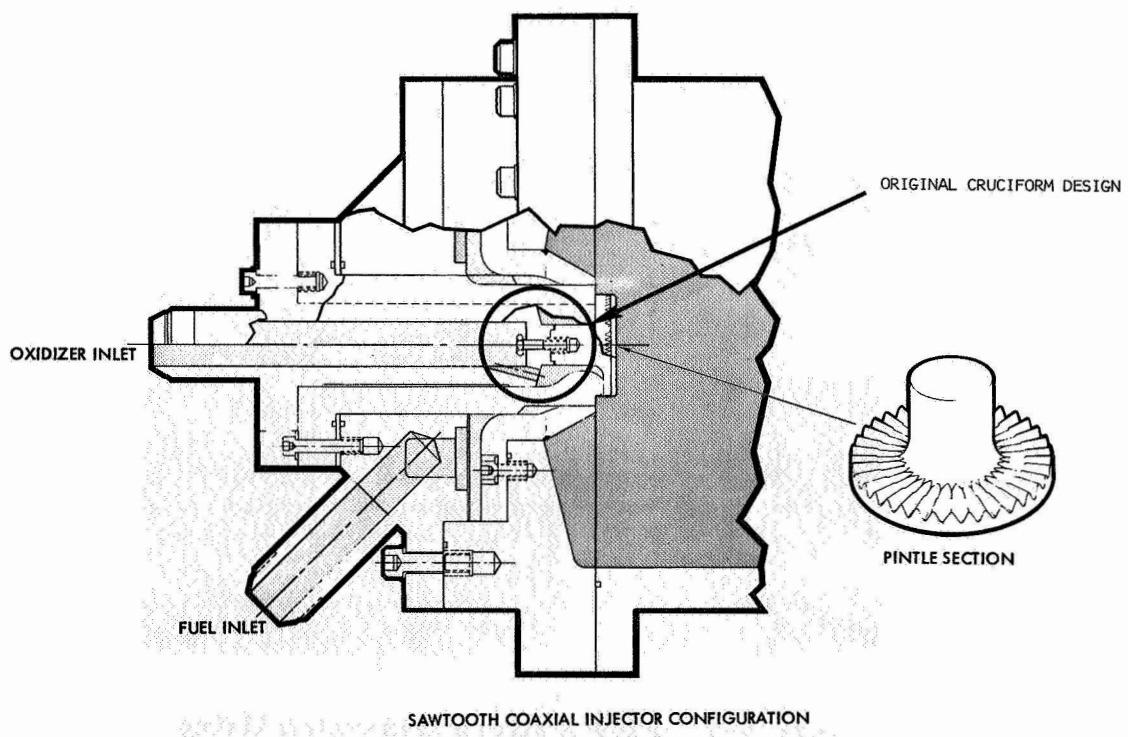


Figure 3-11. Basic Injector Design Showing Original Cruciform Concept

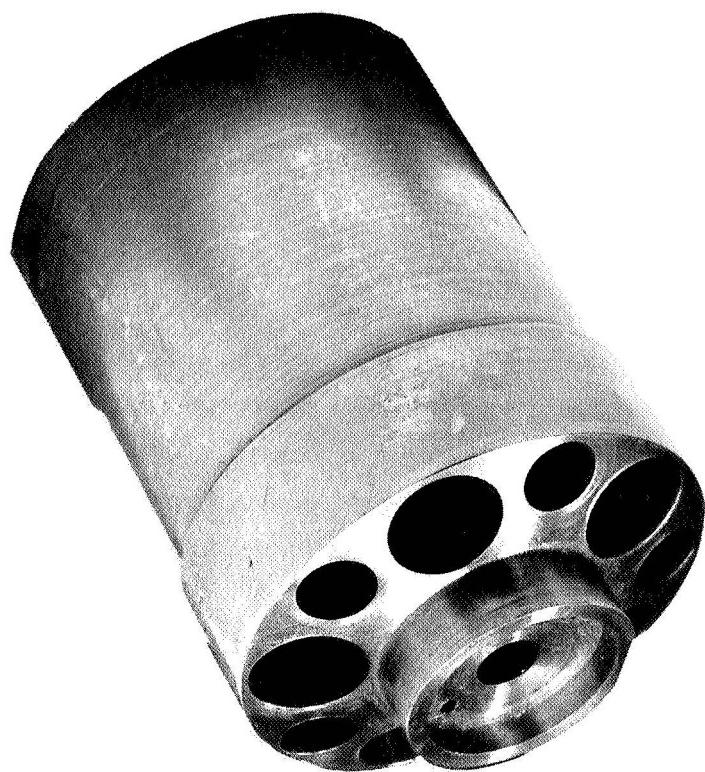


Figure 3-12. Cruciform Assembly

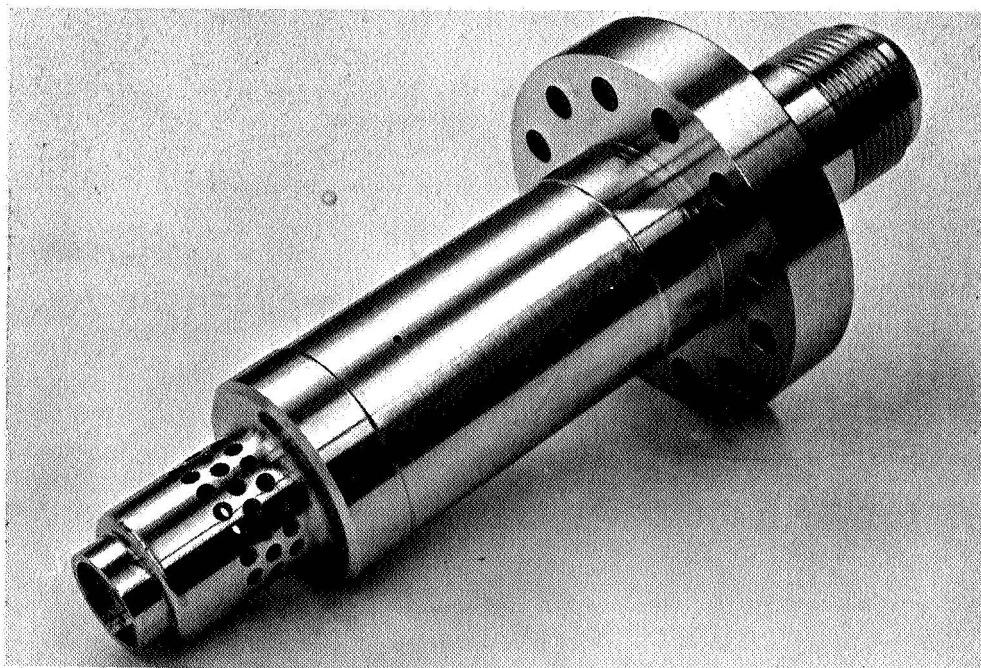


Figure 3-13. Modified Cruciform Showing Multiorifice Radial Flow Passages

### Straight Slot Configuration

The straight slot configuration was an oxidizer element modification which was patterned after the highly successful oxidizer orifice configuration of the LMDE (shown in Figure 3-14). The advantage that the straight slot orifice configuration offered over continuous sheet configurations such as the sawtooth was that combustion venting in the initial reaction zone could occur. TRW has observed that with some hypergolic propellants, propellant venting was necessary to achieve high performance. With a continuous sheet impingement injector, a conical flame zone is created extending from the injector orifices out toward the chamber wall. If the reactivity of the propellants is such that blow-a-part occurs, preventing the propellants from properly mixing, the flame zone tends to trap the fuel behind the conical sheet, resulting in a much lower combustion efficiency than would have occurred if mixing had occurred. With the slot design, propellant reactivity can be used to promote mixing and atomization. As the fuel flows down between the oxidizer orifices blow-a-part reactions only result in the propellants being blown into each other.

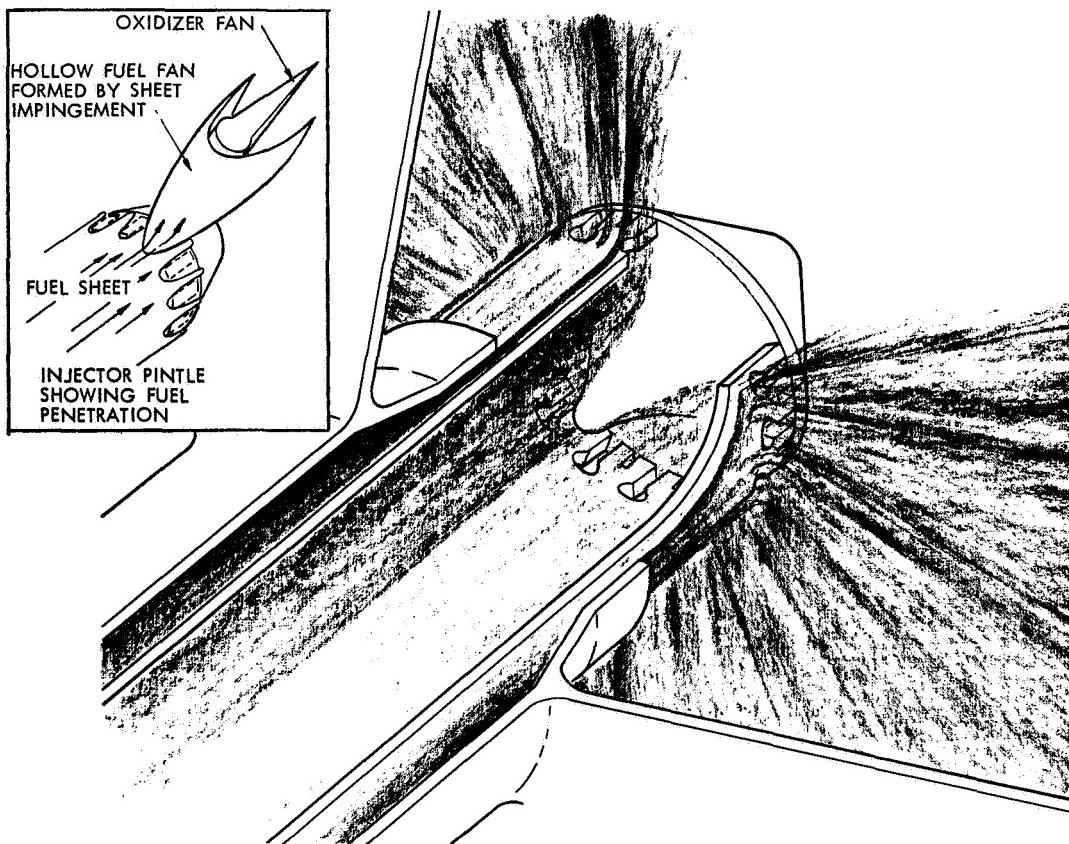


Figure 3-14. Injector Element Schematic Diagram

The original straight slot designs used a single unit outer pintle body and pintle tip and were assembled by brazing the pintle tip to the outer pintle body. It was expected that variations would be made to the primary slots, and in order to make changes in these slots it would be necessary to unbraze one element and braze a new pintle element into the outer pintle body. If any variations had to be made of this orifice design, such as size and shape, it would be necessary to either unbraze and install a new tip or a completely new pintle assembly would have to be fabricated. Because of this flexibility problem, a new innovation was conceived which was a combination of both the sawtooth design and the straight slot design. This innovation involved the use of replaceable rings with a modified sawtooth pintle tip.

Figure 3-15 shows how this ring concept functions. The pintle tip was bolted onto the inner pintle body in the same manner that was used for the sawtooth configuration. The ring was held in place by the pintle tip pressed against the outer pintle body.

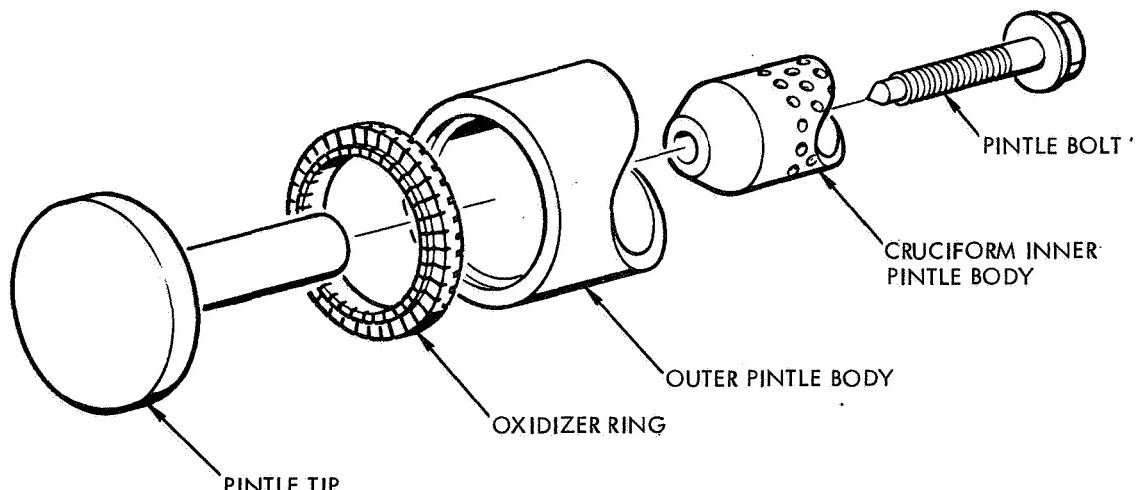


Figure 3-15. Exploded View Showing Ring Concept

The ring concept for fabricating the oxidizer orifice offers a great deal of flexibility to the engine design by allowing many changes to be incorporated and tested.

In order to achieve high performance with a straight slotted configuration, it is necessary to determine several key parameters. These are:

- Percent of Blockage\* — This parameter is determined by using rings with various sizes of primary slots so that the blockage area is optimized.
- Percent of Secondary Flow — Flow is varied by making rings with various sizes of secondary orifices so that the ratio of the orifice area of the secondaries and the primaries is varied.
- Location of the Secondary Orifice with Respect to the Primary Orifice — Purpose of the secondaries is to capture the fuel that escapes through the primary slots; however, if the secondaries are located too close to the primaries, then the secondaries begin to appear as though they were primaries.
- Oxidizer Pressure Drop — Vaporization and atomization of the oxidizer are key parameters to achieving high performance; however, these functions are typically in the direction of high pressure drops which had an adverse effect for ultimate use in a space vehicle, and, therefore, have an upper potential limit.

#### Canted Slot Configuration

The canted slot configuration was a hybrid between the sawtooth and the straight slot configurations. Because of the unknown reactivity effects of the propellants, it was not known how long the slots could be made. The high O/F ratio of space storable propellants (5.35) results in a configuration considerably different than those previously used at TRW with earth storable propellants (2.6). This modification also used the ring concept described in the preceding section. The oxidizer slots were canted at a 60 degree angle to the direction of flow of the fuel. This concept provided a large oxidizer surface area exposed to the impingement of the fuel while at the same time providing the venting which has been required in other propellant combinations. Figure 3-16 shows the coaxial injector with a canted slot ring element. Variations which would be made with the canted slot configuration are:

- Variations in the angle of the slots
- Variations in the length of the slots

---

\* Blockage area is defined as the projected shadow area of oxidizer that is seen by the fuel; 100 percent blockage is a continuous sheet of oxidizer.

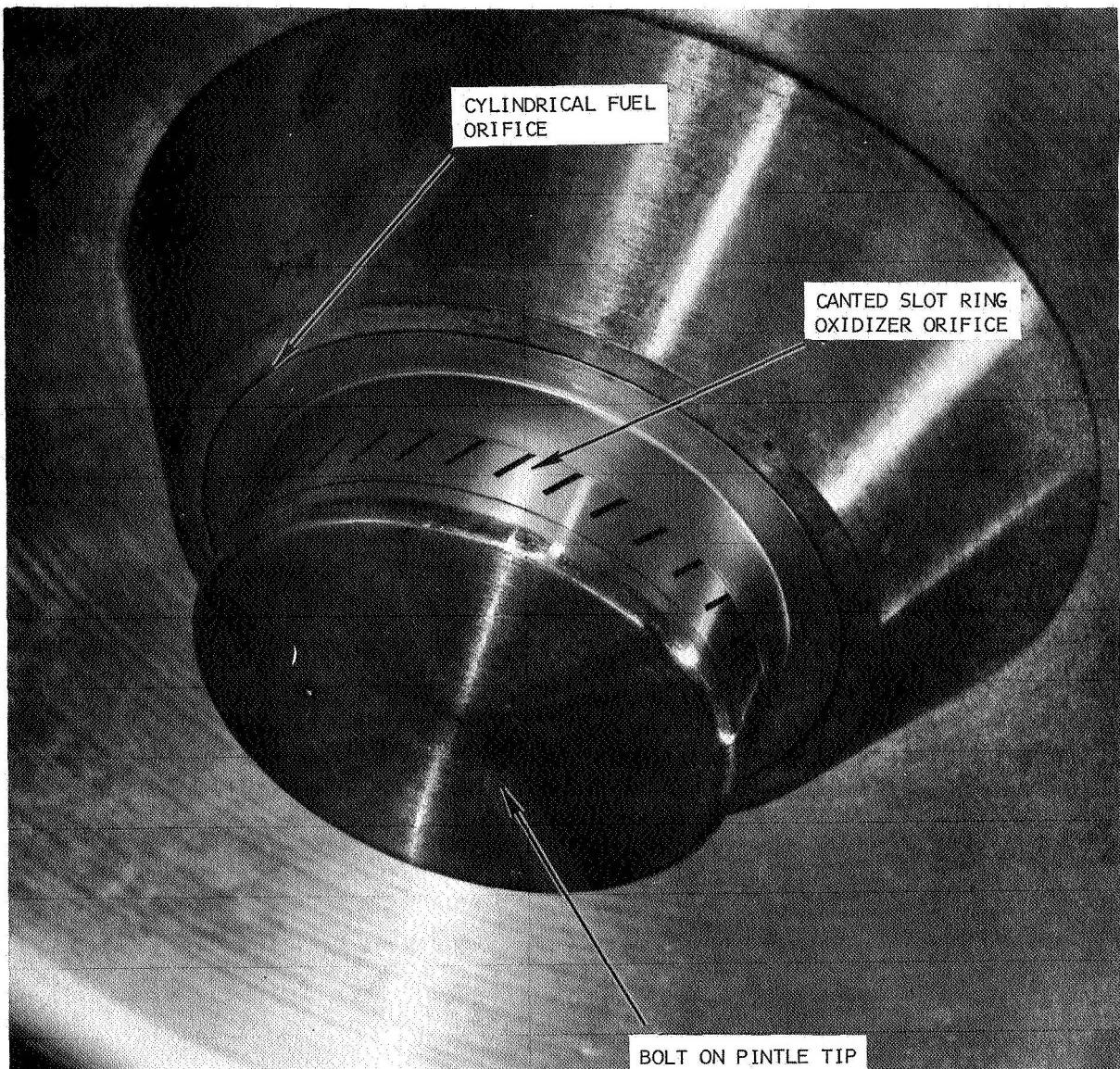


Figure 3-16. Coaxial Injector With Canted Slot Ring Element

- Addition of secondaries following the primaries
- Variations in the length and angle of the secondaries

### 3.1.2 Experimental Thrust Chamber Design

The experimental thrust chamber was a copper heat sink design. The chamber was sized to give nominal run durations of 4 to 6 seconds. It was designed as a flexible piece of hardware being made up of spools and throat sections. With this design, the chamber L\* or throat contraction ratio could be changed by simply changing the spool or throat

section. A nominal contraction ratio of 2.5:1 was selected for the baseline test series. The nominal L\* for the series was 30 inches and consisted of one throat section with a 2.5 contraction ratio and one spool section.

Figures 3-17 and 3-18 show the nominal chamber design. The complete chamber assembly could have L\*'s of 15, 30, 45 and 60 inches, depending on the number of spools included. For off-design testing, a throat section was designed with a contraction ratio of 4.5:1. The flange bolt circles were backed up by steel load distributing rings to insure maximum reuse of the hardware.

The nozzle and throat incorporated a 30- to 40-degree converging angle and a full radius throat blended into a 15-degree angle nozzle. The blending was done to enhance a maximum performance return of the nozzle, based upon the analytical nozzle studies. The nozzle expansion (1.85) was truncated for optimum test site ambient pressure.

#### Wall Thickness

The chamber wall thickness was sized for stress limits, accounting for the wall temperature profile. The wall temperature profile was estimated by assuming temperature distribution parabolic and a thermal boundary layer,  $\sigma(t)$ , where no heat has penetrated. The temperature distribution is taken as

$$T = a + br + cr^2 \quad (3-14)$$

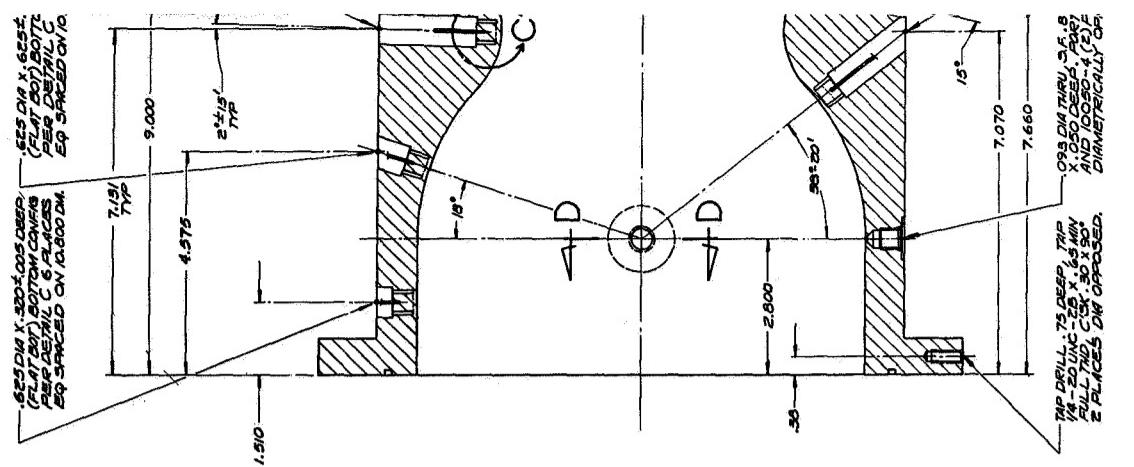
$$T = T_s @ r = 0 \quad (3-15)$$

$$\frac{\partial T}{\partial r} = 0 @ r \quad (3-16)$$

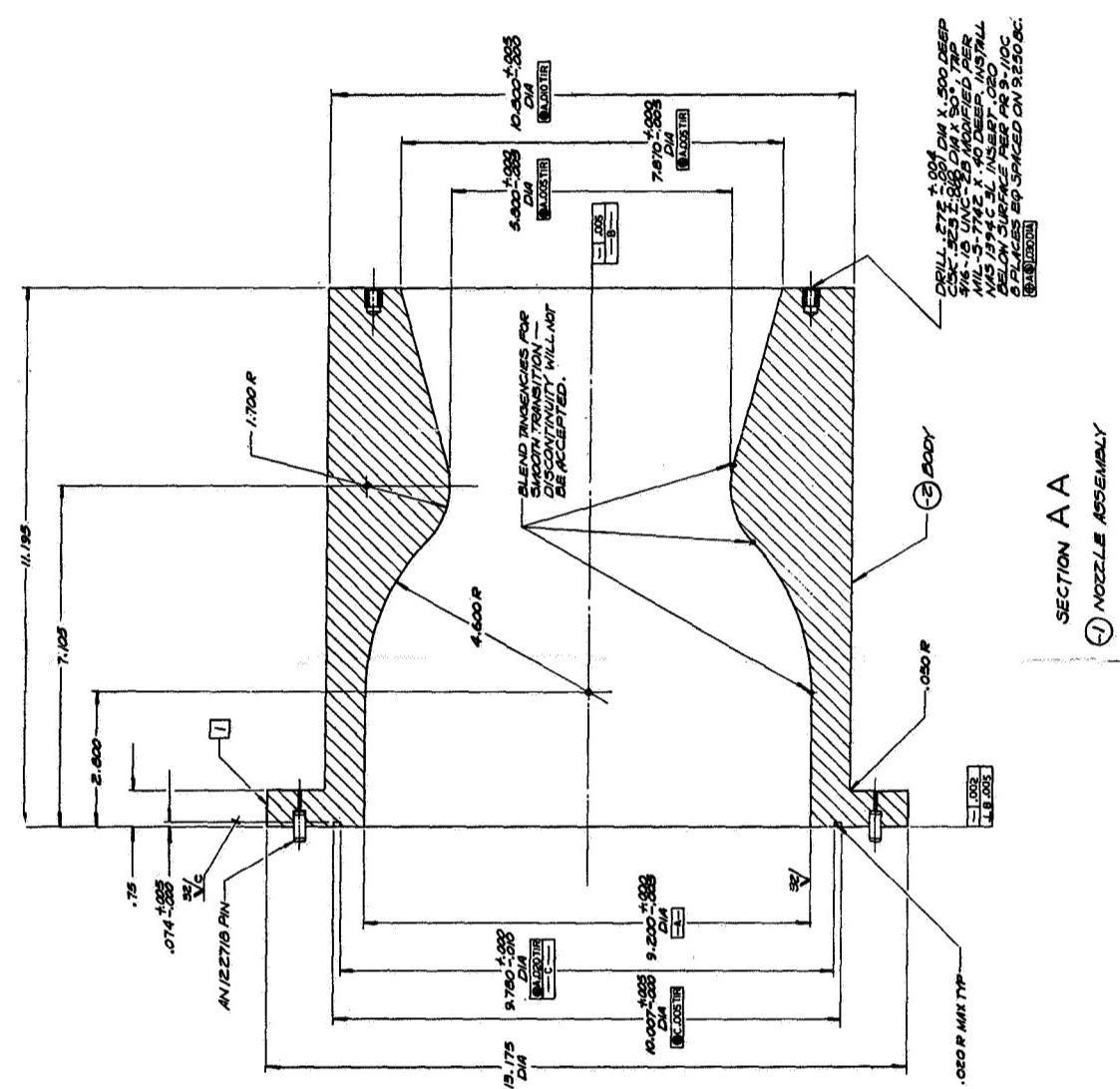
$$T = T_i @ r = \delta \quad (3-17)$$

The thermal penetration distance is found by a moment solution approach

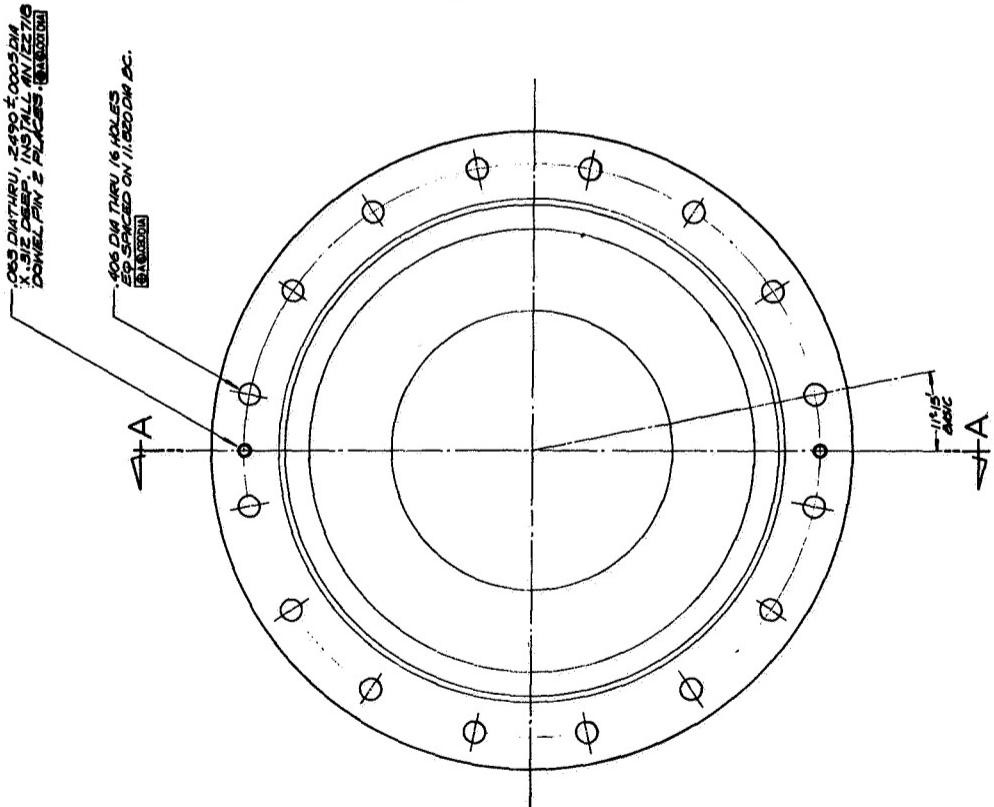
$$\frac{\partial}{\partial t} \int_0^\delta T(X) dX = \int_0^\delta \frac{\partial T}{\partial r} \frac{dr}{r} \quad (3-18)$$



SECTION B-B



**SECTION A A**



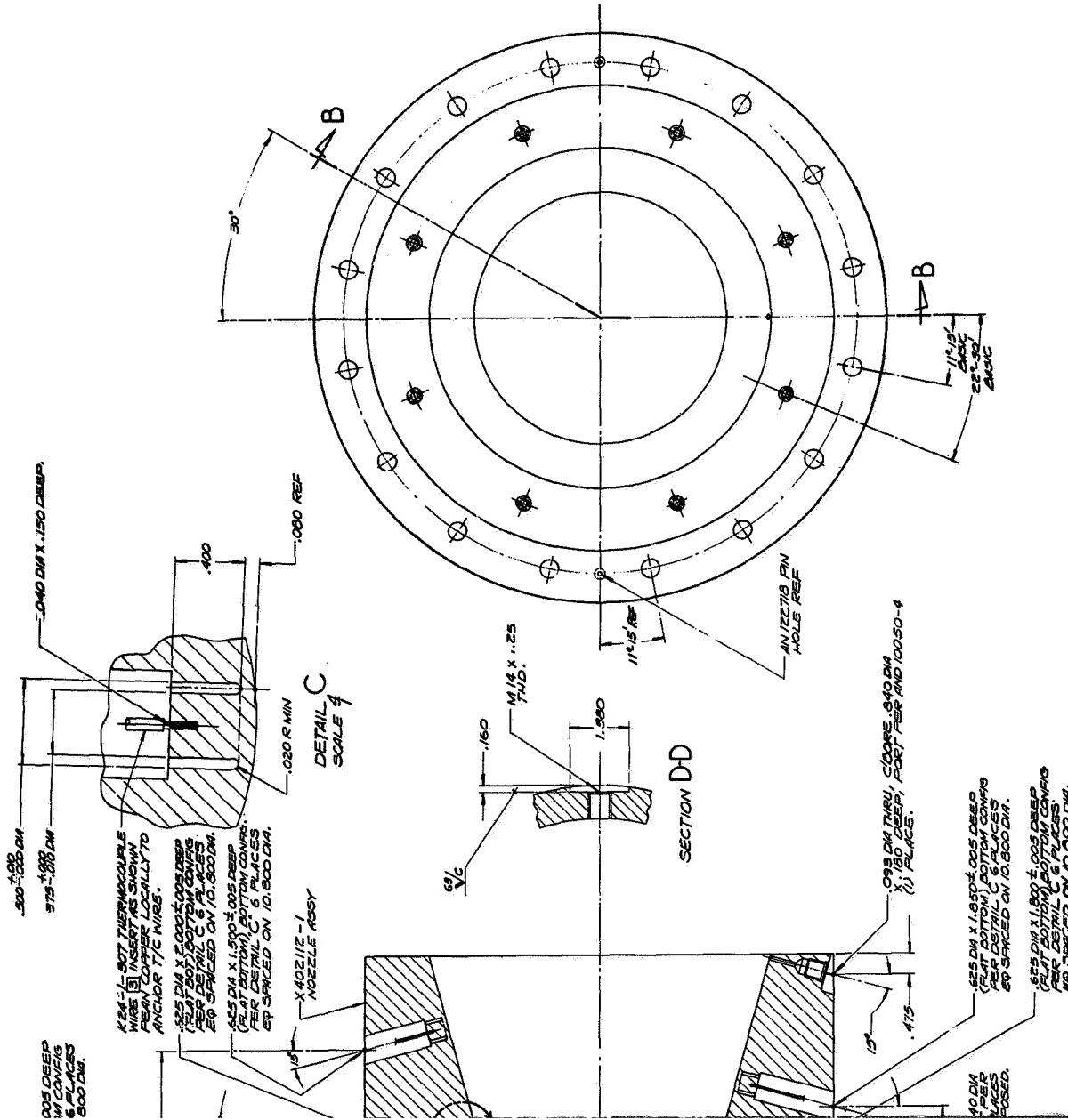


Figure 3-17. Nominal Thrust Chamber Throat Section  $\epsilon = 2.5$

[3] CLAUDIO S. GORDON CO. 1/50 EL SEGUNDO CALIF. 90246.  
2. CLEAN PFR FOR 2-2 LEVEL 1.  
[1] DIMENSION MARKS IN ACCORDANCE WITH THIS SECTION  
LOCATED ON SHEET 2 AS SECTION 1.  
NOTES UNLESS OTHERWISE SPECIFIED



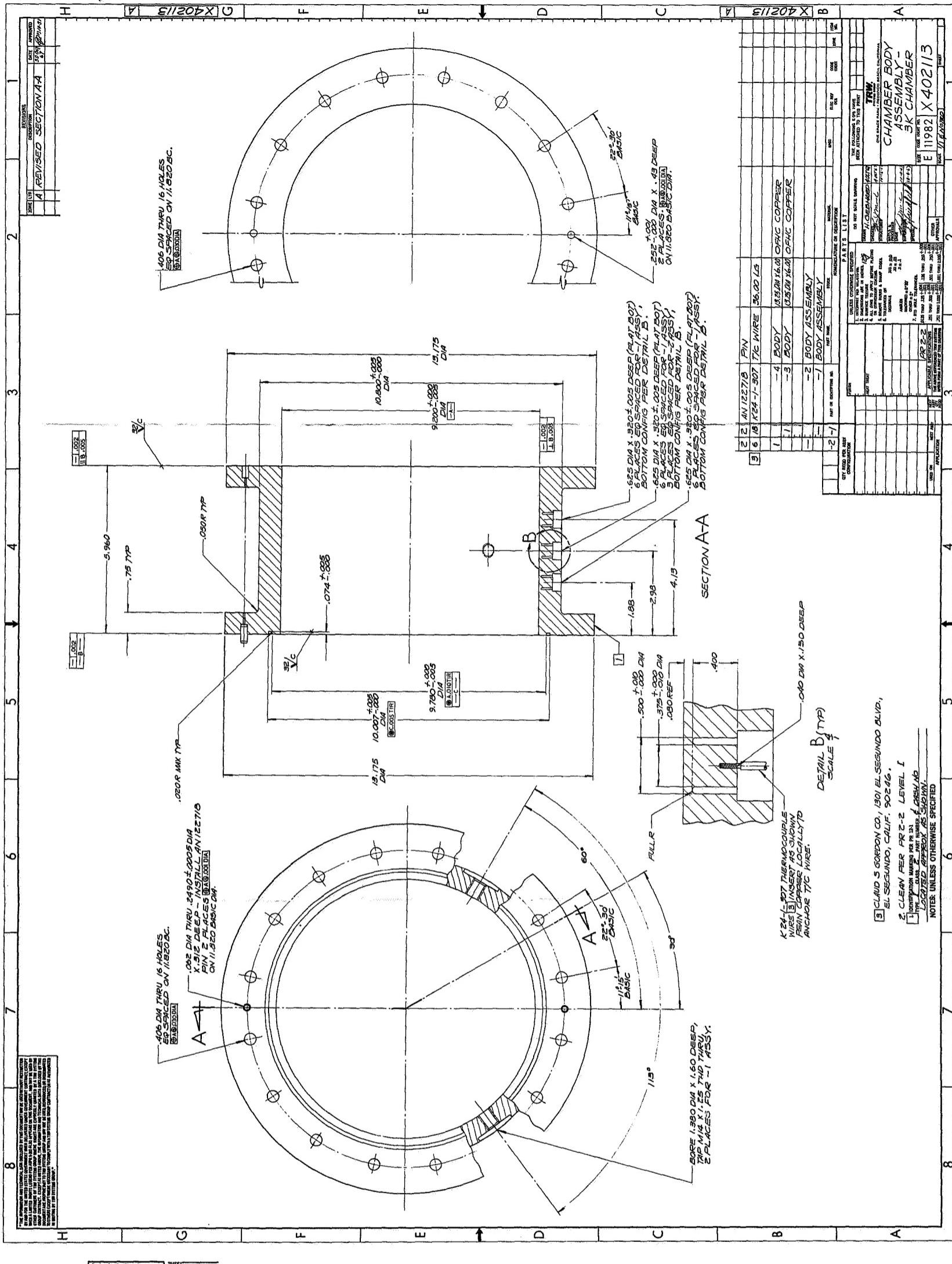


Figure 3-18. Thrust Chamber Spool Sections



The surface temperature is found to be

$$T_s - T_i = \frac{\left( \frac{h}{k} \sqrt{\frac{3}{2} \alpha t} \right) (T_{ad} - T_i)}{1 + \frac{h}{k} \sqrt{\frac{3}{2} \alpha t}} \quad (3-19)$$

Therefore, the thermal penetration distance is approximated by

$$\delta(t) = \sqrt{6\alpha t} \quad (3-20)$$

The stress level is taken as that for a long right circular cylinder internally pressurized. This stress is given by

$$S = \frac{P_c d}{2L} \quad (3-21)$$

For the nominal firings, the thermal penetration distance was approximately 0.8 inch and under these conditions the back side wall temperature was still at ambient temperature. Taking into account 100 percent overpressure, the stress level with a 0.8 inch wall was only approximately 600 psi. This was more than adequate for OFHC forged copper. Furthermore, this wall thickness was also adequate for all instrumentation requirements.

#### Run Duration

To obtain best performance data, it is necessary to have run durations sufficiently long so that operational parameters (flow ratio, propellant temperature, thrust propellant pressures, chamber pressure) have stabilized for a period of time to show overall steady-state operation. This period of time, based on past experience, is at least 1.5 seconds.

To estimate the internal surface temperature as a function of time, Equation B-6 was used. The effective film coefficient,  $h$ , was taken as

$$h = h_{Bartz} \frac{(Q/A_{experimental})}{(Q/A_{theoretical})} \quad (3-22)$$

where the correlation term was determined by the carbon effect data. Previous NASA-sponsored efforts (NAS 3-4195) have shown that the propellant combination of FLOX/LPG will provide free decomposition carbon on cooled thrust chamber walls. The TRW performance program indicated the existence of free carbon in cool zones, such as might occur at or near the combustion chamber wall. The effect of this carbon deposition was to effectively decrease the surface heat transfer film coefficient as follows:

$$h_{\text{eff}} = \frac{hg K}{K + hg\Delta X(t)} \quad (3-23)$$

where

$h_{\text{effective}}$  = the effective film coefficient

K = carbon deposit conductivity

$\Delta X(t)$  = carbon deposit thickness as a function of time

#### Instrumentation

The chambers were instrumented for static and dynamic pressure measurements as well as thermal measurements. Dual static measurements were provided at the start of the convergence and at the injector end. Dynamic pressure measurements were provided through the use of Kistler water-cooled, helium-bleed high frequency transducers. Provision was made to equip each chamber with three Kistler transducers. (In addition to chamber pressure data, thrust data were also obtained to provide a means of correlating characteristic velocity calculations on the basis of both chamber pressure and thrust measurements.)

The chambers were fully instrumented to provide thermal data for heat transfer analysis. The heat transfer data were obtained through the use of heat transfer plugs shown in Figure 3-19. These temperature monitoring points were designed to approach an isothermal condition of the local chamber walls. The plugs were machined in the thrust chamber wall and flush to the inner surface. By having the plug material identical to the wall material, a negligible distortion of the heat flux profile occurs.

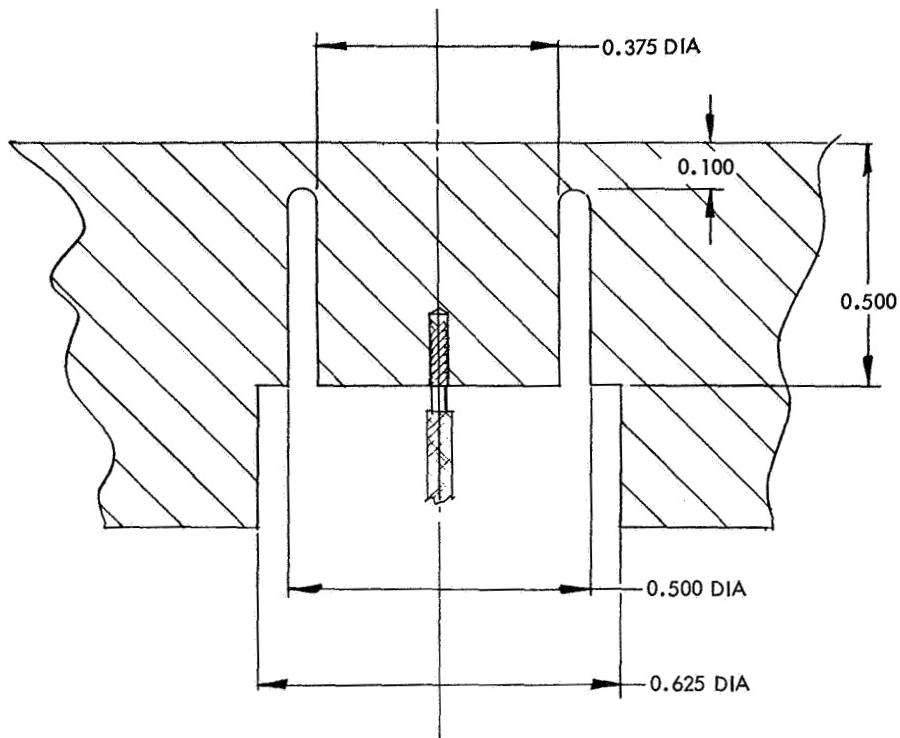


Figure 3-19. Chamber Thermocouple Plug

The temperature data were taken on the back side of the plug to eliminate gas side interference effects. (A detailed analysis of the calorimetric plugs is presented in Appendix A.)

### 3.1.3 Injector Fabrication

The injector assembly, Figure 3-20, was fabricated of 304 stainless steel and nickel 200. Where components would be subjected to the flame zone within the chamber, nickel 200 was used. The entire injector assembly was simple from a fabrication point of view. The primary operations in fabricating a coaxial-type injector are lathe turning operations with some mill work.

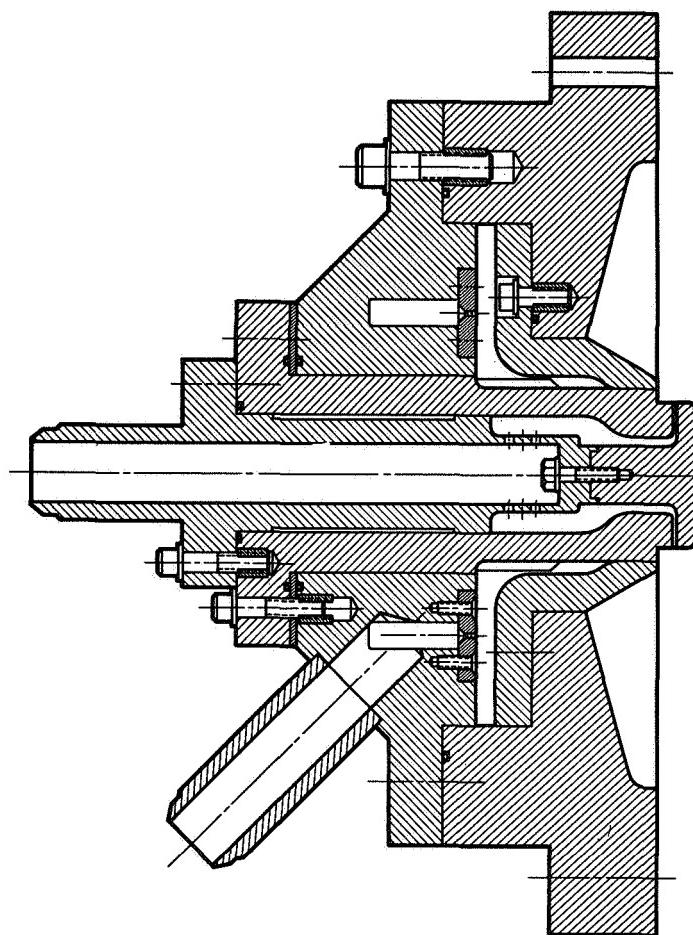


Figure 3-20. Injector Assembly

The first major subassembly was the faceplate body and fuel annulus, described in Section 3.1.1. These components were fabricated independently then assembled and doweled together. The assembly was then concentrically bored to provide precision alignment between the body and the fuel annulus which acts as the fuel metering surface. Using this technique, the fuel annulus could be removed and replaced without loss of concentricity.

The faceplate and body were machined of 304 stainless, while the fuel annulus was machined from a nickel 200 forging. Standard AN type fittings were used for the propellant feed lines. The dowel pin holes in the fuel annulus were jig-bored to the faceplate because the assembly was designed to accommodate interchangeable fuel annuli, each of which

must be aligned precisely with the bore of the injector body. This capability enabled injector assembly with various fuel annuli to vary the fuel pressure drop.

The second major subassembly of the injector was the oxidizer injector element, Figure 3-21. This element consisted of the outer pintle body, inner pintle body, and pintle tip described in Section 3.1.1. The outer pintle body was fabricated from a nickel 200 forging. In order to avoid any inner-propellant welds, this assembly was made of a single piece of nickel. However, consideration was given to welding a flange to a smaller nickel forging. This method, however, was discarded when the cost of welding was compared to the cost of a larger nickel forging. After machining, the outer pintle body was chrome plated on the register surfaces in order to provide a lubricity and antiabrasive coating to the nickel. The inner pintle body was fabricated of 304 stainless and was aligned by precision fit between the registers and the inner bore of the outer pintle body.

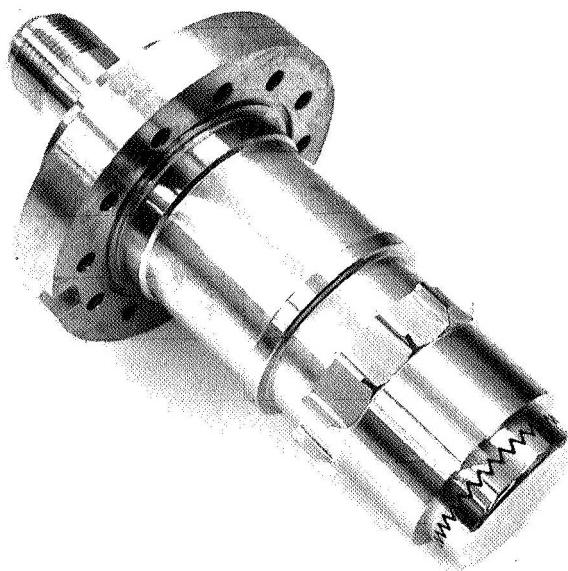


Figure 3-21. Oxidizer Subassembly

The pintle tip was attached to the end of the inner pintle body by means of a bolt which was fitted through the inner pintle body and screwed into the pintle tip. In the case where rings were used for the oxidizer orifice, a fourth component was fabricated for this major subassembly. The basic blank ring was fabricated to size and then, using a rotary end mill, the slots were added in accordance with the necessary design. A unique feature of the overall concept was that this oxidizer element assembly could be completely removed from the injector without disassembly of either of the two major subassemblies.

Each component of the injector assembly was thoroughly cleaned prior to assembly. This procedure involved cleaning by means of degreasing baths and neutralizing baths in ultrasonic cleaners. After the ultrasonic cleaning process, each component was thoroughly cleaned with Freon then packaged in plastic bags, sealed, and placed in the clean room assembly area. Figure 3-22 shows a typical scene in the assembly process in the TRW laminar flow tunnel. Before the components were assembled, they were inspected for hydrocarbon deposits by means of blacklight and each component was washed with Freon again.

### 3.1.4 Chamber Fabrication

The chambers were fabricated from OFHC copper forgings. The copper in these forgings was worked at least 50 percent to insure a fine grain structure. Basic fabrication of the thrust chamber components, i.e., spools and the nozzle assemblies, was a straightforward machining operation. The nozzle sections were machined on tracer lathes to develop the proper contours. Figure 3-23 shows a typical chamber spool section.

Because of the number of thermocouple calorimetric plugs in the chamber assembly (54 for the nominal thrust chamber assembly), the installation of these plugs represented a sizeable portion of the fabrication effort. The most difficult of these to fabricate were the plugs located in the throat sections, because of the difficulty in establishing a true reference point from an angle and a complex contour.

Assembly of the thermocouples in the calorimetric plug was done by inserting the thermocouple wire into the drilled hole in the center of the plug. The copper base metal of the plug was then "peened" into the wire to insure attachment.

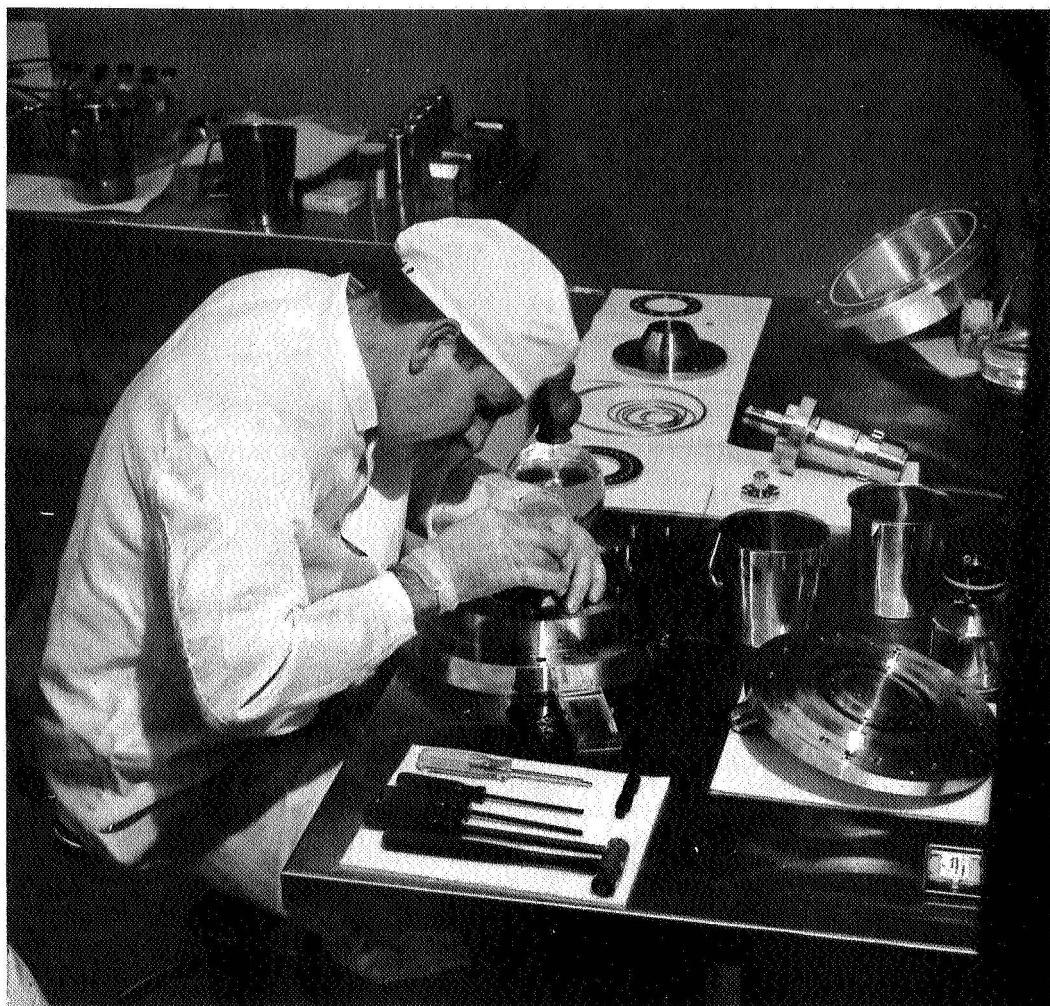


Figure 3-22. Injector Assembly in Clean Room

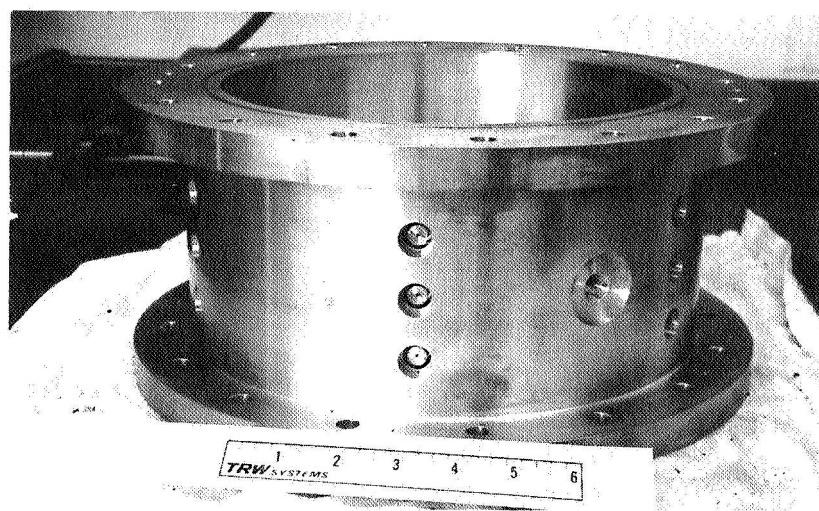


Figure 3-23. Chamber Spool Section

## 4. TEST EFFORT

### 4.1 TEST DESCRIPTION

Fifty-eight uncooled sea-level tests were conducted for the baseline test series: 10 with the sawtooth injector configuration, 11 with the canted slot injector configuration, and 37 with the straight slot injector configuration. The test objectives were to determine the relative merits of the three injector configurations with the specified FLOX, light hydrocarbon propellant combination. All of the injector configurations were designed for liquid injection (cryogenic conditions) and the chambers were uncooled, being made of OFHC copper.

Figure 4-1 shows a typical engine installation on the test stand. The engine was mounted on the thrust stand on a split yoke so that it rests on the chamber flange. The engine was installed by slipping the chamber into the yoke, then closing and bolting the yoke together. The injector was then bolted to the top flange of the chamber. Rigid lines were used to feed both the oxidizer and fuel to the engine. This type of engine

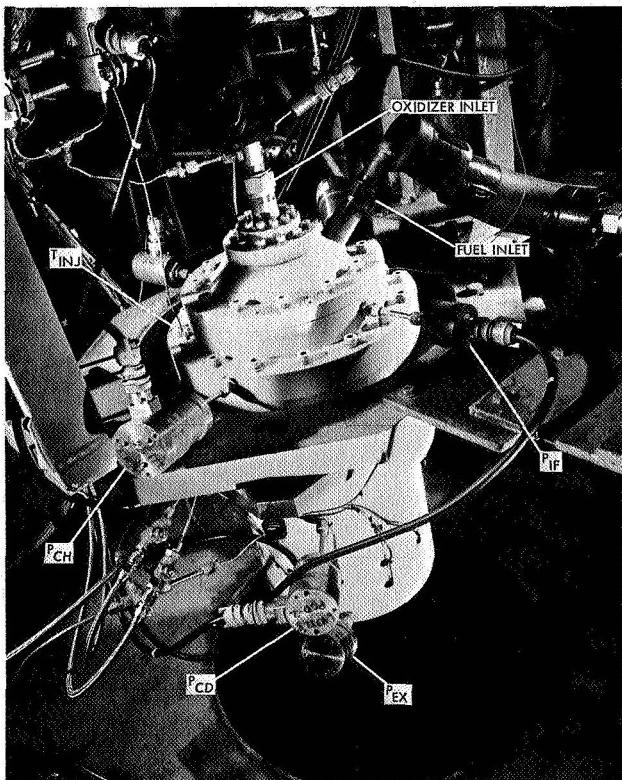


Figure 4-1. Engine Installation on Test Stand

installation provided the most convenient technique for making changes on the stand with a minimum of effort. To make changes to the injector it was not necessary to remove the chamber assembly and its associated instrumentation. The injector was removed by disconnecting the feed lines and the injector instrumentation and then unbolting the injector from the upper chamber flange.

The engine installation without the injector thermal insulation in place is also shown in Figure 4-1. Prior to operating the engine, a four-piece molded insulation was installed around the injector to insure complete chilldown of the injector and minimize heat losses during operation. This insured that liquid propellant was supplied to the injector at all times during the run.

Instrumentation consisted of pressure transducers at the injector entrance of both the oxidizer and fuel lines to monitor the injector inlet pressures. Temperature probes were also located in both propellant lines just upstream from the injector.

Two pressure transducers located 180 degrees apart in the injector faceplate monitored the fuel pressure downstream from the internal distribution ring. Two transducers monitored the head end chamber pressure at the faceplate of the injector. These transducers were located on the injector faceplate flange. Two thermocouples, located 180 degrees apart in the injector body, monitored the injector temperatures during chilldown.

Two pressure transducers, located upstream of the throat section of the chamber monitored the downstream chamber pressure. Data from these transducers were used to calculate the stagnation pressure in the chamber. The chamber was equipped to monitor high frequency pressure conditions by means of Kistler helium bleed water cooled transducers. On the nominal chamber, 54 thermocouples were used to monitor chamber heat flux distributions (see Figures 6-4 and 6-5 for locations).

Early in the test program, some difficulties arose with respect to the operation of the test stand. These difficulties, however, were all minor being primarily associated with system chill down procedures and insulation. The program did not have a single major failure. The fact

that no major failures occurred during the program can be attributed in part to the constructive advice and guidance from the Lewis Research Center staff. Some of the more notable recommendations made by Lewis included a complete burn wire system throughout the entire feed system. This burn wire system was set up to provide an automatic shutdown of the system in the event that a fire from the propellants occurred at any time during the test sequence.

Purges were done with GN2 and a low pressure positive purge existed on the engine at all times while the engine was mounted on the stand. This techniques precluded moisture and other contaminants from getting into the engine. In addition, a high pressure GN2 purge was used to blow out all residual propellants at the end of a test.

#### 4.2 TEST SUMMARY

Table 4-1 is a summary of all of the tests conducted on the program. This table is a composite of the test results and does not include any performance corrections. The numbers are measured values and taken as averages for the entire run. Table 4-2 is a nomenclature key for all the injector configurations. Three basic injector configurations were tested to determine their relative performance values. These configurations were the sawtooth, the canted slot, and the straight slot injectors. Within the framework of these configurations, several modifications were made to each basic configuration to investigate effects on performance. The sawtooth used two modifications to the basic configuration; the canted slot used six modifications; and the straight slot used nine modifications to its basic configuration.

In conjunction with Table 5-1, a summary is given of each test and its results in the following pages.

#### Test 070

The first hot firing test of the program was assigned run number 070. This test used the sawtooth configuration SW-1 and was set up to operate at the optimum design conditions for this sawtooth injector. The test was also intended to check out the newly constructed test stand. At this time, the test stand was equipped with only a 4-gallon fuel tank which limited the amount of fuel available for the test. Only one K bottle of fuel

Table 4-1a. Test Summary

Run No.	Injector Element	MR 0/F	P <sub>O</sub> psia	ω <sub>T</sub> lb/sec	ω <sub>O</sub> lb/sec	ω <sub>F</sub> lb/sec	ΔP <sub>O</sub> psi	ΔP <sub>F</sub> psi	C <sub>O</sub> ft/sec	F	Run Duration	FLOX Concen- tration %	Comments
HB2-070	SW-1												
071	SW-1	5.6	44.9	10.9	9.2	1.7	155	330	3481	1028			
072	SW-1	5.3	56.4	10.9	9.2	1.7	77.7	32.6	4000	1314	5		
073	SW-1	3.6	47.6	12.6	9.8	2.8	94	153	3214	1036	5		
074	SW-1	3.7	43.0	12.7	10.0	2.7	63	140	2882	919	5		
075	SW-1	5.0	41.8	11.4	9.6	1.9	121	65	3080	868	5		
076	CS-1	5.4	46.9	12.2	10.3	1.9	72.2	52.7	3244	1061	5		
077	CS-1	5.5	76.4	12.4	10.5	1.9	173	63.7	5208	2146	5		
078	SS-1	3.8	78.0	12.9	10.2	2.7	130	167	5118	2158	5		
079	CS-1	5.2	67.4	12.6	10.6	2.0	149	278	4529	1792	5		
080	SW-2	5.2	71.4	11.9	10.0	1.9	149	87.1	5013	2119	5		
081	CS-1	5.3	66.0	12.9	10.9	2.1	163	102	4222	1739	6		
082	CS-1	4.8	79.9	12.1	10.0	2.1	383	73	5615	2227	6		
083	SS-2	4.2	57.4	13.1	10.6	2.5	94	92	3726	1411	7		
084	SS-3	5.1	63.2	12.9	10.8	2.1	92	50	4166	1647	6		
085	SS-3	5.7	62.9	14.1	12.0	2.1	116	42	3793	1498	6		
086	CS-2	5.4	61.6	12.2	10.3	1.9	156	368	4293.	1413			
087	CS-2	5.3	37.7	12.5	10.5	2.0	23	258	2565	1241	6		
088	CS-3	4.7	58.3	11.4	9.4	2.0	430	53	4348	1259	2		
089	CS-3	5.3	90.7	12.5	10.5	2.0	367	86	6170	2547	3		
090	CS-4	5.3	82.8	12.6	10.6	2.0	220	72	5588	2330	6		
091	CS-5	5.3	82.4	12.5	10.5	2.0	198	72	5605	2222	6		
092	CS-6	5.1	81.4	12.2	10.2	2.0	142	76	5673	2170	2		
093	SS-4	5.2	93.1	12.4	10.4	2.0	251	39	6384	2630	6		
094	SS-5	5.3	80.2	12.5	10.5	2.0	218	39	5456	2145	6		
095	CS-3A	5.3	90.0	12.5	10.5	2.0	339	39	6122	2515	6		

Table 4-1b. Test Summary

Run No.	Injector Element	Average Measured Values During Run						Peak Measured Values During Run						Comments			
		P <sub>o</sub> psia	MR O/F	ω <sub>T</sub> lb/sec	ω <sub>O</sub> lb/sec	ΔP <sub>O</sub> psi	ΔF <sub>F</sub> psi	C <sub>O</sub> ft/sec	F	P <sub>o</sub> psia	MR O/F	ω <sub>T</sub> lb/sec	ω <sub>O</sub> lb/sec	C <sub>O</sub> ft/sec	F	Run duration %	
<b>HB2-096</b>																	
097	SS-6	5.3	96.6	12.6	10.6	2.0	268	4.2	651.9	2747	5.2	96.5	12.4	10.4	2.0	661.7	2746
098	SS-6	5.9	93.2	12.4	10.6	1.8	275	4.7	6391	2614	5.9	93.3	12.4	10.6	1.8	6398	2636
099	SS-6	4.7	97.5	12.5	10.3	2.2	259	62	6632	2799	4.6	97.3	12.3	10.1	2.2	6727	2797
100	SS-6	4.4	90.7	11.8	9.6	2.2	219	54	6536	2549	4.3	90.8	11.6	9.4	2.2	6656	2549
101	SS-6	4.0	92.2	12.0	9.6	2.4	217	50	6533	2598	4.0	90.5	11.7	9.3	2.4	6577	2539
102	SS-7	5.1	97.8	12.8	10.7	2.1	270	23	6197	2792	5.1	98.9	12.8	10.7	2.1	6570	2831
103	SS-8	5.5	97.7	12.9	10.9	2.0	194	39	6440	2795	5.1	97.7	12.9	10.8	2.1	6440	2777
104	SS-9	5.1	97.2	12.9	10.8	2.1	249	41	6497	2842	5.1	98.2	12.9	10.8	2.1	6473	2869
105	SS-8	5.4	96.3	12.7	10.7	2.0	248	41	6448	2750	5.1	97.6	12.8	10.7	2.1	6484	2787
106	SS-10	5.3	93.1	12.6	10.6	2.0	253	38	6154	2744	5.1	97.0	12.8	10.7	2.1	6444	2771
107	SS-11	5.3	81.0	12.6	10.6	2.0	208	41	5466	2199	4.3	95.1	12.8	10.4	2.4	6318	2703
108	SS-6	4.2	96.4	13.1	10.6	2.5	267	57.4	6257	2633	4.9	95.7	13.0	10.8	2.2	6260	2645
109	SS-6	4.7	95.9	13.2	10.9	2.3	281	67.0	6178	2663	5.6	96.4	13.2	11.2	2.0	6210	2680
110	SS-6	5.4	96.7	13.4	11.3	2.1	294	59.1	6136	2706	6.0	96.2	13.3	11.4	1.9	6150	2667
111	SS-6	6.0	95.4	13.3	11.4	1.9	310	50.2	6099	2697	5.3	92.1	12.5	10.5	2.0	6265	2601
112	SS-6	5.3	92.8	12.6	10.6	2.0	281	40.0	6263	2664	5.7	92.6	12.7	10.8	1.9	6200	2588
113	SS-6	5.7	91.7	12.8	10.9	1.9	289	44.1	6092	2570	5.5	95.0	13.0	11.0	2.0	6214	2554
114	SS-6	5.2	95.4	13.1	11.0	2.1	290	50.0	6192	2692	4.4	95.6	13.0	10.6	2.4	6253	2689
115	SS-6	4.4	94.2	13.0	10.6	2.4	261	73.7	6162	2661	5.0	95.1	12.7	10.6	2.1	6367	2608
116	SS-6	4.9	95.3	13.0	10.8	2.2	273	56.8	6233	2677	5.2	93.1	12.3	10.3	2.0	6436	2606
117	SS-12	5.0	93.4	12.6	10.5	2.1	267	40.8	6303	2592	5.1	95.1	12.1	10.1	2.0	6683	2671
118	SS-12	5.1	94.6	12.2	10.2	2.0	294	49.2	6592	2622	4.3	95.3	12.3	10.6	1.7	6596	2651
119	SS-12	5.9	95.7	12.4	10.6	1.8	301	46.7	6551	2659	4.7	97.6	12.4	10.2	2.2	6693	2711
120	SS-12	4.8	96.7	12.4	10.3	2.1	282	72.3	6594	2728	4.2	96.5	12.4	10.0	2.4	6617	2704
121	SS-12	4.2	95.9	12.4	10.0	2.4	269	79.1	6534	2659	5.1	91.4	12.1	10.1	2.0	6423	2492
122	SS-12	5.2	91.4	12.1	10.2	1.9	282	39.8	6385	2468	4.3	95.8	12.2	9.9	2.3	6468	2485
123	SS-12	4.2	92.9	12.3	9.9	2.4	258	62.6	6373	2471	4.3	96.5	12.3	10.0	2.3	6671	2728
124	SS-12	4.3	96.5	12.3	10.0	2.3	266	64.5	6628	2728	5.3	97.9	12.4	10.4	2.0	6724	2719
125	SS-12	5.3	97.2	12.4	10.4	2.0	282	58.1	6603	2760	5.1	163.8	11.7	10.8	1.9	6670	2864
126	SS-12	5.1	164.3	11.8	9.9	1.9	239	52.2	6609	2891	4.4	163.6	11.7	9.5	2.2	6684	2851
127	SS-12	4.4	163.7	11.8	9.6	2.2	225	61.0	6570	2856	4.2	163.7	11.7	9.5	2.2	6684	2851

Pintle Bolt Failed  
Pintle Bolt Reacted  
With FLOX

FLOX

Run  
duration %

Comments

40

90

4

4

4

4

4

4

4

4

4

4

4

4

4

4

4

4

4

4

4

4

4

4

4

4

4

4

4

4

4

4

4

4

4

4

4

4

4

4

4

4

4

4

4

4

4

4

4

4

4

4

4

4

4

4

4

4

4

4

4

4

4

4

4

4

4

4

4

4

4

4

4

4

4

4

4

4

4

4

4

4

4

4

4

4

4

4

4

4

4

4

4

4

4

4

4

4

4

4

4

4

4

4

4

4

4

4

4

4

4

4

4

4

4

4

4

4

4

4

4

4

4

4

4

4

4

4

4

4

4

4

4

4

4

4

4

4

Table 4-2. Summary of Injector Configurations

<u>Injector</u>	<u>Type of Element</u>	<u>No. Primaries</u>	<u>No. Secondaries</u>	<u>Primary Sizing</u>	<u>Secondary Sizing</u>	<u>C<sub>d</sub></u>	<u>Material</u>	<u>Comments</u>
SW 1	Sawtooth		Continuous Sheet		Sheet Thickness	.8	Ni 200	Equal legs of sawtooth
SW 2	Sawtooth	"	"			.8	Ni 200	Offset-Unequal legs of sawtooth
CS-1	Canted Slot	36	None			.70	Ni 200	
CS-2	Slot	72	None	.020 x .160	None	.65	304 Stainless	
CS-3		36	None	.020 x .175	None	.65	304 Stainless	
CS-3A		36	None	.020 x .175	None	.65	Ni 200	
CS-4		36	36	.020 x .175	.015 x .100	.65	304 Stainless	Secondaries parallel to centerline of engine
CS-5		36	36	.020 x .175	.010 x .082	.65	304 Stainless	Secondaries 90° to centerline of engine
CS-6		36	None	.020 x .278	None	.65	304 Stainless	
SS-1	Straight Slot	36		*	x	*	Ni 200	
SS-2	Slot	36		.020 x	.	.020 x	.65	"T" Slot
SS-3		36		*	x	*	.65	
SS-4		36		*	x	*	.65	
SS-5		60	60	.035 x .111	.016 x .036	.65	304 Stainless	
SS-6		36	36	.036 x .111	.017 x .042	.65	Ni 200	High Performing Element
SS-7		36	36	.036 x .110	.016 x .041	.73	Ni 200	Rounded Entrance Orifice
SS-8		36	36	.035 x .112	.016 x .046	.65	Ni 200	Secondaries Shifted
SS-9		45	45	.036 x .089	.015 x .035	.65	Ni 200	Secondaries Shifted
SS-10		60	60	.037 x .066	.010 x .038			Secondaries Shifted
SS-11		72	72	.025 x .081	.010 x .030	.65	Ni 200	Secondaries Shifted
SS-12		36	36	.036 x .111	.022 x .042	.65	Ni 200	Highest Performing Element

could be installed in this tank since two bottles would exceed the 4-gallon capacity. The use of the partial K bottle was not recommended because of the tendency of the methane and ethane gases to stratify while liquefying the gases in transferring them to the feed tank. As a result, the capabilities of the test stand were limited in the early runs. In order to achieve proper conditioning of the run lines, it was necessary to bleed both oxidizer and fuel through the lines to prevent propellant boiling during the test. Because the system was limited in the fuel capacity, it was not possible to sufficiently cool down the feed lines prior to testing. However, this was not completely known until several tests had been conducted, and an analysis was made of the test results.

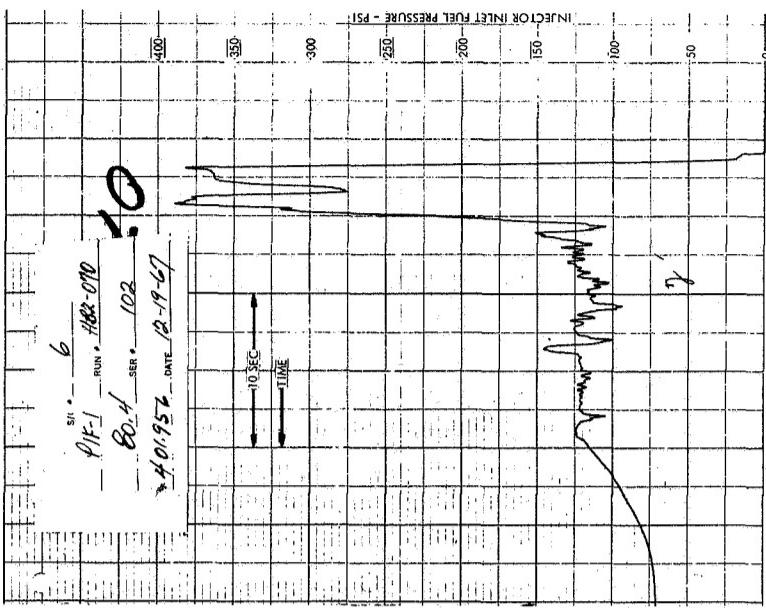
While Table 4-1 tabulates the data for this run, it is not possible to apply valid points to this test because the test system was not sufficiently chilled down. During the test, two-phase flow apparently occurred in the feed lines causing large transients in the injector pressure drops and combustion. Figure 4-2, the strip chart traces from this test, shows the transients that occurred during the startup and that steady-state conditions were never reached.

A post-firing examination of the injector and chamber assembly showed no erosion or damage. Figure 4-3, the post-firing view of the injector, shows some carbon deposition on the injector faceplate. Figure 4-4 shows the post-firing view of the combustion chamber. Carbon in the chamber after this test was very much like lamp black indicating that the characteristic velocity efficiency and combustion temperature were quite low.

#### Test 071

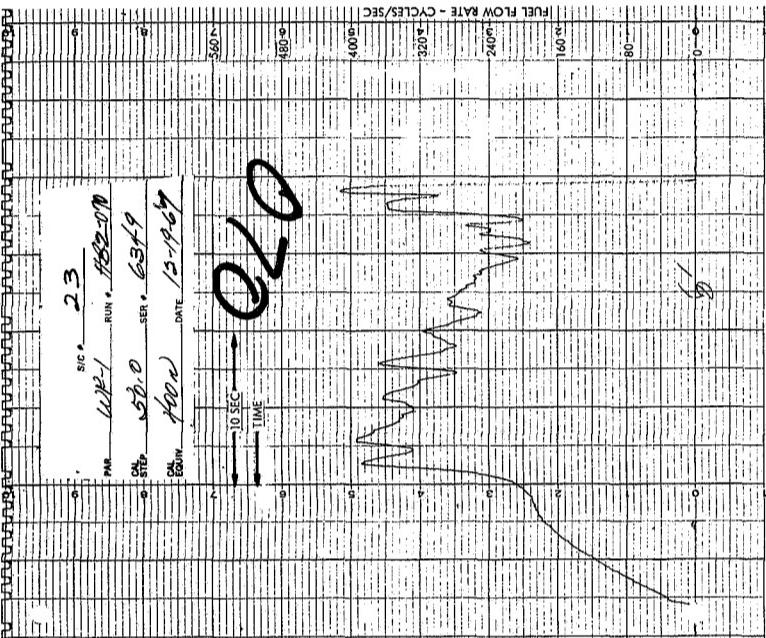
Because of the limited data acquired on Test 070, it was not clear what primary difficulties were associated with the test stand. Evaluating the test data was further complicated by the fact that the injector had been run for the first time and the characteristics of the injector were not defined. In reviewing the data from Test 070, it was clear that the injection pressure drops were not close to the predicted values. In particular, the fuel pressure drop which had been predicted to the 180 psi was nominally 330 psi. Since the fuel injection gap was set at 0.0045 inch, it was

1. 12/19/67 - 10:00 AM - 1000 ft/min - SIC 6 - 1000 ft/min - 1000 ft/min - 1000 ft/min

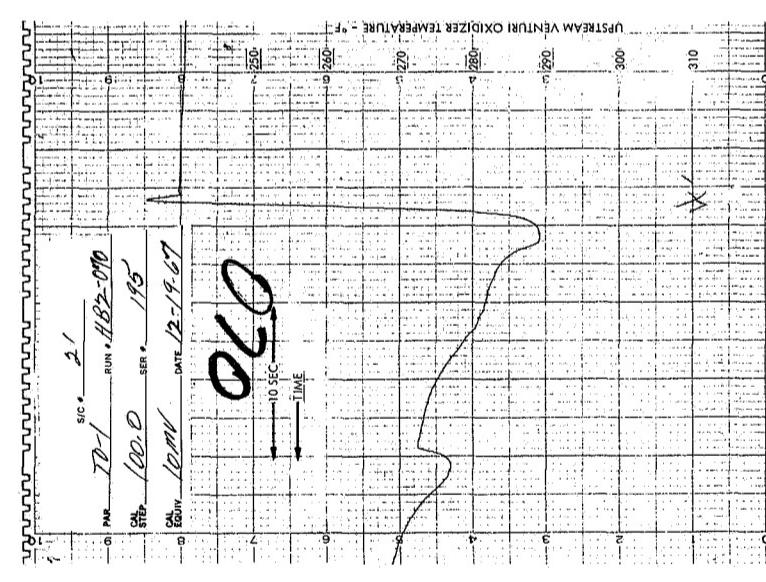


I

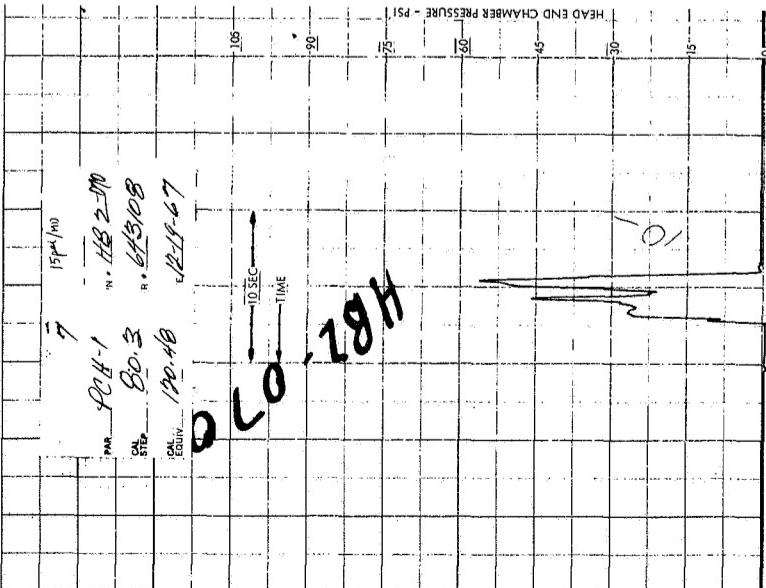
Injector Inlet Fuel Pressure



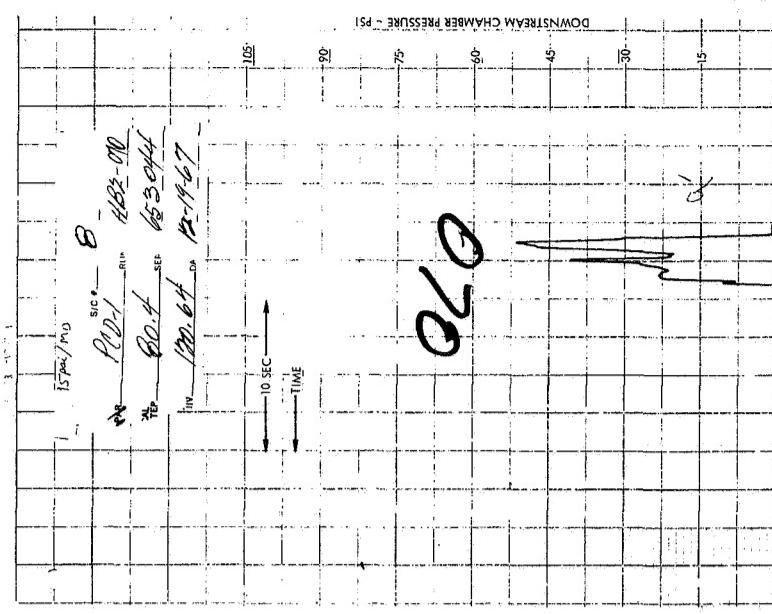
Fuel Flow Rate



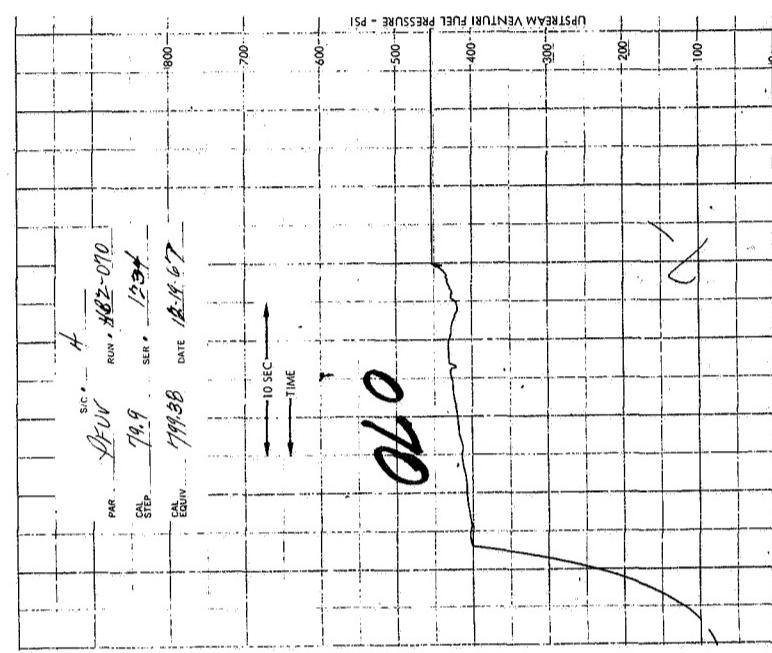
Upstream Venturi Oxidizer Temp



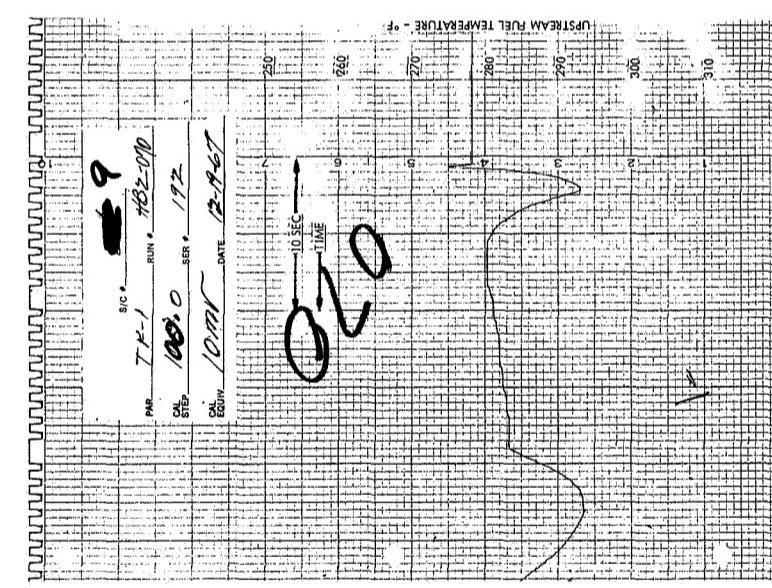
Head End Chamber Pressure



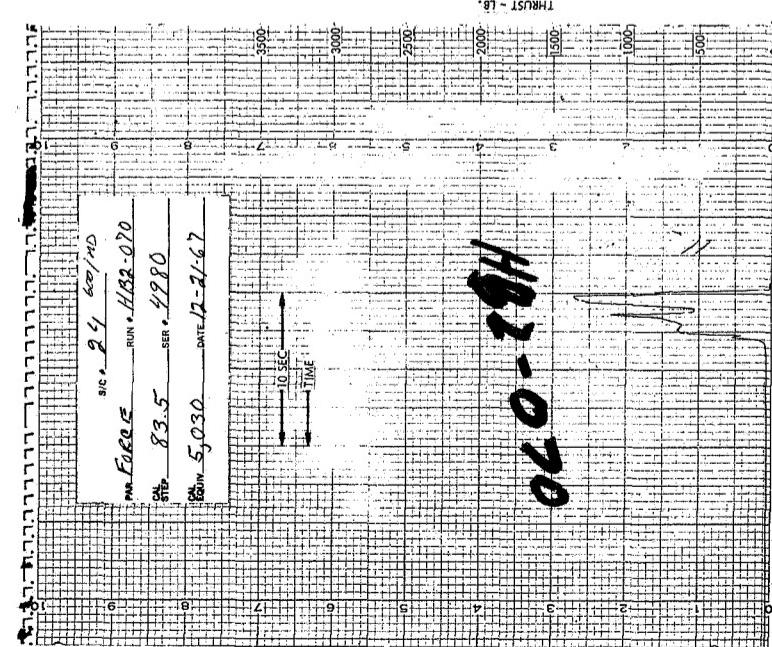
Downstream Chamber Pressure



Upstream Venturi Fuel Pressure

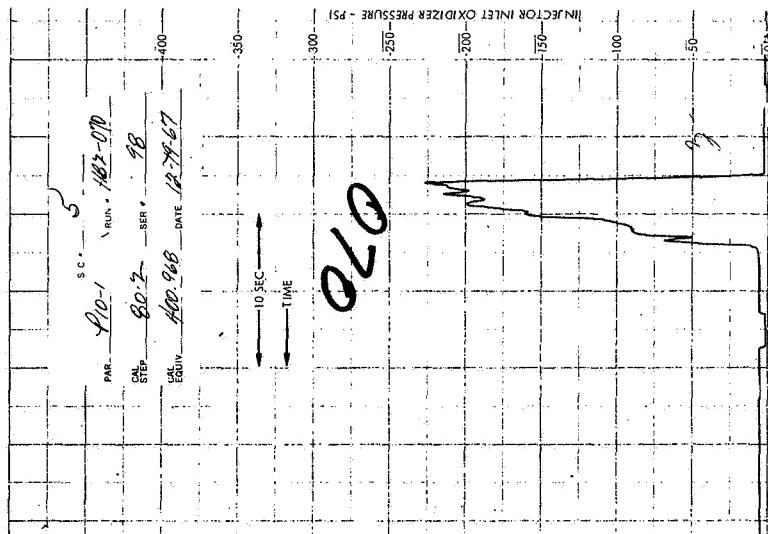


Upstream Fuel Temperature

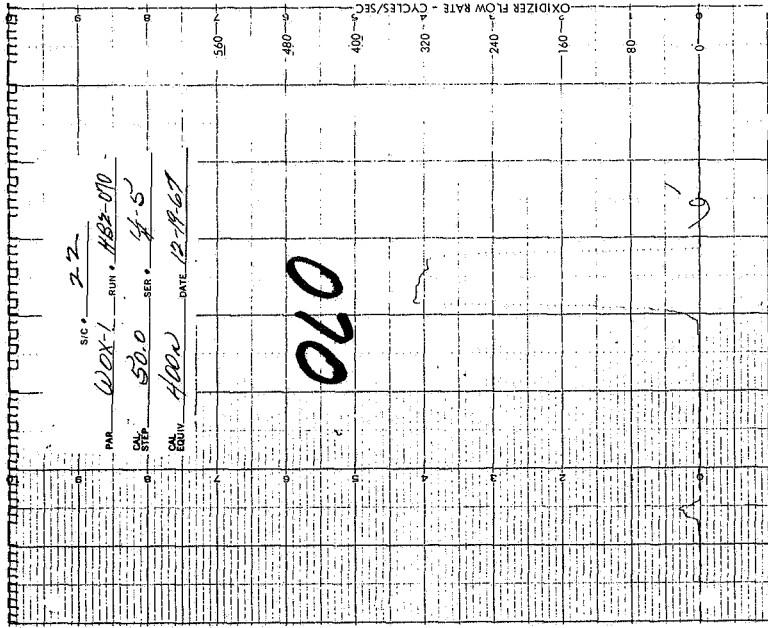


Thrust

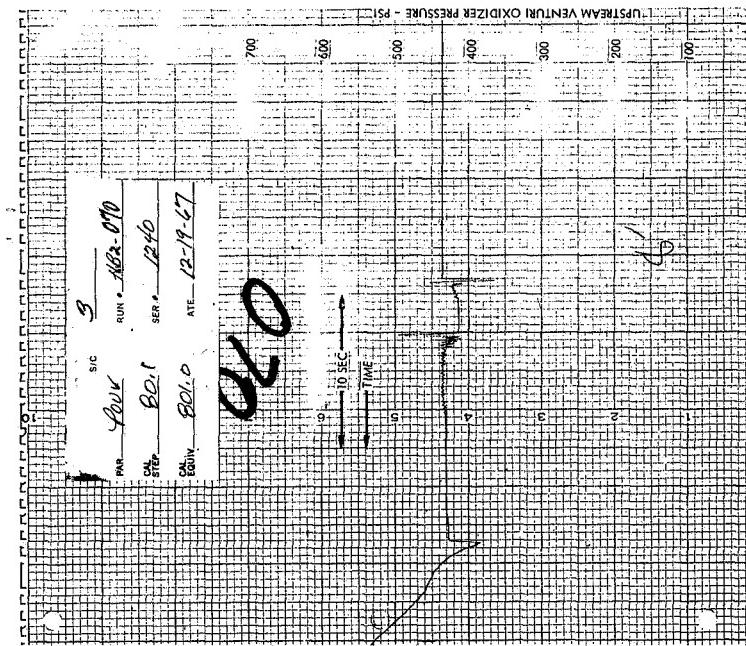
P 2.



Injector Inlet Oxidizer Pressure



Oxidizer Flow Rate



Upstream Venturi Oxidizer Pressure

Figure 4-2. Strip Chart Data for Run 070



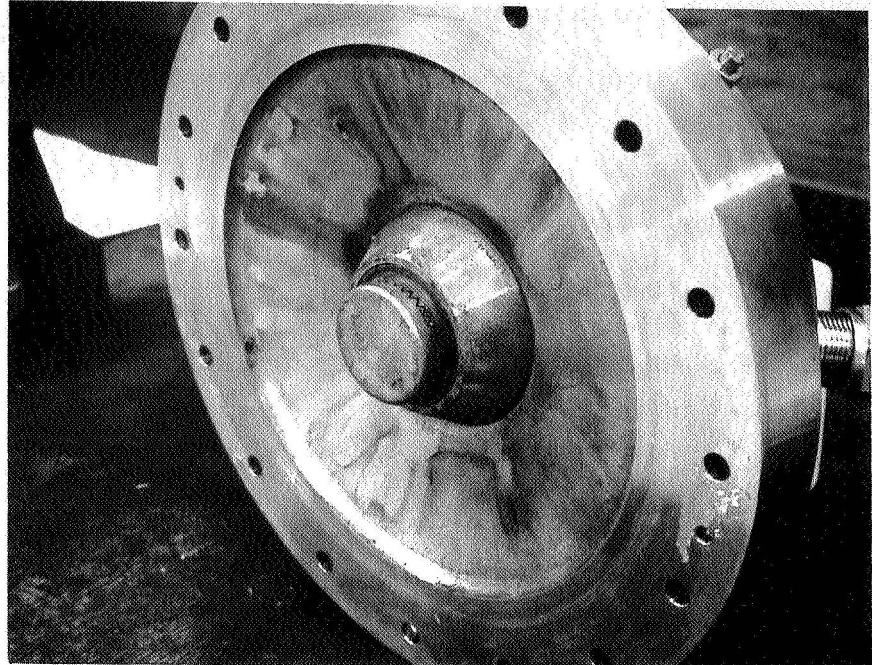


Figure 4-3. Post-Firing View of Sawtooth Injector  
After Test 070

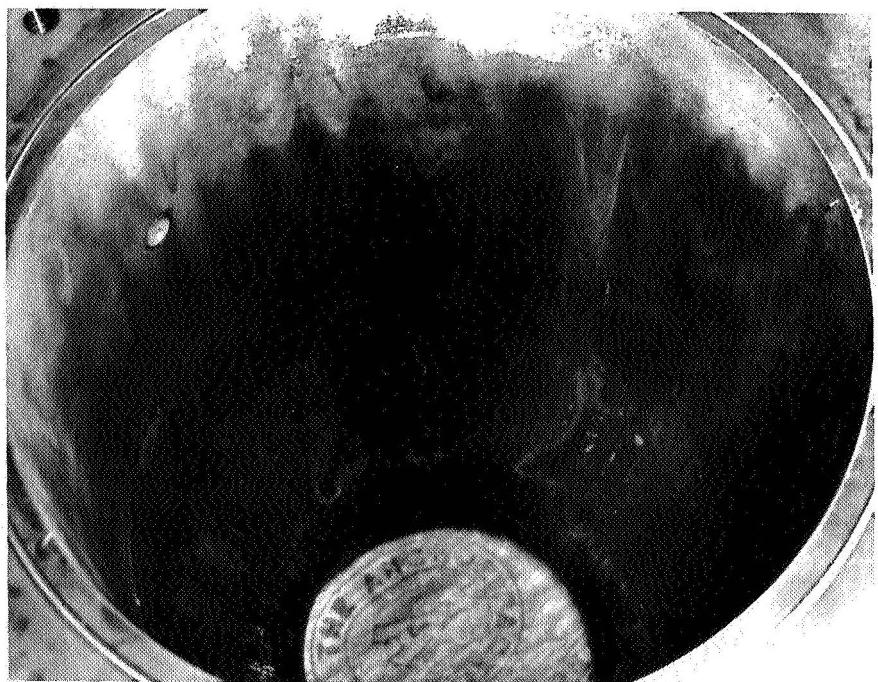


Figure 4-4. Post-Firing View of Chamber After  
Test 070

felt that this small gap could have been constricted during the test. It was therefore decided to increase the fuel gap to 0.010 inch.

The resulting injection pressure drops were closer to the predicted values than in Test 070; however, large transients were experienced and the performance was extremely low. Again, it was difficult to assign a steady-state value for tabulation because of the severe transients. Two conditions, however, seem apparent from the result of this test. These were that propellant separation was occurring in the injection process preventing the fuel from mixing with the oxidizer, and that two-phase flow was occurring in the feed lines and the injector.

#### Test 072

Test 072 used the same oxidizer configuration as for previous test, SW-1. The mixture ratio on this test was decreased from 5.3 to 3.6. The chill down procedure was extended in order to minimize the effects of two-phase flow which had been observed in the previous test.

Large transients were observed at the start-up of the tests and again were apparently caused by two-phase flow in the propellant feed systems. The engine performance was relatively low, but again the transients that were occurring throughout the run make it difficult to assign true performance steady-state values.

#### Test 073

Test 073 used oxidizer configuration SW-1. The oxidizer injection gap, however, was reduced from 0.035 to 0.025 inch.

Due to extended liquid nitrogen cool down procedures prior to the run, the transients in this test were not as severe as the transients which had been observed in the previous tests; however, it was apparent that a more effective chill down system would have to be developed. The pressure drops at the injector were closer to the predicted values than had been observed in the previous tests.

While in each of these tests difficulties had been experienced with two-phase flow in the propellants, it was possible to observe that the propellant mixing was not occurring because of the reactivity of the oxidizer and the fuel. In establishing the design criterion of this injector

configuration, it was known that the sheet thicknesses of the oxidizer and the fuel would be critical parameters; that is, if the sheet thickness of either propellant was too large, effective mixing could not be achieved. The maximum sheet thickness established was 0.030 to 0.035. However, the selection of this thickness was a compromise arising from some fundamentals of the momentum ratio and mixture ratio which dictate a given area ratio between the oxidizer and the fuel. A lower limit for the fuel gap was established as 0.004 to 0.005. Any gap smaller than this would not have been practical for an engine of this size, although a much smaller oxidizer gap would have been desirable. From observations of these tests, it seemed apparent that the oxidizer sheet thickness would have to be reduced even at the expense of compromising the propellant momentum ratio.

The injector was removed from the test stand so that changes could be made in the oxidizer sheet thickness. At the same time, the engine hardware was examined thoroughly for any signs of erosion or damage. No damage was found either in the injector or the chamber. Carbon depositions were found on both; however, the carbon was very light and powdery indicating low-temperature combustion.

#### Test 074

Adjustments in the oxidizer sheet thickness were made after Test 073. The engine was run again at a MR of 5.0. Problems still existed with the stand operation, however it was becoming apparent that propellant mixing was not occurring.

#### Test 075

Test 075 used oxidizer configuration SW-1. The oxidizer injection gap was reduced from 0.025 to 0.0225 inch. Some two-phase flow transients occurred; however, they were not as severe as had been previously experienced. Low performance indicated that propellant separation apparently was still occurring.

#### Test 076

Test 076 used oxidizer configuration CS-1, the first in a series of canted slot injectors. Studies of the previous tests indicated that fuel was not penetrating the oxidizer sheets, due to blow apart, therefore, in order

to provide a more positive penetration, the oxidizer orifices were modified with openings. This was done by simply taking the sawtooth pintle configuration and adjusting it to one side so that the teeth of both the outer pintle body and the pintle tip came in contact with each other. This, in effect, closed off one leg of the sawtooth and left the other leg open creating a canted tooth.

#### Test 077

Test 077 used the same oxidizer element configuration, CS-1, of the previous test. The mixture ratio was reduced from 5.5 to 3.8. This change was done by proportionally reducing and increasing the oxidizer and fuel flow rates, respectively, to maintain the same approximate total flow rates.

#### Test 078

Test 078 used oxidizer element SS-1, the first straight slot configuration. A modification was made to the injector to create a straight slot pattern using a sawtooth pintle tip. This was done by mill cutting small slots in the tops and bottoms of a sawtooth pintle tip. Figure 4-5 shows this pintle tip installed on the injector. With this arrangement, the oxidizer comes out in a radial flow pattern broken up into 36 primary slots and 36 smaller secondary slots. At the impingement point of the oxidizer and fuel, a gap of 0.050 inch existed between the secondary and primary slots, allowing the fuel to mix into the oxidizer.

#### Test 079

Test 079 used oxidizer element SW-2. In the various sawtooth configurations, each side of the sawtooth pattern was set at exactly the same size gap. A change was now made to decrease the gap on one side to 0.010 inch and the gap on the other side to 0.020 inch. The purpose of this test was to determine if the fuel could penetrate the oxidizer if the oxidizer sheets were made thin enough. Difficulties were experienced with two-phase flow in the fuel feed system which caused very large pressure drops at the fuel injection orifice. Figure 4-6 shows a post-firing view of injector element SW-2.

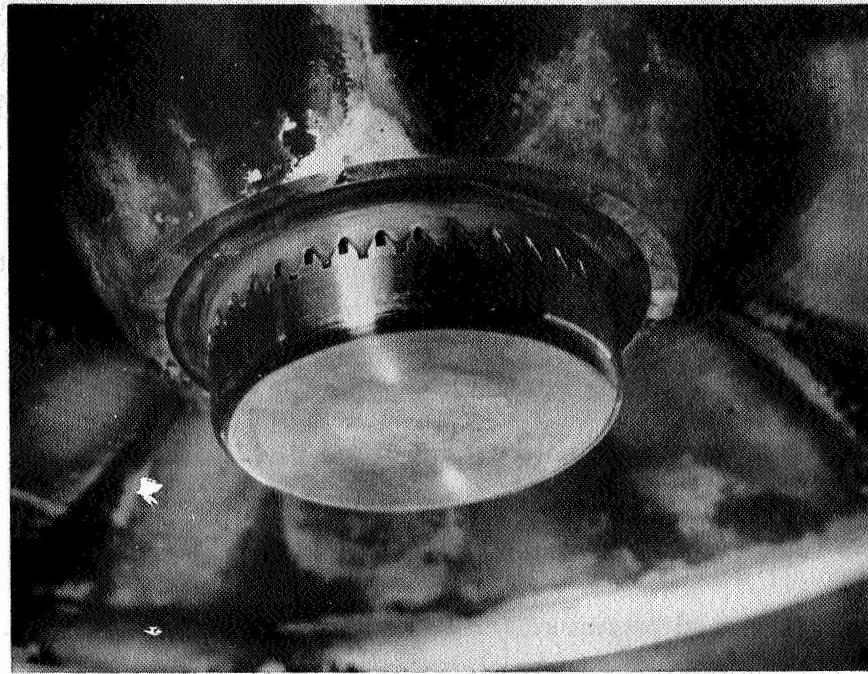


Figure 4-5. Injector Modification SS-1



Figure 4-6. Post-Firing View of Injector Element SW-2

### Test 080

Test 080 used sawtooth configuration SW-2 with a turbulence ring in the chamber. Use of the turbulence ring allows determination of whether or not any additional performance due to better mixing could be achieved. The results of this test did not indicate any significant additional performance, and therefore it was decided that no further tests would be conducted with the sawtooth configuration.

Figure 4-7 shows the turbulence ring-assembly on the thrust chamber in the post-firing conditions. The marks on the straight section of the turbulence ring spool were caused by the heavy oxidizer streams impinging against the wall. The oxidizer pattern is made up of alternate and light oxidizer streams from the 0.010 and 0.020 inch gaps.

### Test 081

Test 081 was intended to be a repeat of Test 079 except that the oxidizer slots would be narrowed from 0.030 to 0.020 inch. However, the test was aborted shortly after startup as a result of a facility failure.

### Test 082

Test 082 was repeat of the test conditions for Test 081; however, modifications were made to the test stand and a larger fuel tank was installed. With the installation of the new fuel tank it was possible to conduct a more extensive propellant bleed-in prior to conducting the test. This provided sufficient chill down so that two-phase flow transients which had been experienced in previous tests were eliminated. Injection pressure drops were close to predicted values, and all system parameters were steady.

Figure 4-8 shows the post-firing view of the thrust chamber. Some carbon deposit can be seen on the chamber wall; however, the carbon deposit was very light indicating that a rather heavy oxidizer penetration was occurring. The carbon in this case was very hard and flaky.

### Test 083

In this test, the pintle configuration of Test 078 was modified to increase the flow area of the oxidizer. This was done by mill slotting both the primaries and the secondaries with a cutter slightly narrower

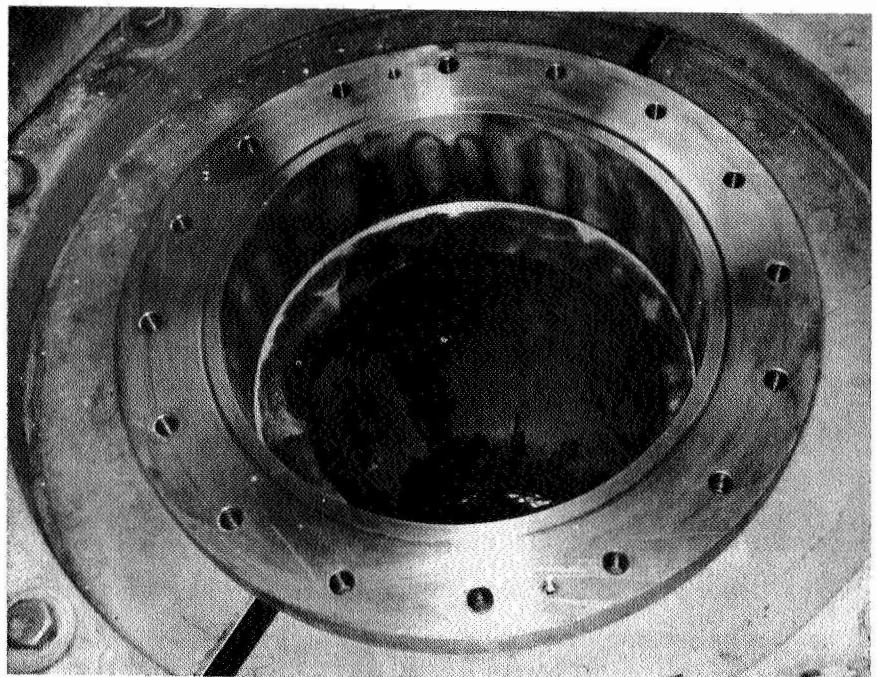


Figure 4-7. Turbulence Ring After  
Test 080

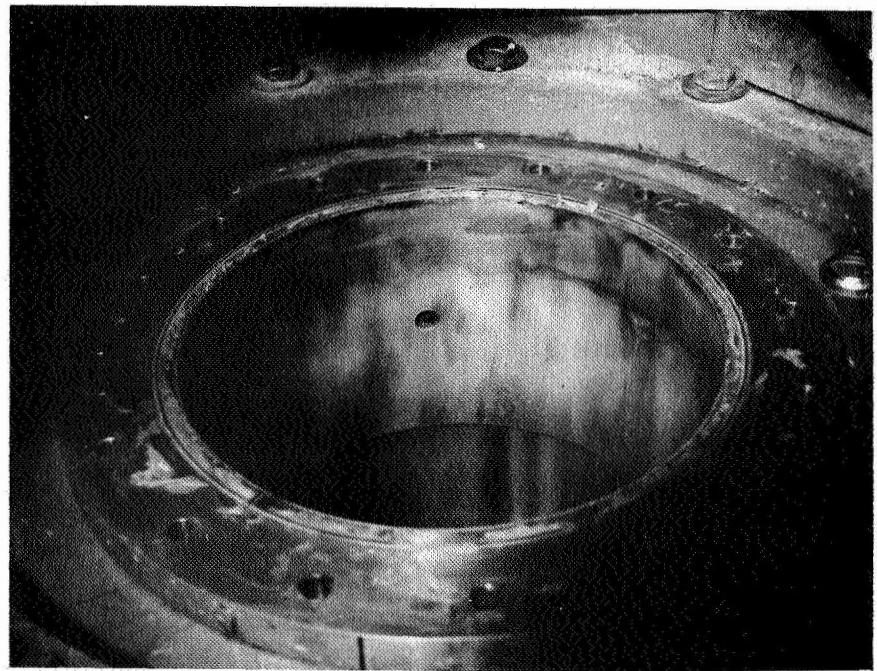


Figure 4-8. Post-Firing View of Thrust  
Chamber After Test 082

than the original slots. Figure 4-9 shows this configuration in the post-firing view. It was apparent from the markings on the pintle tip after the firing and from the performance level that the fuel did not penetrate down into the slots. The probable cause of this was oxidizer leakage through the annular joint between the pintle tip and the outer pintle body. Any leakage of oxidizer through this path would tend to block fuel from penetrating into the primaries and secondaries.

#### Test 084

Test 084 used a modified straight slot, configuration SS-2. This configuration was also referred to as the "T" slot configuration. Figure 4-10 shows the post-firing view of this configuration. The purpose of the "T" slot configuration was to provide a maximum area with minimum thickness, and at the same time allow some venting of the fuel. However, the reaction of the fuel with the oxidizer tended to prevent the fuel from coming into contact at the bottom end of the slots where the T is formed, in effect venting did not occur.

This configuration was the first to use the ring concept which uses a modified sawtooth pintle tip and the outer pintle body. The various orifice configurations for the oxidizer are machined into the ring. The ring was relatively inexpensive to make since it requires simply a disc blank with the slots end milled onto the ring. The ring was installed by slipping it onto the outer pintle body or pintle tip and then bolting the pintle tip in place. The ring concept was modified in later configurations, and it did prove to be one of the more valuable innovations of the program.

#### Test 085

This test was the same as Test 084 except that the mixture ratio was increased to 5.7. This was done by increasing the oxidizer flow rate thereby increasing the total flow rate.

#### Test 086

With the innovation of the ring concept, a whole new series of configurations was generated. The first of these was CS-2, a 72-canted-slot ring. The ring was fabricated of 304 stainless steel and the pintle tip was fabricated of nickel 200. The test was aborted by a fire on the test stand.



Figure 4-9. Post-Firing View of Injector Modification  
SS-1A After Test 083



Figure 4-10. Post-Firing View of Injector  
Modification SS-2 After Test 084

The fire was caused by a minor leak in a fitting and caused only slight damage to the installation around the propellant feed lines.

#### Test 087

This test represented a repeat of Test 086. The test, however, was of short duration because the steel ring ignited with the oxidizer and 80 percent of the ring burned away. Figure 4-11 shows a post-firing view of the remaining portion of the ring. The injector, however, did not sustain any damage. Figure 4-12 shows the post-firing view of the chamber assembly. The chamber was not damaged by this ring failure.

#### Test 088

This test used a 36-slot ring, configuration CS-3, fabricated of 304 stainless, with a beveled edge on the pintle tip. The purpose of the beveled edge on the pintle tip was to allow for future additions of secondaries at any angle to the primary radial flow pattern of the oxidizer. Figure 4-13 shows this ring in the prefiring condition. This test was aborted shortly after startup as a result of a malfunction in the stand control system.

#### Test 089

This test was a repeat of Test 088 using ring configuration CS-3. The test was again aborted shortly after startup when a malfunction in the control system again occurred. A post-firing examination of the injector revealed that some erosion of the injector ring had occurred. Figure 4-14 shows the post-firing view of the ring and pintle tip. The erosion appeared to be a chemical attack of the oxidizer on the 304 stainless. In particular, the erosion appeared at the roots of the slots and at the trailing edge of the ring, resulting from the higher performance achieved from this configuration. No damage, however, was sustained to either the injector or the chamber.

#### Test 090

This test used a modification of 36 canted slot configuration of Test 089. The modification was the addition of secondary slots downstream from canted primaries referred to as CS-4. The purpose of the secondary slots was to capture the fuel passing between the canted



Figure 4-11. Post-Firing View of Injector Tip After Test 087

primary slots. The secondaries were axial with the engine centerline, however, they were located at an angle to the fuel flow after the fuel passed through the canted primaries. Figure 4-15 shows the post-firing view of this ring. A large amount of carbon deposit was found on the ring itself. This was the first time that a carbon deposit had been found on the ring.

#### Test 091

This test again used a modification of the 36-slot configuration of Test 089. The modification was the addition of secondaries, referred to as CS-5. The secondaries were located 90 degrees to the axis of the engine and were directed at an angle 30 degrees downstream from the primaries. The purpose of this concept was to provide a flat thin secondary that would catch the fuel and carry it out to the chamber wall. The

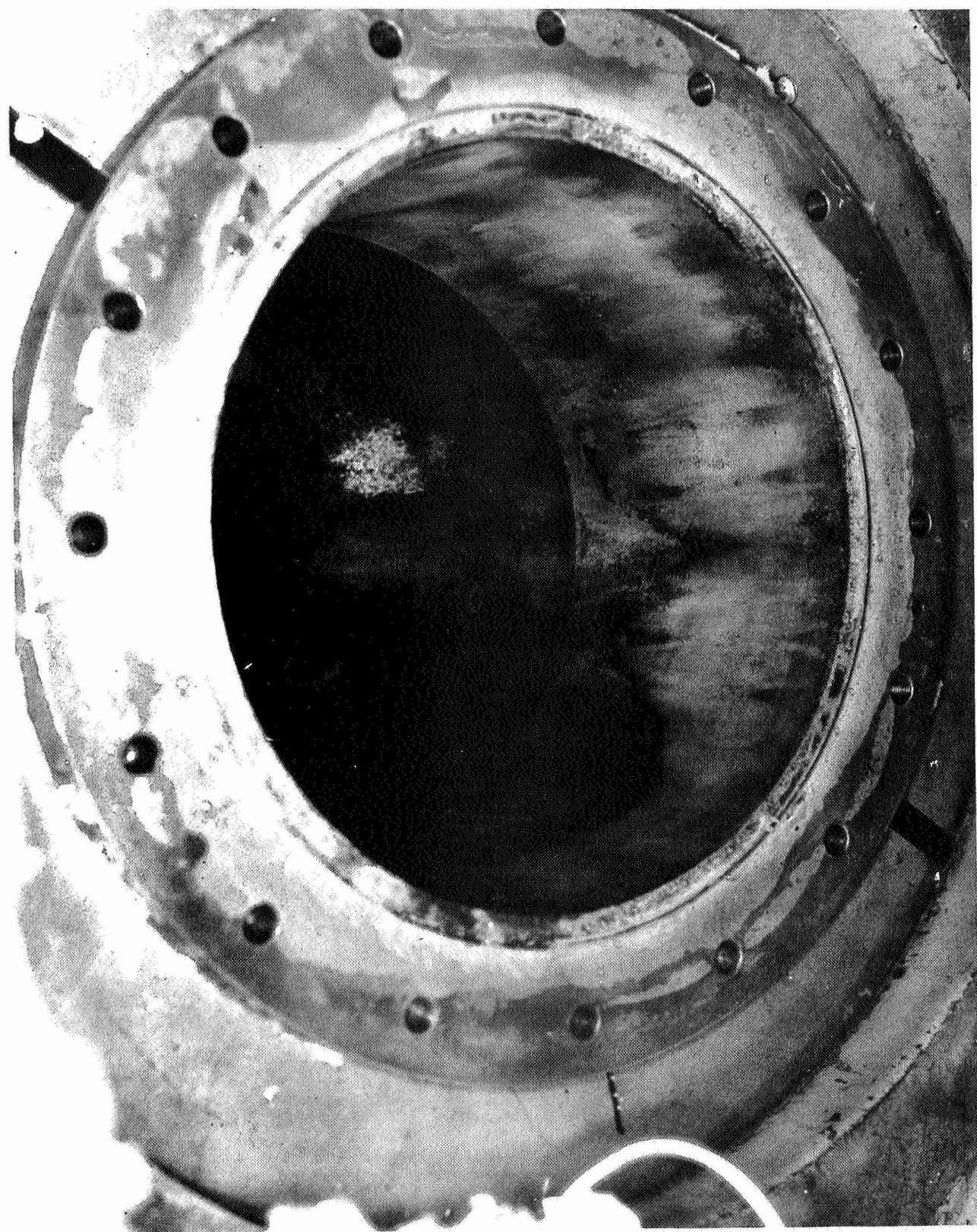


Figure 4-12. Post-Firing View of Chamber Assembly After Test 087



Figure 4-13. Prefiring View of Canted Slot Injector  
Modification Before Test 088

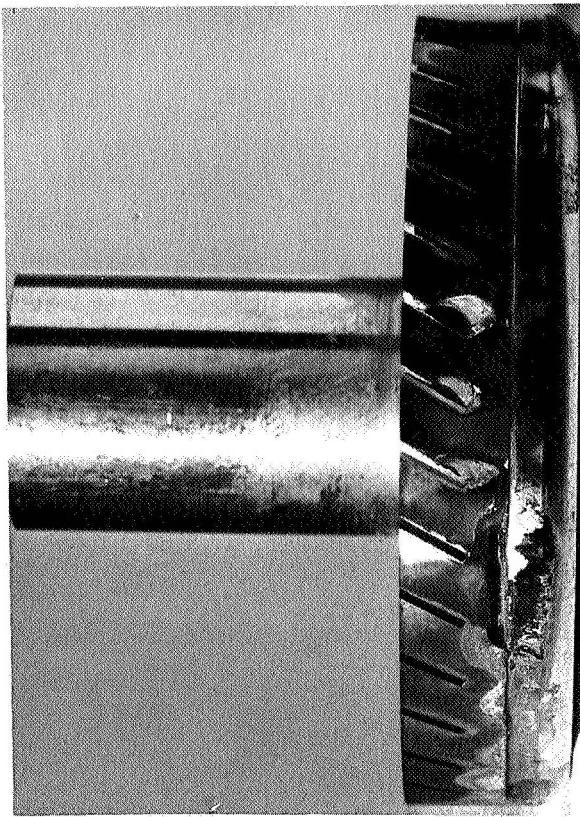


Figure 4-14. Post-Firing View of Injector With Stainless Steel Modification CS-3 After Test 089

purpose of the 30 degree angle on the secondaries was to allow maximum venting of the fuel. This ring configuration, however, entrained the propellant combustion so that the ring overheated and reacted with the oxidizer. This reaction burned up the ring and the pintle tip. The edge of the pintle tip melted from local heating when the ring ignited with the oxidizer. Other than the pintle tip and the ring, no other parts of the injector or chamber were damaged.

#### Test 092

This test used canted slot configuration CS-6. The slots of this configuration were 0.100 inch longer than those of previous tests. Results of this test indicated that by increasing the length of the canted slots, the effective blockage to the fuel penetration was increased. The result was a slight drop in performance.

#### Test 093

Test 093 was the first in a series of high performance runs. This test used a straight slot ring configuration SS-4 with large primaries and



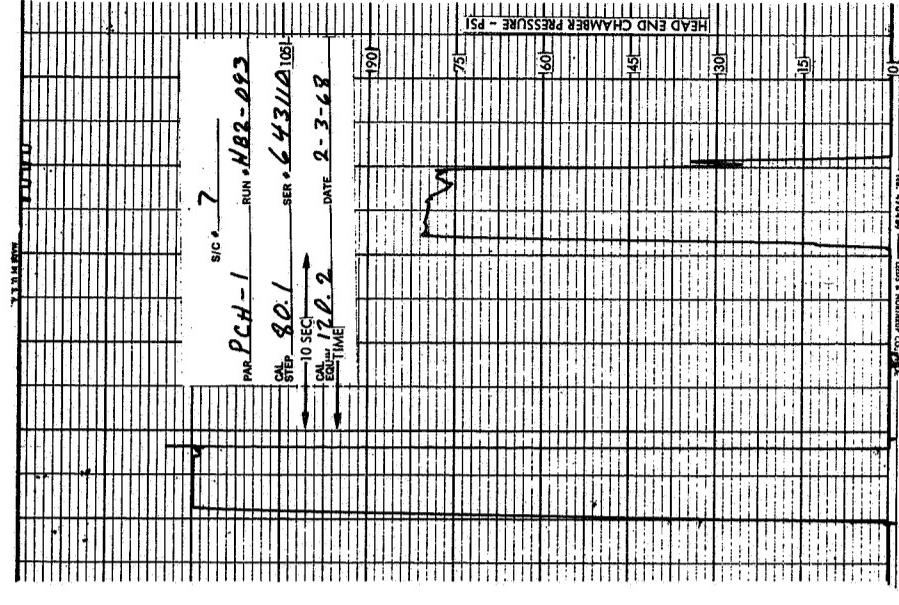
Figure 4-15. Post-Firing  
View of Injector  
Ring CS-4  
After Test 090

small secondaries. The ring was fabricated from 304 stainless. The effective blockage of this ring configuration was approximately 17 percent. Blockage here is defined as the projected area of the oxidizer streams compared with the total area of the element. Figure 4-16 shows the strip chart traces from this test. The traces show that the transients, occurring early in the program as a result of two-phase flow, no longer exist and that good steady-state data may be obtained.

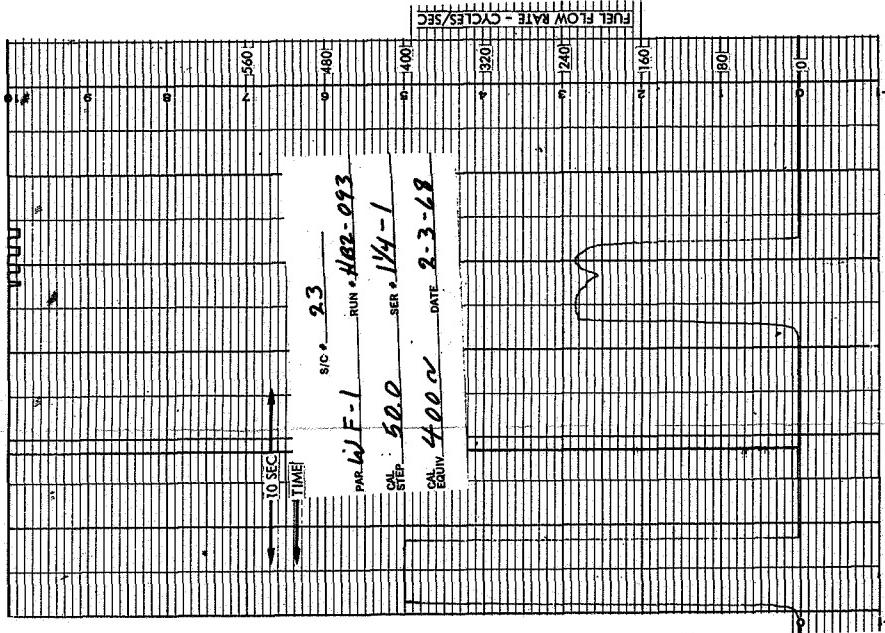
This test was considered very successful in that relatively high performance ( $C^*$  of 95 percent) was achieved with no injector or chamber erosion. The fact that this ring was made of 304 stainless and did not show any signs of erosion or chemical attack during a 6-second firing indicated the injector element was running cool. Figure 4-17 shows the post-firing view of the steel ring. The flow patterns of the fuel can be seen in this view. Post-



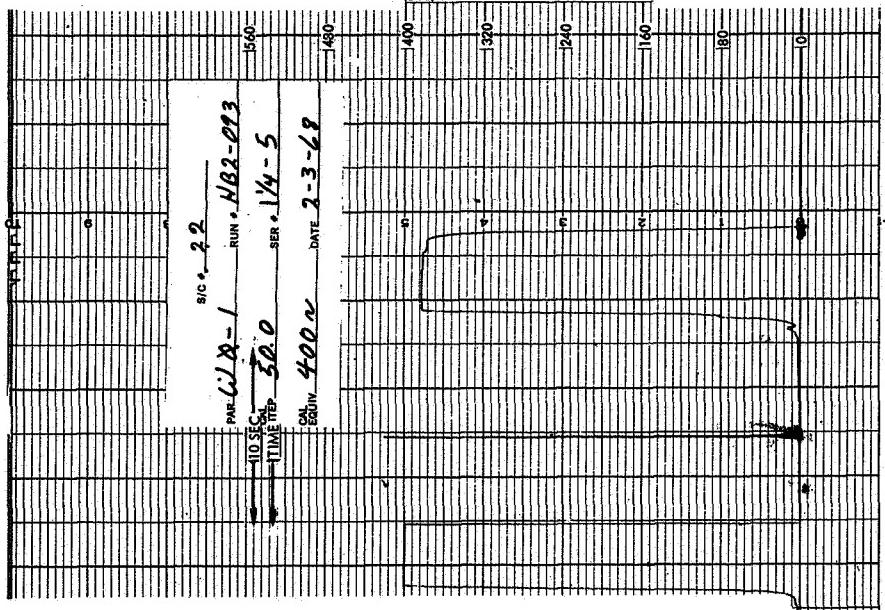
part 1



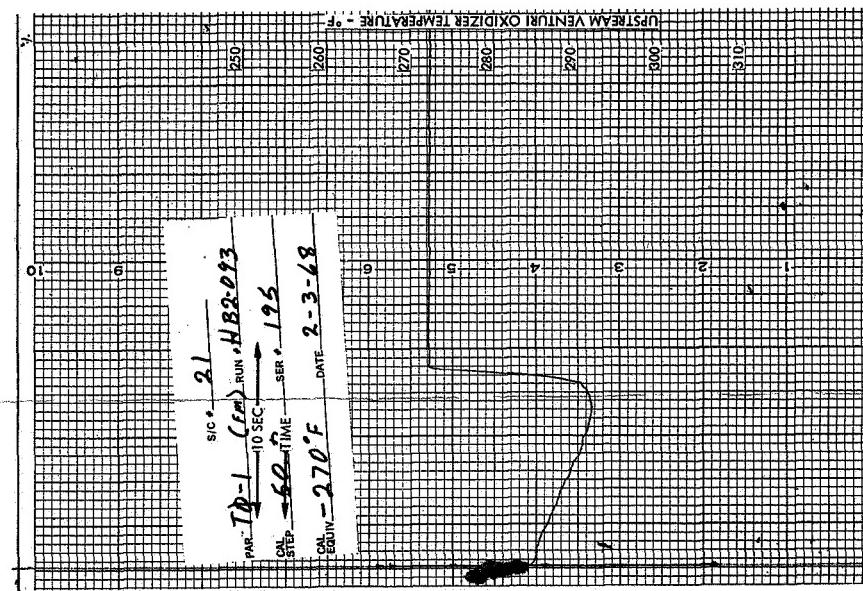
Part 2



Fuel Flow Rate



Oxidizer Flow Rate



Upstream Venturi Oxidizer Temp.

Figure 4-16. Strip Chart Data for Run 093



firing studies of this ring indicated that some performance loss may have occurred as a result of fuel escapement through the area between the secondaries and the primaries. Two techniques for capturing this fuel were apparent. The first of these was to move the secondaries closer to the primaries, thereby reducing the effective areas between the secondaries and the primaries. The other was to enlarge the secondaries, thereby

increasing the total oxidizer flow through the secondaries.

Since previous tests conducted with the coaxial injector using low fuel pressure drops had been encouraging, it was decided to reduce the fuel pressure drop to approximately 40 psi. This was done by installing a new fuel insert into the injector assembly.

#### Test 094

This test used a straight slot configuration SS-5. Ring configuration SS-5 consisted of 60 primary slots and 60 secondary slots. The effective fuel blockage for this ring configuration was approximately 17 percent. The ring was fabricated of 304 stainless. A complete loss of the ring occurred during the test; apparently the ring was consumed by the oxidizer. A post-firing examination of the injector and the chamber assembly indicated that neither sustained any damage as a result of the reaction with the ring. Indications were that this configuration of slot tended to entrain the flame zone around the ring, thereby resulting in heating of the ring to temperatures that allowed the oxidizer to react with

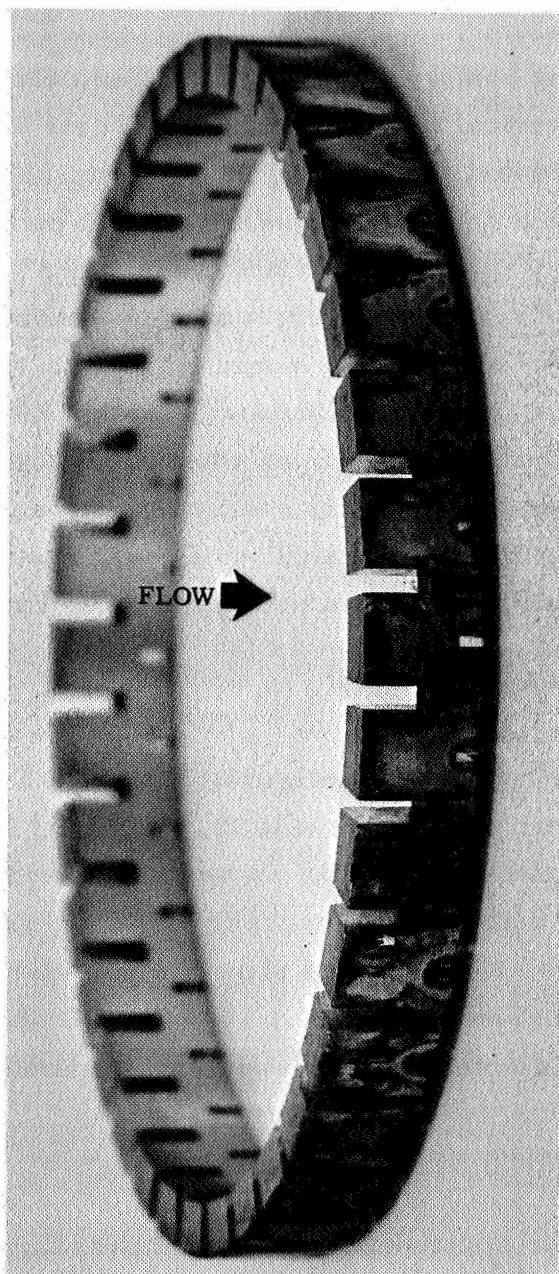


Figure 4-17. Post-Firing View of Stainless Steel Injector Ring SS-4 After Test 093

the stainless steel. It was therefore decided that future rings would be fabricated from nickel 200. The nickel 200 would provide a better conductivity to the adjacent outer pintle body and pintle tip. In addition, the nickel would eliminate the compatibility temperature problem associated with the stainless steel and fluorine.

#### Test 095

Test 095 used a canted slot ring configuration CS-3A. Geometrically, this ring configuration was identical to the ring used in Tests 088 and 089; however, the ring was fabricated from nickel 200. Tests 088 and 089 were prematurely aborted as a result of a control system malfunction on the test stand. This test was intended to provide a more valid data point to this ring configuration by achieving a 5- to 6-second firing. Post-firing inspection of the ring assembly revealed that no erosion occurred. This demonstrated the value of using the nickel 200 for the rings since this configuration had exhibited erosion when fabricated from stainless steel. Since the performance of this configuration was not as good as the performance achieved from the straight slot configuration, it was decided that no further tests would be conducted on the canted slot configuration.

#### Tests 096 through 100

Tests 096 through 100 were run with ring configuration SS-6. These tests represented a complete mixture ratio survey with this injector element. This ring was fabricated from nickel 200. A post-firing examination of the ring assembly revealed that no erosion occurred to the ring, pintle injector, or chamber. Figures 4-18 and 4-19 show the post-firing views of the injector ring and chamber, respectively. Figure 4-20 shows the post-firing view of the complete injector assembly with an accumulation of 31 tests without damage.

#### Test 101

This test was intended to provide additional data on fuel pressure drop characteristics on the injector performance. The same ring assembly used in Tests 096 through 100 was used on this test. A new fuel insert was installed which provided fuel pressure drop of approximately 20 psi.

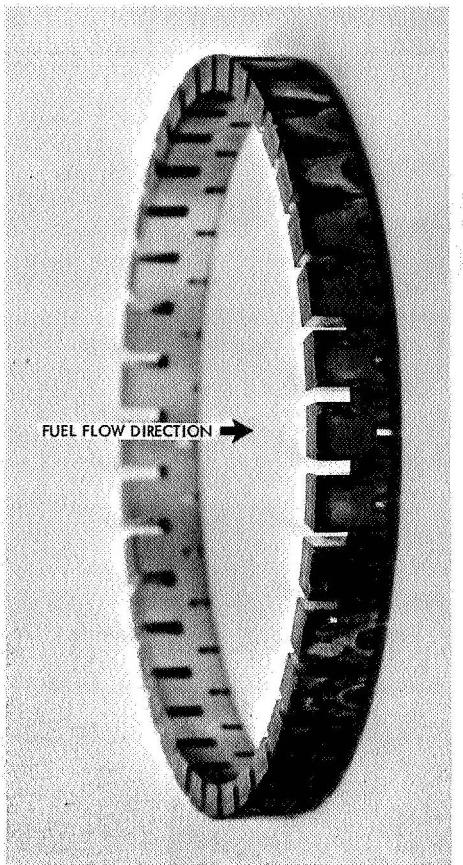


Figure 4-18. Post-Firing View  
of Nickel Ring SS-6  
After Tests 096  
Through 100

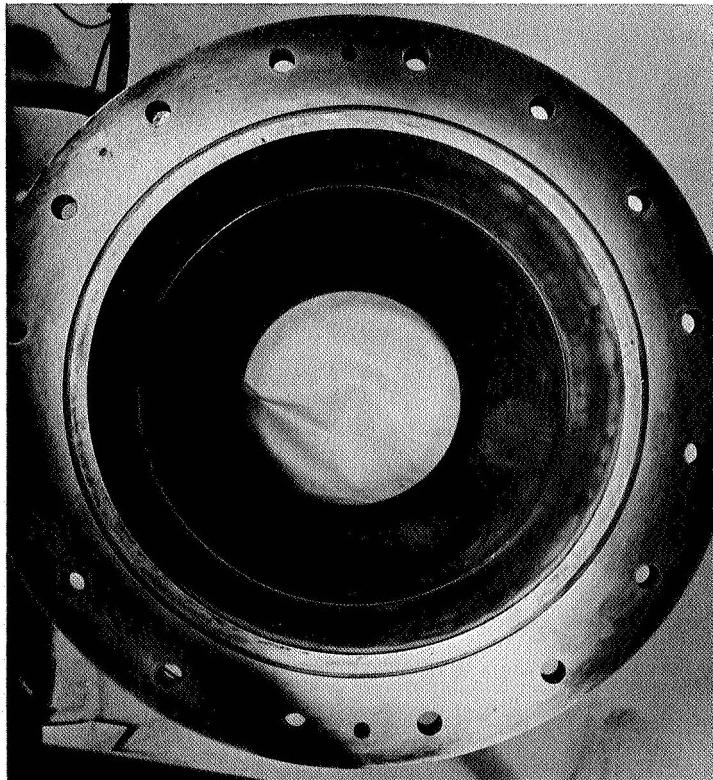


Figure 4-19. View of Chamber  
Assembly After  
Tests 096  
Through 100



Figure 4-20. Complete Injector Assembly After Completing Tests 096 Through 100 with Ring SS-6

#### Test 102

The purpose of this test was to investigate the feasibility of reducing the oxidizer pressure drop by means of a  $C_D$  change in the orifice characteristic. Rings previously fabricated had a low  $C_D$  characteristic of approximately 0.65. The reason for this was that the rings were manufactured in the most economical manner by end milling a piece of ring stock resulting in square edged entrances. To increase the  $C_D$  characteristic of the orifice it would be necessary to change the slots from a square edge orifice entrance to a rounded entrance. For this test, a ring fabricated of nickel 200 with the dimensions of SS-6 was modified to a slightly rounded entrance. The modification was done by hand, using Swiss files. While this technique of rounding the entrance to the orifice did not produce the most desirable contour nor the smoothest entrance, it did demonstrate the value and feasibility of improving the orifice  $C_D$ .

to reduce the oxidizer pressure drop. A significant change (approximately 80 psi) was experienced in the oxidizer pressure drop without any significant loss in performance. Figure 4-21 shows the post-firing view of the rounded orifice ring.

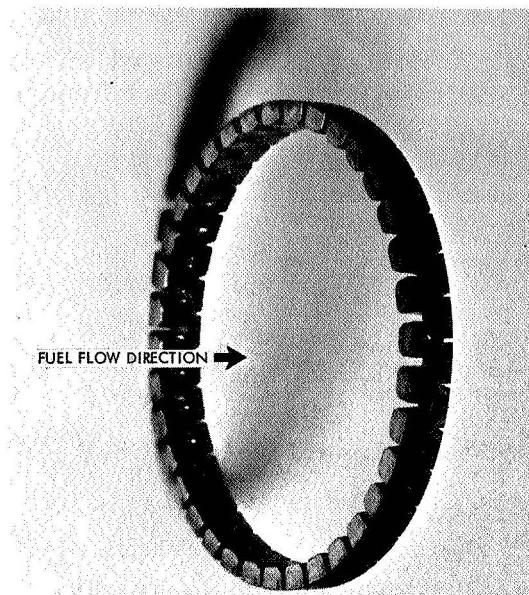


Figure 4-21  
Post-Firing View of Injector Ring  
SS-7 with Rounded Entrances After  
Test 102

#### Test 103

As previously stated, studies of the rings from Tests 093 and 096 indicated that some fuel was being lost through the oxidizer slots. One possibility for capturing this fuel was to shift the secondaries closer to the oxidizer primaries, thereby reducing the effective area through which the fuel could pass. The purpose of this test was to measure any performance change that might occur as a result of shifting the secondaries closer to the primaries.

#### Test 104

The purpose of this test was to study the effects of oxidizer blockage area on performance. The ring used in this test was SS-9, a 45-slot primary and a 45-slot secondary. The effective oxidizer blockage of this configuration was 22 percent. Figure 4-22 shows a post-firing view of ring SS-9 after this test.

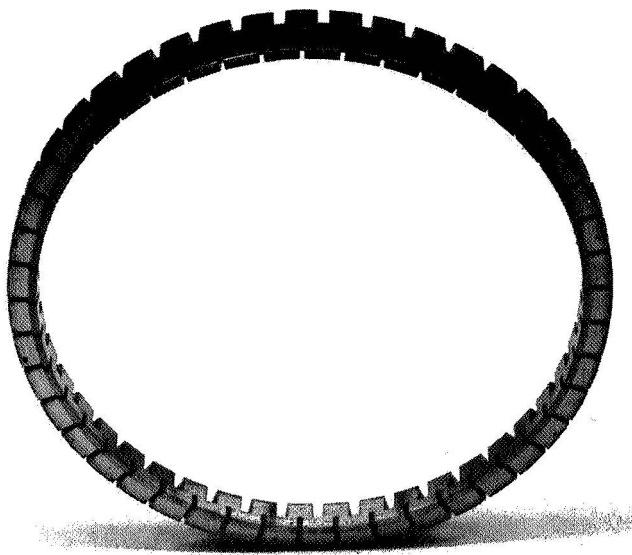


Figure 4-22

Post-Firing View of Injector Element SS-9 After Test 104

Test 105

Test 105 was a repeat of Test 103 using configuration SS-9. Since the rings in the test from 102 through 107 all had secondaries which had been shifted close to the primaries, it was necessary to obtain a valid data point on the effects of the secondary shift. The results of this test reconfirmed the results obtained on Test 103. Figure 4-23 shows a post-firing view of element SS-8 after this test.

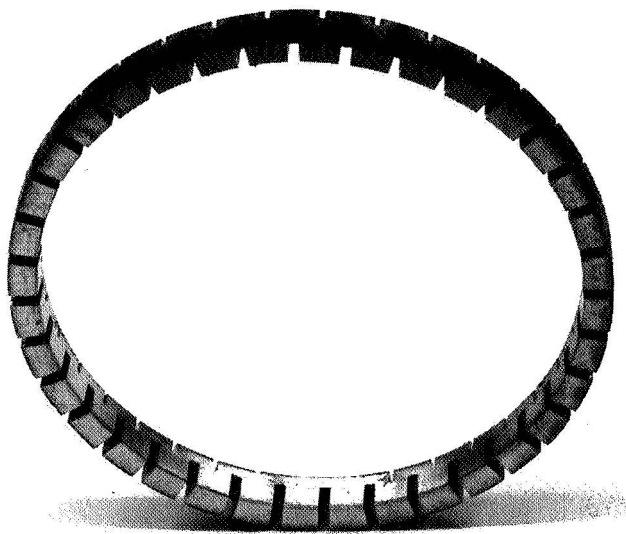


Figure 4-23

Post-Firing View of Injector Element SS-8 After Test 105

Test 106

The purpose of this test was again to obtain data points on the effect of oxidizer blockage with respect to performance. This ring configuration was SS-10 and contained 60 primaries and 60 secondaries. The effective

blockage of this ring was 17 percent. The test was aborted shortly after startup because the bolt retaining the pintle tip failed. The pintle tip and the ring were recovered in the flame pit of the test stand. The ring was no longer salvageable, however, the pintle tip received only some minor nicks in its surface which were subsequently machined out. Neither the engine chamber nor the injector sustained any damage as a result of this malfunction.

#### Test 107

Test 107 used ring configuration SS-11 which was a 72-slot primary and secondary configuration. The test was terminated shortly after startup when the pintle bolt failed again. The failure was caused by a chemical reaction of the fluorine with the stainless steel pintle bolt. The reaction was caused by contamination on either the threads in the pintle assembly or on the threads of the pintle bolt. The pintle and the ring were recovered in the flame pit; however, neither were salvageable. Neither the injector nor the chamber sustained any damage as a result of this failure.

#### Summary of Tests Through 107

The above tests were sufficient to establish the qualitative characteristics of the TRW coaxial injector design requirements for high performance combustion. These runs were made with 74 percent  $F_2/O_2$  FLOX mixtures. The subsequent runs were made to satisfy remaining contract objectives at two different  $F_2/O_2$  mixtures and complete the performance evaluation of the basic selected injector slot configurations. FLOX was being mixed at TRW and some difficulty was experienced in this mixing process. FLOX used in the earlier runs had a lower fluorine concentration than was intended for the tests. However, adjustments in the fluorine concentration would have required another large load of fluorine at considerable cost. Therefore, the concentration was not corrected until the oxidizer tank needed refilling.

#### Tests 108 through 117

The fluorine concentration of the FLOX was increased to 90 percent for this series of tests. Injector element SS-6 was used in Tests 108 through 116; however, cold flow tests had indicated that adjustments in the secondary flow would produce a more even mixture ratio throughout

the injection fan. Therefore, Test 117 was conducted with element SS-12 which was similar to SS-6 with a modified secondary flow configuration. Element SS-12 demonstrated an increased performance characteristic and this element was used on all subsequent tests. Figure 4-24 shows the engine assembly on the test stand with the insulation coverings in place.

#### Tests 118 through 121

The fluorine concentration of the FLOX was decreased to 80 percent by the addition of oxygen. This test series represented a mixture ratio survey using the highest performing injector element.

#### Tests 122 and 123

The chamber length was reduced to an  $L^*$  of 15 inches by removing the spool section from the nominal chamber configuration. Two mixture ratio points were obtained using this short chamber.

#### Tests 124 and 125

The chamber was rebuilt by installing two spool sections with the nominal throat section. This chamber configuration had an  $L^*$  of 45 inches. Two mixture ratio points were obtained using this long chamber.

#### Tests 126 and 127

These tests were conducted to study the effects of increasing contraction ratio to 4.5. The chamber was built up from the throat section and one spool section. This chamber had an  $L^*$  of 54 inches. Two mixture ratio points were obtained using this chamber. Figure 4-25 shows a closeup post-firing view of injector element SS-12 after Test 127. Carbon deposition can be seen on the face of the pintle tip. Figure 4-26 shows a view of the thrust chamber after Test 127. Carbon deposition can be seen throughout the chamber.



Figure 4-24. Engine Assembly on Test Stand with Insulation Coverings in Place



Figure 4-25. Post-Firing View of Injector Element SS-12 After Completing Test 127 Showing Carbon Deposition on Face of Pintle Tip

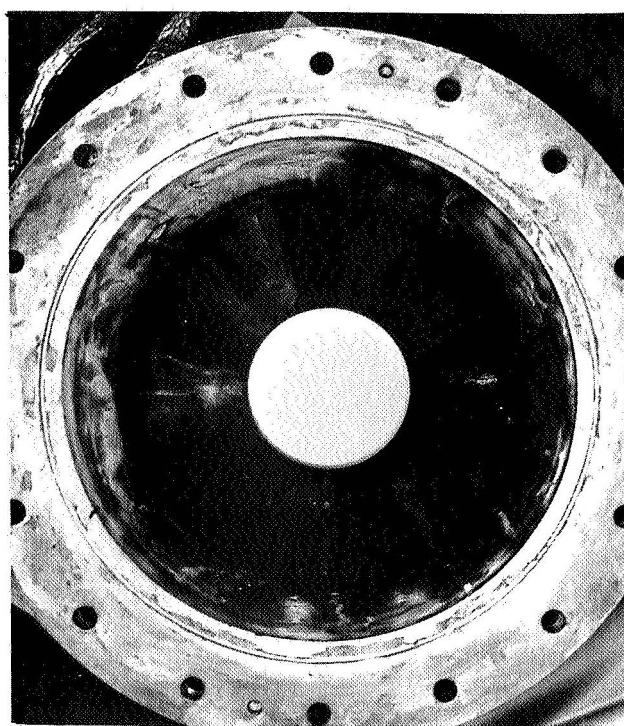


Figure 4-26. Post-Firing View of Thrust Chamber After Test 127 Showing Carbon Deposition on Chamber Walls

## 5. PERFORMANCE EVALUATION SUMMARY

### 5.1 GENERAL PERFORMANCE DATA REDUCTION

For performance evaluation, the injectors were grouped into the three general categories: sawtooth configuration, canted slot configuration, and the straight slot configuration. Performance was determined on the basis of corrected characteristic velocity values. The  $C^*$  values were calculated from chamber pressure and thrust, and comparisons were made between these  $C^*$  efficiencies. The raw data reduction was done by on-line computer techniques which take data directly from the test stand. Because this was a propellant performance evaluation program, the data reduction effort was set up to provide two reduced  $C^*$  quantities: (1) a small time slice maximum  $C^*$ , and (2) a time averaged  $C^*$  data slice. The small time slice was an arbitrary 200 ms which was read out of the computer during a run as the maximum observed performance after ignition transients. The time averaged  $C^*$  value was the overall run averaged value following ignition transients. Since the peaks actually occurred in the short runs they represent potential performance to be obtained. On the other hand, the time averaged values may be of more value to the system designer.

The peak  $C^*$  values were obtained from the on line data by

$$C^*(t) = g A_t \frac{\int_t^{t+200 \text{ ms}} \frac{P_c(t)}{w_o(t) + w_f(t)} dt}{200 \text{ ms}} \quad (5-1)$$

The time averaged  $C^*$  data were obtained by

$$C^*(t) = g A_t \frac{\int_{t_1}^{t_2} \frac{P_c(t)}{w_o(t) + w_f(t)} dt}{\int_{t_1}^{t_2} dt} \quad (5-2)$$

The heat loss corrections were based on measured temperature rise rates from the thermocouples located on the thrust chamber. A complete summary of this heat flux data is found in Section 6.

Redundant measurements were taken throughout the entire system to insure maximum reliability of the data. Two flow meters were located in each propellant feed system along with a calibrated venturi. A computer program was used to calculate the propellant densities entering each flowmeter by using temperature probes to monitor the propellant temperatures at the inlet tube of the flowmeters. The chamber stagnation pressure was calculated on the basis of downstream chamber pressure measurement.

Corrections made to the  $C^*$  values are covered in detail in Appendix B. The correction factors and ranges applied to the data are summarized in the following listing:

Applicable to  $\left[ \eta_{C^*} \right]_{P_c}$  (based on chamber pressure)

$f_p = 1.038$  (momentum)

$f_{TR} = 0.997$  to  $0.998$  (transient throat effects)

$f_{DIS} = 0.992$  (discharge coefficient)

$f_{FR} = 1.000$  (friction)

$f_{HL} = 1.014$  to  $1.023$  (heat loss)

$f_{KE} = 1.002$  (kinetic)

Applicable to  $\left[ \eta_{C^*} \right]_F$  (based on thrust)

$FR = 1.005$  to  $1.007$  (friction)

$DIV = 1.017$  (divergence)

$HL = 1.017$  to  $1.025$  (heat loss)

$KE = 1.009$  (kinetic)

## 5.2 SAWTOOTH CONFIGURATION PERFORMANCE SUMMARY

Table 5-1 is a tabulation of performance values for the sawtooth configuration. The various modifications which are tabulated are detailed in Section 4. The performance of the sawtooth configuration was poor for these propellants. The element design apparently did not permit proper

Table 5-1. Sawtooth Configuration Summary Performance Evaluation

Injector Element	Test No.	O/F MR	Wt 1b/sec	Po Psi	F 1bf	C* Theo	C* <sub>Pc</sub> Corr	NC* <sub>Pc</sub> %	C* <sub>F</sub> Corr	NC* <sub>F</sub> %
SW-1	070	5.6	10.9	44.9	1028	6865	3551	51.72	3827	55.74
SW-1	071	5.3	10.9	56.4	1314	6910	4460	64.55	4457	64.49
SW-1	072	3.6	12.6	47.6	1036	6715	3256	48.49	3326	49.53
SW-1	073	3.7	12.7	43.0	919	6730	2919	43.36	3078	45.74
SW-1	074	5.0	11.4	41.8	868	6930	3161	45.61	3322	47.94
SW-1	075	5.4	12.2	46.9	1061	6900	3314	48.02	3484	50.49
SW-2	080	5.3	12.9	66.0	1739	6910	4410	63.82	4556	65.94

mixing of the two propellants. Various combinations of momentum ratios and sheet thicknesses were tried; however, proper mixing was not achieved. The maximum performance achieved with the sawtooth configuration was 65 percent of C\* efficiency. With continued efforts, some additional increase in performance could probably be achieved; however, in view of the low performance of the injector, it did not appear to be a worthwhile effort.

### 5.3 CANTED SLOT CONFIGURATION PERFORMANCE EVALUATION

Table 5-2 gives the tabulation of performance data on the canted slot configurations. A total of six modifications were made to the canted slot configurations. (These modifications are detailed in Section 4.) This configuration demonstrated a significant performance increase over the sawtooth configuration which was attributed to the venting characteristic of the canted slots; that is, the alternate openings between the oxidizer slots. These openings allowed the fuel to pass down between the oxidizer flow streams allowing a more complete mixing to occur than with the continuous sheets of the sawtooth configuration. Attempts were made to utilize the fuel passing down between the canted slots by adding secondaries. In general, these modifications did not increase the performance.

Table 5-2. Canted Slot Configuration Summary Performance Evaluation

<u>Injector Element</u>	<u>Test No.</u>	<u>O/F MR</u>	<u><math>\dot{w}_t</math> lb/sec</u>	<u><math>P_o</math> psi</u>	<u>F lb f</u>	<u><math>C^*</math> Theo</u>	<u><math>C^*</math> pc Corr</u>	<u><math>\eta_{C^*}</math> %pc</u>	<u><math>\eta_{C^*}</math> F Corr</u>	<u><math>\eta_{C^*}</math> %F</u>
CS-1	076	5.5	12.4	76.4	2146	6880	5311	77.19	5528	80.35
CS-1	077	3.8	12.9	78.0	2158	6750	5212	77.21	5336	79.05
CS-1	082	4.8	12.1	79.9	2227	6910	5692	82.37	5825	84.30
CS-2	086	5.6	12.3	61.6	1413	6740	4317	64.05	6484	96.20
CS-2	087	5.3	12.7	37.7	1241	6790	2559	37.68	3687	54.30
CS-3	088	4.8	11.5	58.3	1259	6855	4370	63.75	4109	59.94
CS-3	089	5.3	12.6	90.7	2547	6790	6205	91.38	6204	91.37
CS-4	090	5.3	12.8	82.8	2330	6790	5576	82.12	5700	83.95
CS-5	091	5.2	12.7	82.4	2222	6805	5593	82.19	5541	81.43
CS-6	092	5.1	12.3	81.4	2170	6820	5704	83.64	5620	82.40
CS-3A	095	5.2	12.6	90.0	2515	6805	6157	90.48	6143	90.27

The maximum performance achieved with the canted slots was 91 percent of characteristic velocity efficiency. This was accomplished with Ring CS-3, a canted slot configuration without secondaries. Increased performance could probably be achieved by optimizing the canted slot dimensions and secondaries. However, the canted slot configuration appeared to have a serious erosion problem. This was probably caused by the entrainment of combustion gases around the pintle assembly causing the ring to overheat.

#### 5.4 STRAIGHT SLOT CONFIGURATION PERFORMANCE SUMMARY

Table 5-3 is a tabulation of performance data on the straight slot configurations. A total of 12 modifications were made to the basic straight slot configuration. (These modifications are detailed in Section 4.) The straight slot configuration demonstrated the highest performance of the three injector modifications that were tested under this contract. Not only did this injector demonstrate the capability of high performance, but also demonstrated durability of the coaxial injector.

Table 5-3. Straight Slot Configuration Performance Evaluation

Injector Element	Te <sub>i</sub>	Concen- tre	FLOX	Average Measured Values During Run				Peak Measured Values During Run			
				φ <sub>t</sub> lb/sec	P <sub>o</sub> psi	C* lb <sub>p</sub>	η <sub>C*</sub> Corr.	φ <sub>t</sub> lb/sec	P <sub>o</sub> psi	C* lb <sub>p</sub>	η <sub>C*</sub> Corr.
SS-1	78	80	5.2	12.6	67.4	1792	6805	67.73	4712	69.24	
SS-2	83	74	4.2	13.1	57.4	1411	6820	55.72	3867	56.70	
SS-3	84	5.1	12.9	63.2	1647	6790	4256	62.69	4371	64.38	
SS-3	85	5.7	14.1	62.9	1498	6728	3875	57.59	4309	64.05	
SS-4	93	5.2	13.4	93.1	2630	6820	6497	95.27	6492	95.20	
SS-5	94	5.3	12.5	80.2	2145	6790	5551	81.75	5441	80.13	
SS-6	96	5.3	12.6	96.6	2747	6805	6624	97.34	6603	97.03	5.2
SS-6	97	5.9	12.4	93.2	2614	6695	6517	97.34	6473	96.68	5.9
SS-6	98	4.7	12.5	97.5	2799	6860	6738	98.22	6733	98.44	4.6
SS-6	99	4.4	11.8	90.7	2539	6885	6673	96.92	6655	96.66	4.3
SS-6	100	4.0	12.0	92.2	2598	6900	6660	96.52	6655	96.45	4.0
SS-6	101	5.1	12.8	97.8	2792	6805	6632	97.46	6631	97.45	5.1
SS-6	102	5.5	12.9	97.7	2795	6775	6574	97.03	6569	96.96	5.1
SS-7	103	5.1	12.9	97.2	2842	6775	6593	95.98	6619	97.69	5.1
SS-8	104	5.4	12.7	96.3	2750	6790	6593	97.09	6598	97.17	5.1
SS-9	105	5.4	12.7	96.4	2744	6760	6581	97.35	6567	97.15	5.1
SS-10	106	5.3	12.6	93.1	2633	6790	6488	95.55	6387	94.06	
SS-11	107	5.3	12.6	81.0	2199	6790	5600	82.48	5538	81.56	
SS-6	108	90	4.2	13.1	96.4	2883	6648	6351	95.50	6273	94.36
SS-6	109	4.7	13.2	95.9	2663	6644	6271	94.38	6189	93.09	4.9
SS-6	110	5.4	13.4	96.7	2706	6668	6234	93.49	6180	92.69	5.6
SS-6	111	6.0	13.3	95.4	2697	6645	6203	93.34	6217	93.55	6.0
SS-6	112	5.3	12.6	92.8	2834	6670	6376	95.59	6505	97.52	5.3
SS-6	113	5.7	12.8	91.7	2570	6660	6202	93.12	6224	93.46	5.7
SS-6	114	5.2	13.1	95.4	2692	6670	6297	94.41	6302	94.48	5.5
SS-6	115	4.4	13.0	94.2	2601	6635	6254	94.26	6168	92.97	4.4
SS-6	116	4.9	13.0	95.3	2677	6655	6326	95.04	6310	94.80	5.0
SS-12	117	5.0	12.6	93.4	2592	6665	6406	96.27	6366	95.51	5.2
SS-12	118	5.1	12.2	94.6	2622	6936	6704	96.66	6628	95.55	5.1
SS-12	119	5.9	12.4	95.7	2659	6805	6662	97.90	6593	98.96	5.9
SS-12	120	4.8	12.4	96.7	2728	6932	6659	96.05	6602	95.45	4.7
SS-12	121	4.2	12.4	95.9	2689	6820	6632	97.24	6639	97.55	4.2
SS-12	122	5.2	12.1	91.4	2168	6932	6500	93.77	6379	92.03	5.1
SS-12	123	4.2	12.3	92.9	2471	6820	6469	94.85	6263	91.83	4.3
SS-12	124	4.3	12.3	96.5	2728	6840	6727	98.35	6770	98.97	4.3
SS-12	125	5.3	12.4	97.2	2160	6925	6709	96.88	6784	97.96	5.3
SS-12	126	5.1	11.8	161.1	2334	6936	6576	94.81	6635	95.66	5.1
SS-12	127	4.4	11.8	163.7	2391	6856	6659	97.27	6752	98.49	4.4

The first three straight slot injector configurations that were tested, that is, SS-1, -2, and -3 on Tests 078, 083, and 084, respectively, did not demonstrate a high performance characteristic. However, studies of these injector modifications revealed that the total venting area which can be related to the element blockage on each element was very low and, therefore, the configuration appeared more like a continuous sheet injector than a vented straight slot injector.

Straight slot configuration SS-4 was the first of a series of modifications which produced high combustion performance. This element had an effective blockage area of 17.5 percent, including the secondaries. The secondaries accounted for approximately 15 percent of the oxidizer flow. While the ring element was fabricated from 304 stainless, there were no signs of erosion, indicating that the element ran cool.

Tests 096 through 107 represented minor changes to the basic element used on Test 093 and included some mixture ratio surveys using a 74 percent FLOX mixture. In this series of tests, element SS-6 was used with the exception of Test 117 which used element SS-12. Element SS-12 showed a significant increase in performance over SS-6. Because element SS-12 appeared to be the highest performing modification it was used entirely for the test with 80 percent FLOX. Figure 5-1 shows a summary of the corrected performance using the 90 percent FLOX. Figure 5-1a shows the average calculated performance data for each of the tests. Using regression analysis of the data, a second order curve was computed through the data points. Figure 5-1b shows the same test but the selective peak performance data points. Again, a regression analysis was conducted to fit a second order curve through the data. The figure also indicates the statistical standard deviations associated with this analysis.

Element SS-12 produced the highest performance of all the straight slot configurations that were tested. The results indicate that the higher performance of element SS-12 can be attributed to the larger secondary flow rate that was designed into that element. A mixture ratio survey was conducted over a range of 4.2 to 5.9 and showed that the element had relatively flat performance over this range as shown in Figure 5-2. The performance efficiencies shown in Figure 5-2 have been corrected to reflect the losses accounted for in Appendix B. The heat rejection losses

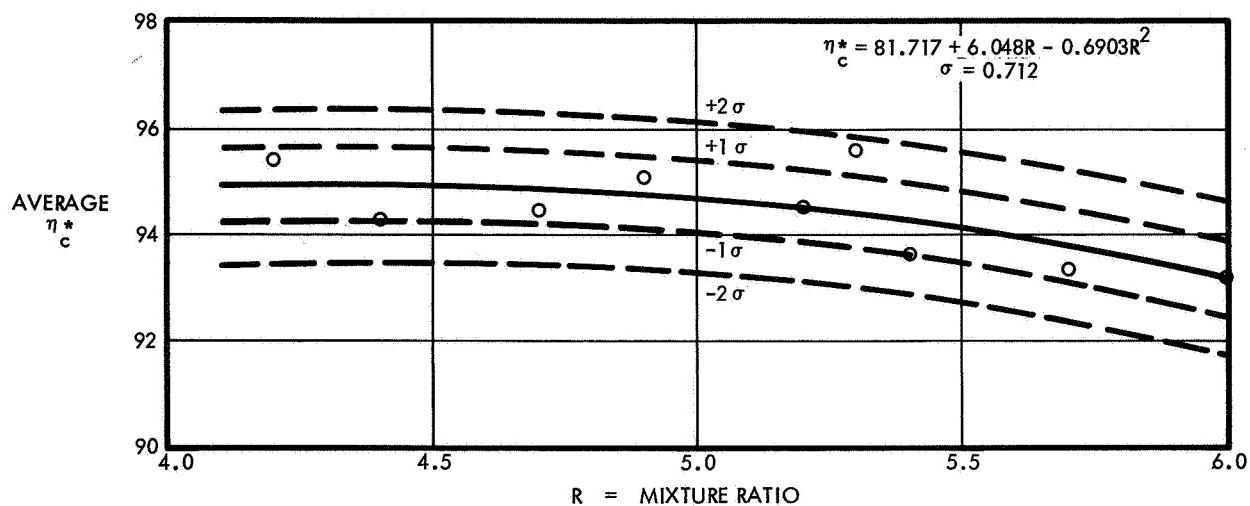


Figure 5-1a. Average Performance Values of Base Line Test with 90% FLOX and 55% Methane-45% Ethane. Injector Element SS-6 and a Chamber Contraction Ratio of 2.5

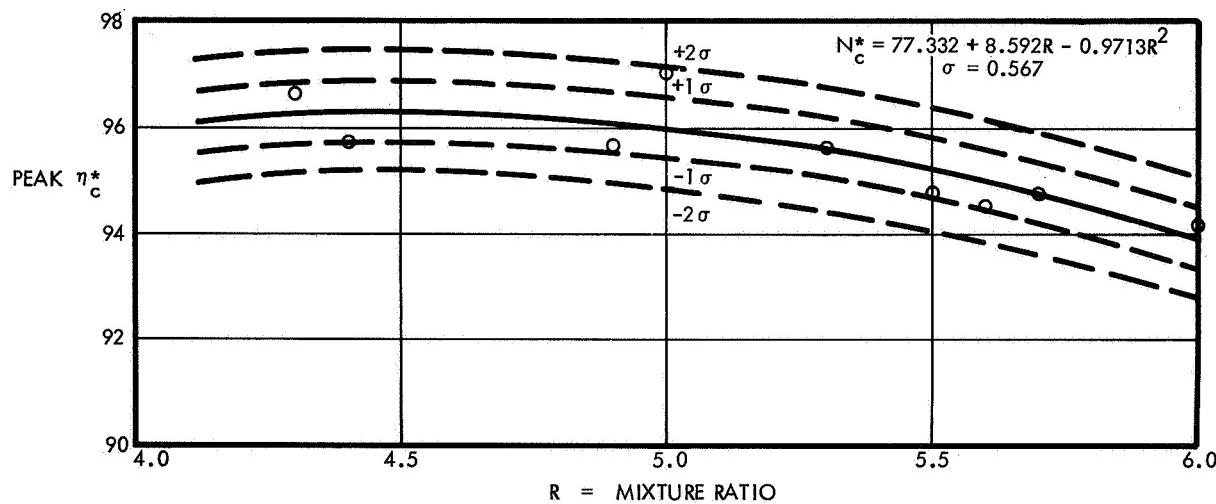


Figure 5-1b. Peak Performance Values of Base Line Test with 90% FLOX and 55% Methane-45% Ethane. Injector Element SS-6 and a Chamber Contraction Ratio of 2.5

were 1.5 percent for the lower mixture ratios and 1.7 percent for the higher mixture ratios. A regression analyses was conducted on the data in Figure 5-2 to determine the curve fit. The figure also indicates the statistical standard deviations associated with this analysis.

Fluorine concentrations were varied from 74 to 90 percent with the nominal concentration at 80 percent. Table 5-4 is a tabulation of the performance results as a function of the fluorine concentration.

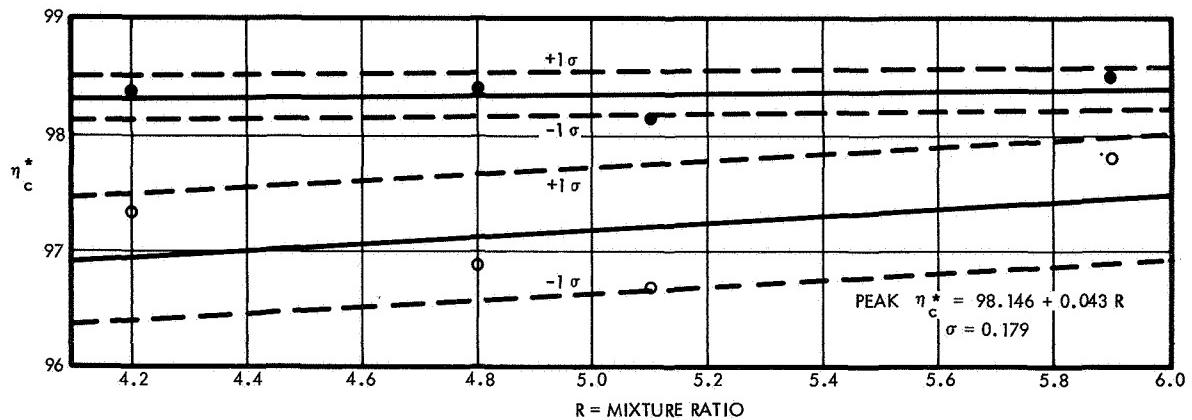


Figure 5-2. Peak and Average Performance Values of Base Line Test Using SS-12 Ring Element with 80 Percent FLOX and 55 Percent Methane and 45 Percent Ethane

Table 5-4. C\* Performance as a Function of FLOX Concentration

FLOX Concentration %	Test No.	Element	MR O/F	C* Pc Corr.	$\eta_c^*$
74	96	SS-6	5.3	6723	98.8
74	101	SS-6	5.1	6675	97.9
90	112	SS-6	5.3	6378	95.6
90	114	SS-6	5.2	6320	94.8
90	117	SS-12	5.0	6552	98.2
80	118	SS-12	5.1	6797	98.0

The two final tests in the program were with a high contraction ratio chamber. The throat size of this chamber was reduced from the nominal to give a contraction ratio of 4.5. The same injector element SS-12 was used and the propellant flow rates were maintained the same as with the nominal conditions. Chamber pressures were approximately 160 psia. Figure 5-3 shows the performance curve as a function of mixture ratio for the high contraction ratio chamber.

The nominal test series were conducted with a chamber L\* of 30 inches. Tests 122 through 125, however, were conducted with L\*'s of 15 and 45 inches. Figure 5-4 shows the performance using the 15-inch L\*. A loss in performance of from 1.5 to 2 percent was experienced when using this short chamber compared to the nominal chamber. Figure 5-5

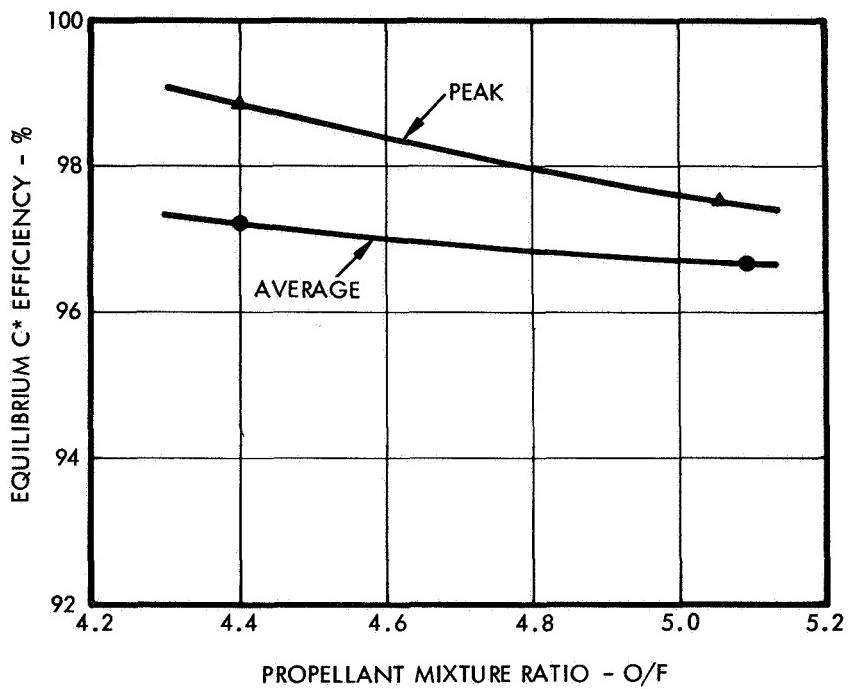


Figure 5-3. Peak and Average Performance Values of High Contraction Ratio Chamber  $\epsilon = 4.5$  Using SS-12 Ring Element with 80 Percent FLOX

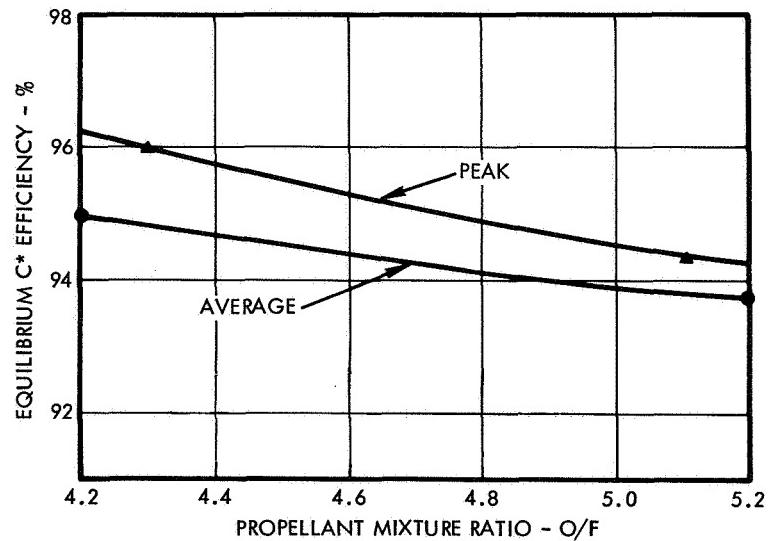


Figure 5-4. Peak and Average Performance Values of 15 Inch L\* Chamber Using SS-12 Ring Element with 80 Percent FLOX

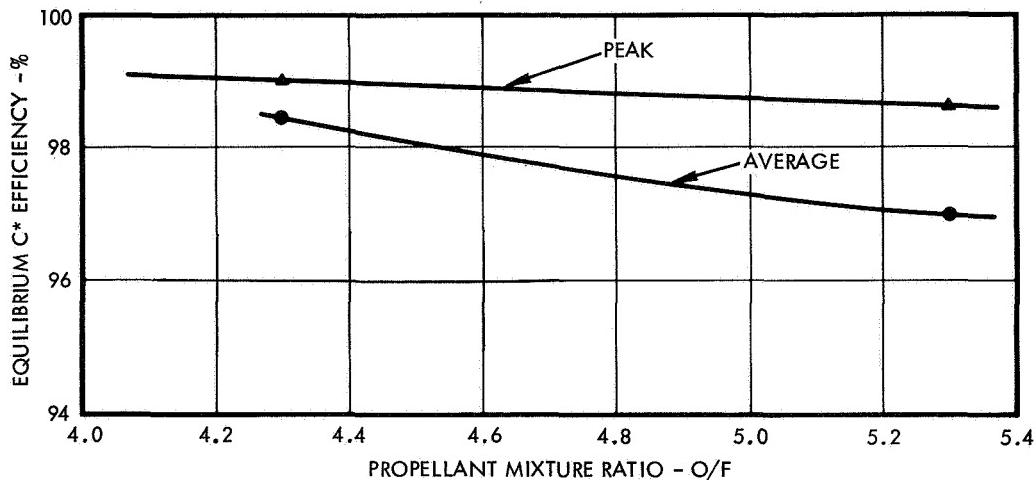


Figure 5-5. Peak and Average Performance Values of 45 Inch L\* Chamber Using SS-12 Ring Element with 80 Percent FLOX

shows the performance using the longer 45-inch L\* chamber. Approximately a 1 percent increase occurred using this chamber. Results of these tests show that the injector element should be adjusted to improve the propellant mixing characteristics.

### 5.5 PRESSURE DROPS

The oxidizer pressure drop necessary to achieve the high performance has not been fully defined. The elements used in these tests had an orifice  $C_d$  of 0.65 in most cases, and this low  $C_d$  represents a significant amount of the pressure drop across the oxidizer orifice. As explained in Section 4, no attempt was made to optimize the  $C_d$  of these orifices. In Test 102, the orifice entrance was rounded slightly to demonstrate the effect of an increased  $C_d$  on the oxidizer pressure drop. In this case, the orifice  $C_d$  was increased to 0.73 with no performance degradation.

### 5.6 STABILITY OBSERVATIONS

The tests were instrumented for high frequency instability. Water-cooled helium bleed, Kistler transducers were used for this instrumentation. No spontaneous instabilities appeared with any of the tests conducted under this program. The straight slot injector configuration exhibited a smooth combustion characteristic with a maximum peak-to-peak combustion noise of  $\pm 3$  psi.

## 5.7 DATA CONSISTENCY

As a measure of data consistency,  $C^*$  results for both  $P_c$  and  $F$  determinations are cross-plotted in Figure 5-6. It is seen that the data correlate to within  $\pm 0.5$  percent, indicating excellent thrust stand instrumentation calibration.

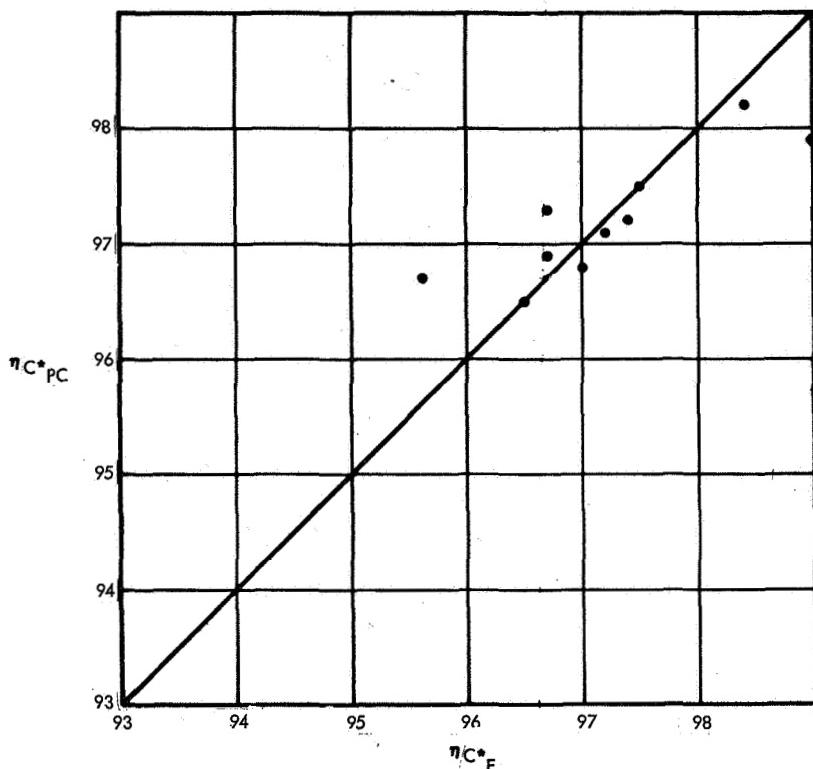


Figure 5-6. Correlations of Thrust Measurements with Chamber Pressure Measurements for Performance

## 5.8 SUMMARY

The contractual performance goals were met with the TRW coaxial injector. This program represented the first all-cryogenic, liquid propellant evaluations with this type of injector. The basic factor for successful design of the injector for the specified propellants appears to be associated with obtaining proper initial liquid phase mixing, once the elemental droplet size criteria is specified. The reactive nature of the FLOX/LPG's is unknown and empirical evaluation was necessary to arrive at a configuration to deliver the specified performance. The inexpensive design fabrication qualities of the injector allowed a ready evaluation of geometrical effects.

## 6. HEAT TRANSFER DESIGN AND RESULTS

### 6.1 INJECTOR HEAT TRANSFER DESIGN

In order to complete the injector design and characterize the proper operating conditions, an analysis was conducted to determine the pintle temperatures and pre-conditioning necessary for unrestricted injector operation at the nominal operating conditions. The pintle injector model was analyzed by using the TRW Thermal Analysis Program, TAP, and pertinent design data.

This study showed that the injector pintle should be cooled to  $-240^{\circ}\text{F}$  to  $-300^{\circ}\text{F}$  before ignition and the FLOX should be approximately  $-300^{\circ}\text{F}$  at the injector to insure that no boiling occurs in the injector after ignition. FLOX film boiling behind the pintle head would restrict the FLOX flow and the pintle face temperatures would exceed  $300^{\circ}\text{F}$ .

Figure 6-1 shows the pintle chamber profile which illustrates the important heat transfer variables. The temperature behavior of the pintle cold side wall as a function of time, initial temperature, FLOX temperature, and hot side film coefficient is shown in Figure 6-2. Finally, Figure 6-3 shows the expected steady-state temperature profile through the pintle for stable (no film boiling) liquid injection. The maximum indicated thermal gradient from the pintle centerline through the maximum OD was  $350^{\circ}\text{F}$ .

In order to prevent FLOX from film boiling in the pintle, the analysis indicated that the following operating conditions should be maintained; 1) Cooldown injector to temperatures to less than  $-220^{\circ}\text{F}$  (saturation temperature at 160 psi), 2) Introduce and maintain FLOX flowing to the injector to approximately  $-300^{\circ}\text{F}$ .

### 6.2 EXPERIMENTAL HEAT FLUX MEASUREMENTS

The program, while not specifically oriented towards chamber heat transfer analysis, did provide an extensive heat transfer evaluation. The uncooled copper heat sink chamber was instrumented with 54 thermocouples. These thermocouples were attached to calorimetric plugs machined into the copper base metal of the chamber. A complete analysis of these calorimetric plugs is given in Appendix C. Because of limitations in the number of amplifiers available for heat transfer data acquisition, it was

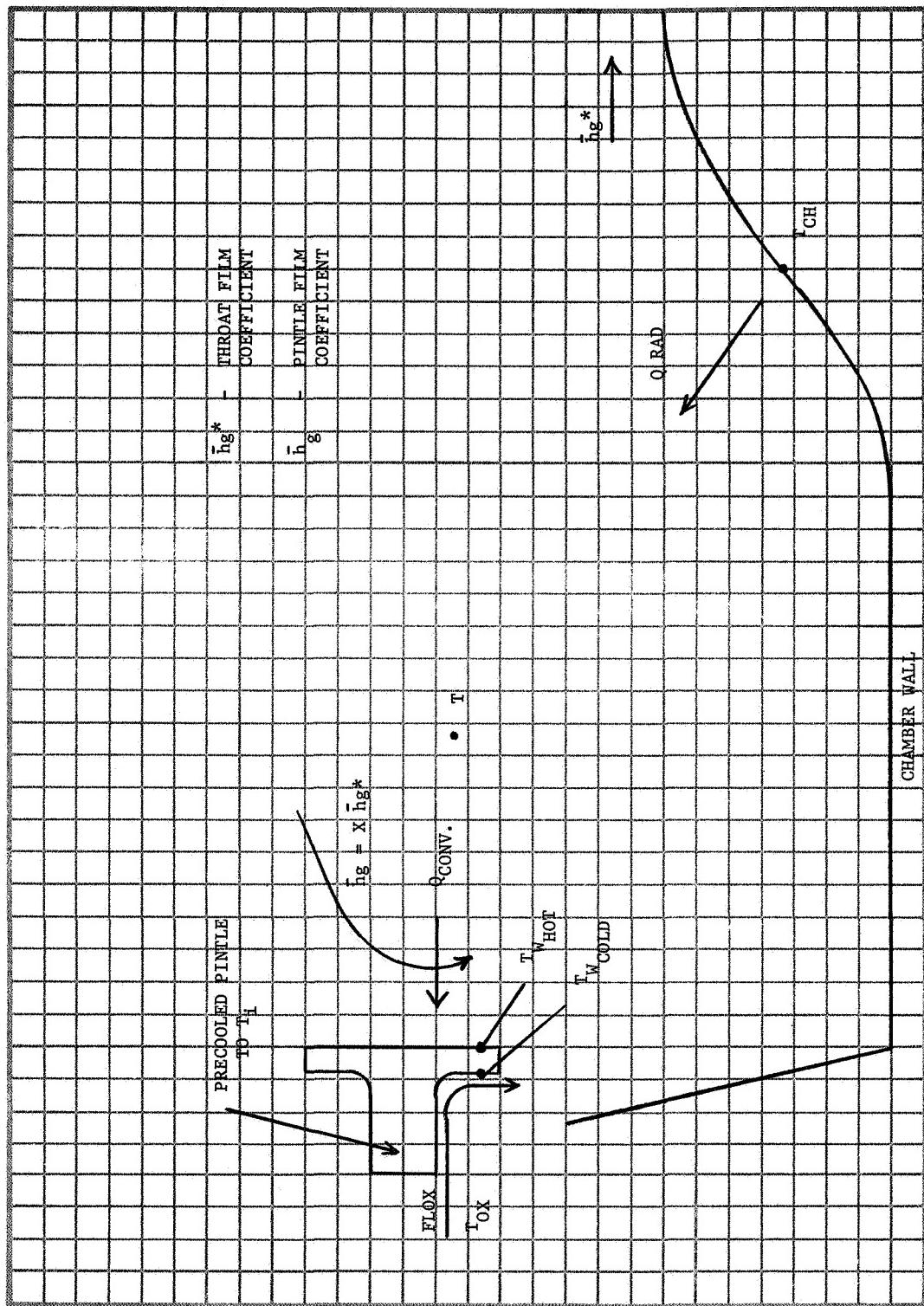


Figure 6-1. Pintle Heat Transfer Analysis Model

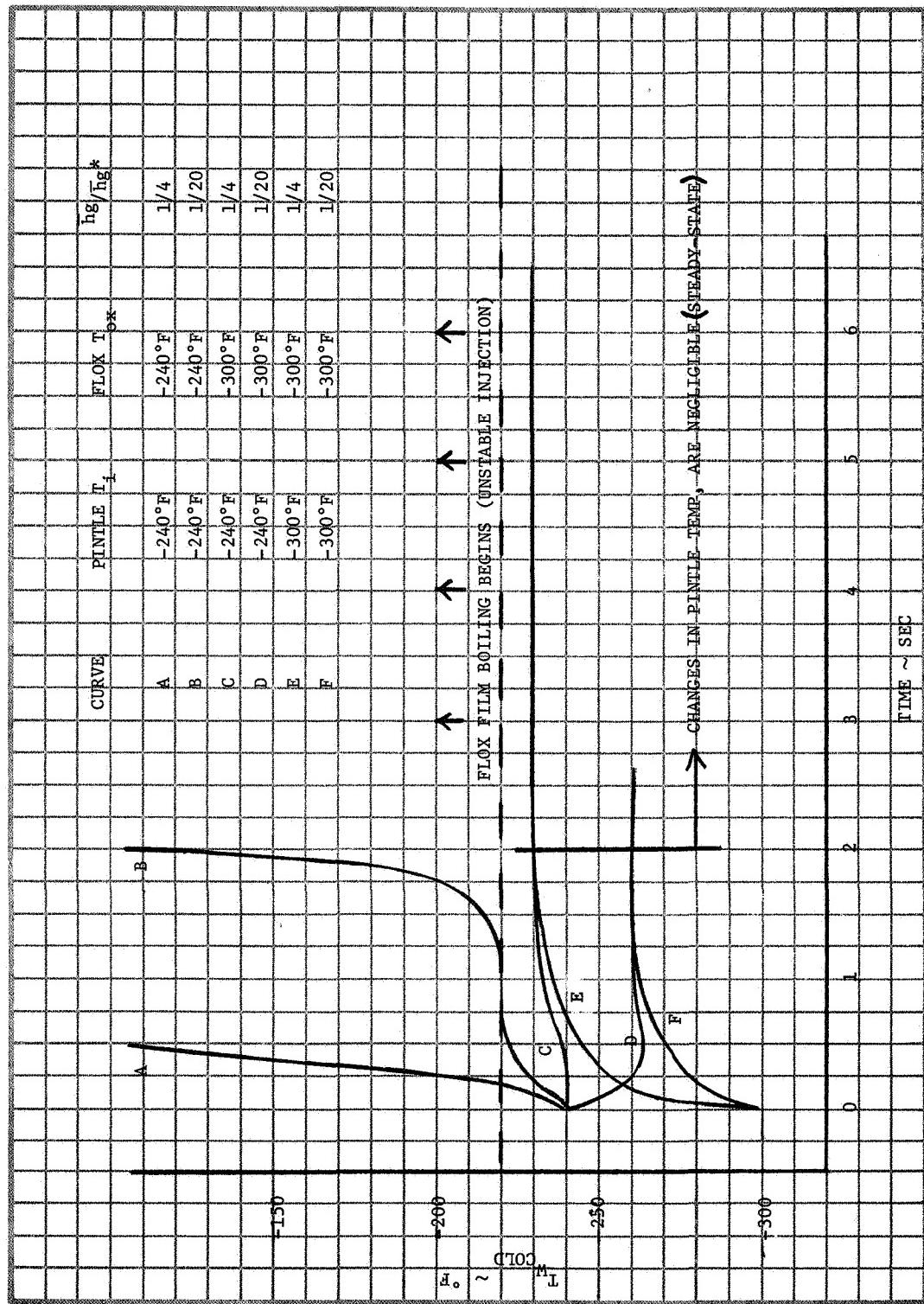


Figure 6-2. Transient Pindle Heat Transfer Analysis

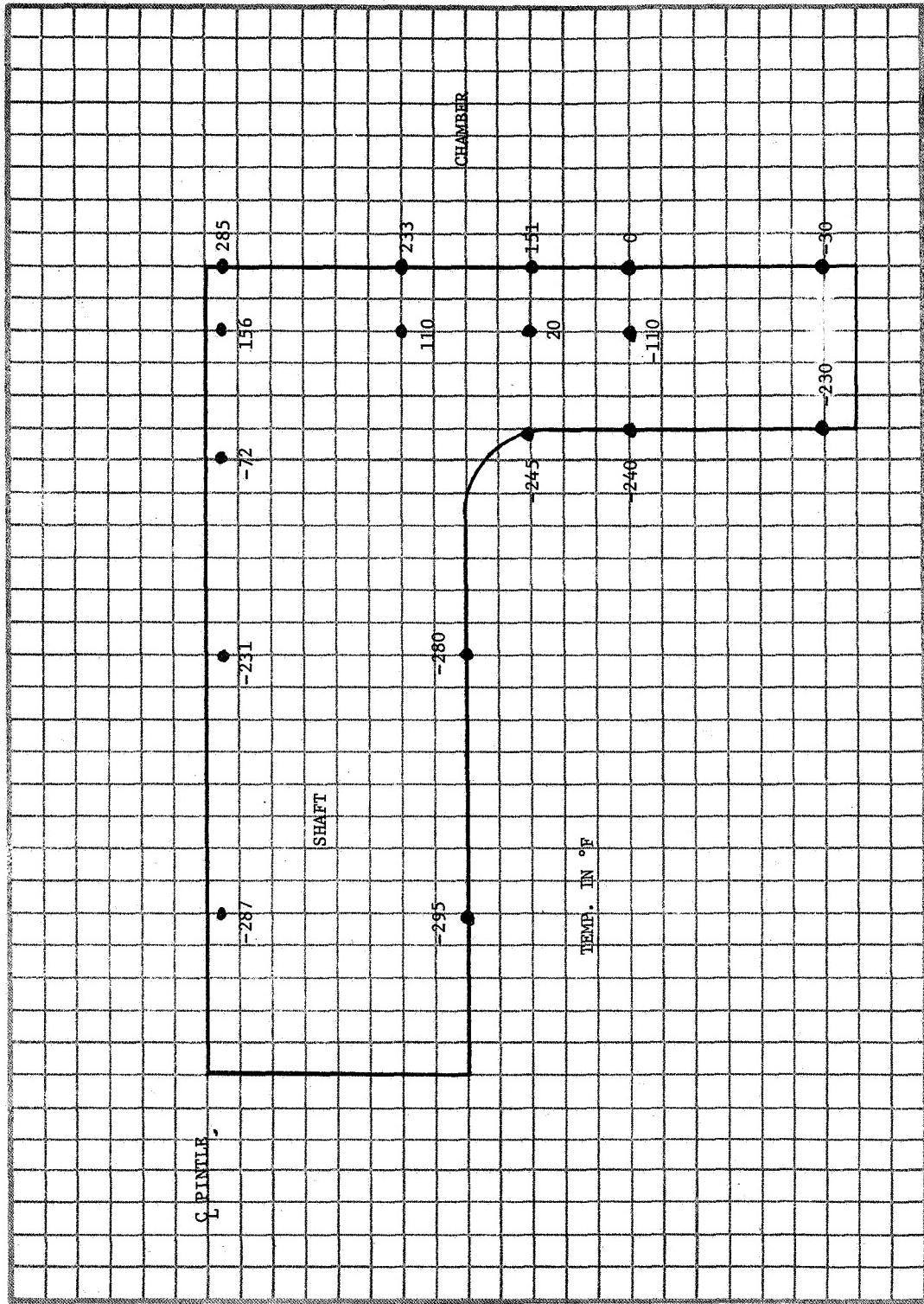


Figure 6-3. Pintle Temperature Profile

necessary for TRW to install a multiplexer system to sample the data from the 54 thermocouples. The multiplexer system was not immediately available to the program and therefore the first series of tests did not include all of the thermocouples.

The heat transfer data collected from the tests provided the necessary information for making corrections to the V characteristic velocity calculations. The heat transfer data also provided a means for evaluating the operating characteristics of the injector. The spool section of the chamber contained three rings of 6 thermocouples each. The thermocouples were located three in a row, 60 degrees apart. The nominal throat section contained four rings of 6 thermocouples each, plus one ring of 12 thermocouples monitoring the convergent and divergent sections of the throat. In all, the throat section contained 36 thermocouples. With this arrangement of thermocouples, a very extensive evaluation could be made of the heat transfer profiles throughout the chamber.

Figure 6-4 shows an axial layout of the uncooled heat sink chamber. The chamber was divided into 9 axial sections. A surface area inside the chamber was associated with each of these sections. Each section contains 6 thermocouples located 60 degrees apart. The chamber spool was made up of Sections I, II and III. The thermocouples in these sections were numbered TC-R1 through TC-R18. The throat section of the chamber was made up of Sections IV through IX. Each of these sections contains 6 thermocouples and these were noted as TC-1 through TC-36. Each thermocouple in the chamber has a thermocouple number: the locations of these thermocouples was shown in Figures 6-5 and 6-6.

The chamber heat flux was determined from the temperature rise rates associated with each of the thermocouples located throughout the chamber. A complete analysis was done with a thermocouple plug design. These data were presented in Appendix C. The analysis of the calorimetric plugs showed that the optimum time to evaluate the heat flux data would be between two and four seconds into a firing. During this time period, the errors associated with the heat flux measurement would be minimum. Therefore, heat flux data for the tests conducted on this program were determined at 3 seconds into the test firing unless the test was terminated

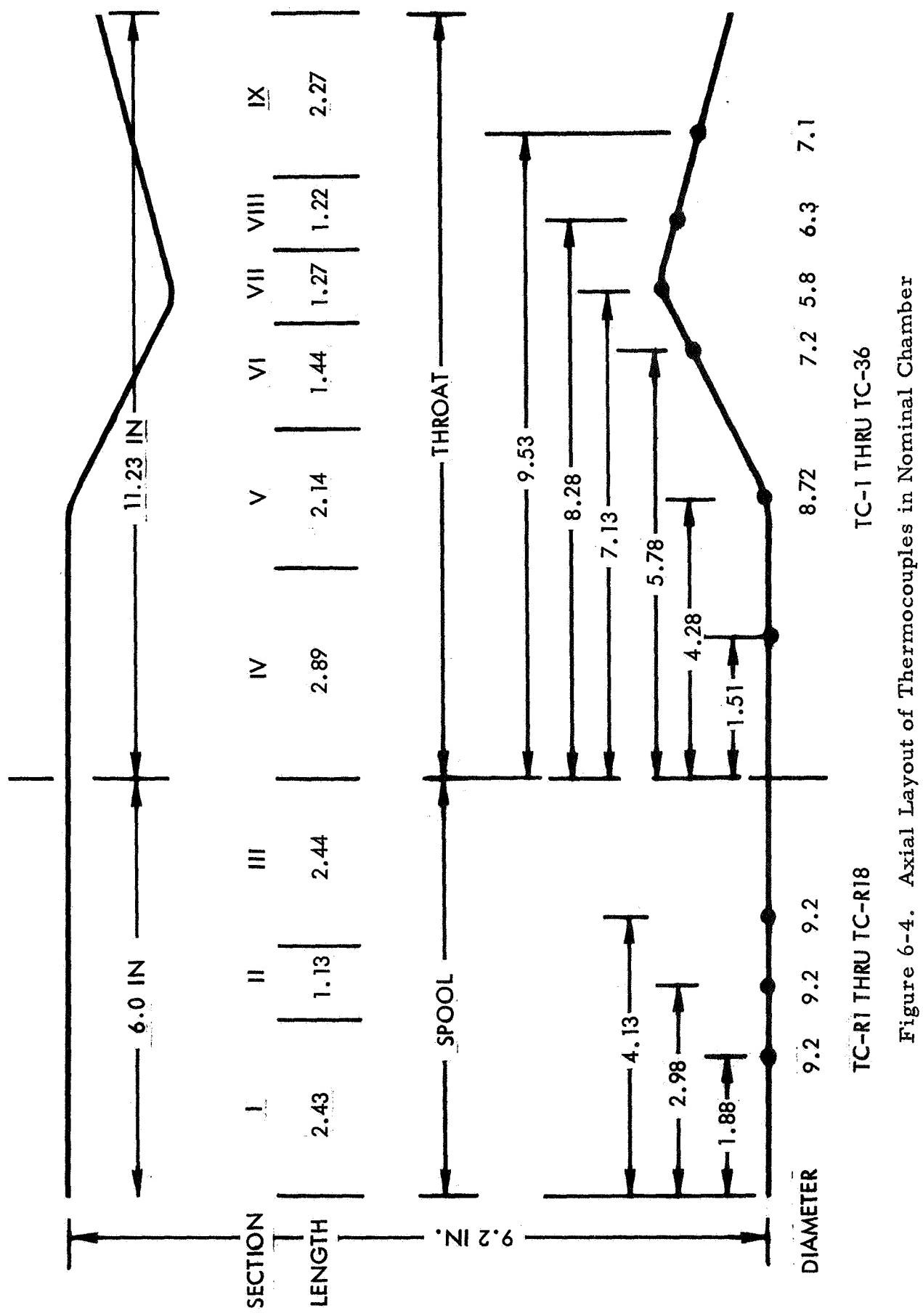


Figure 6-4. Axial Layout of Thermocouples in Nominal Chamber

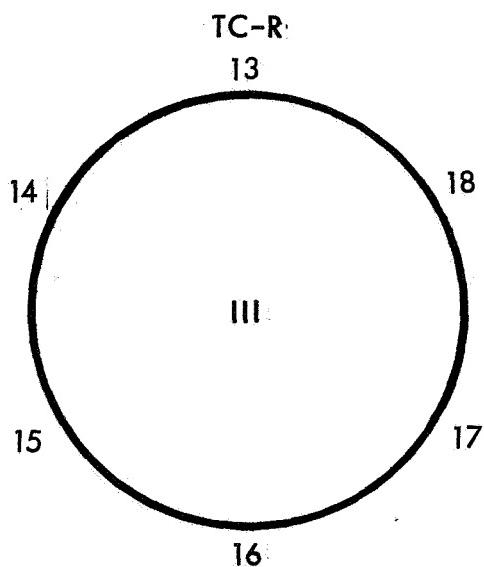
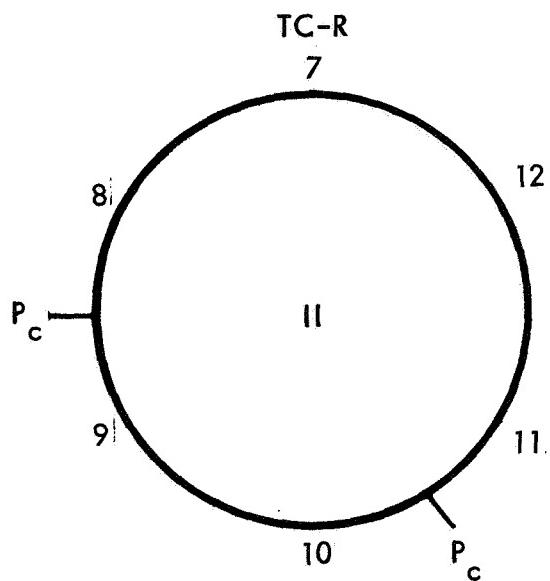
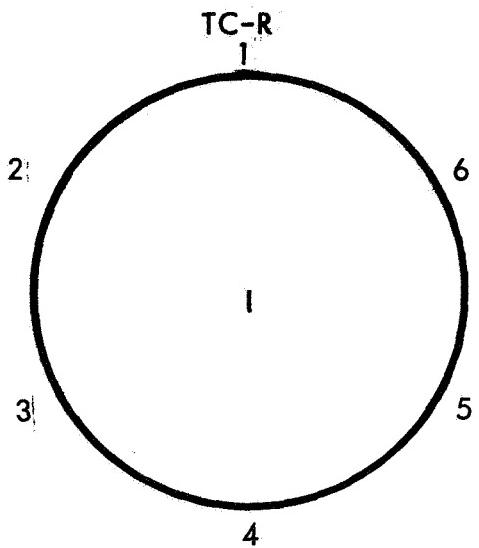


Figure 6-5  
Thermocouple Key by Axial  
Section Number in the  
Chamber Spool

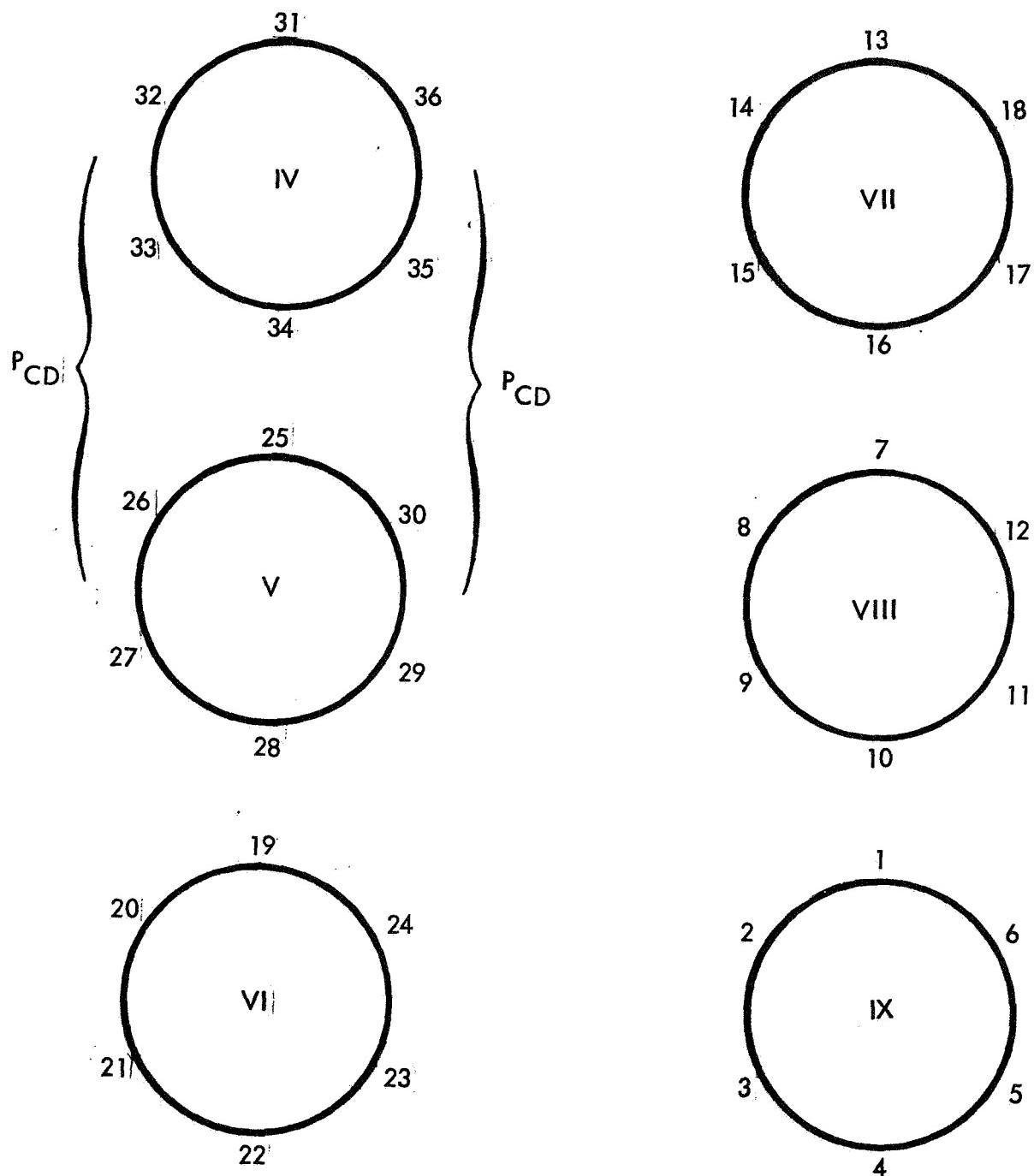


Figure 6-6. Thermocouple Key by Axial Section Number in the Chamber Throat

earlier than 3 seconds. From temperature rise rates determined at 3 seconds into a firing, the heat flux associated with the calorimetric plug was determined by

$$\left(\frac{Q}{A}\right)_{\text{plug}} = \rho C_p L \frac{dT}{dt} \quad (6-1)$$

where

- $\rho$  = density of OFHC copper  
 $C_p$  = specific heat of OFHC copper  
 $L$  = length of plug  
 $\frac{dT}{dt}$  = temperature rate

Because the web supporting the calorimetric plug was not completely free of conduction, a radial loss occurred from the plug to the surrounding material of the chamber. Therefore, the plug was not a perfect isothermal body and the heat flux measured with the plug had to be corrected to represent heat flux into the chamber. This correction was determined analytically and is presented in Appendix C. After correcting each thermocouple plug to determine the heat flux associated with that thermocouple, an average heat flux was determined for the given section of the chamber.

Tables 6-1 through 6-8 present the heat flux data summary for tests 101 through 105 and 118 through 121 respectively. These tables are laid out to present the nine sections and heat flux associated with each thermocouple in each section. The heat flux in each section was averaged and multiplied by the area associated with each section, in order to determine the heat loss of the gas to the thrust chamber.

Tables 6-1 through 6-4 show that typical heat flux losses were on the order of 0.5 percent. Run 101 had a heat flux loss of 2.5 percent and this was associated with the lower fuel pressure drop. A correlation was made between the propellant momentum ratio and heat flux losses in the chamber. This relationship is presented in Figure 6-7. This relationship shows that heat flux losses to the chamber go up proportional with increasing O/F momentum ratio.

Table 6-1. Heat Flux Data Summary - Run 101

Chamber Sections	I						II						III					
	1	2	3	4	5	6	7	8	9	10	11	12	13	14	15	16	17	18
TG-R	1	2	3	4	5	6	7	8	9	10	11	12	13	14	15	16	17	18
$\Delta T/t$	267	224	213	268	273	278	161	127	187	204	205	205	300	317	311	343	325	
$(Q/A)_{\text{plug}}$	3.14	2.63	2.50	3.15	3.21	3.27	1.89	1.49	2.20	2.40	2.41	2.41	3.53	3.72	3.65	4.03	3.82	
$(Q/A)_{\text{corr}}$	3.76	3.16	3.00	3.78	3.85	3.92	2.27	1.79	2.64	2.88	2.89	2.89	4.23	4.47	4.39	4.84	4.58	
$\frac{(Q/A)}{(Q/A)\Delta A}$				3.58					2.56							4.50		
				251.2					83.7							317.4		
Chamber Sections	IV						V						VI					
	31	32	33	34	35	36	25	26	27	28	29	30	19	20	21	22	23	24
TG-R	31	32	33	34	35	36	25	26	27	28	29	30	19	20	21	22	23	24
$\Delta T/t$	221	336					280	322	254	340	253					279	309	3.20
$(Q/A)_{\text{plug}}$	2.60	3.95					3.29	3.78	2.98	4.00	2.97					3.28	3.63	3.20
$(Q/A)_{\text{corr}}$	3.12	4.74					3.95	4.54	3.58	4.79	3.57					3.93	4.36	3.84
$\frac{(Q/A)}{(Q/A)\Delta A}$				3.93					4.22							3.93		
				328.2					247.0							127.6		
Chamber Sections	VII						VIII						IX					
	13	14	15	16	17	18	7	8	9	10	11	12	1	2	3	4	5	6
TG-R	13	14	15	16	17	18	7	8	9	10	11	12	1	2	3	4	5	6
$\Delta T/t$	345	301	283	317	289	194	201	206	181	195	168	175	189	113	187	206		
$(Q/A)_{\text{plug}}$	4.05	3.54	3.65	3.33	3.72	3.40	2.28	2.36	2.42	2.13	2.29	1.97	2.06	2.22	1.33	2.20	2.42	
$(Q/A)_{\text{corr}}$	4.86	4.24	4.39	3.99	4.47	4.07	2.74	2.83	2.90	2.55	2.75	2.37	2.47	2.66	1.59	2.64	2.90	
$\frac{(Q/A)}{(Q/A)\Delta A}$				4.34					2.69							2.45		
				100.2					65.1							130.7		

Table 6-2. Heat Flux Data Summary - Run 102

Table 6-3. Heat Flux Data Summary - Run 104

Chamber Sections																			
TC-R	1	2	3	4	5	6	7	8	9	10	11	12	13	14	15	16	17	18	
$\Delta T/t$	111	90	98	60	52	230	217	144	120	175	187	110	255	256	127	183	142		
(Q/A) plug	1.30	1.06	1.15	.71	.61	2.70	2.55	1.69	1.41	2.06	2.20	1.29	3.00	3.01	1.49	2.15	1.67		
(Q/A) corr	1.57	1.27	1.38	.85	.73	3.24	3.06	2.03	1.69	2.47	2.64	1.55	3.60	3.61	1.79	2.58	2.00		
$\overline{(Q/A)}$		$\overline{(Q/A)}$						$\overline{(Q/A)}$						$\overline{(Q/A)}$					
			1.16	81.4						2.52	82.5				2.52	177.8			
Chamber Sections																			
TC-	31	32	33	34	35	36	25	26	27	28	29	30	19	20	21	22	23	24	
$\Delta T/t$	177	199					87	257	213	218	231	63	272	294	176	279	271		
(Q/A) plug	2.08	2.34					1.02	3.02	2.50	2.56	2.71	.74	3.20	3.45	2.07	3.28	3.18		
(Q/A) corr	2.50	2.81					1.23	3.62	3.00	3.07	3.26	.89	3.84	4.15	2.48	3.93	3.82		
$\overline{(Q/A)}$		$\overline{(Q/A)}$						$\overline{(Q/A)}$						$\overline{(Q/A)}$					
			2.66	221.7						2.84	166.2				3.19	103.5			
Chamber Sections																			
TC-	13	14	15	16	17	18	7	8	9	10	11	12	1	2	3	4	5	6	
$\Delta T/t$	159	213	204	270	156	226	168	124	121	223	135	154	144	168	171	160	163		
(Q/A) plug	1.87	2.50	2.40	3.17	1.83	2.66	1.97	1.46	1.42	2.62	1.59	1.81	1.69	1.97	2.01	1.88	1.92		
(Q/A) corr	2.24	3.00	2.88	3.81	2.20	3.19	2.37	1.75	1.71	3.14	1.90	2.17	2.03	2.37	2.41	2.26	2.30		
$\overline{(Q/A)}$		$\overline{(Q/A)}$						$\overline{(Q/A)}$						$\overline{(Q/A)}$					
			2.89	66.68						2.17	52.6				2.27	121.2			

Table 6-4: Heat Flux Data Summary - Run 105

Chamber Sections		I				II				III								
TG-R	1	2	3	4	5	6	7	8	9	10	11	12	13	14	15	16	17	18
$\Delta T/t$	103	97	116	80	93	209	189	218	195	210	221	159	234	253	198	207	261	
$(Q/A)_{\text{plug}}$	1.21	1.14	1.36	.94	1.09	2.46	2.22	2.56	2.29	2.47	2.60	1.87	2.75	2.97	2.33	2.43	3.07	
$(Q/A)_{\text{corr}}$	1.45	1.37	1.64	1.13	1.31	2.95	2.66	3.07	2.75	2.96	3.12	2.24	3.30	3.57	2.79	2.92	3.68	
$\frac{\overline{(Q/A)}}{(Q/A)\Delta A}$				1.38								2.92			3.08			
				96.9								95.4			217.4			
Chamber Sections		IV				V				VI								
TG-R	31	32	33	34	35	36	25	26	27	28	29	30	19	20	21	22	23	24
$\Delta T/t$	220	164					106	249		214	223	201	117	266	286	178	274	288
$(Q/A)_{\text{plug}}$	2.59	1.93					1.25	2.93		2.51	2.62	2.36	1.37	3.13	3.36	2.09	3.22	3.38
$(Q/A)_{\text{corr}}$	3.10	2.31					1.49	3.51		3.02	3.14	2.83	1.65	3.75	4.03	2.51	3.86	4.06
$\frac{\overline{(Q/A)}}{(Q/A)\Delta A}$					2.71							2.80			3.31			
					225.9							164.0			107.6			
Chamber Sections		VII				VIII				IX								
TG-R	13	14	15	16	17	18	7	8	9	10	11	12	1	2	3	4	5	6
$\Delta T/t$	248	247	237	298	228	232	201	135	209	232	122	116	143	152	157	142	167	
$(Q/A)_{\text{plug}}$	2.91	2.90	2.78	3.50	2.68	2.73	2.36	1.59	2.46	2.73	1.43	1.36	1.68	1.79	1.84	1.67	1.96	
$(Q/A)_{\text{corr}}$	3.50	3.48	3.34	4.20	3.21	3.27	2.83	1.90	2.95	3.27	1.72	1.64	2.02	2.14	2.21	2.00	2.35	
$\frac{\overline{(Q/A)}}{(Q/A)\Delta A}$					3.50							2.39			2.14			
													80.9			57.7	114.3	

Table 6-5. Heat Flux Data Summary—Run 118

Chamber Sections	I				II				III										
	TCR	1	2	3	4	5	6	7	8	9	10	11	12	13	14	15	16	17	18
TCR	1.57	112	70	107	30	70	177	183	89	85	78	83	110	148	151	134	134	161	
$\Delta T/t$																			
Q/A plug	1.84	1.31	.82	1.25	.35	.82	2.08	2.14	1.04	1.0	.91	.97	1.29	1.73	1.77	1.57	1.89		
Q/A corr	2.21	1.57	.98	1.56	.42	.98	2.50	2.57	1.24	1.20	1.09	1.16	1.54	2.08	2.12	1.88	2.27		
$\frac{(\overline{Q/A})}{(Q/A)\Delta A}$																			
TC	31	32	33	34	35	36	25	26	27	28	29	30	19	20	21	22	23	24	
$\Delta T/t$	213		126	244	182	215		168	65	146	233	202			214	60	234		
Q/A plug	2.49		1.48	2.86	2.14	2.52		1.97	.76	2.29	2.73	2.36			2.50	.70	2.74		
Q/A corr	2.99		1.77	3.43	2.57	3.02		2.36	.91	2.76	3.27	2.83			3.00	.84	3.28		
$\frac{(\overline{Q/A})}{(Q/A)\Delta A}$																			
TC	13	14	15	16	17	18	7	8	9	10	11	12	1	2	3	4	5	6	
$\Delta T/t$	150	212	183		216		132		177	110	186				160	177			
Q/A plug	1.75	2.48	2.14		2.52		1.54		2.07	1.28	2.18				1.87	2.07			
Q/A corr	2.10	2.98	2.57		3.02		1.85		2.48	1.54	2.62				2.24	2.48			
$\frac{(\overline{Q/A})}{(Q/A)\Delta A}$																			
TC	1.3	1.4	1.5	1.6	1.7	1.8	1.7	1.8	1.9	1.10	1.12	1.13	1.14	1.15	1.16	1.17	1.18	1.19	
$\Delta T/t$	1.50	2.12	1.83		2.16		1.32		1.77	1.10	1.86				1.60	1.77			
Q/A plug	1.75	2.48	2.14		2.52		1.54		2.07	1.28	2.18				1.87	2.07			
Q/A corr	2.10	2.98	2.57		3.02		1.85		2.48	1.54	2.62				2.24	2.48			
$\frac{(\overline{Q/A})}{(Q/A)\Delta A}$																			
TC	1.3	1.4	1.5	1.6	1.7	1.8	1.7	1.8	1.9	1.10	1.12	1.13	1.14	1.15	1.16	1.17	1.18	1.19	
$\Delta T/t$	1.50	2.12	1.83		2.16		1.32		1.77	1.10	1.86				1.60	1.77			
Q/A plug	1.75	2.48	2.14		2.52		1.54		2.07	1.28	2.18				1.87	2.07			
Q/A corr	2.10	2.98	2.57		3.02		1.85		2.48	1.54	2.62				2.24	2.48			
$\frac{(\overline{Q/A})}{(Q/A)\Delta A}$																			
TC	1.3	1.4	1.5	1.6	1.7	1.8	1.7	1.8	1.9	1.10	1.12	1.13	1.14	1.15	1.16	1.17	1.18	1.19	
$\Delta T/t$	1.50	2.12	1.83		2.16		1.32		1.77	1.10	1.86				1.60	1.77			
Q/A plug	1.75	2.48	2.14		2.52		1.54		2.07	1.28	2.18				1.87	2.07			
Q/A corr	2.10	2.98	2.57		3.02		1.85		2.48	1.54	2.62				2.24	2.48			
$\frac{(\overline{Q/A})}{(Q/A)\Delta A}$																			
TC	1.3	1.4	1.5	1.6	1.7	1.8	1.7	1.8	1.9	1.10	1.12	1.13	1.14	1.15	1.16	1.17	1.18	1.19	
$\Delta T/t$	1.50	2.12	1.83		2.16		1.32		1.77	1.10	1.86				1.60	1.77			
Q/A plug	1.75	2.48	2.14		2.52		1.54		2.07	1.28	2.18				1.87	2.07			
Q/A corr	2.10	2.98	2.57		3.02		1.85		2.48	1.54	2.62				2.24	2.48			
$\frac{(\overline{Q/A})}{(Q/A)\Delta A}$																			
TC	1.3	1.4	1.5	1.6	1.7	1.8	1.7	1.8	1.9	1.10	1.12	1.13	1.14	1.15	1.16	1.17	1.18	1.19	
$\Delta T/t$	1.50	2.12	1.83		2.16		1.32		1.77	1.10	1.86				1.60	1.77			
Q/A plug	1.75	2.48	2.14		2.52		1.54		2.07	1.28	2.18				1.87	2.07			
Q/A corr	2.10	2.98	2.57		3.02		1.85		2.48	1.54	2.62				2.24	2.48			
$\frac{(\overline{Q/A})}{(Q/A)\Delta A}$																			
TC	1.3	1.4	1.5	1.6	1.7	1.8	1.7	1.8	1.9	1.10	1.12	1.13	1.14	1.15	1.16	1.17	1.18	1.19	
$\Delta T/t$	1.50	2.12	1.83		2.16		1.32		1.77	1.10	1.86				1.60	1.77			
Q/A plug	1.75	2.48	2.14		2.52		1.54		2.07	1.28	2.18				1.87	2.07			
Q/A corr	2.10	2.98	2.57		3.02		1.85		2.48	1.54	2.62				2.24	2.48			
$\frac{(\overline{Q/A})}{(Q/A)\Delta A}$																			
TC	1.3	1.4	1.5	1.6	1.7	1.8	1.7	1.8	1.9	1.10	1.12	1.13	1.14	1.15	1.16	1.17	1.18	1.19	
$\Delta T/t$	1.50	2.12	1.83		2.16		1.32		1.77	1.10	1.86				1.60	1.77			
Q/A plug	1.75	2.48	2.14		2.52		1.54		2.07	1.28	2.18				1.87	2.07			
Q/A corr	2.10	2.98	2.57		3.02		1.85		2.48	1.54	2.62				2.24	2.48			
$\frac{(\overline{Q/A})}{(Q/A)\Delta A}$																			
TC	1.3	1.4	1.5	1.6	1.7	1.8	1.7	1.8	1.9	1.10	1.12	1.13	1.14	1.15	1.16	1.17	1.18	1.19	
$\Delta T/t$	1.50	2.12	1.83		2.16		1.32		1.77	1.10	1.86				1.60	1.77			
Q/A plug	1.75	2.48	2.14		2.52		1.54		2.07	1.28	2.18				1.87	2.07			
Q/A corr	2.10	2.98	2.57		3.02		1.85		2.48	1.54	2.62				2.24	2.48			
$\frac{(\overline{Q/A})}{(Q/A)\Delta A}$																			
TC	1.3	1.4	1.5	1.6	1.7	1.8	1.7	1.8	1.9	1.10	1.12	1.13	1.14	1.15	1.16	1.17	1.18	1.19	
$\Delta T/t$	1.50	2.12	1.83		2.16		1.32		1.77	1.10	1.86				1.60	1.77			
Q/A plug	1.75	2.48	2.14		2.52		1.54		2.07	1.28	2.18								

Table 6-6. Heat Flux Summary - Run 119

Chamber Sections		I				II				III								
TCR	1	2	3	4	5	6	7	8	9	10	11	12	13	14	15	16	17	18
$\Delta T/t$	1.67	1.73				1.63			1.87	1.55	2.02		1.64	2.00	1.80		2.04	
Q/A plug	1.96	2.03				1.91			2.19	1.82	2.37		1.92	2.35	2.11		2.39	
Q/A corr	2.35	2.43				2.29			2.63	2.18	2.84		2.31	2.82	2.53		2.87	
(Q/A) (Q/A)ΔA		2.39 167.7				2.49 81.4				2.63 185.5								
Chamber Sections		IV				V				VI								
TC	31	32	33	34	35	36	25	26	27	28	29	30	19	20	21	22	23	24
$\Delta T/t$	182		120	250	196	244		150	94	185	210	187			193	114	216	
Q/A plug	2.14		1.41	2.93	2.30	2.87		1.76	1.10	2.17	2.46	2.19			2.26	1.34	2.53	
Q/A corr	2.56		1.69	3.53	2.76	3.43		2.11	1.32	2.61	2.96	2.63			2.72	1.60	3.04	
(Q/A) (Q/A)ΔA		2.79 233.0				2.33 136.4				2.56 79.5								
Chamber Sections		VII				VIII				IX								
TC	13	14	15	16	17	18	7	8	9	10	11	12	1	2	3	4	5	6
$\Delta T/t$	94	150	142	170	125γ	162	205	208	158	127		196	155	133	56	131	37	93
Q/A plug	1.10	1.76	1.67	2.00	1.47	1.90	2.41	2.44	1.85	1.49		2.30	1.82	1.56	.66	1.54	.43	1.09
Q/A corr	1.32	2.11	2.00	2.39	1.76	2.28	2.89	2.93	2.22	1.79		2.76	2.18	.187	.79	1.84	.52	1.31
(Q/A) (Q/A)ΔA		1.98 45.7				1.94 46.9				1.42 75.8								

Table 6-7. Heat Flux Data Summary—Run 120

Chamber Sections		I				II				III									
TCR	1	2	3	4	5	6	7	8	9	10	11	12	13	14	15	16	17	18	
$\Delta T/t$	1.58	1.80				160			170	164	210		162	225	204		2.37		
Q/A plug	1.85	2.11				1.87			1.99	1.92	2.46		1.90	2.64	2.39		2.78		
Q/A corr	2.22	2.53				2.24			2.39	2.30	2.95		2.28	3.17	2.87		3.33		
(Q/T <sub>A</sub> )		2.38				2.47				2.47				2.91					
$(\overline{Q}/\overline{T}_A)\Delta A$		167.0				80.8				80.8				204.5					
Chamber Sections		IV				V				VI				VII					
TC	31	32	33	34	35	36	25	26	27	28	29	30	30	19	20	21	22	23	24
$\Delta T/t$	193		134	217	211	238		176	100	212	230		204			120	105	220	
Q/A plug	2.26		1.57	2.54	2.47	2.79		2.06	1.17	2.49	2.70		2.39			1.41	1.23	2.58	
Q/A corr	2.71		1.88	3.06	2.96	3.35		2.47	1.40	2.98	3.23		2.87			1.69	1.48	3.10	
(Q/T <sub>A</sub> )		2.80				2.59				2.59				2.09					
$(\overline{Q}/\overline{T}_A)\Delta A$		233.8				151.6				151.6				67.9					
Chamber Sections		VII				VIII				IX				X					
TC	13	14	15	16	17	18	7	8	9	10	11	12	1	2	3	4	5	6	
$\Delta T/t$	91	118	184	162	182	175	173	183		122	140		193	150	139	91	121	72	113
Q/A plug	1.07	1.38	2.16	1.90	2.13	2.06	2.03	2.15		1.43	1.64		2.26	1.76	1.63	1.07	1.42	.84	1.33
Q/A corr	1.28	1.66	2.59	2.28	2.56	2.47	2.44	2.57		1.72	1.97		2.72	2.11	1.96	1.28	1.70	1.01	1.59
(Q/T <sub>A</sub> )		2.14				2.28				2.28				1.61					
$(\overline{Q}/\overline{T}_A)\Delta A$		49.4				55.2				55.2				85.9					

Table 6-8. Heat Flux Data Summary—Run 121

Chamber Sections	I				II				III									
	1	2	3	4	5	6	7	8	9	10	11	12	13	14	15	16	17	18
TCR	102	150					136	141	153	135	164		156	171	185		206	
$\Delta T/t$							1.60	1.65	1.80	1.58	1.92		1.83	2.01	2.17		2.42	
Q/A plug	1.20	1.76					1.92	1.99	2.15	1.90	31		2.20	2.41	2.61		2.90	
Q/A corr	1.44	2.11																
$(\overline{Q/T_A})$		1.77		124.2		2.05		2.53		2.05		2.53		2.05		2.53		
Chamber Sections	IV				V				VI				VII				VIII	
	31	32	33	34	35	36	25	26	27	28	29	30	19	20	21	22	23	24
TC																		
$\Delta T/t$	174	128	167	170	186				122	154	174	198		178	170	138		186
Q/A plug	2.04	1.50	1.96	2.00	2.18				1.95	1.43	1.81	2.04		2.32	2.09	1.99	1.62	2.19
Q/A corr	2.46	1.80	2.35	2.39	2.62				2.34	1.72	2.17	2.46	2.80		2.51	2.40	1.94	2.64
$(\overline{Q/T_A})$		2.33		194.6		2.30		2.37		2.30		2.37		2.30		2.37		
Chamber Sections	VII				VIII				IX				X				XI	
	13	14	15	16	17	18	7	8	9	10	11	12	1	2	3	4	5	6
TC																		
$\Delta T/t$	181	135	186	164	180	181	174	169	125	123	154	102	142	137	85	132	106	129
Q/A plug	2.12	1.58	2.18	1.92	2.11	2.12	2.04	1.98	1.47	1.44	1.81	1.20	1.67	1.61	1.00	1.55	1.24	1.51
Q/A corr	2.55	1.90	2.62	2.31	2.54	2.55	2.45	2.38	1.76	1.73	2.17	1.44	2.00	1.93	1.20	1.86	1.49	1.82
$(\overline{Q/T_A})$		2.41		55.6		1.99		1.72		1.99		1.72		1.99		1.72		
91.8																		

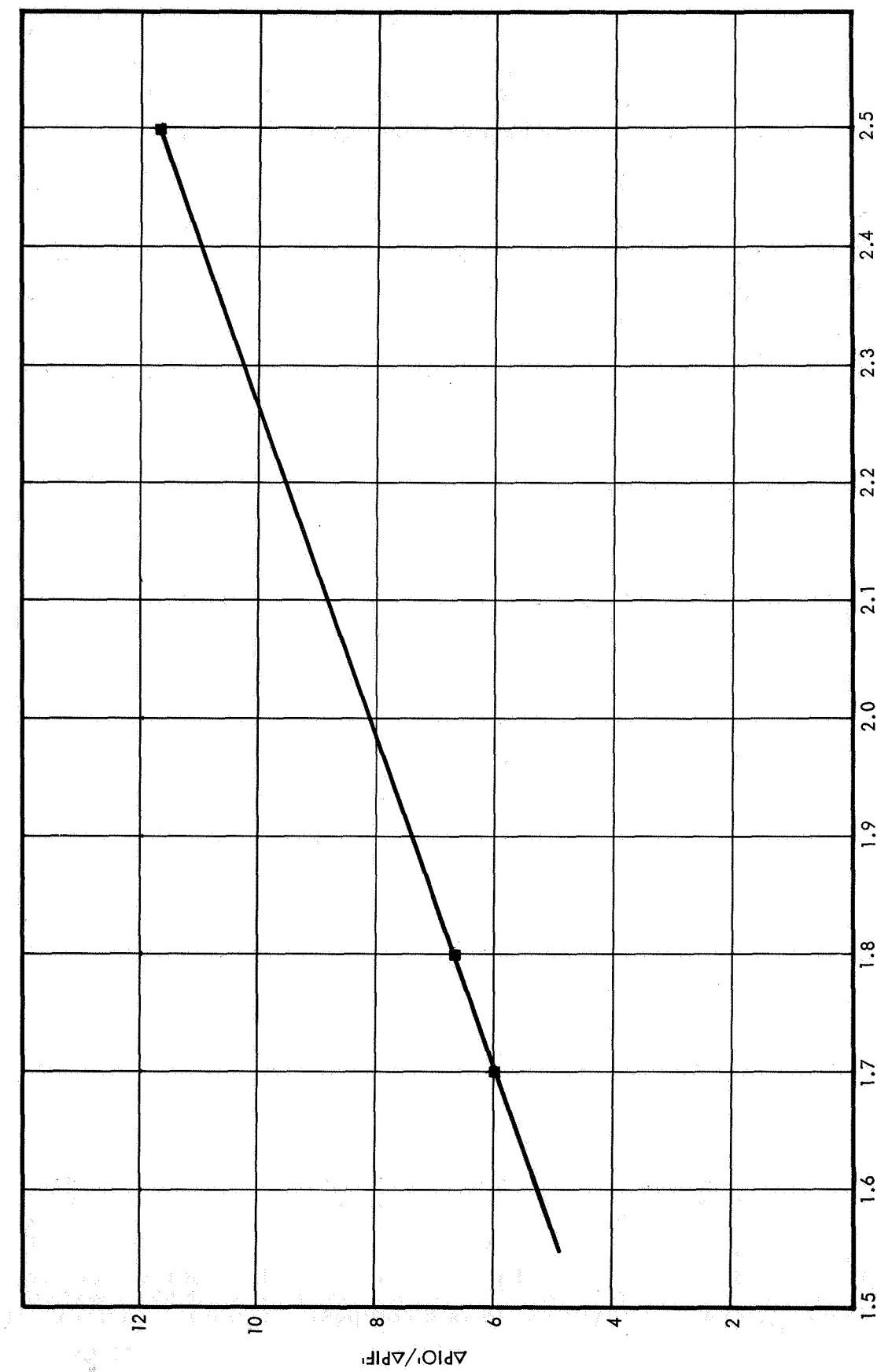


Figure 6-7. Chamber Heat Flux as a Function of Propellant Momentum Ratio

Figure 6-8 presents the average axial heat flux profiles associated with runs 101, 102, 104, and 105. These profiles show that heat flux to the chamber was a strong function of the propellant momentum ratio. Minor injector configuration changes were made in runs 102, 104, and 105 and the heat flux profiles were generally the same. In these runs the average heat flux to the chamber was approximately 2.5 to 3.0 Btu/in<sup>2</sup>-sec. However, on Run 101 the momentum ratio of the propellants was doubled and a large change in the heat flux profile occurred. The average heat flux jumped to approximately 4.0 Btu/in<sup>2</sup>-sec. On this run in chamber section II, the heat flux dropped to approximately 2.5 Btu/in<sup>2</sup>-sec; however, it tended to remain high throughout the chamber. The drop at the beginning of the chamber was associated with a narrow mass distribution of the propellant in the injector fan. (This distribution was measured in the cold flow test described in Section 7.) Figure 6-9 presents the average axial heat flux profiles associated with runs 118, 119, 120, and 121. These runs were made with element SS-12 and show a significant decrease in the heat flux into the chamber walls being less than 3.0 Btu's/in<sup>2</sup>/sec.

Figure 6-10 is a composite of the six radial thermocouple locations throughout the length of the chamber for runs 101 through 105. This composite provides a comprehensive study of the heat flux variations associated with the various axial locations. However, in order to thoroughly evaluate the heat flux profiles throughout the chamber in each run, it is also necessary to examine the radial heat flux distributions as well. The radial heat flux distributions are presented in Figures 6-11 through 6-13 for runs 101, 104, and 105, respectively. Figure 6-11 shows that run 101 had a relatively uniform injection pattern. However, Figures 6-12 and 6-13 show that runs 104 and 105 had a slight nonuniformity to the injection pattern. This non-uniformity was exhibited in the nonuniform heat flux profile associated with Sections 5 and 6. The nonuniformity was later detected in cold flow tests conducted with the injector assembly. Two occlusions were located in the fuel injection orifice approximately 150 degrees apart. These occlusions were small and did not affect the fuel mass flow measurably; however, it was suspected that the occlusions caused a heavier deposition of carbon along those sectors of the chamber, causing the heat flux profile to change noticeably. Figure 6-14 is a composite of the six radial thermo-couple location throughout the length of the chamber for runs 118 through

121. This figure shows the relative continuity in the thermocouple readings. Figures 6-16 through 6-18 are the radial heat flux distributions for runs 118 through 121. These figures show that the heat profiles were relatively uniform.

Figures 6-19 through 6-22 show a comparison of the experimental ( $Q/A$ ) values with the predicted Bartz( $Q/A$ ) values for runs 118 through 121. Generally these comparisons show that experimental results were slightly higher in the base of the chamber and lower in the throat. Examinations of the chamber walls after test firings indicate heavier carbon depositions in the throat. The overall heat transfer results showed that the resulting heat flux levels were considerably reduced from the theoretical no carbon values.

The heat fluxes are reasonably uniform, and the distributions are relatively uniform. The indicated local gas recovery temperatures were on the order of  $3200-4000^{\circ}\text{F}$ , indicating that the injector did provide well controlled wall environments. Of particular interest is the fact that the wall heat flux and local recovery temperature could be readily controlled by small shifts in fuel/oxidizer momentum ratios with negligible effect on overall performance.

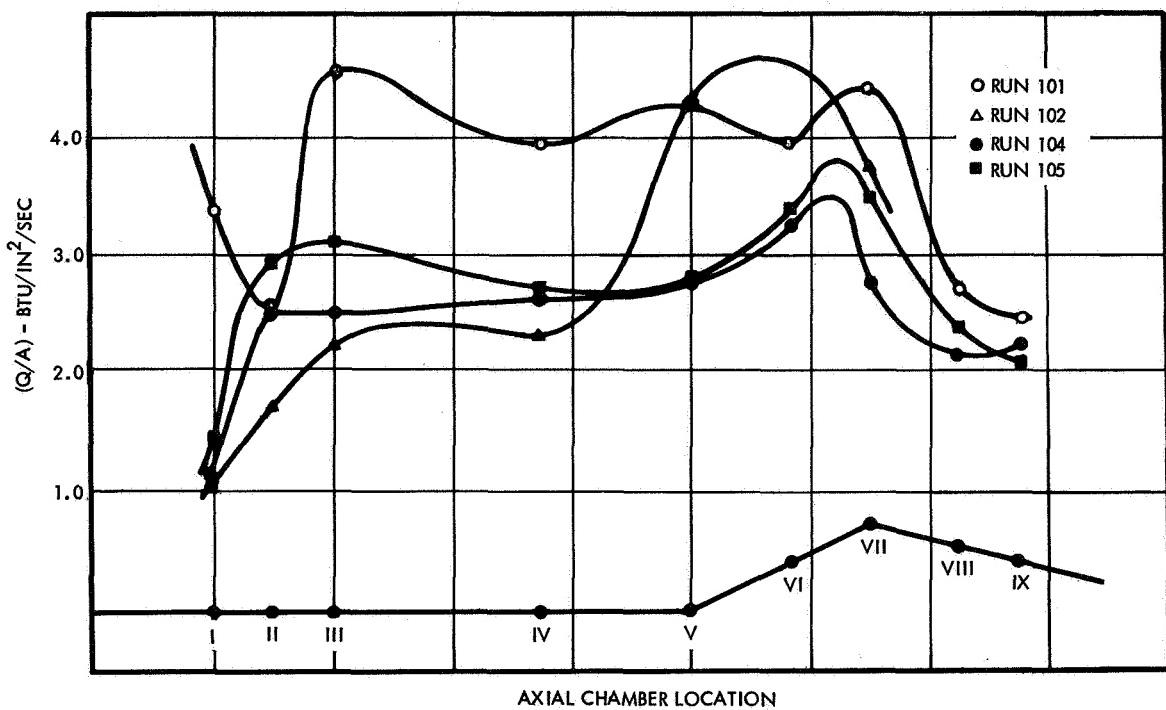


Figure 6-8. Average Axial Heat Flux Profiles for Runs 101 through 105

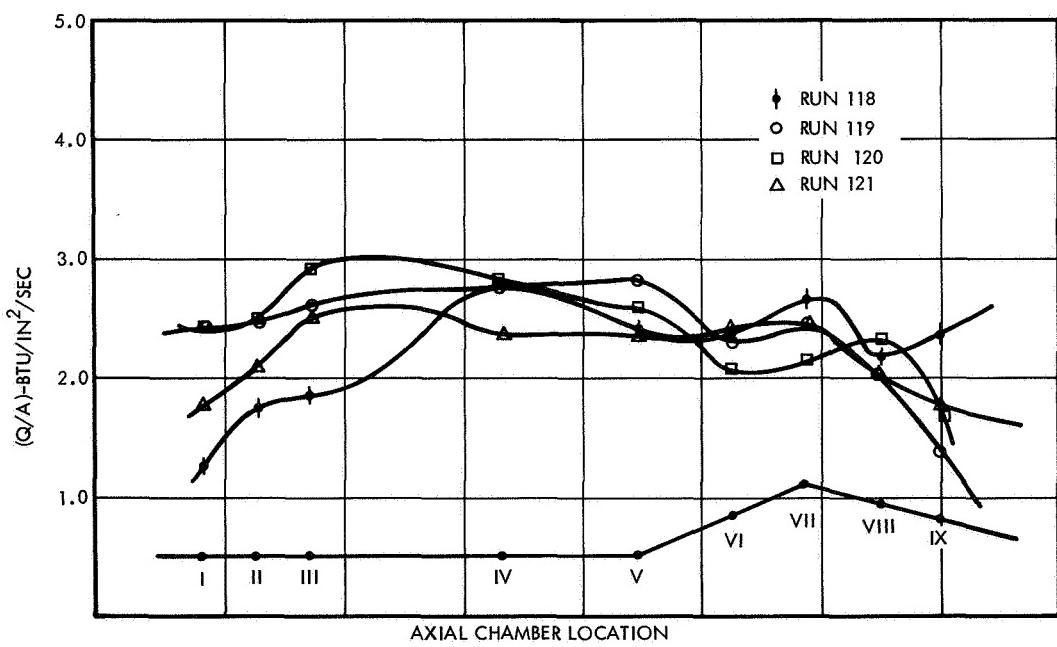


Figure 6-9. Axial Heat Flux Profiles for Runs 118 through 121

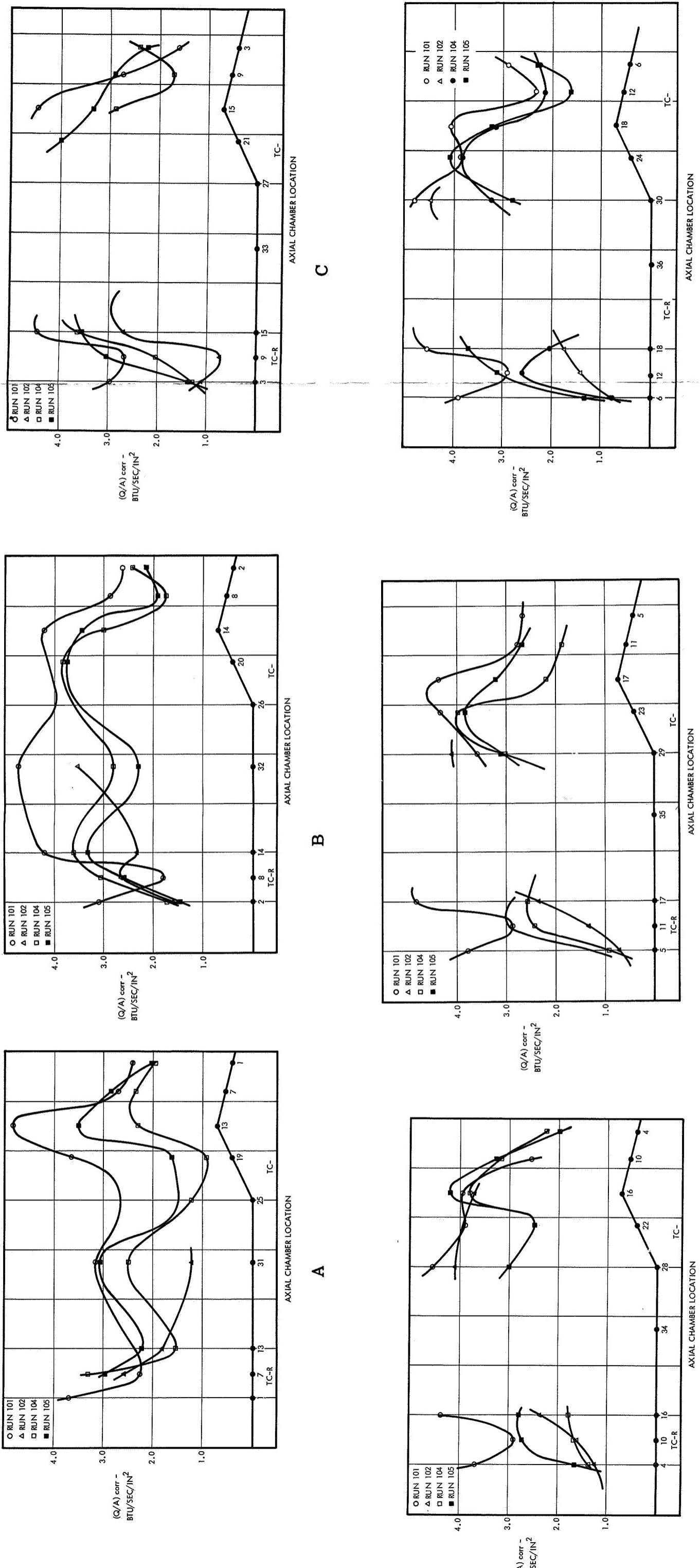
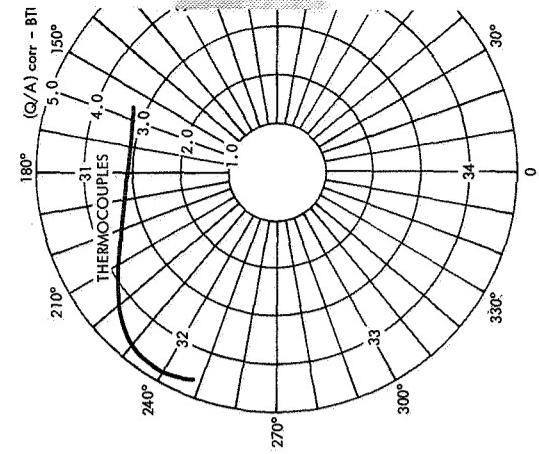


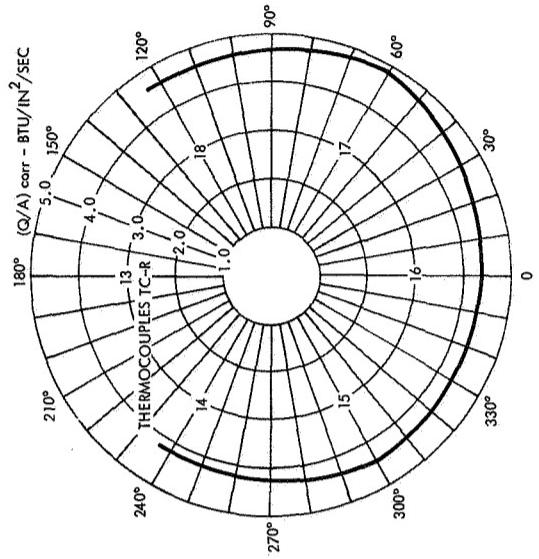
Figure 6-10. Heat Flux Composite of the Six Radial Thermocouple Locations for Runs 101, 102, 104 and 105



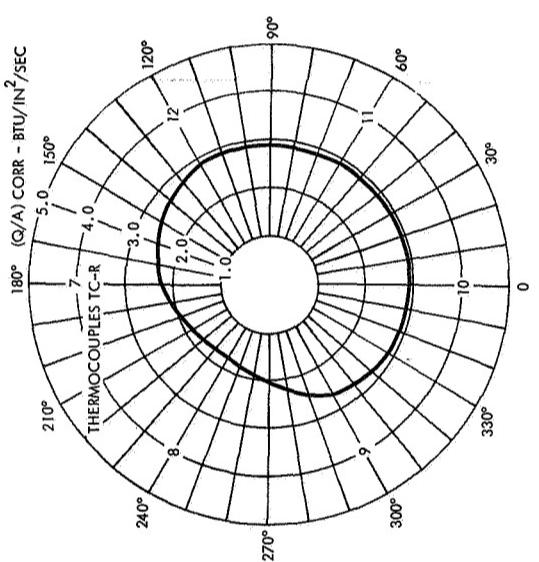
# Section A



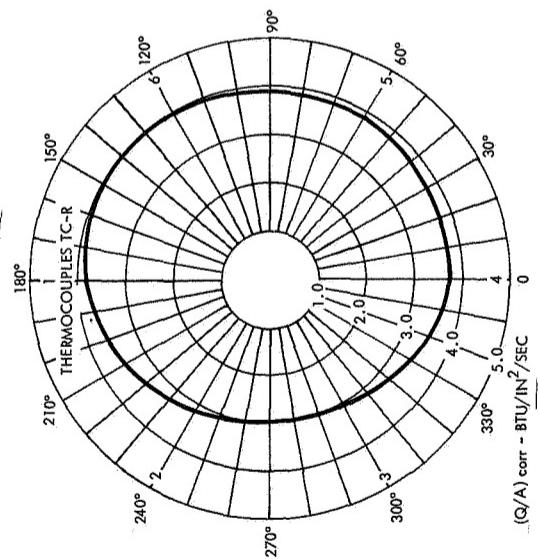
SECTION IV RUN 101



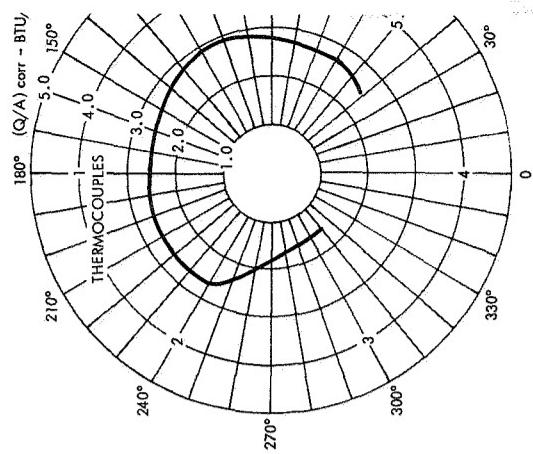
SECTION III RUN 101



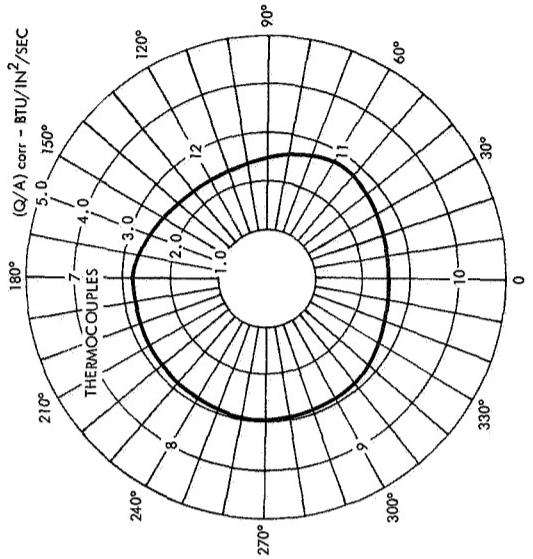
SECTION II RUN 101



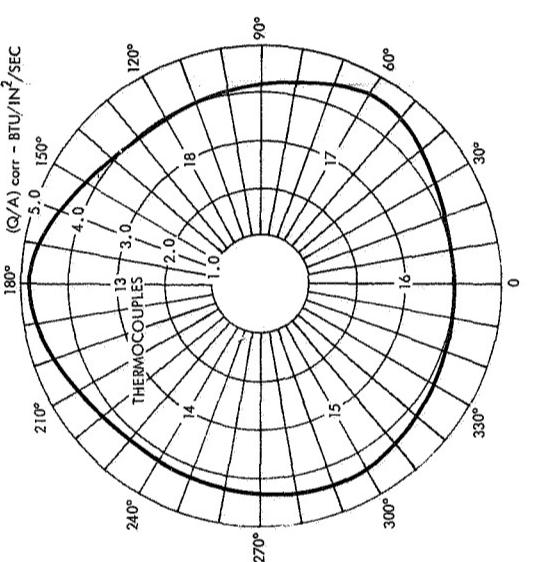
SECTION I RUN 101



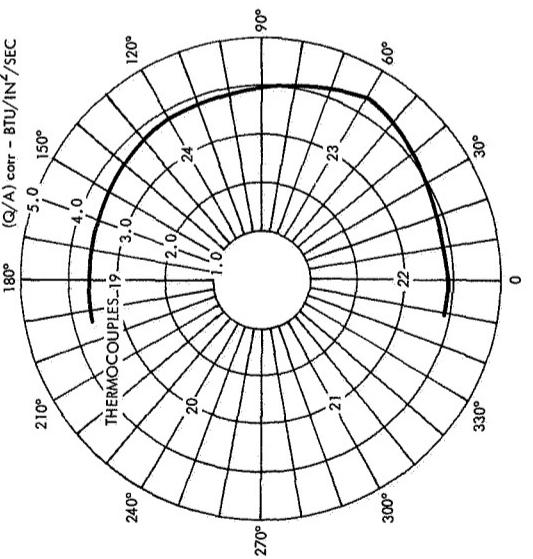
SECTION IV RUN 101



SECTION III RUN 101



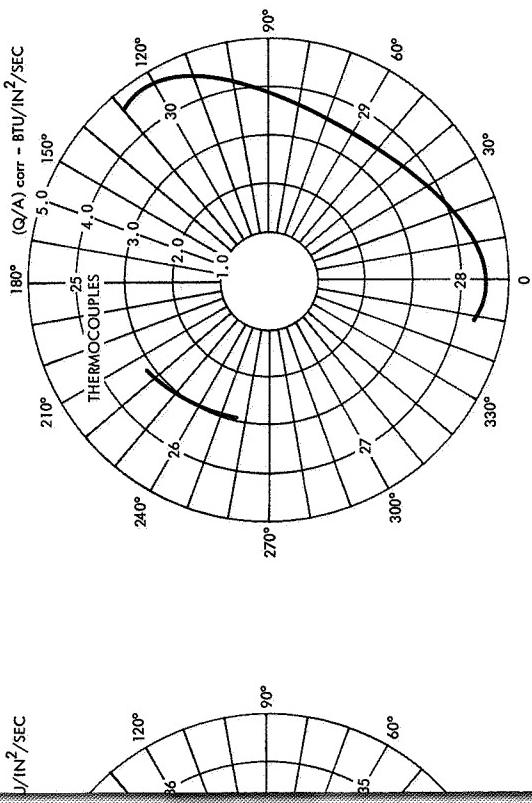
SECTION II RUN 101



SECTION VI RUN 101

SECTION IX RUN 101

## Section B



SECTION V RUN 101

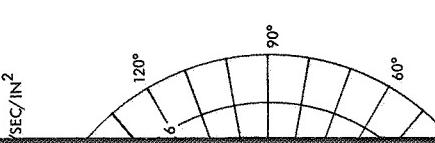
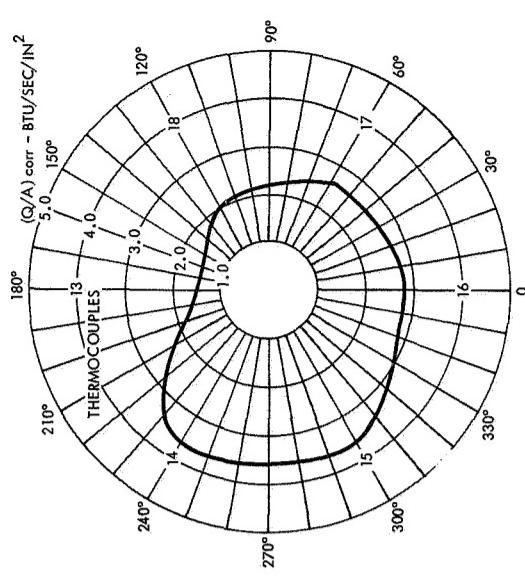


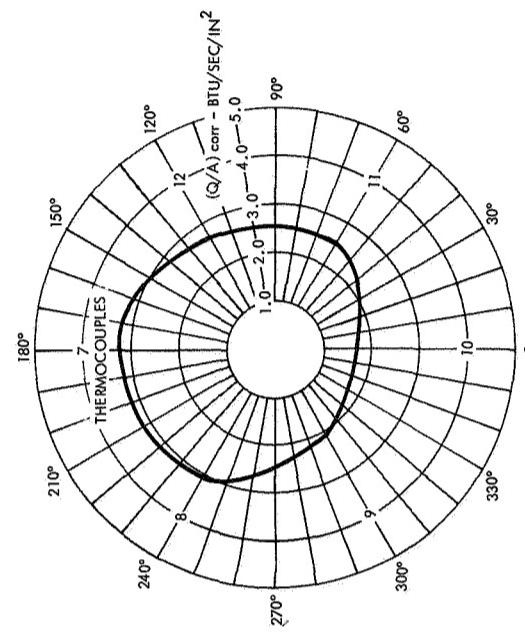
Figure 6-11. Radial Heat Flux Distribution for Run 101



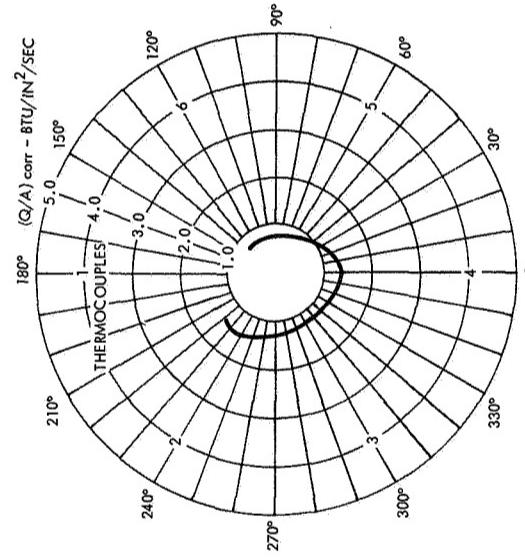
PAPER I



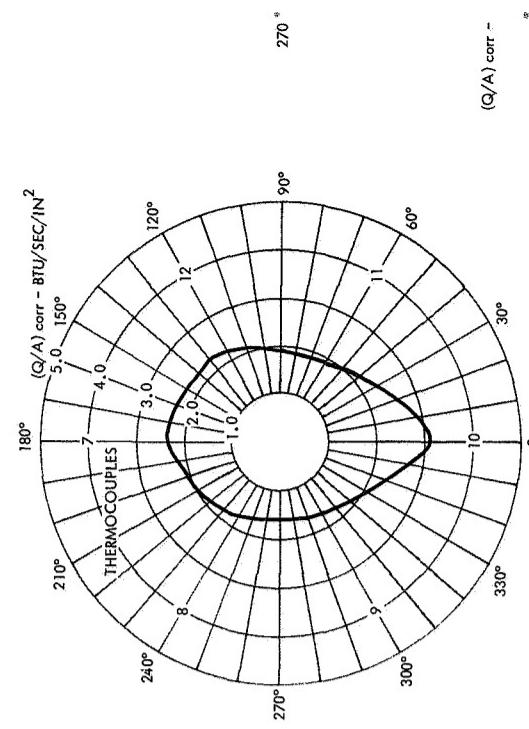
SECTION III RUN 104



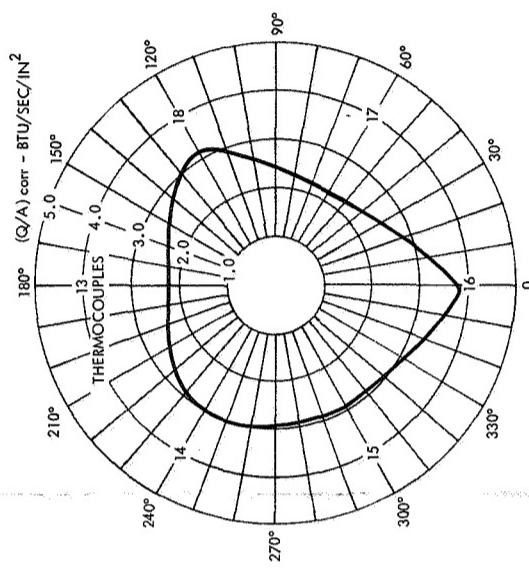
SECTION II RUN 104



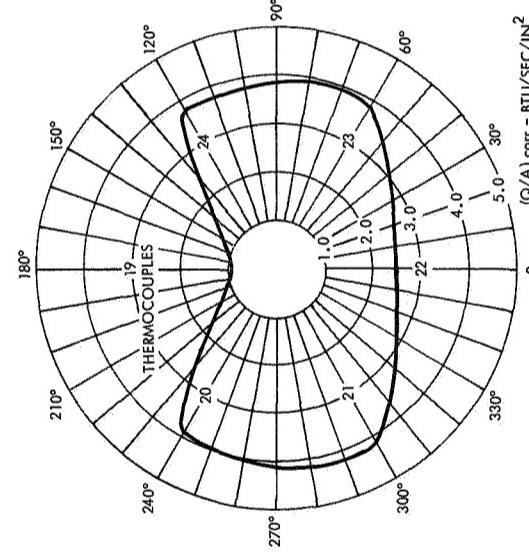
SECTION 1 RUN 104



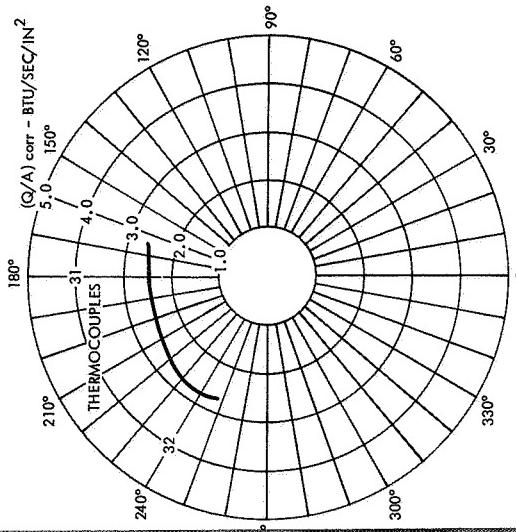
SECTION VTTT BIM 104



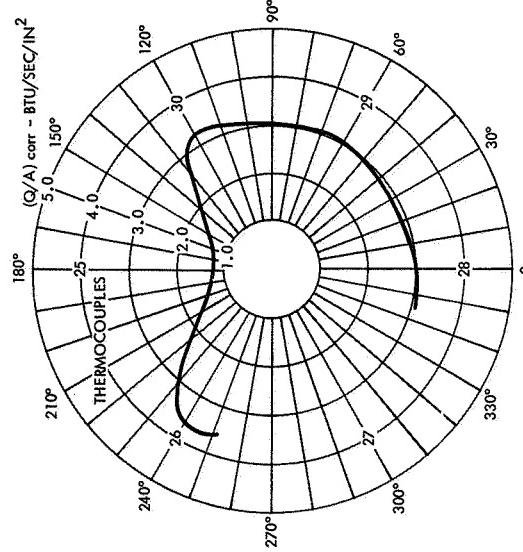
SECTION VTT BIM 104



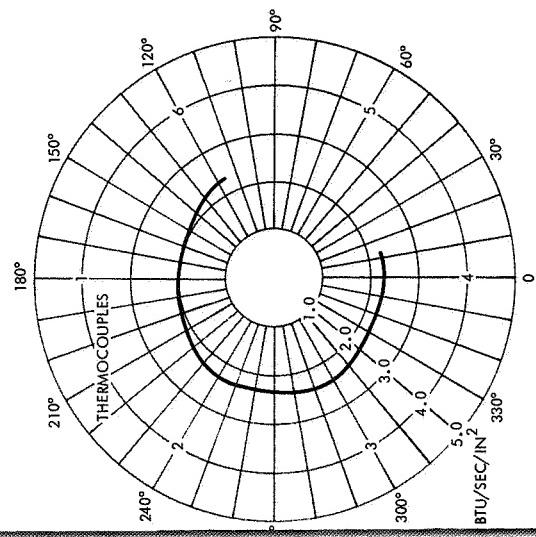
SECTION VI RTN 104



SECTION IV RUN 104



SECTION V RUN 104

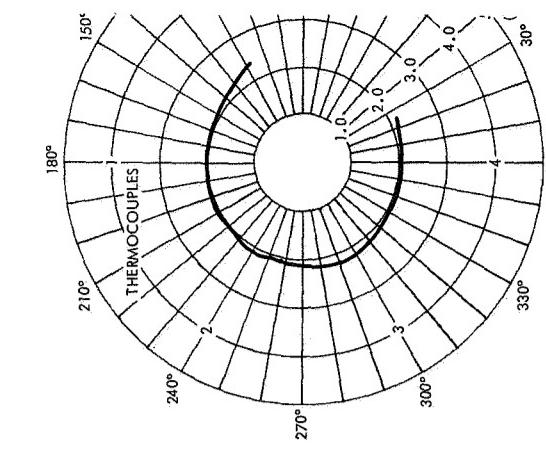
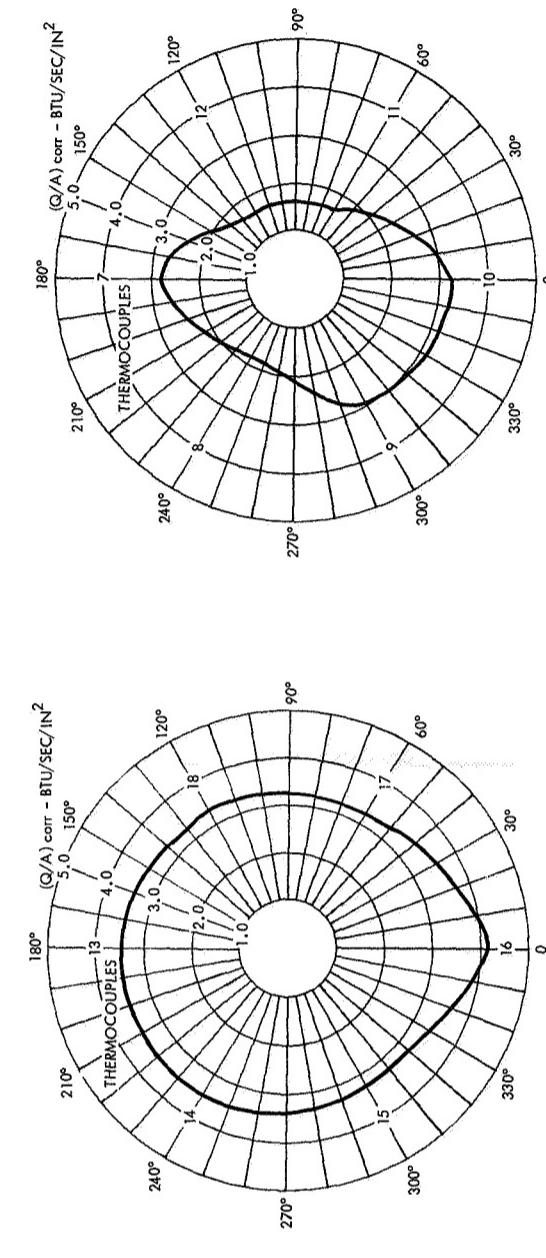
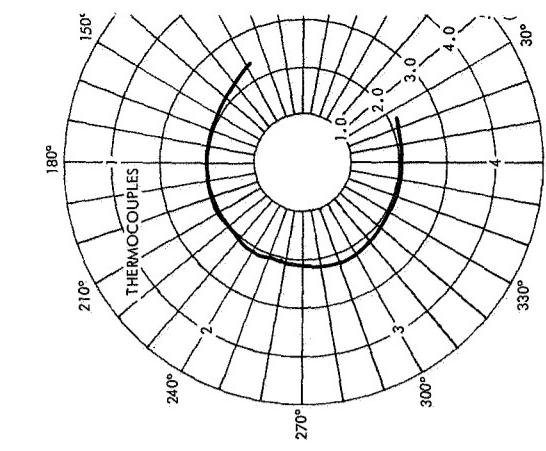
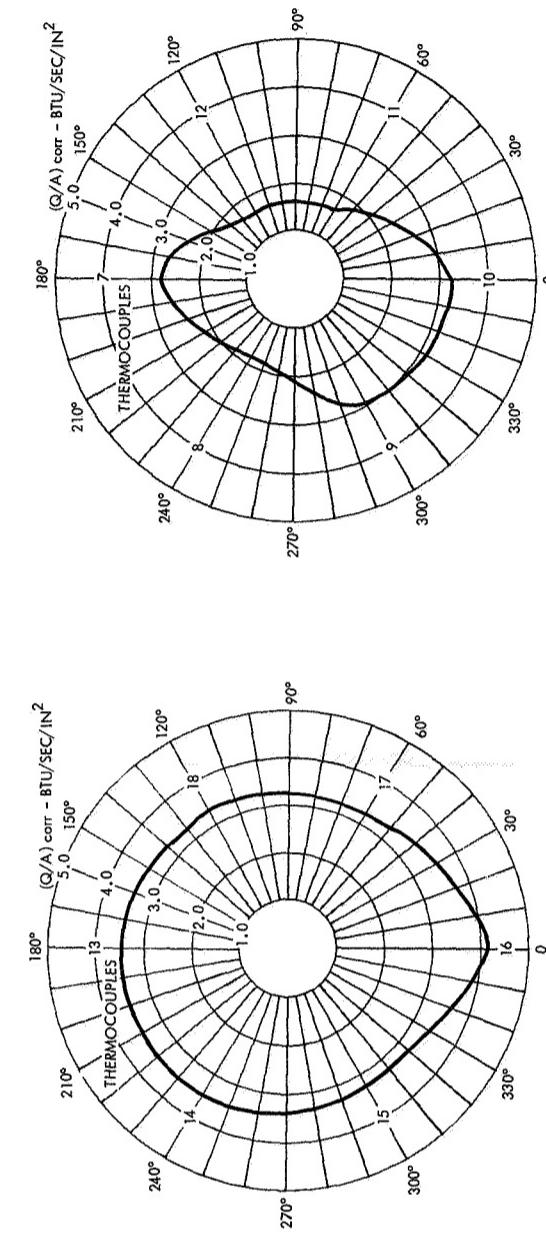
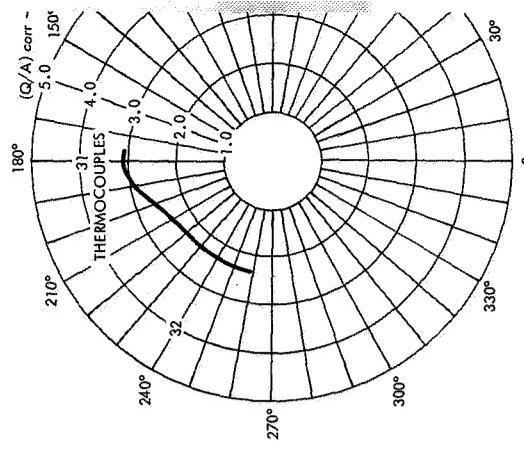
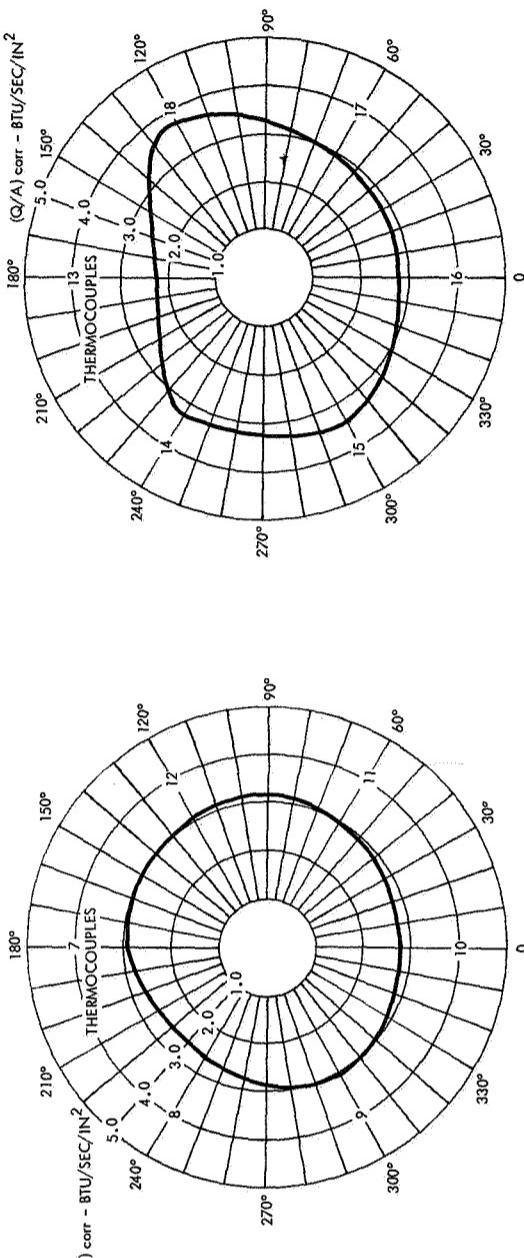
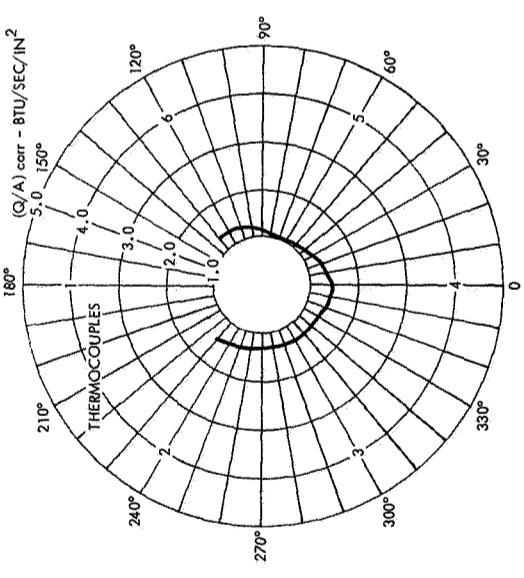


SECTION IX RUN 104

Figure 6-12. Radial Heat Flux Distribution for Run 104



# /



SECTION VIII RUN 105

SECTION VII RUN 105

SECTION VI RUN 105

SECTION III RUN 105

SECTION IX RUN 105

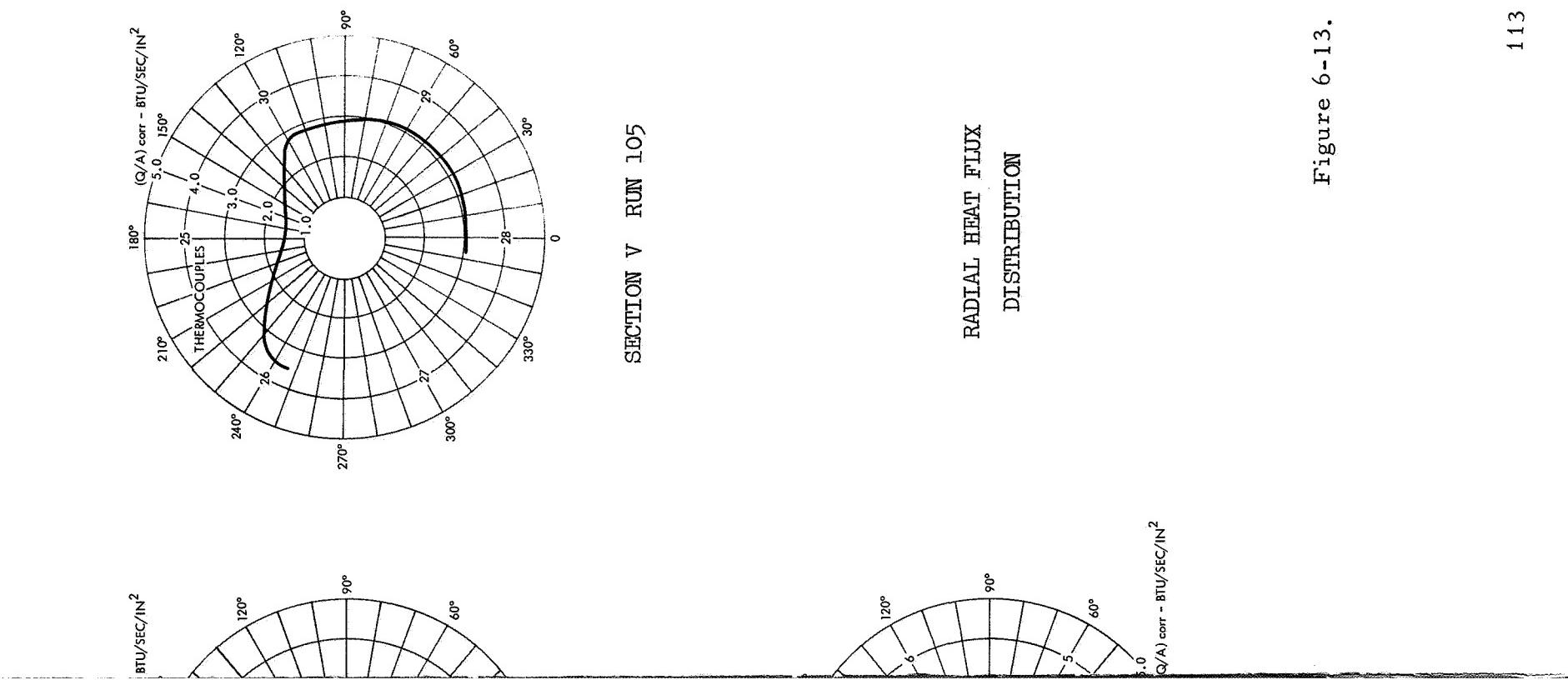
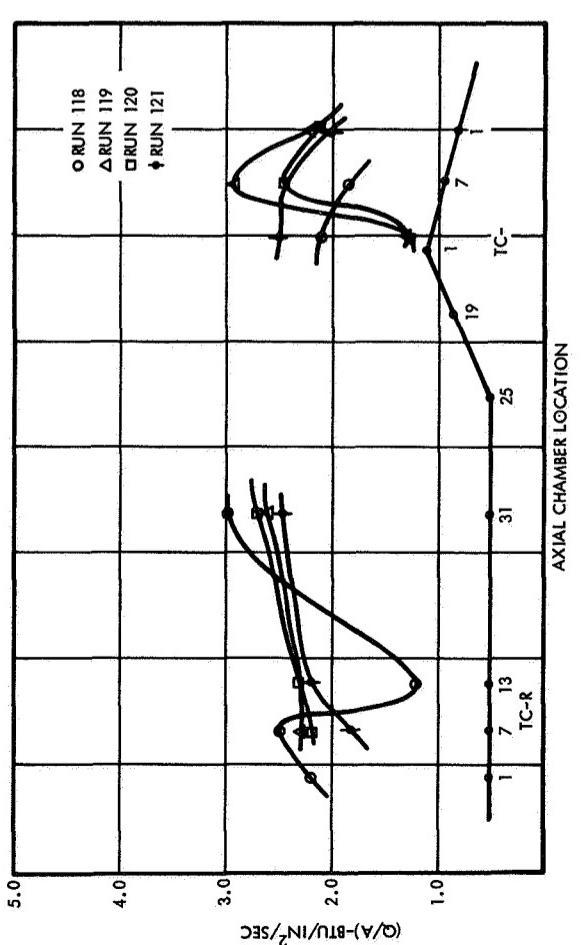
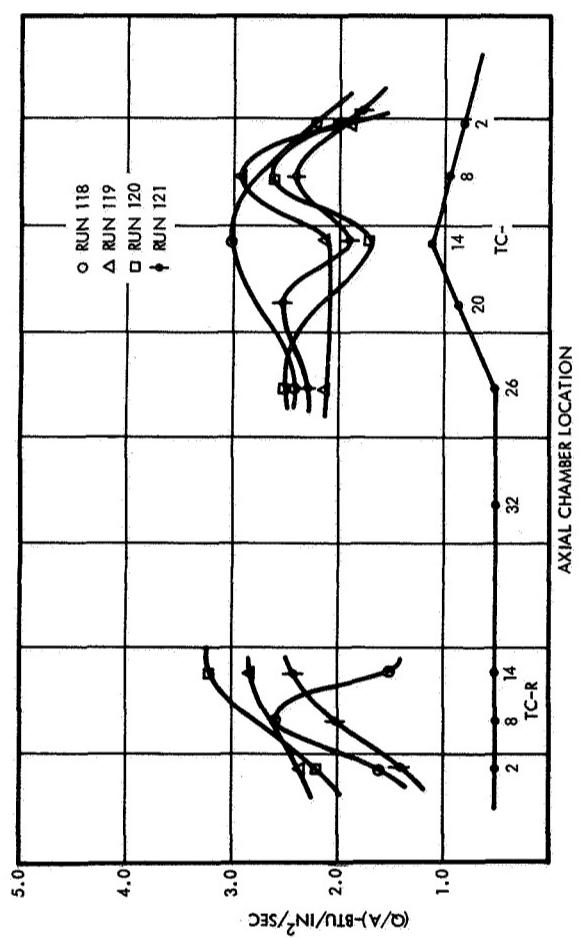


Figure 6-13. Radial Heat Flux Distribution for Run 105

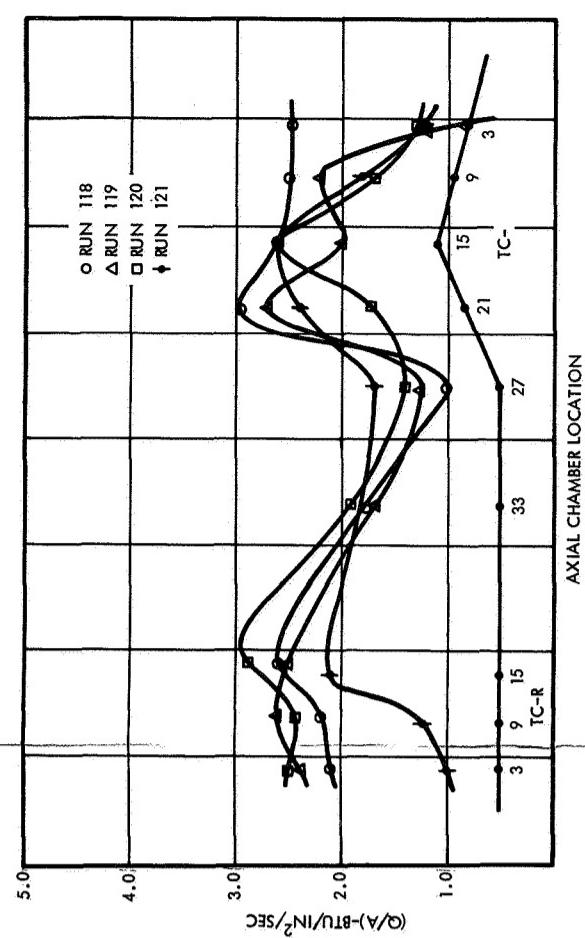




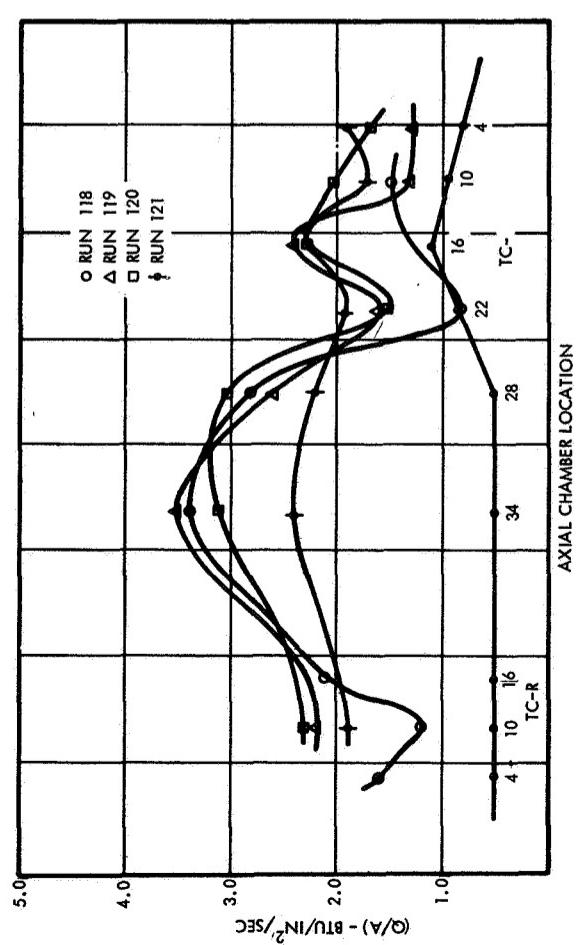
A



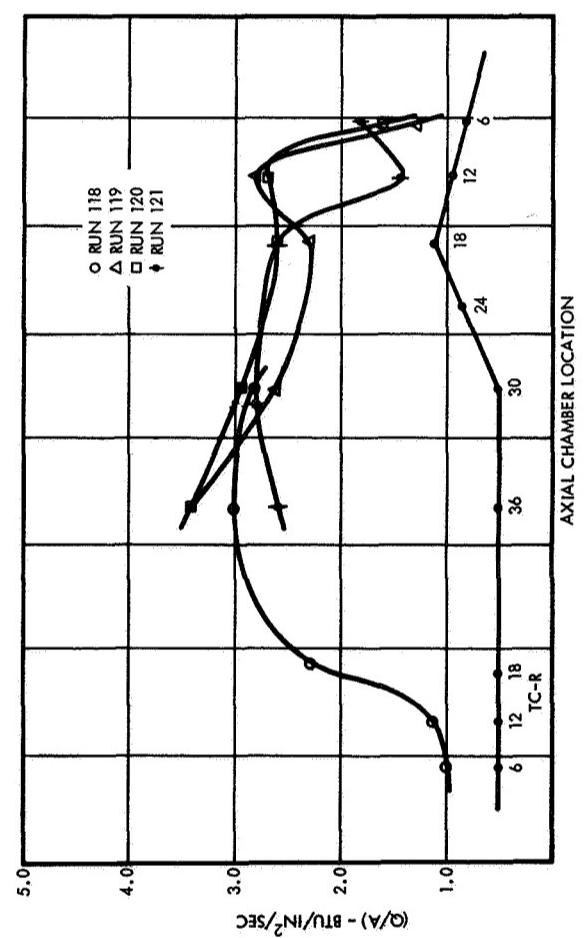
B



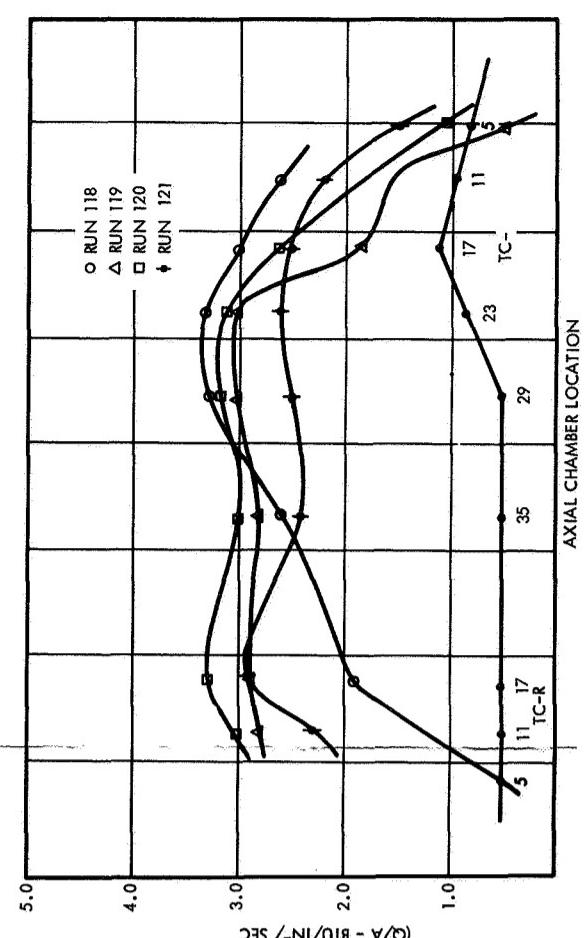
C



D



E

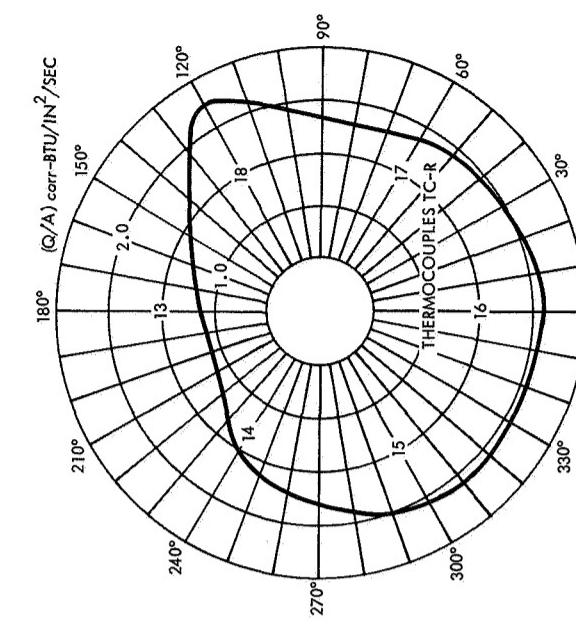


F

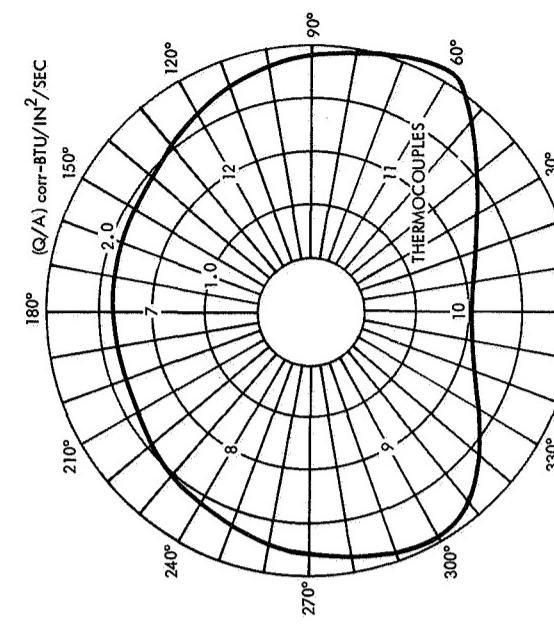
Figure 6-14. Heat Flux Composite of Six Radial Thermocouple Locations for Runs 118 through 121



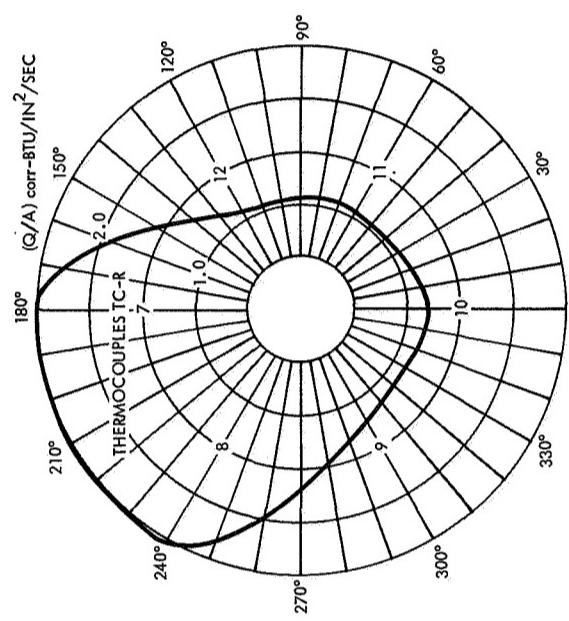
Daret A



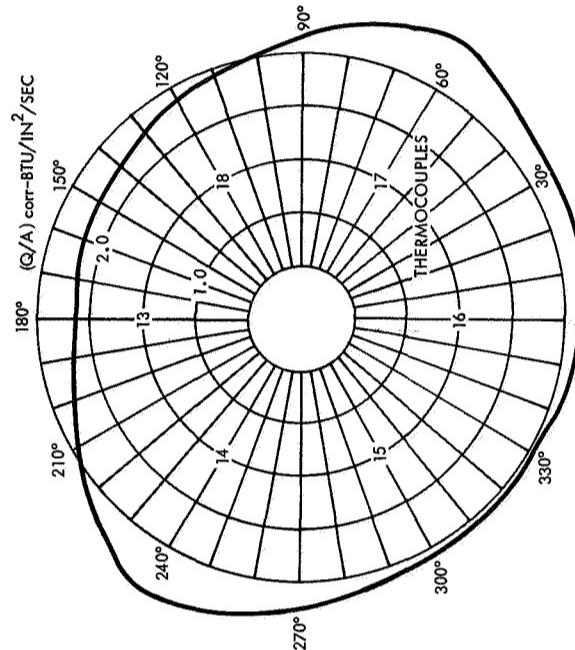
SECTION III RUN 118



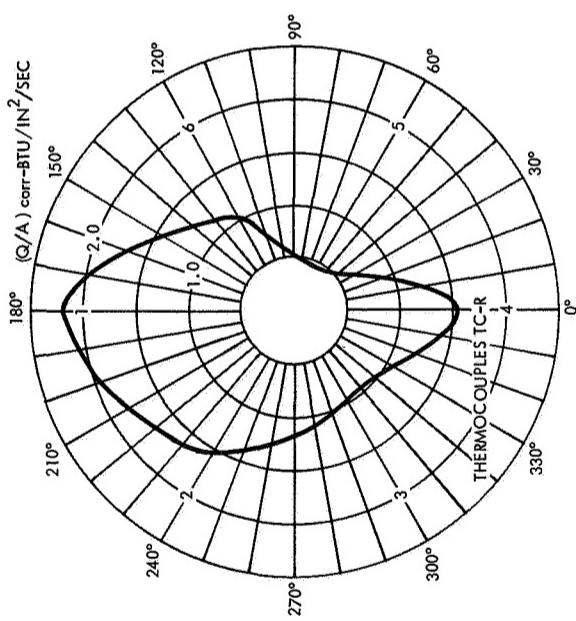
SECTION VIII RUN 118



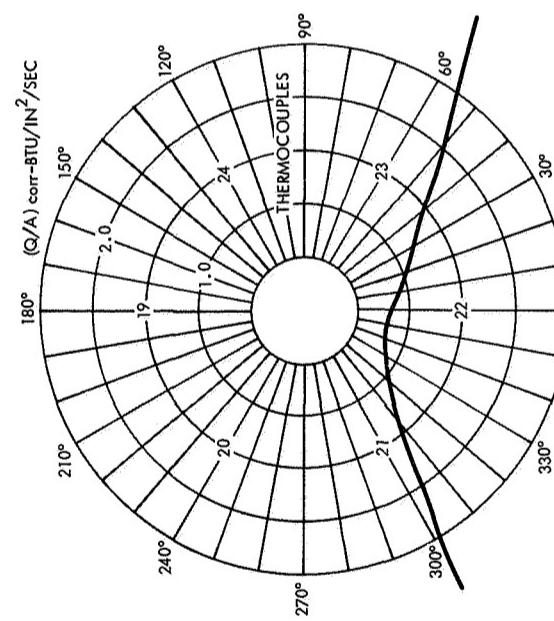
SECTION II RUN 118



SECTION VII RUN 118



SECTION I RUN 118



SECTION VI RUN 118

Paket B

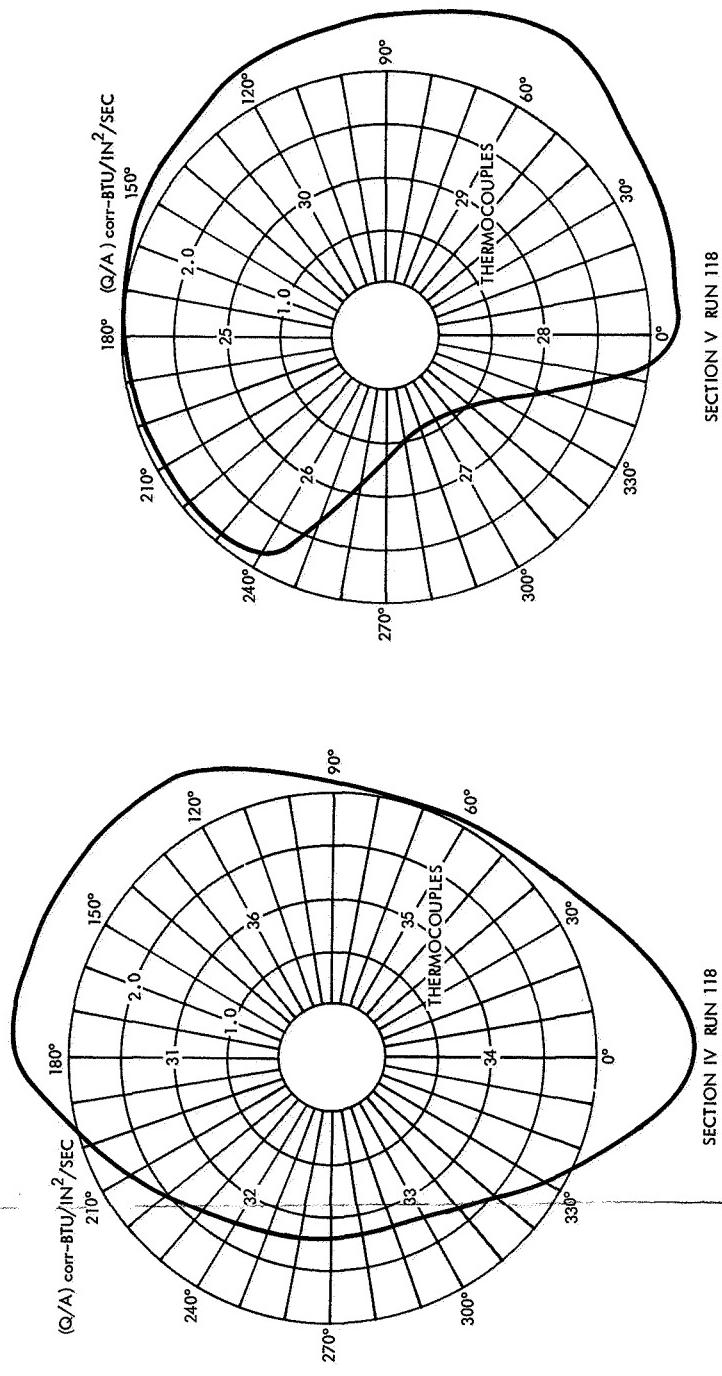
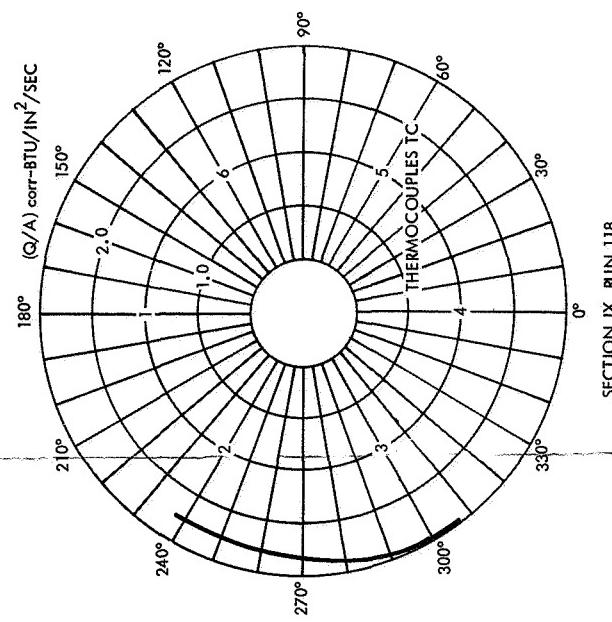


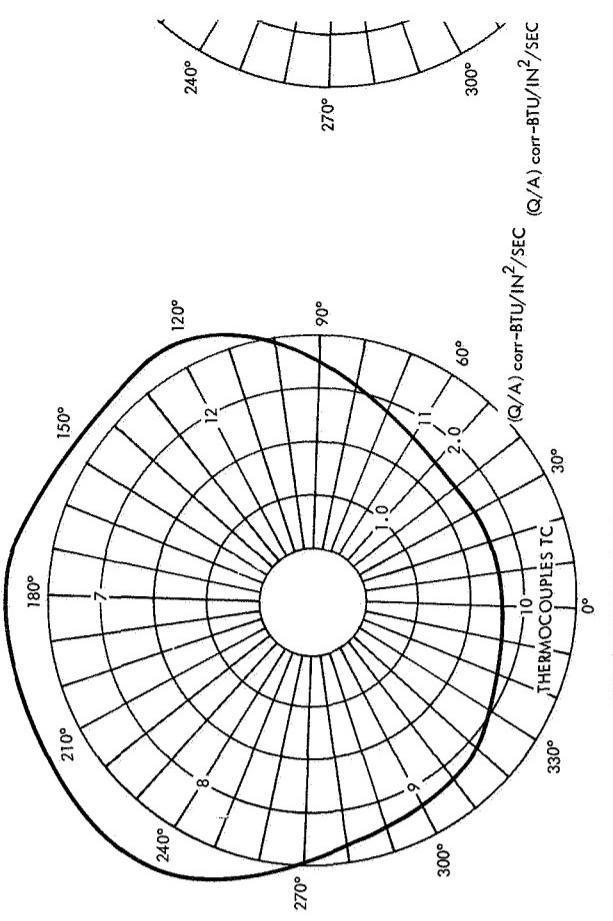
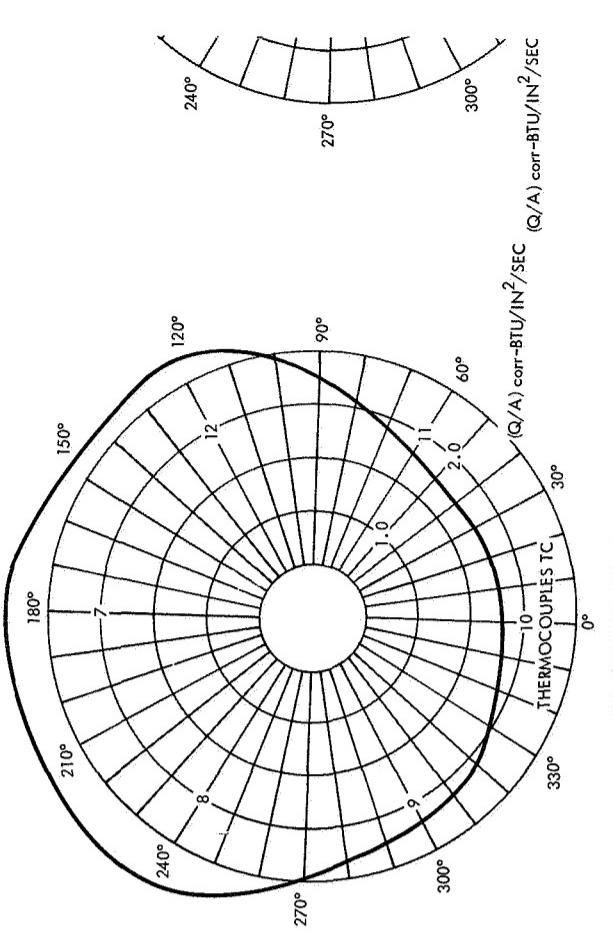
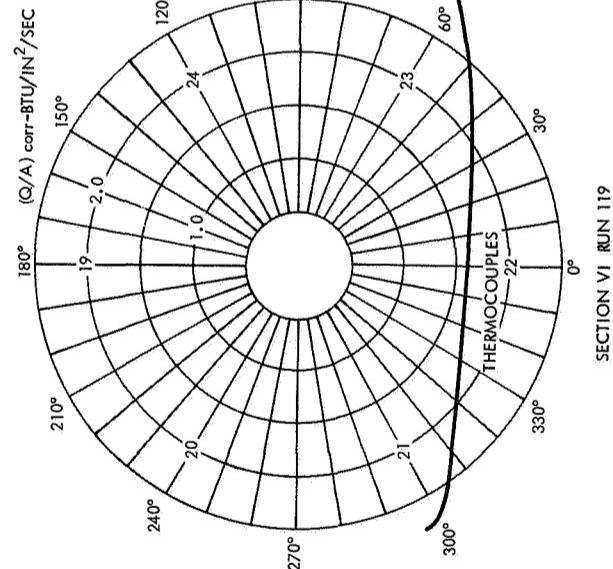
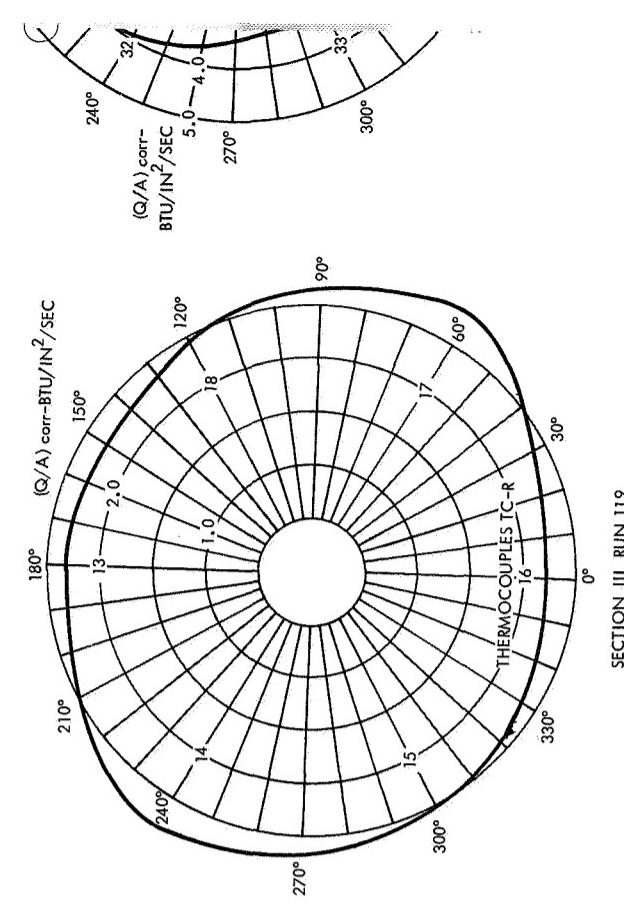
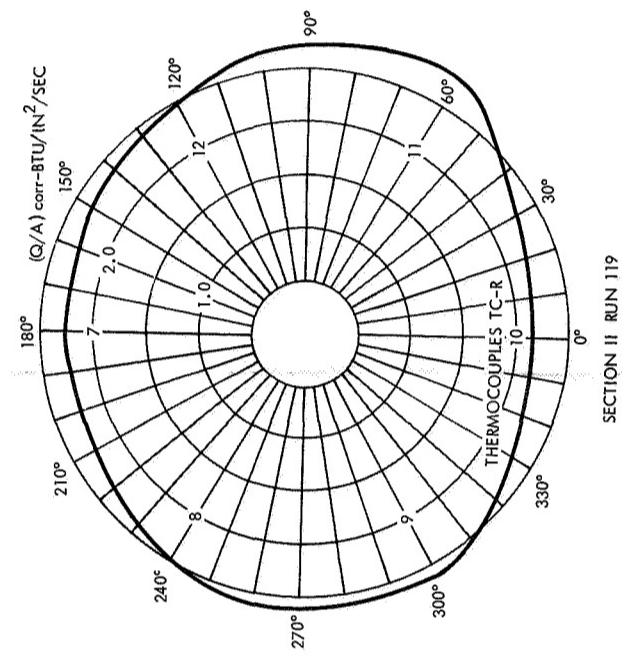
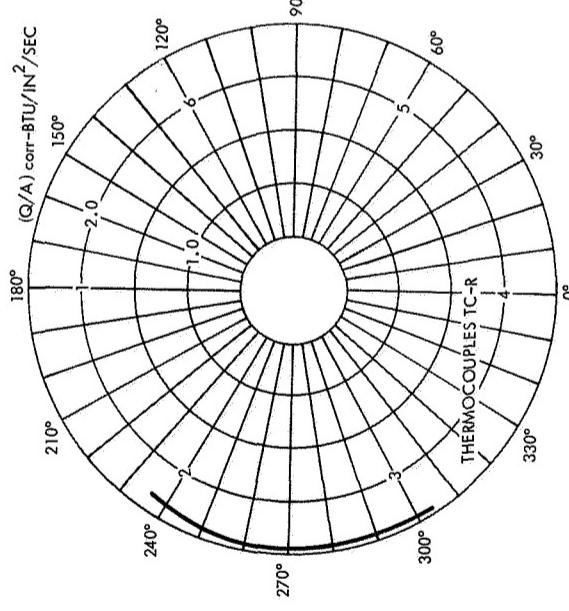
Figure 6-15. Radial Heat Flux Distribution for Run 118



SECTION IV 201



# Section I



## Section 2

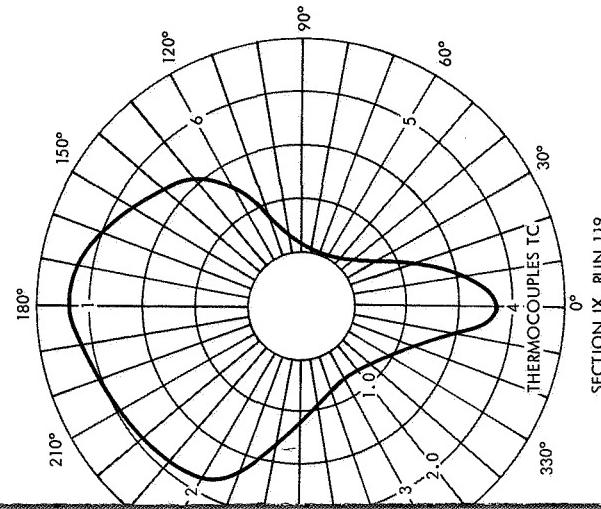
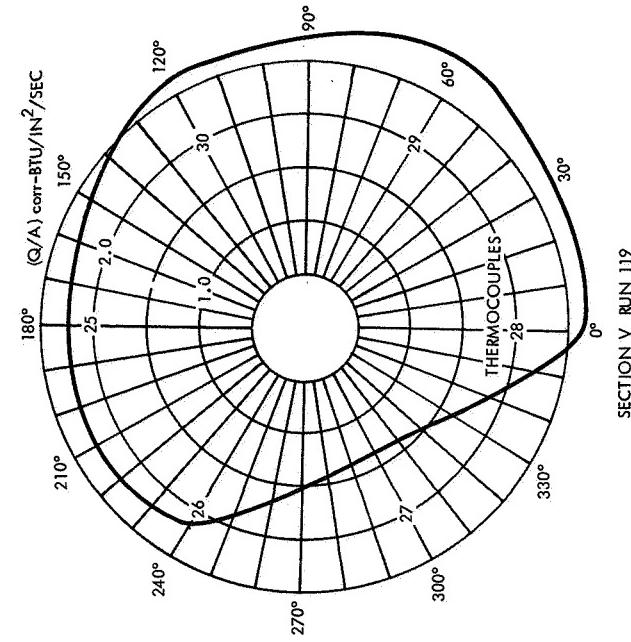
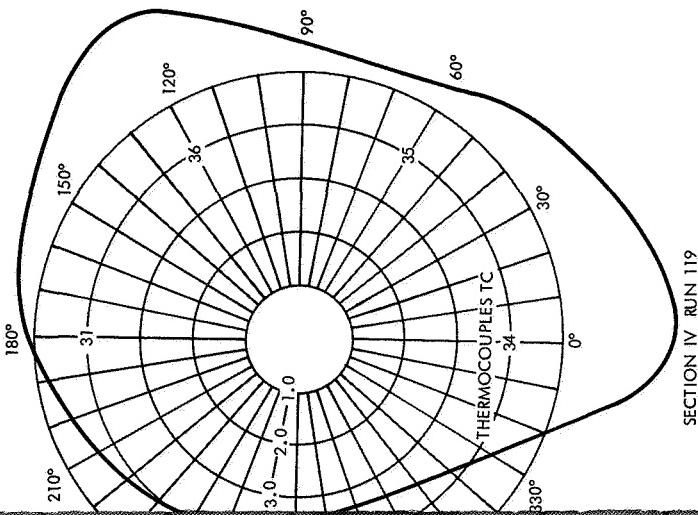
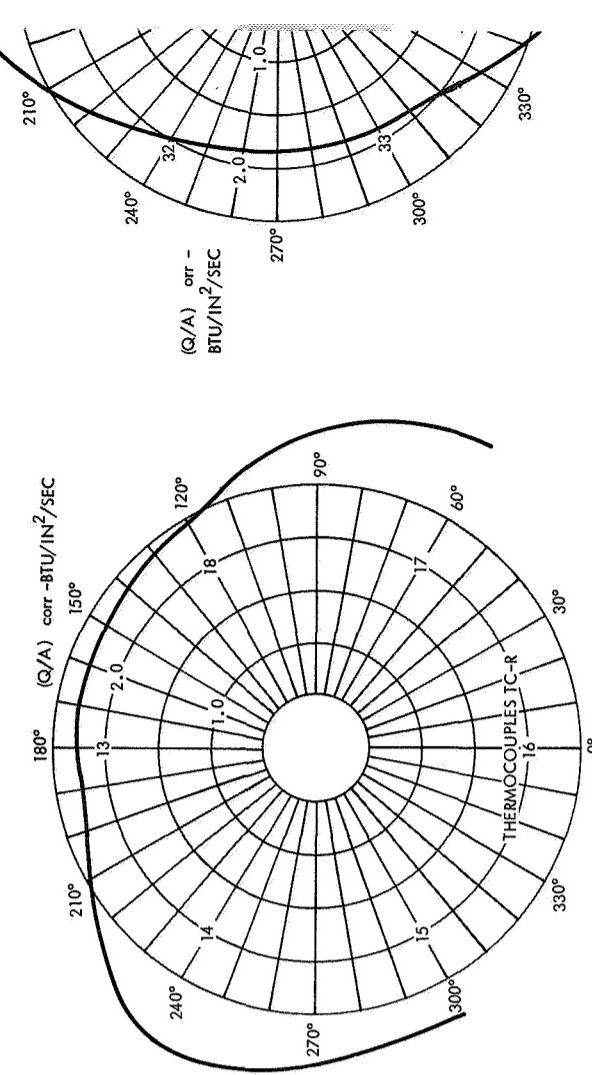
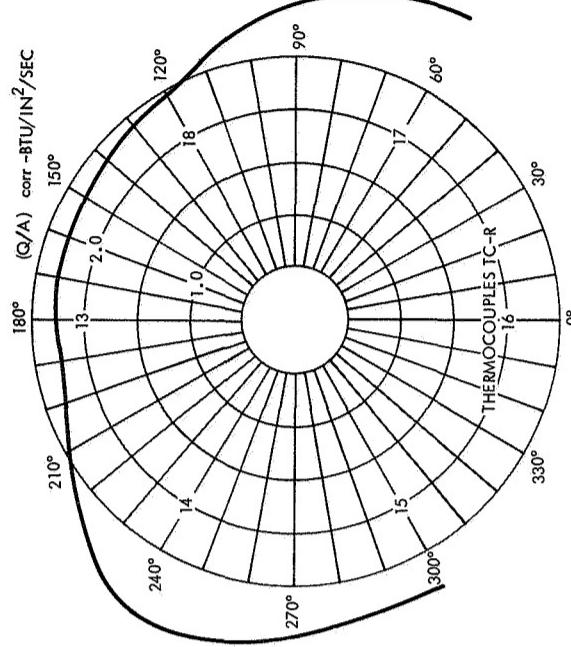
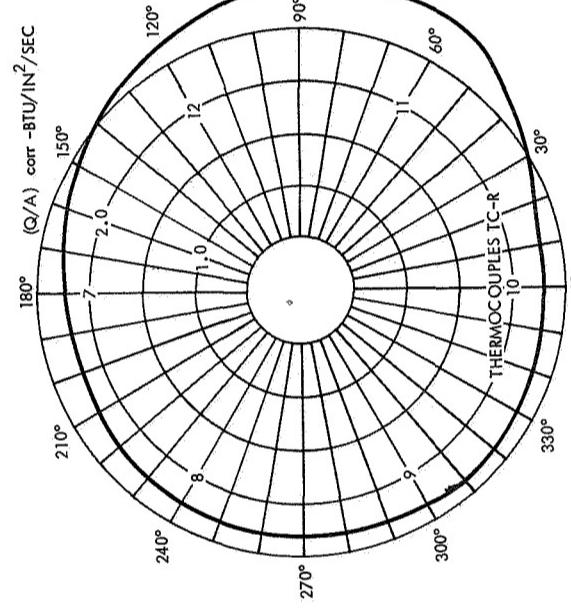
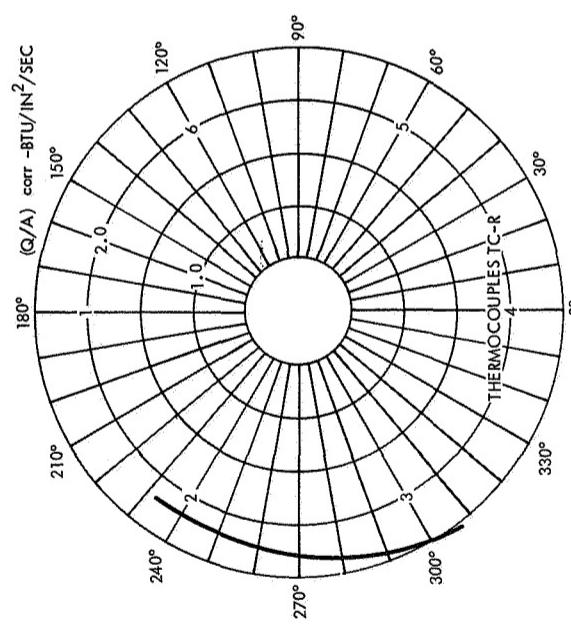


Figure 6-16. Radial Heat Flux Distribution for Run 119



# Section A

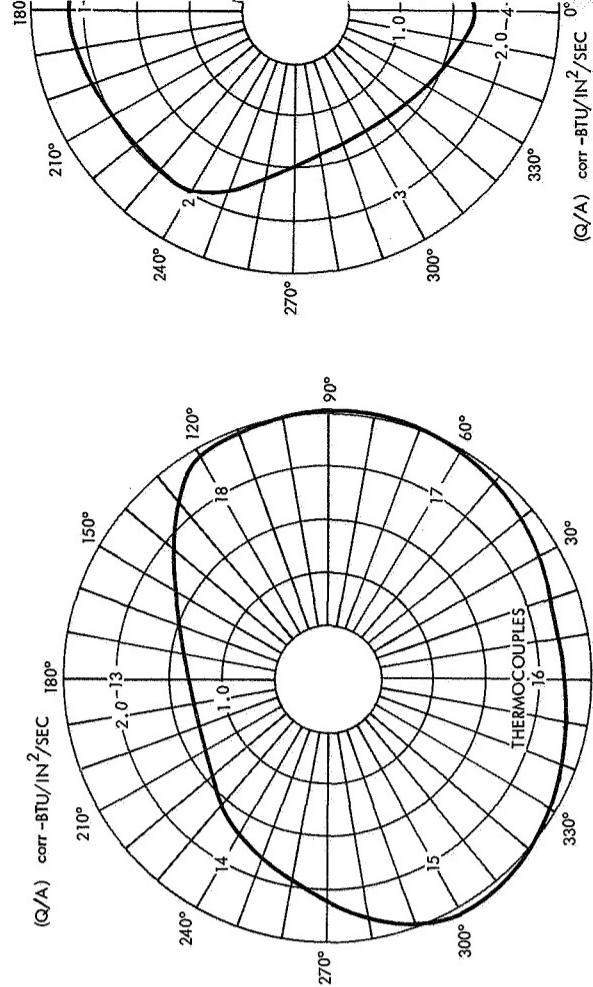
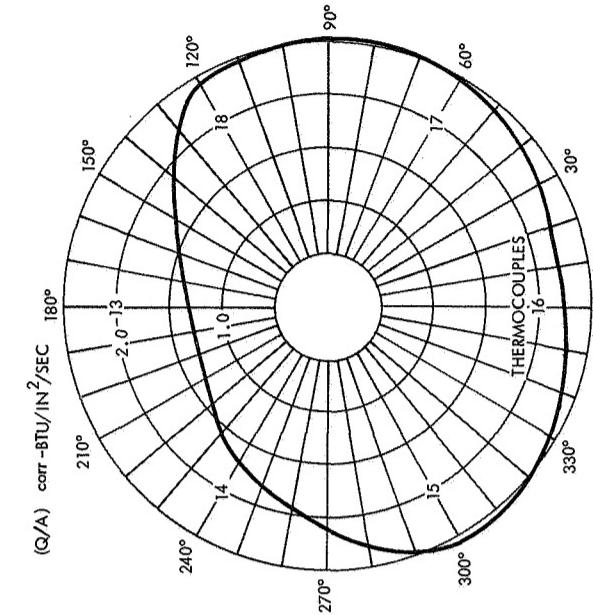
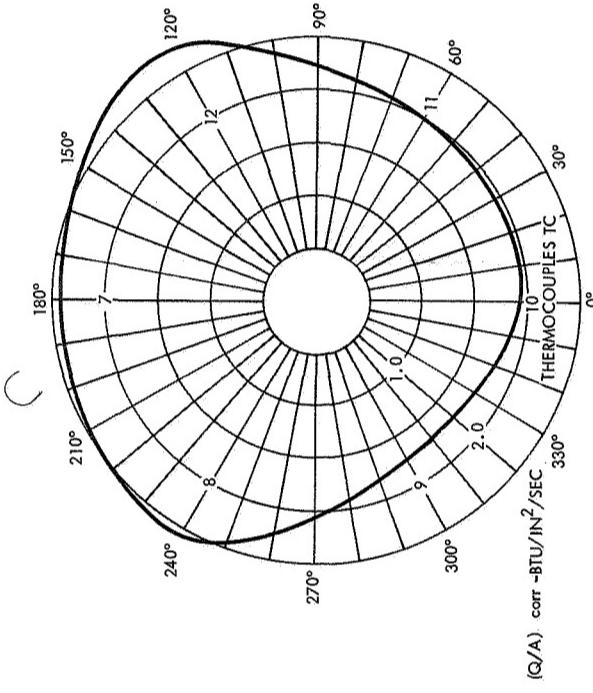
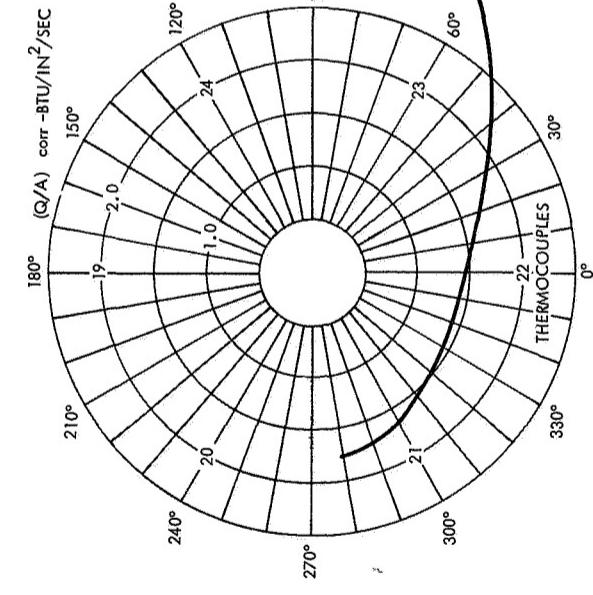


S

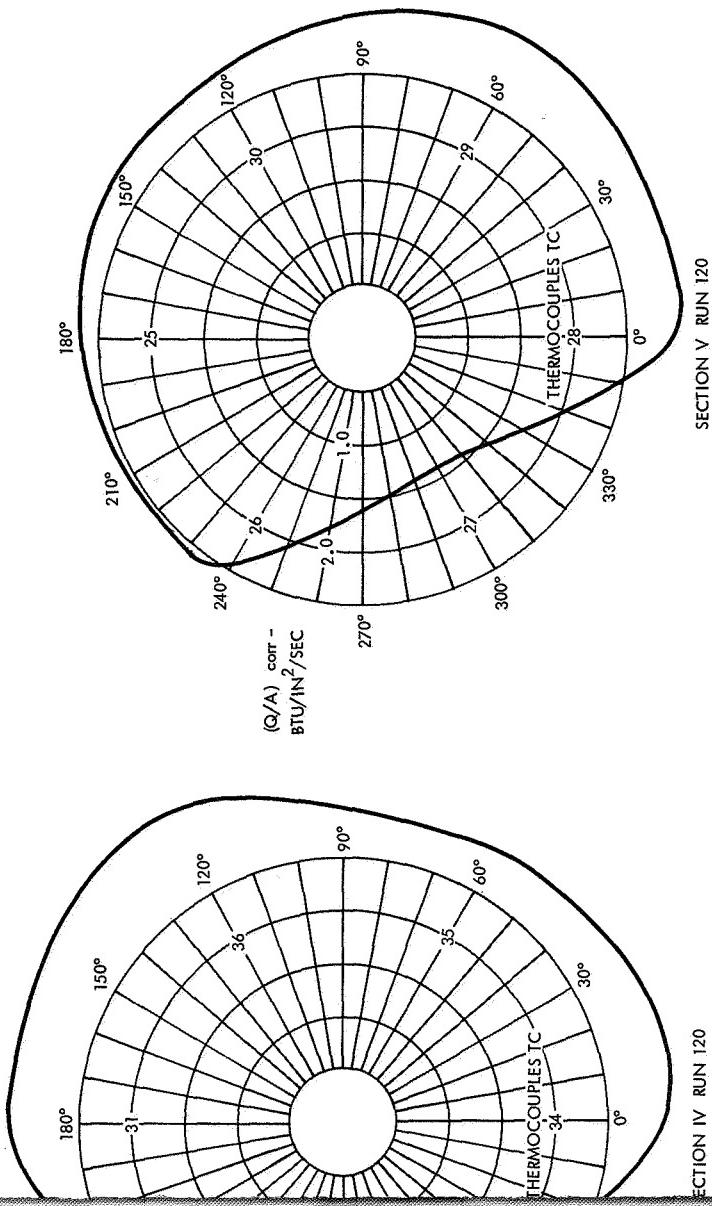
S

S

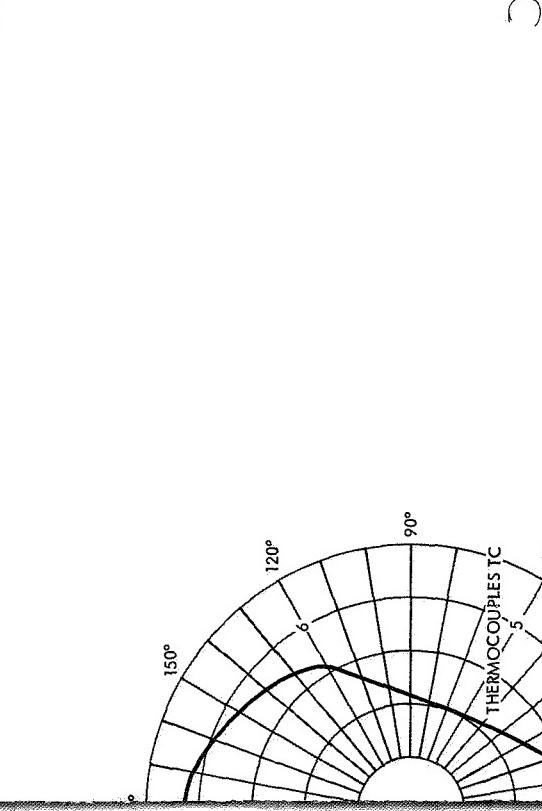
S



*Section B.*



SECTION V RUN 120



SECTION IV RUN 120

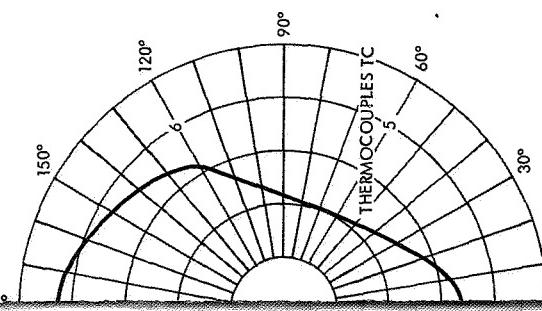
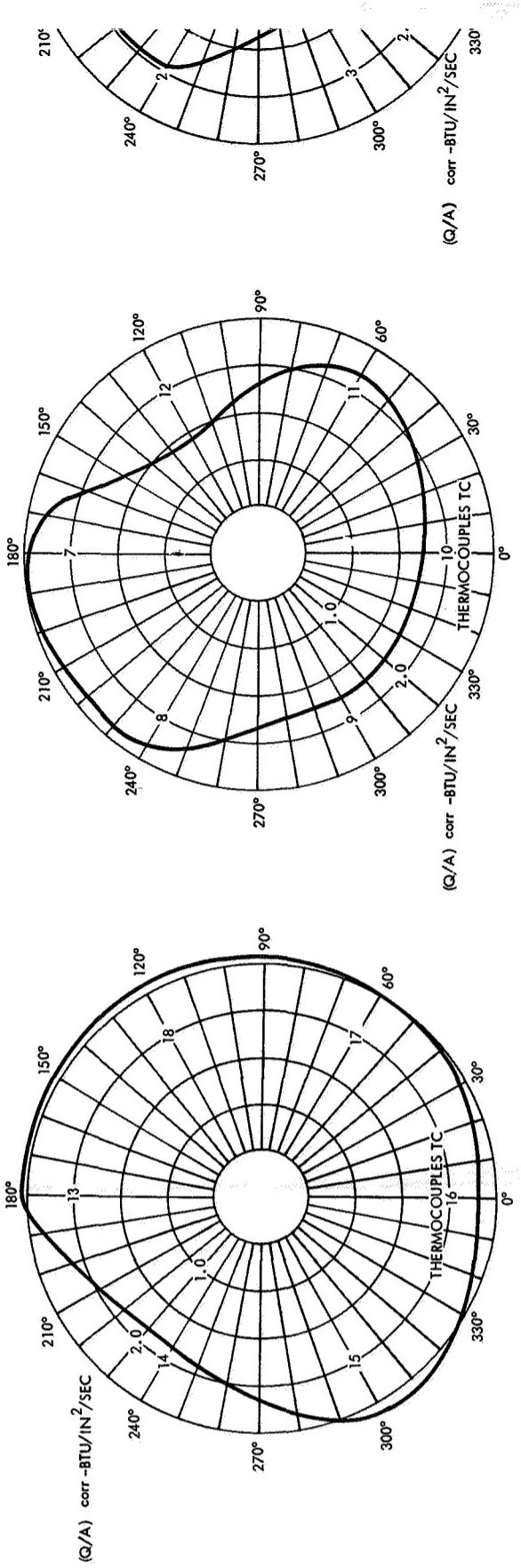
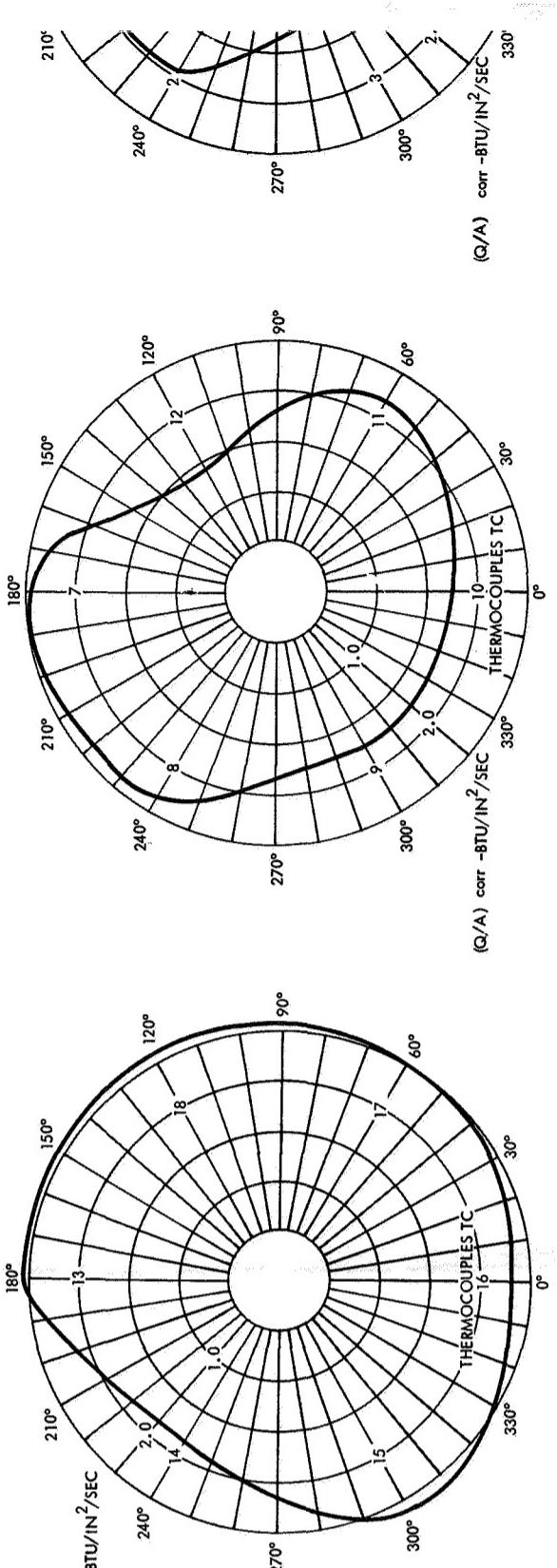
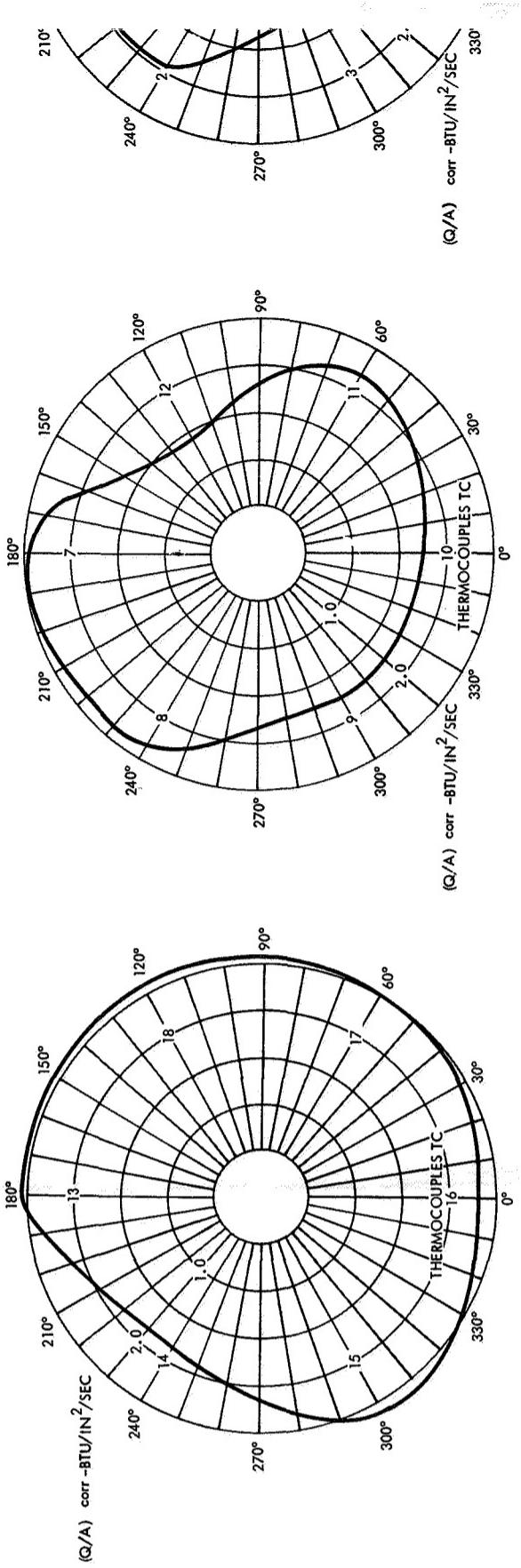
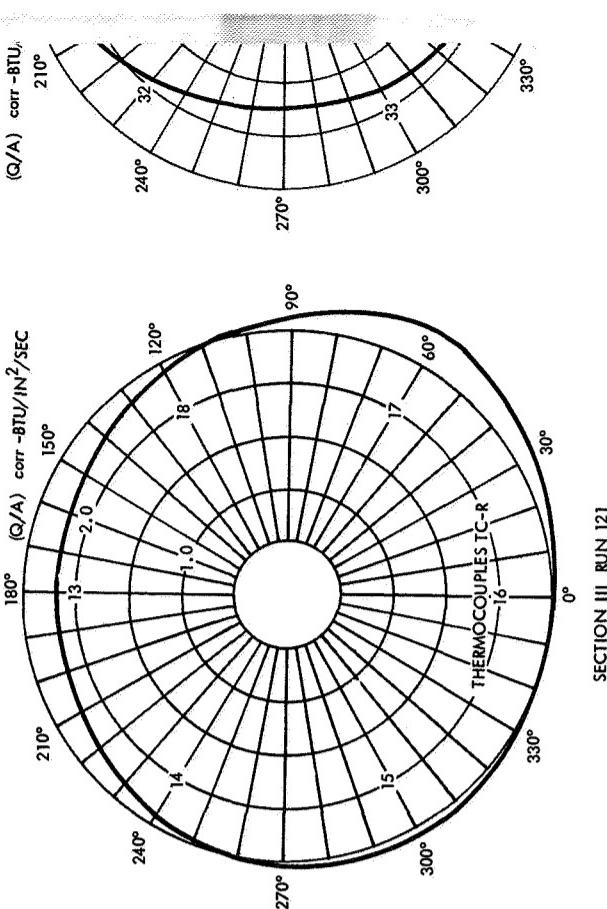
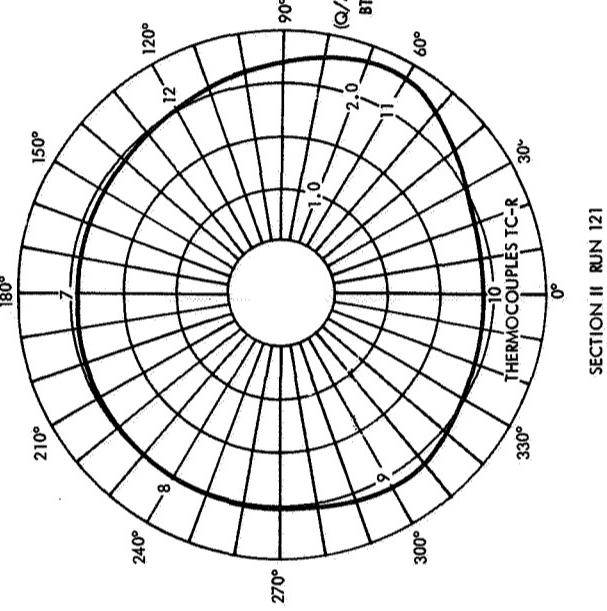
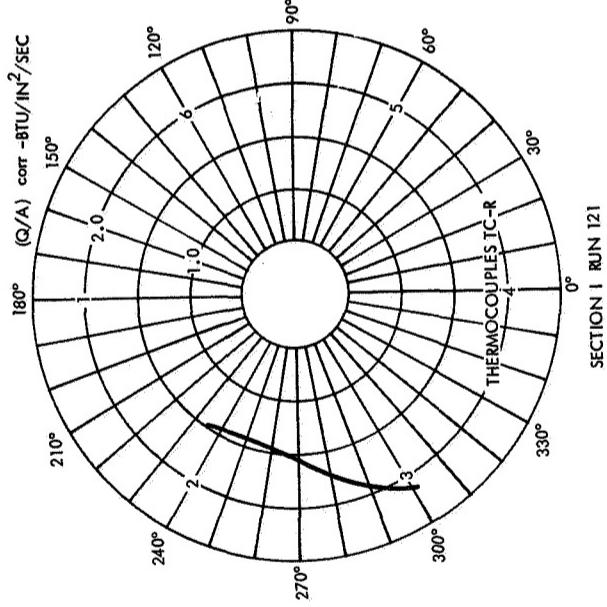


Figure 6-17. Radial Heat Flux Distribution for Run 120



Draft - 1



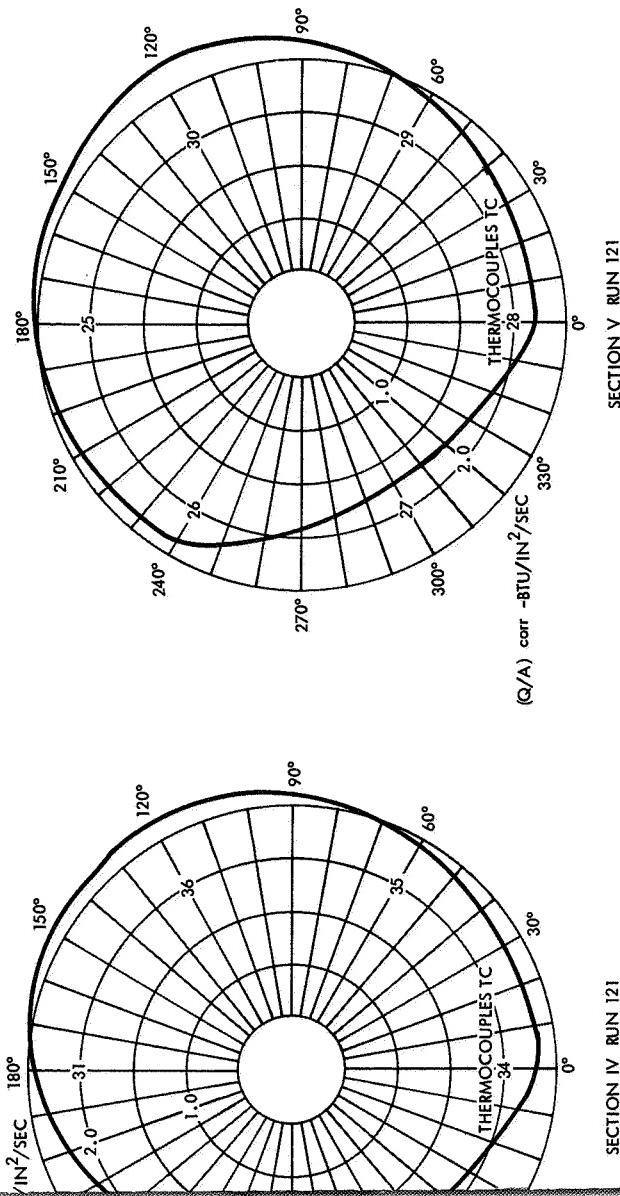
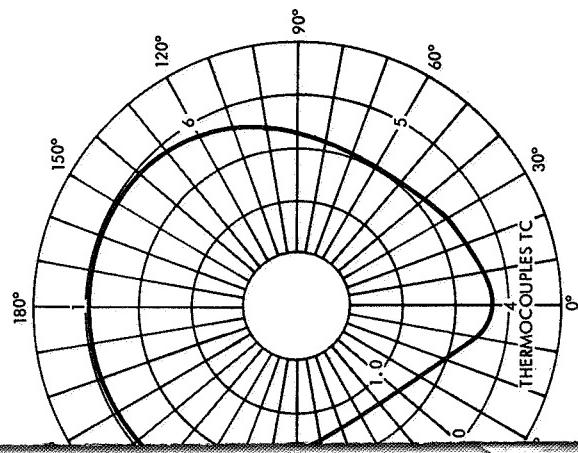


Figure 6-18. Radial Heat Flux Distribution for Run 121



卷之三



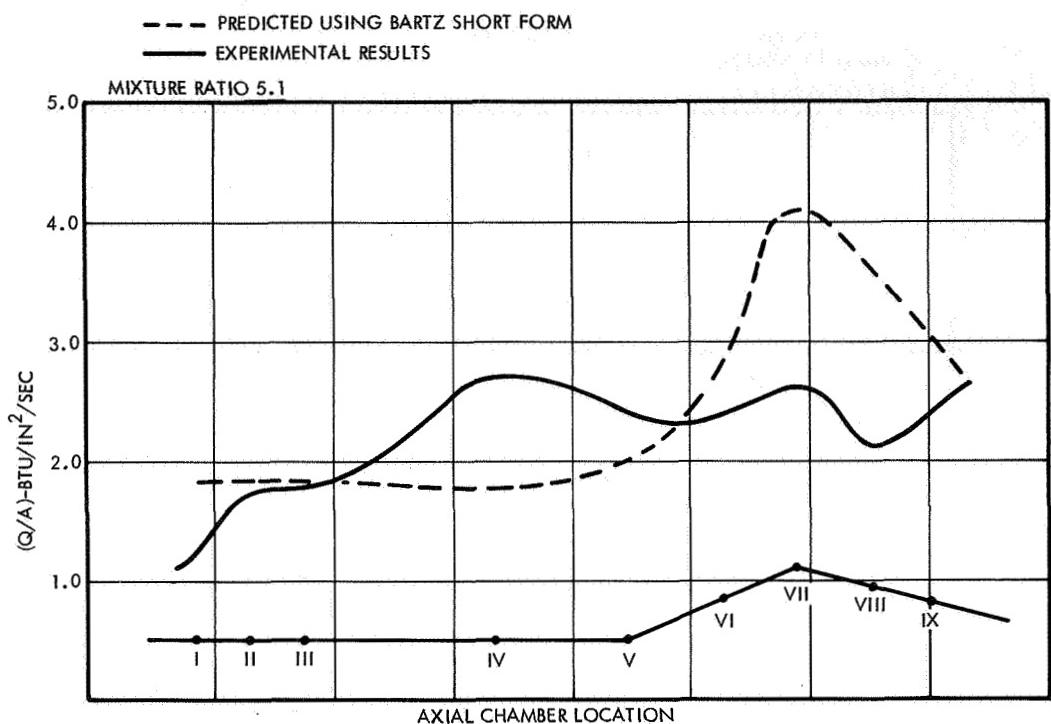


Figure 6-19. Axial Heat Flux Profiles for Run 118

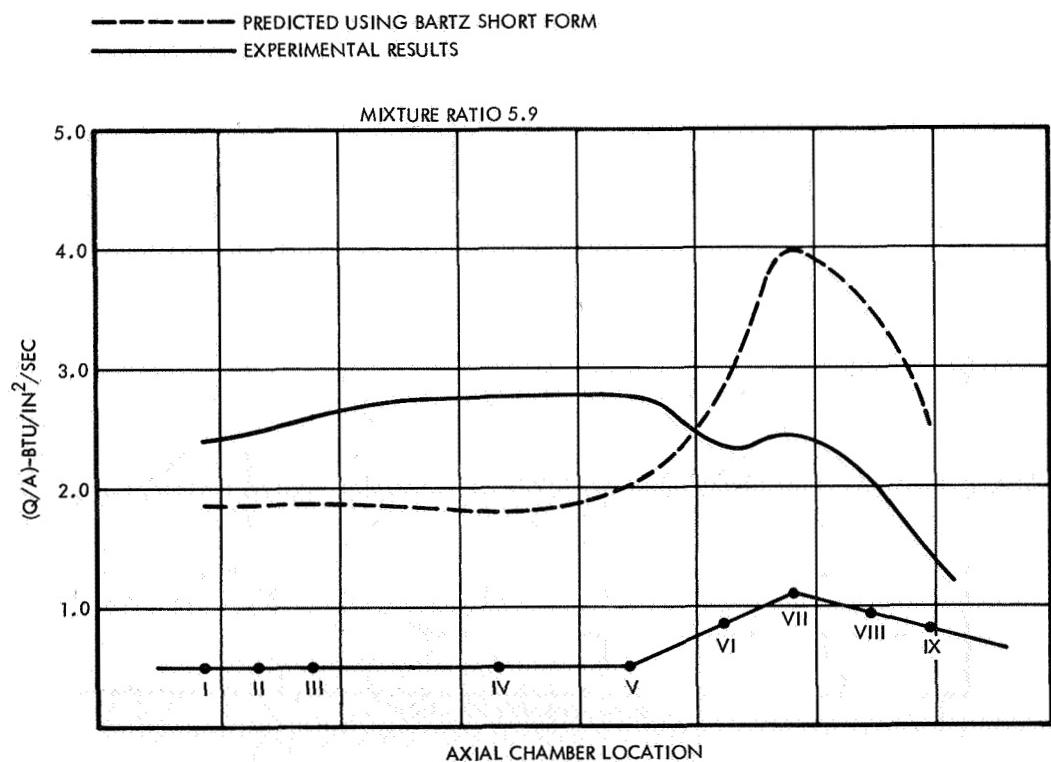


Figure 6-20. Axial Heat Flux Profiles for Run 119

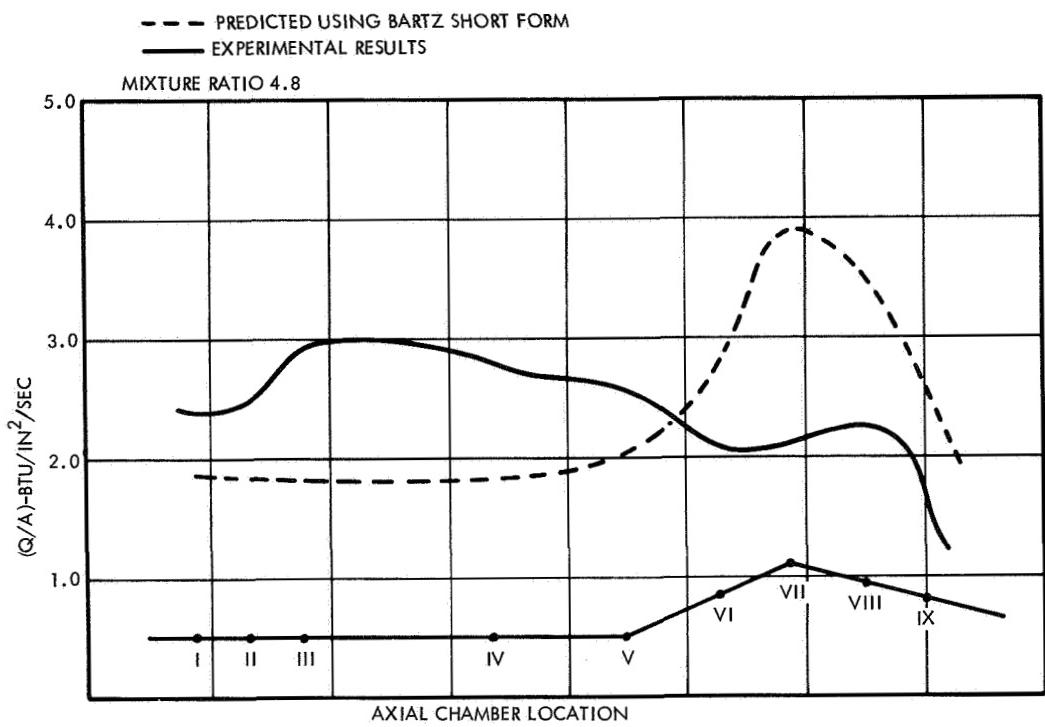


Figure 6-21. Axial Heat Flux Profiles for Run 120

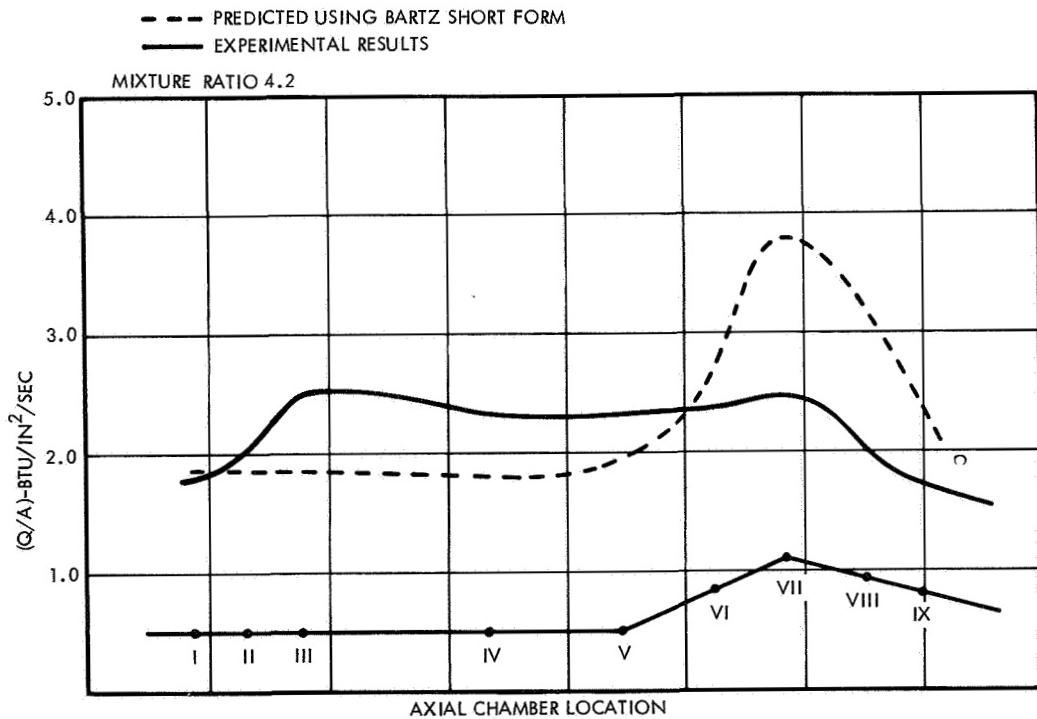


Figure 6-22. Axial Heat Flux Profiles for Run 121

## 7. COLD FLOW ANALYSES AND RESULTS

Very good progress has been made in analysis of injector performance in terms of cold flow characterization for conventional impinging jet injectors (References 8 through 10). The most promising results have been obtained with an approach which provides a resulting drop size distribution and a weighted mass and mixture ratio distribution as inputs to a combustion model. Correlation to hot firing results is made in terms of vaporization and mass-mixture ratio efficiencies.

$$\eta_C^* = \eta_M \eta_V \quad (7-1)$$

where

$\eta_M$  is a measure of mass and mixture ratio uniformity

$\eta_V$  is a measure of overall vaporization efficiency

The TRW coaxial flow injector has not received the detailed cold flow analysis and technique development of more conventional injectors. Best drop size distribution results are uncertain, consequently, it is difficult to assess a vaporization efficiency related to the resultant spray distribution of a particular element. It is, however, possible to compute a maximum size based on a used hydraulic diameter of slot on a single impingement model such as that of Ingebo (Reference 2) and to hydraulically size the injector elements. Because this was done in this program, and the resultant interlocking reaction could only result in subsequent size reduction of the initial spray sizes in the TRW injector, it was felt that the resultant characteristic velocity efficiency was primarily controlled by mass and mixture ratio distribution. Examination of the expected reacting spray trajectory further indicated that mixture ratio uniformity would be the primary key to achievement of high performance, once the spray criteria were met.

To provide a more complete understanding of the operation of the injector and the various effects of changes on the engine performance, cold flow analyses were conducted using a specially developed collector,

peculiarly suited to a radial flow type injector. Measurements acquired in the cold flow test provide indications of the radial mass flow distribution as well as mixture ratio distributions.

The cold flow collector shown in Figure 7-1 consisted of a mounting stand for the coaxial injector, collecting tubes, and a catch tank. The injector was mounted overhead and was operated using two immiscible fluids to simulate the propellants. The injected fluids were collected in a dome arranged with a matrix of tubes shown in Figure 7-2. The fluid entering these tubes was collected in graduated cylinders around the tank.

The cold flow program determined flow rate, pressure drop characteristics; mass and mixture ratio distributions; and overall impingement characteristics. In addition to overall pressure drop data, the various pressure drops associated with the overall pressure drop were determined. These included: (1) oxidizer distribution, and (2) oxidizer and fuel injection gaps. This was necessary so that actual injection pressure drops and, hence, injection velocities could be determined.

The mass and mixture ratio distributions were obtained with use of the apparatus shown in Figures 7-1 and 7-2. The apparatus collected flow from the conical fan of the coaxial injector in 90 collecting tubes; readouts were taken manually from burlettes located along the sides. Mixture ratio was measured by flowing two immiscible fluids through the oxidizer and fuel injection gaps. After collection, these simulated propellants were allowed to separate, thus giving a measure of both the mass and mixture ratio circumferential distribution as well as the axial and radial distribution. Measurement of these distributions can be used to determine the effects of any nonuniformities on the expected combustion efficiency. For unlike stream impingement (which the TRW coaxial injector is assumed to approximate), the collected cold flow simulants with equal momentum ratios can be converted to actual propellants through

$$\text{Equivalent MR} = (\text{MR})_{\text{simulants}} \left[ \left( \frac{\rho_o}{\rho_F} \right)_{\text{Propellant}} \left( \frac{\rho_F}{\rho_o} \right)_{\text{Simulants}} \right]^{1/2} \quad (7-2)$$

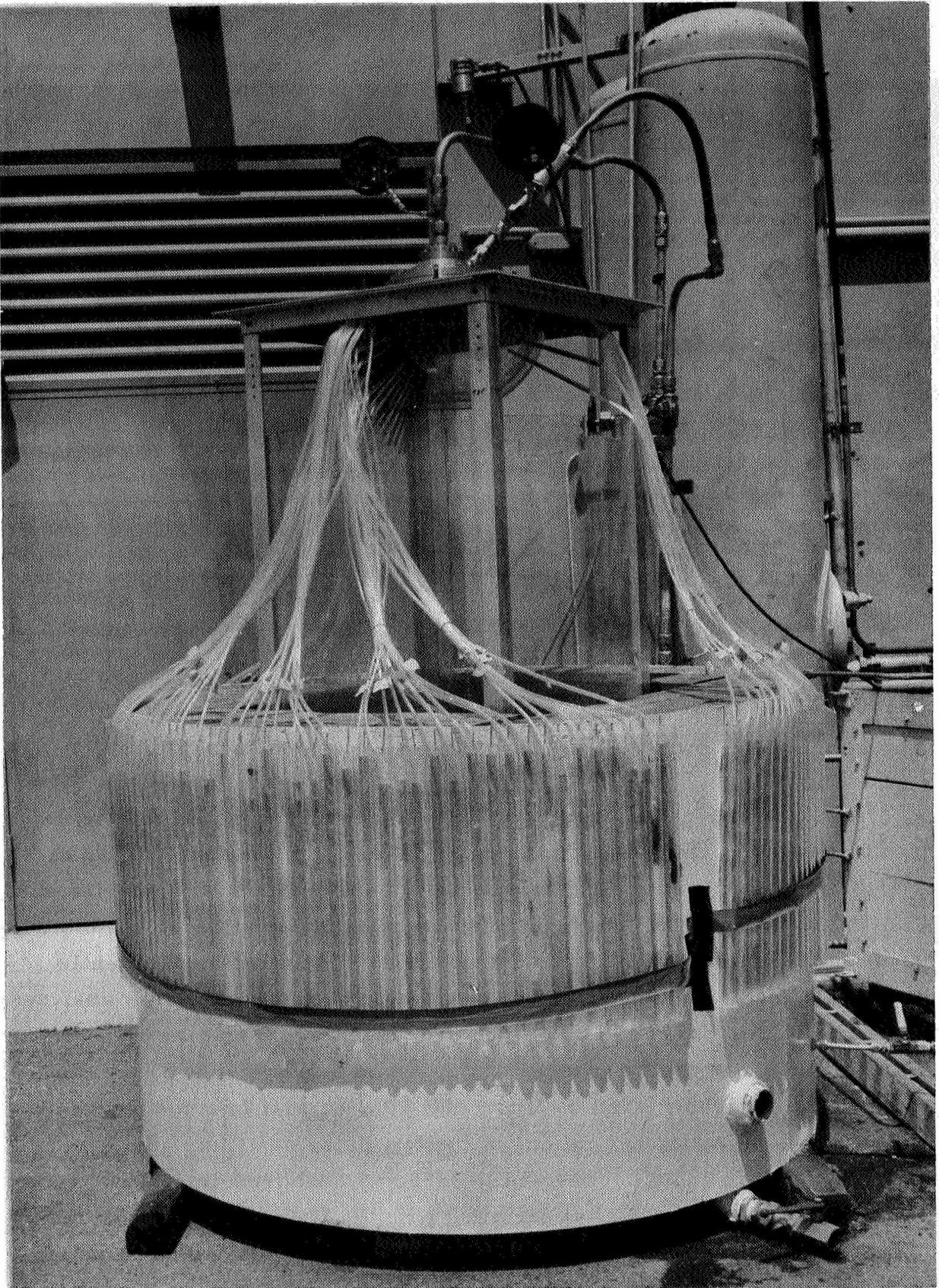


Figure 7-1. Coaxial Injector Cold Flow Collector

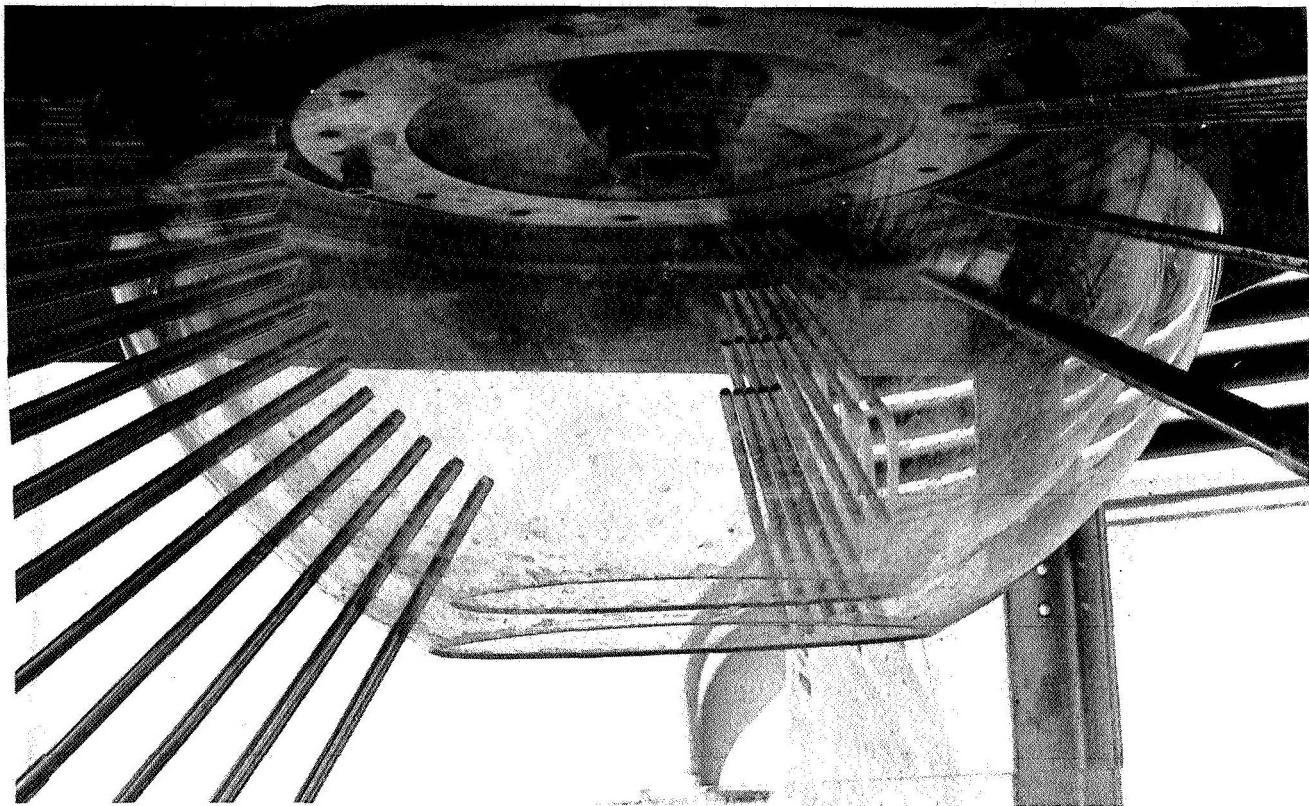


Figure 7-2. Coaxial Injector Cold Flow Collector Head End Assembly

For conventional injectors, trichloroethylene and water have been used to simulate oxidizer and fuel, respectively, for the earth storables propellants. In this case, the density ratios are nearly identically matched. With the space storables, there is no simple combination of readily handled fluids which will provide density ratio simulation; consequently, attention to the above relation must be given to properly cold-flow analyze injectors. In this program, both trichloroethylene/H<sub>2</sub>O and kerosens/H<sub>2</sub>O combinations were used. Contrary to the usual findings with conventional injectors with trichloroethylene/H<sub>2</sub>O, the TRW coaxial injector provided such a fine atomization and mixing of the two fluids, that immediate separation of the fluids could not be readily achieved, thus requiring long setting times. A similar phenomenon occurred with the hydrocarbon/H<sub>2</sub>O combination; however, because of facility handling ease, the latter combination was chosen to carry out the bulk of the cold flow effort.

To interpret the results, once it was established that vaporization was not a controlling factor, the stream tube approach was used. A given mass rate of oxidizer and associated with each stream tube.

$$\dot{W}_i = \dot{W}_{i_O} + \dot{W}_{i_F} \quad (7-3)$$

The stream tube mixture ratio was

$$MR_i = \frac{\dot{W}_{i_O}}{\dot{W}_{i_F}} \quad (7-4)$$

At this point, the following assumptions were made:

- 1) Complete combustion occurred in the stream tube, prior to expansion
- 2) The stream tube expansion was one-dimensional and isentropic through the nozzle
- 3) The static pressure distribution was isotropic in the flow field
- 4) The gases are perfect gases.

If the stream tube gases could be assumed to have approximately the same ratio of specific heat values,  $\gamma_i$ , the individual stream tube  $C_i^*$  values were given by

$$C_i^* = \frac{P_o A_i^* g_o}{\dot{W}_i} \quad (7-5)$$

For the above assumptions, the sonic area  $A_i^*$  is given by

$$A_i^* \approx \frac{\dot{W}_i}{\dot{W}_T} A_t \quad (7-6)$$

In this simplified model, the overall  $C^*$  becomes

$$C_{\text{eff}}^* \approx i \frac{W_i}{W_t} C_i^* \quad (7-6)$$

For computational purposes from a cold flow analysis, the collection efficiency must enter into the physical processing of the data. This can be handled in one of two ways: (1) correct to a level collection, or (2) correct to total mass flow. In this effort, the  $C_{\text{eff}}^*$  calculation was made on the basis of the normalized collected fluids, i.e.,

$$\frac{W_i}{\Sigma W_t} \quad (7-8)$$

The  $C_i^*$  is taken as the equilibrium  $C^*$  associated with the indicated equivalent mixture ratio as computed by Equation 7-4. A complete derivation for variable specific heat ratios is given in Reference 11. The more exact results were not used here, since FLOX/LPG propellant interaction effects on the TRW coaxial injector are not completely understood. (Errors between the exact analysis and the approximate analysis are small as shown in Reference 11.)

For comparison purposes, two different injector configuration cold flow results are presented here. In Figure 7-3 the mass and mixture ratio distribution for the high performance SS-6 injector, operating at an equivalent overall mixture ratio of 5.9, and corresponding to Test 97, is given. The computed  $C^*$  performance on the basis of the cold flow results is 97 percent, while the hot firing performance was 97.3 percent. This is considered to be excellent correlation. In Figure 7-4 a similar set of curves is shown for injector SS-4 at an overall equivalent mixture ratio of 5.2, corresponding to Test 093. The cold flow result computed  $C^*$  performance is 97 percent while the corresponding hot firing data show a performance level of 95.3 percent. This again is considered to be excellent correlation.

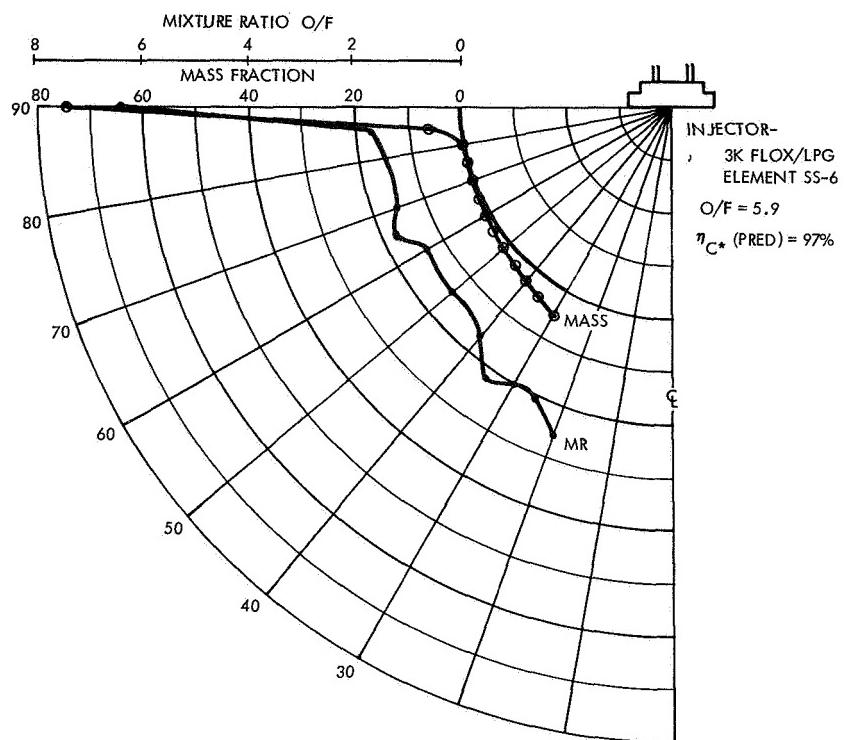


Figure 7-3. Cold Flow Test on Element SS-6

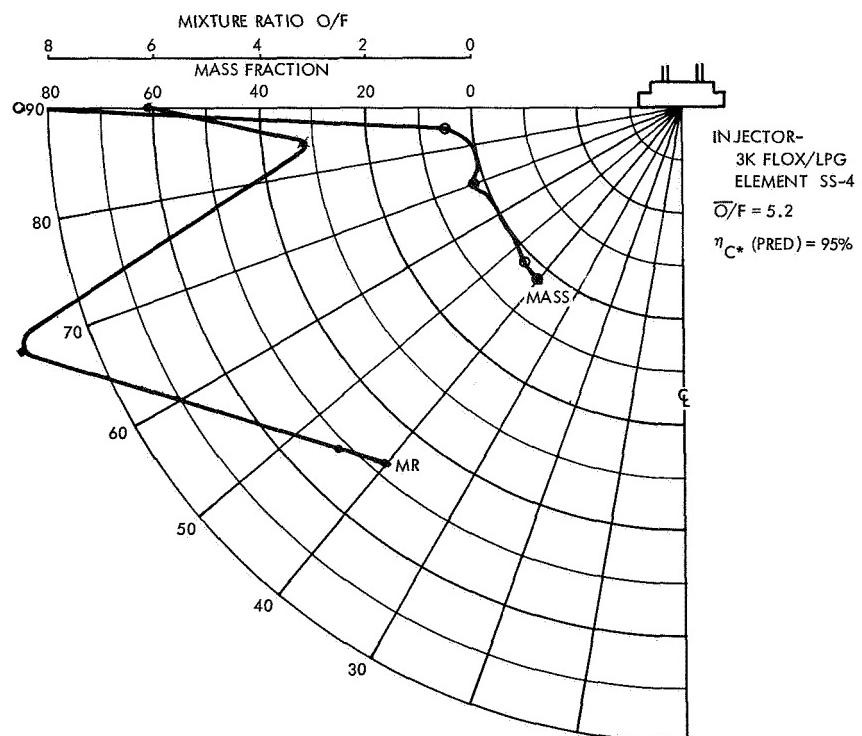


Figure 7-4. Cold Flow Test on Element SS-4

In analyzing the results, it is seen that the distributions have interesting characteristics. In a conventional injector mass uniformity across the injector face would be expected to provide maximum performance. Here, it is observed that apparently uniformity in the MR associated with the mass distribution is of far more importance.

Additional data can be inferred from the cold flow data once comparative experimental data are available. Figure 7-5 shows results for the SS-8 injector with equivalent MR of 5.4 (Test 101). Here, it is seen that the injector exhibits high performance but with a somewhat different characteristic mass and mixture ratio distribution. In this case, the secondary slots were moved upward into the primary region. The resultant distribution is different, but still retains the feature that high performance should be expected from this distribution. The resulting heat transfer is, however, markedly different (see Figures 6-8 and 6-9) between Tests 118 and 101, shown in Figure 7-6. The broader distribution of Test 97 has a much more desirable heat flux distribution.

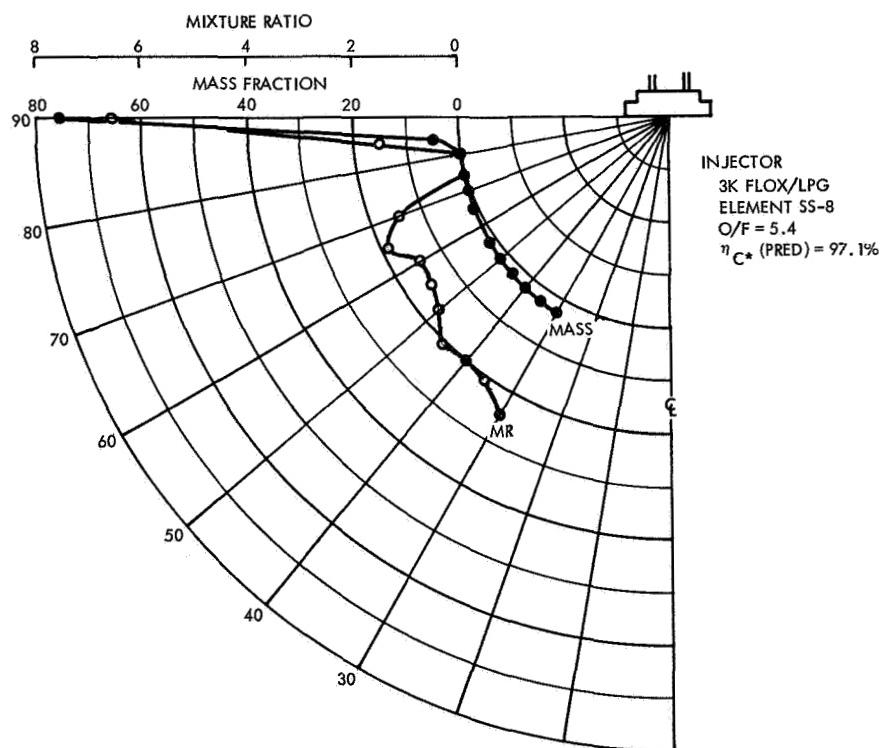


Figure 7-5. Cold Flow Test on Element SS-8

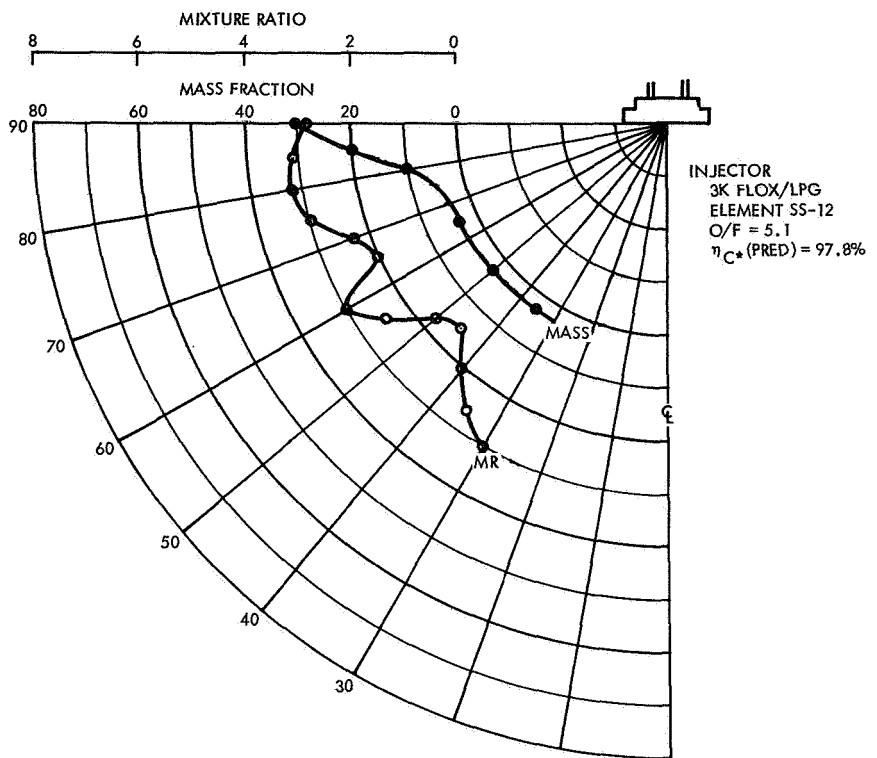


Figure 7-6. Cold Flow Test on Element SS-12

## 8. SUMMARY OF RESULTS

The primary objective of this program was to investigate the feasibility of the TRW coaxial injector to meet the performance goal of 97 percent shifting equilibrium characteristic velocity performance with the nominal 80 percent FLOX mixture and 55/45 methane-ethane fuel blend. Secondary objectives included obtaining heat flux data and performing cold flow, hot firing performance correlations to provide insight into the required design characteristics of the injector for high performance. The summary of results discussion is divided into four parts: combustion, performance heat transfer, cold flow correlation, and operational characteristics.

### 8.1 COMBUSTION PERFORMANCE

In this brief experimental program the three coaxial injector configurations (sawtooth, canted, and slotted) evaluated showed the conventional TRW approach with the straight slotted oxidizer slots to be the highest performing. The primary requirement for getting high performance with the high mixture ratio FLOX/LPG propellants was one of achieving local mixture ratio control through the control of the percent secondary flows and their location with respect to the primary flows. The reactivity of the liquid surface interactions was unknown and required empirical adjustment of the geometries of the oxidizer elements to optimize the performance.

The performance met the required goals of the program with the basic 30-inch L\*, CR of 2.5 thrust chamber. The combustion performance was essentially constant across the contractually specified MR of 4.3 to 5.9 for the nominal FLOX mixture. Data from 74 percent and 90 percent FLOX mixtures indicate that the basic injector performance was reasonable insensitive to  $F_2$  concentration changes, with more loss occurring in the 90 percent mixture runs. However, it is probable that the surface reactivity effects are markedly different between the FLOX and LPG propellants as the  $F_2$  concentration approaches 100 percent.

Assuming the reactivity to increase, results in optimum secondaries for the 80 percent FLOX mixture to not enter into critical reaction, i.e., the fuel would not penetrate the oxidizer elements sufficiently to obtain uniformity in mixture ratio. By a change in position of the secondaries and in their flow percentage, the elemental approach should result in increased performance at the 90 percent FLOX mixture.

The geometrical changes in the combustion chamber reflected upon the general operating characteristics of the injector.  $L^*$  reductions to 15 inches with a fixed CR of 2.5 resulted in a performance loss of nominally 3 percent, whereas an  $L^*$  increase to 45 inches resulted in only a nominal performance increase of 0.57 percent. These results strongly inferred that the performance of the injector was not atomization controlled, but instead was primarily controlled by MR and mass distribution control. The results indicated that some performance gain optimization was still possible through MR control brought about by variation in the geometry of the oxidizer elements.

The CR change essentially resulted in the same performance as the long  $L^*$  chamber. This was not too surprising since the resultant  $L^*$  was about the same as the extended length chamber. Of interest was the fact that the  $P_c$  was 167 psia for these runs and no performance increase occurred, thus indirectly inferring again that basic atomization was not the cause of performance loss. This conclusion was made since the burning rate should be somewhat proportional to the pressure in the combustor.

Finally, of interest in this program was the absence of any spontaneously occurring combustion instability. The random combustion roughness was less than  $\pm 3$  psi, for the final injector configurations indicating very smooth combustion.

## 8.2 HEAT TRANSFER

The detailed heat transfer measurements made in the program showed reasonable uniformity in the circumferential distributions. The data were reproducible, and the magnitude of the heat fluxes was on the order of 40 percent of the theoretical, carbon-free Bartz technique predicted values for the values throat. The indicated recovery temperatures were on the order of  $3500^{\circ}$  to  $4000^{\circ}$ F in the chamber and nozzle for the final evaluated configuration.

The carbon buildup in the chamber appeared to occur reproducibly and uniformly. Of particular interest was the tenacity of the carbon-copper metal interface bond. The carbon residue further begins from a near-zero thickness at the head end of the chamber and maximizes in the convergence part of the nozzle.

The injector showed a capability for strongly controlling the wall environment and resulting heat flux with minimal adjustments in injector geometry or pressure drop ratios and with no significant effect on combustion performance. This factor was significant to actual thrust chamber design.

No injector heat transfer problems appeared in the straight slot configuration. Carbon residue appeared on the coaxial injector pintle tip, but only trace carbon deposits appeared on the face plate assembly. This would indicate a relatively cool head end gas zone, since equilibrium carbon breakdown of the fuel would occur near 500°F. The maximum run durations were on the order of 6 seconds, a time sufficient to establish near steady-state operating temperature profiles in the injector coaxial assembly. Long duration demonstrated durability, however, remains to be proven.

### 8.3 COLD FLOW CORRELATION

The cold flow correlating results were encouraging for this injector type. Although not conclusive, they did indicate that a uniformity in mixture ratio with circumferential mass distribution uniformity results in maximized performance. The results also showed some promise as an aid in design for minimum wall heat transfer. Additional correlation effort was required to fully appreciate the value of cold flow analysis with this type of injector.

### 8.4 OPERATIONAL CHARACTERISTICS

The TRW coaxial injector concept performed quite well from an operational sense in this program. The simple, lathe-turned parts were easily assembled and disassembled with reproducible results. The replaceable oxidizer rings were inexpensive, requiring a total of 4 man-hours for fabrication, starting from a billet. These features enabled a rapid

empirical optimization of the injector to be achieved, once the basic analytical design was established. The passivation of the injector was readily accomplished with new ring changes, and test firing was resumed within a short period following disassembly and assembly.

The pressure drop characteristics of the injector require additional investigation. The fuel pressure drops were quite acceptable, whereas the oxidizer pressure drops needed to be reduced. However, it is noted that in this program performance effort, no particular effort was made to improve the oxidizer discharge coefficients. The hydraulic inlets were all sharp-edged in most of the tests. In one test the discharge coefficient was increased from 0.65 to 0.73 with a  $\Delta P_o$  reduction of 10 percent and no loss in performance. Raising the discharge coefficient to 0.90 from 0.65 will reduce the  $\Delta P_o$  to approximately 100 psi.

In the early tests two-phase flow occurred and impeded the approach to steady-state operation. The injector showed no durability problems; however, in actual service two-phase flow startups may be of real significance. Additional effort is required to investigate this aspect of the injector operation.

The demonstrated stability of the concept to date has been excellent. However, no dynamic rating of the injector through induced pulse or bomb techniques with the FLOX/LPG propellants has been accomplished yet. The injector concept was designed as a fundamentally dynamically stable injector. This has been proven at TRW with a variety of other propellants. Additional effort is required with the space storable propellants.

## APPENDIX A

### CALORIMETRIC PLUG DESIGN

The heat sink chamber was instrumented with calorimetric plugs for obtaining heat flux measurements with the plugs an integral part of the chamber material itself. This method was used to rapidly obtain heat flux through a one dimensional constant property heat transfer analysis or a more sophisticated multi-dimensional variable property analysis. All data were computed for a given segment through analysis of the output from a single thermocouple attached to the "cold" side of the segment.

Figure A-1 shows a typical plug arrangement. In order to instrument properly for the heat flux, it was necessary to establish a satisfactory design. The isolation slot size, from a heat transfer standpoint, can be as small as can be practically machined since the air conductivity is considerably smaller than the conductivity of the metal. The effects of lateral conduction are influenced by the web thickness,  $W$ . The minimum values of  $W$  are determined, therefore, from stress considerations. The plug height,  $L$ , is a variable which must be chosen on the basis of the compromise of the run duration, method of data reduction, and the local heat flux. The plug cross-sectional area is limited only to the area required for thermocouple attachment.

A detailed analytical study was made to evaluate this plug concept and to determine the validity of heat flux data evaluated from its use. The uncooled copper heat sink chamber was thermally modeled with and without plug instrumentation. Figure A-2 shows the general thermal model of the thrust chamber which contains 161 nodes. Additional nodes were also added for analysis involving carbon deposition on the chamber wall. Circumferential conduction was not considered.

Figure A-3 shows the thermal model that was used at a calorimeter plug location. The plug was simulated by five nodes and the surrounding wall by the seven nodes of the general model. These analyses were

thermally modeled on the TRW Thermal Analyses Program (TAP). The models included the following conditions:

- a) Carbon deposition on the wall
- b) Two-dimensional and radial conduction
- c) Hot side film resistance as a function of temperature
- d) Copper properties as a function of temperature
- e) 100 percent recovery temperature

The analysis was limited to the chamber throat section. It was felt that one throat section contained all of the conditions that would be analyzed in a spool. Figure A-4 shows the general layout of the throat section that was analyzed.

Figures A-5 and A-6 show the combustion gas resistance and carbon deposition resistance, respectively, as functions of the chamber area ratio. The area ratio was determined by applying unity to the throat area.

Figure A-7 shows the variations of transient temperature profiles of calorimetric plugs for three different throat locations. The profiles are then given as a function of rib proximity dimensions and engine firing time. From these profiles it is seen that little difference should be expected in the measured profiles of these plugs. The profiles also show that with web thickness of the order of 0.1 inch a good correlation should be expected at approximately 2 seconds into the run.

Figure A-8 shows the temperature distribution around a throat plug after 5 seconds into a firing. A relative comparison is shown with the solid wall temperatures. This figure illustrates the relative effectiveness of the plug as an isothermal source. Figures A-9 and A-10 show the throat gas side input heat flux and the calculated plug calorimeter heat flux as a function of firing time and rib dimension. Finally, taking these results, Figure A-11 shows the ratio of the measured heat flux to the gas side input heat flux as a function of the rib thickness. This function is shown parametrically as a function of time into the firing.

It was felt that heat flux data should not have to be adjusted by large correction factors to render the data useful. For the plug designs used in the thrust chamber, the reasonable data-taking range was from 1 to 3 seconds into the firing. The heat flux correction curves for all of the plug calorimeters are presented in Figure A-12.

The heat flux correction factors are minimum for the plugs located in the straight-walled chamber section. The throat plug requires the most heat flux correction. The heat leakage rates at the throat are inherently higher due to the throat point experiencing the "peak" imposed heat load, while the converging and diverging sections adjacent to it exhibit lower imposed heat loads.

The following throat plug data are presented to further the understanding of the thermal behavior of the plug:

- a) Figure A-13 shows the effect of rib thickness on heat flux correction factor.
- b) Figure A-14 shows the transient heat flux measured by the plug for several geometry changes and for isolated (no heat loss) plugs.
- c) Figure A-15 shows the plug base and plug cold side transient temperatures for several geometry changes and for isolated plugs.
- d) Figure A-16 shows the throat plug design transient temperature behavior. The temperatures of all the plug nodes and adjacent base nodes are presented.

Reasonable care was exercised in the use of model dimensions in and around the plugs to ensure correct two-dimensional thermal behavior during the transient analysis. The preselected plug length of 0.5 inch appeared to be reasonable for firing durations less than 7 seconds. A shorter plug would, of course, give more accurate heat flux data but would be limited to permissible firing durations of less than 7 seconds.

Figure A-13 shows that the plug heat flux correction factor is nonlinear with rib thickness. Also, it is evident that the correction factor has an increasing rate of change with firing time and with increasing rib thickness.

The following thermal analysis of the plug rib is presented to increase the understanding of the many variables involved in the proper design of the plug. (Figure A-1 is used as the reference.)

Since, in the optimum case, no heat is transferred between the rib and the plug, the plug heat balance will be

$$Q_{IN} = Q_{stored} \quad (A-1)$$

or,

$$Q_1 = \rho_1 C p_1 (VOL)_1 \left[ \frac{d\bar{T}}{d\theta} \right]_{PLUG} \quad (A-2)$$

where

$$(VOL)_1 = A_1 L \quad (A-3)$$

Rearranging,

$$Q/A_1 = \rho_1 C p_1 L \left[ \frac{d\bar{T}}{d\theta} \right]_{PLUG} \quad (A-4)$$

The rib heat balance is,

$$Q_{IN} = Q_{stored} + Q_{loss} \quad (A-5)$$

Or,

$$Q_2 = \rho_2 C p_2 (VOL)_2 \left[ \frac{dT}{d\theta} \right]_{RIB} + \frac{k A_L}{x} (T_2 - T_L) \quad (A-6)$$

Where,

$$(VOL)_2 = A_2 (PD) \quad (A-7)$$

Rearranging,

$$\frac{Q}{A_2} = \rho_2 C p_2 (PD) \left[ \frac{dT}{d\theta} \right]_{RIB} + \frac{A_L}{A_2} \frac{k}{X} (T_2' - T_L) \quad (A-8)$$

Since  $Q/A_1 \approx Q/A_2$ ,

$$\rho_1 C p_1 L \left[ \frac{dT}{d\theta} \right]_{PLUG} = \rho_2 C p_2 (PD) \left[ \frac{dT}{d\theta} \right]_{RIB} + \frac{A_L}{A_2} \frac{k}{X} (T_2' - T_L) \quad (A-9)$$

The imposed requirement is that  $T_2' = T_1$  and  $\left[ \frac{dT}{d\theta} \right]_{PLUG} = \left[ \frac{dT}{d\theta} \right]_{RIB} = \frac{dT}{d\theta}$

Thus;

$$\rho_1 C p_1 L \frac{dT}{d\theta} = \rho_2 C p_2 (PD) \frac{dT}{d\theta} + \frac{A_L}{A_2} \frac{k}{X} (T_1 - T_L) \quad (A-10)$$

Since,

$$\rho_1 C p_1 = \rho_2 C p_2 \text{ and } \alpha = \frac{k}{\rho C p} \quad (A-11)$$

Rearranging,

$$L \frac{dT}{d\theta} = (PD) \frac{dT}{d\theta} + \frac{A_L}{A_2} \frac{\alpha}{X} (T_1 - T_L) \quad (A-12)$$

Or,

$$\frac{dT}{d\theta} = \frac{A_L}{A_2} \left( \frac{a}{X} \right) \frac{(T_1 - T_L)}{(L - PD)} \quad (A-13)$$

Since

$$A_L = \pi(D + 2 \text{ GAP}) (PD) \quad (A-14)$$

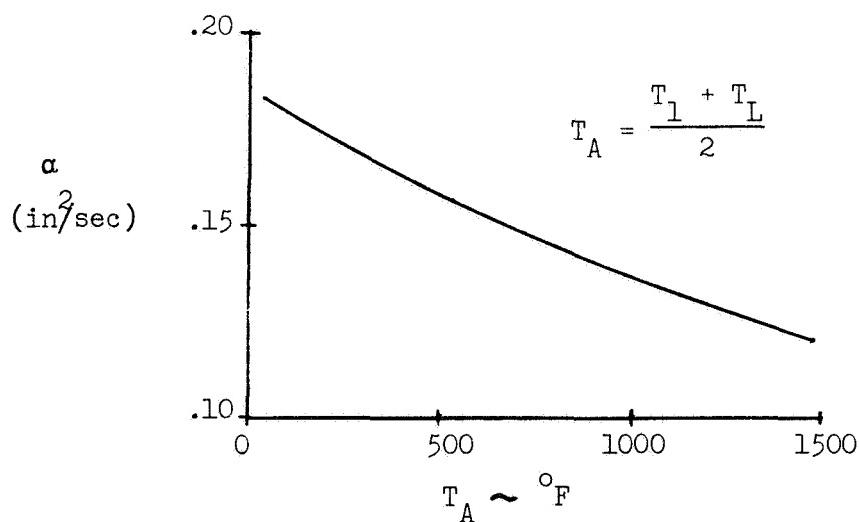
And

$$A_2 = \pi(D + \text{GAP}) (\text{GAP}) \quad (A-15)$$

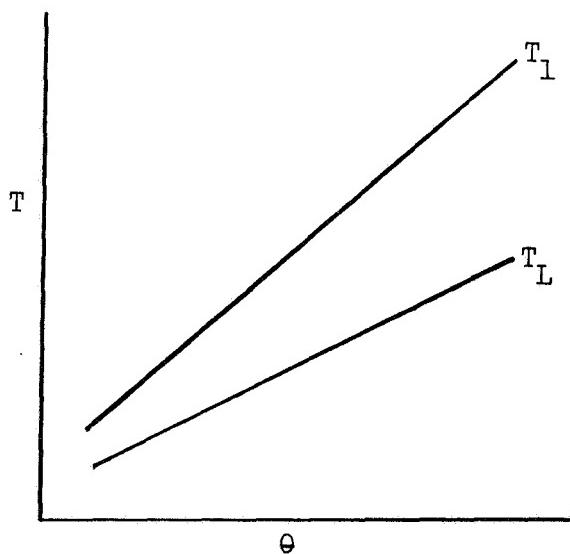
$$\frac{dT}{d\theta} = \frac{(D + 2 \text{ GAP}) (PD)}{(D + \text{GAP}) (\text{GAP})} \frac{a}{X} \left( \frac{T_1 - T_L}{L - PD} \right) \quad (A-16)$$

Rearranging,

$$\frac{\text{GAP} (X) (L - PD) (D + \text{GAP})}{PD (D + 2 \text{ GAP})} = \frac{a(T_1 - T_L)}{\left[ \frac{dT}{d\theta} \right]} \quad (A-17)$$



For small plug calorimeters  $\frac{dT}{d\theta} = \text{constant}$ ; for copper,  $\alpha$  varies as shown in Figure A-17. Therefore,  $(T_1 - T_L)$  must be an increasing quantity as shown in Figure A-18, in order for a set plug and rib configuration (GAP, L, D, PD, X) to be valid and provide an accurate calorimeter device. It should be noted that the curve of  $T_1$  and  $T_L$  is a true indication of the temperature behavior of the plug and its surrounding material as was borne out by the thermal analysis covered by this report. However, the interdependence of  $T_1$  and  $T_L$ , due to 2-D conduction effects and variable input heat flux axially along the wall, obviously cannot be accurately dealt with in a closed form approximate solution.



## NOMENCLATURE

$\theta$	time
$T_L$	average temperature of the surrounding material at distance X from the rib
$T_1$	plug base mean temperature
$T_2'$	rib mean temperature
Q/A	heat flux
Q	heat rate
L	plug length
PD	rib proximity dimension
GAP	rib radial thickness
X	distance from mid-rib to $T_L$
D	plug diameter
VOL	volume of material
$A_L$	area through which heat is lost from $T_2$ to $T_L$
$A_1$	plug input heating area
$A_2$	annular rib heating area
$\frac{dT}{d\theta}$	time rate of change of temperature
$\rho$	material density
Cp	material specific heat
k	material thermal conductivity
a	material thermal diffusivity

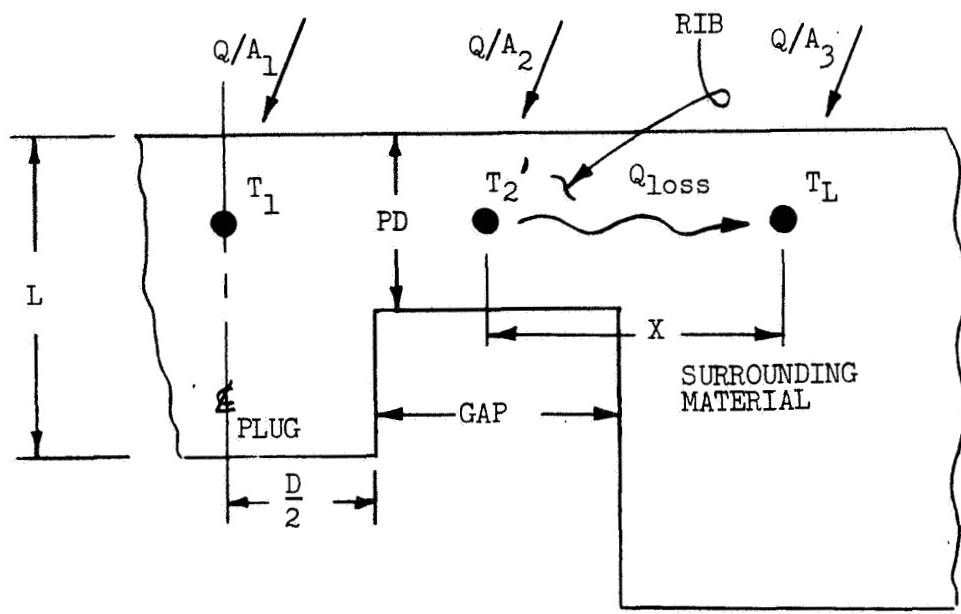


Figure A-1. Reference Heat Transfer Model of  
Calorimetric Plug

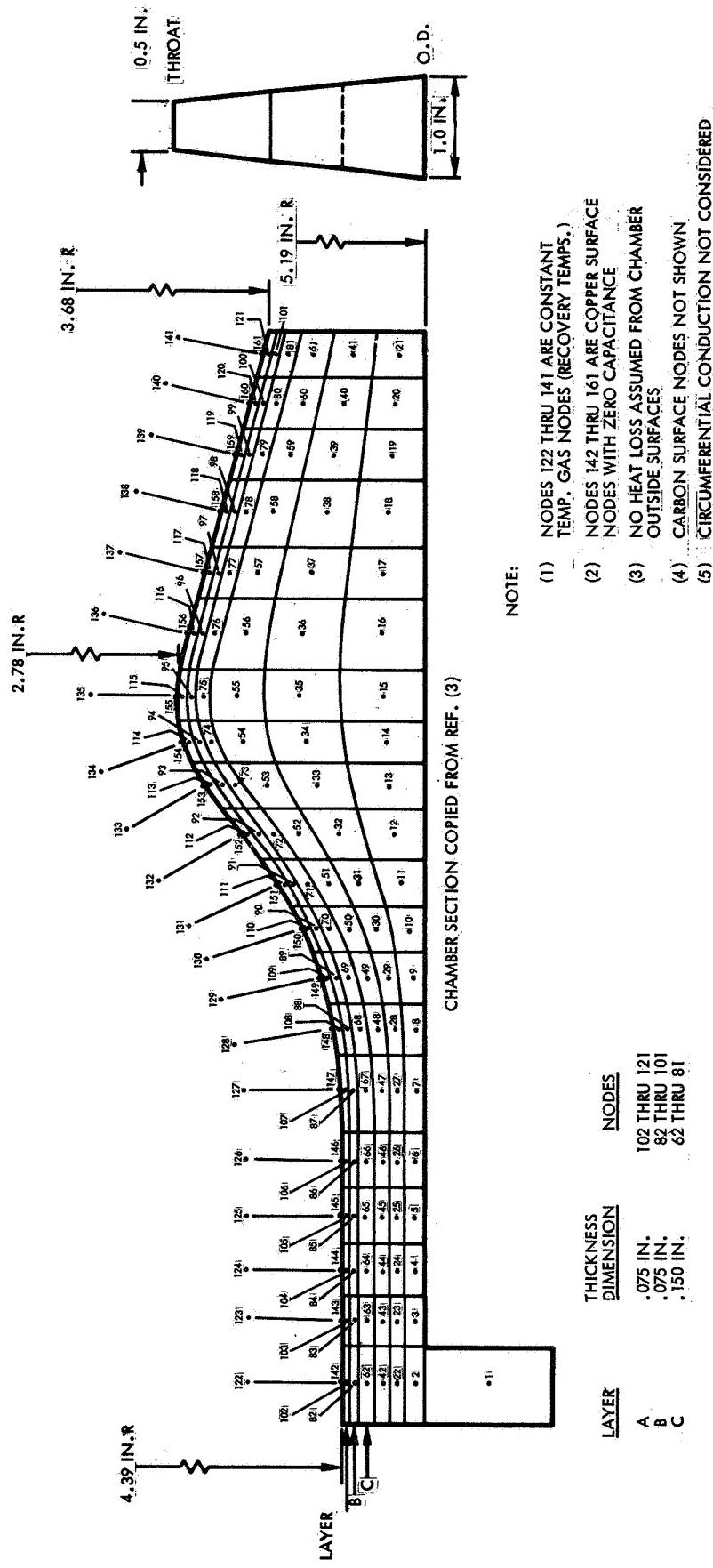


Figure A-2. General Thermal Model of the Thrust Chamber

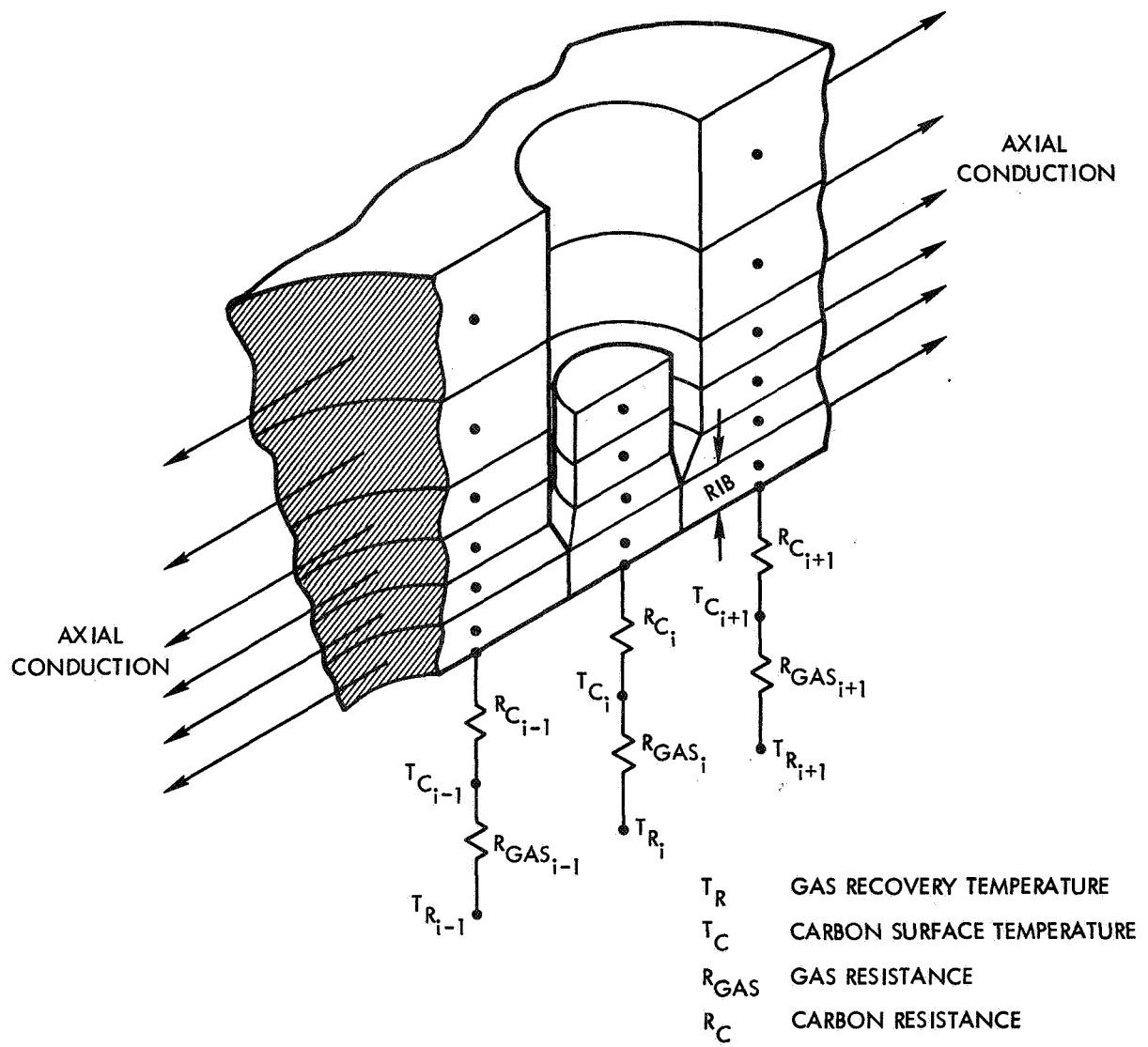


Figure A-3. Detailed Thermal Model of Calorimetric Plug Location

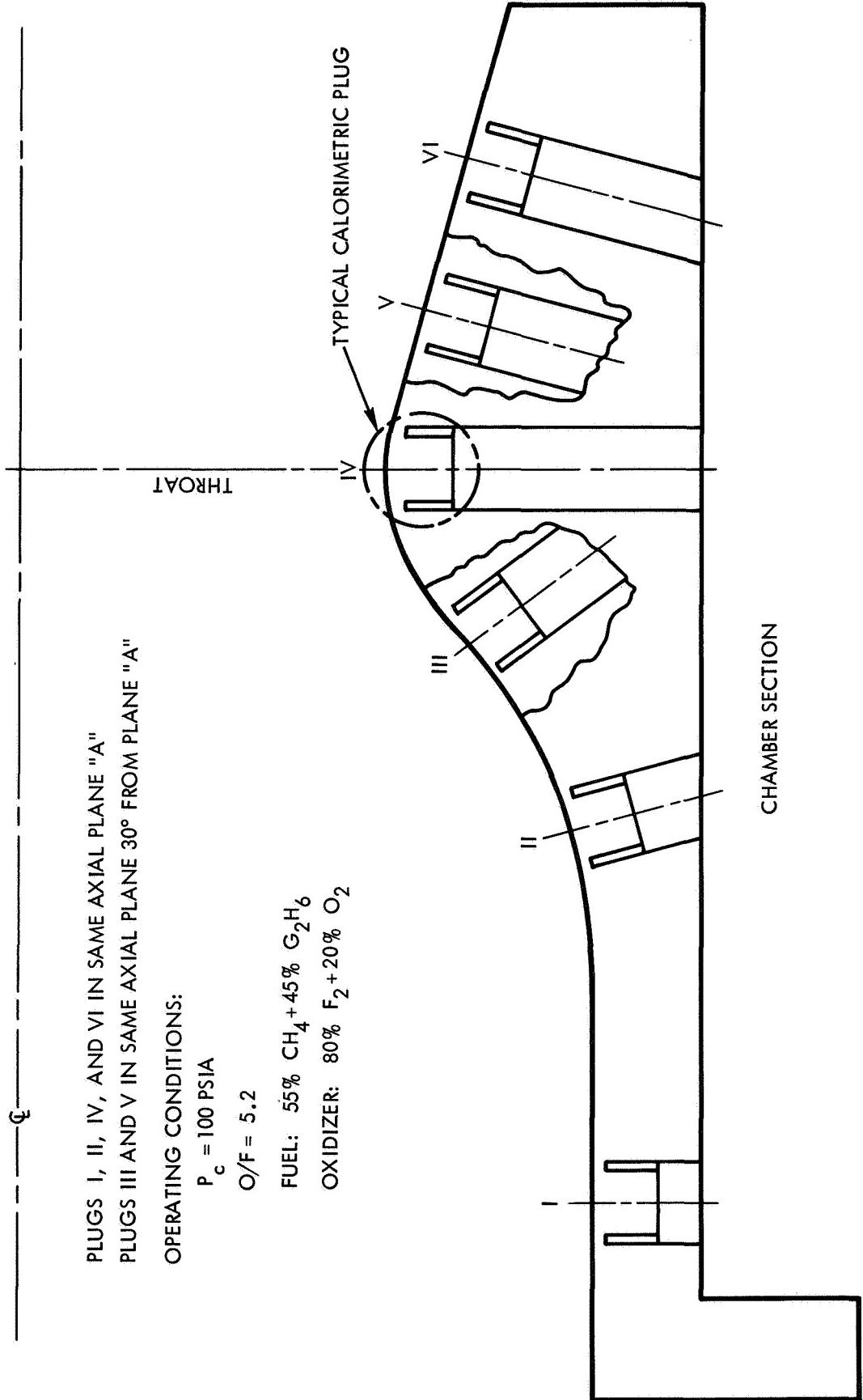


Figure A-4. General Layout of a Chamber Throat Section

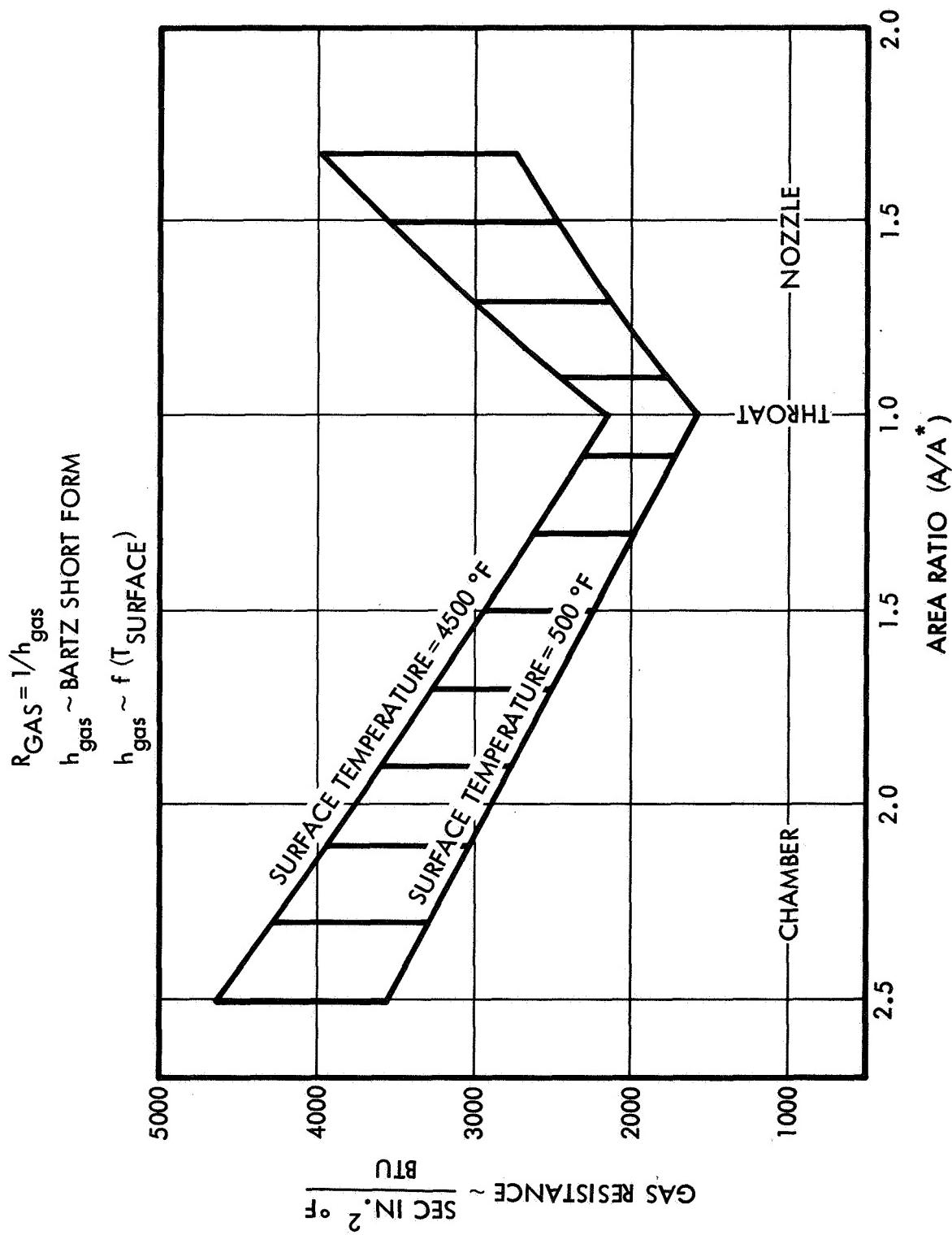


Figure A-5. Combustion Gas Resistance as a Function of Area Ratio

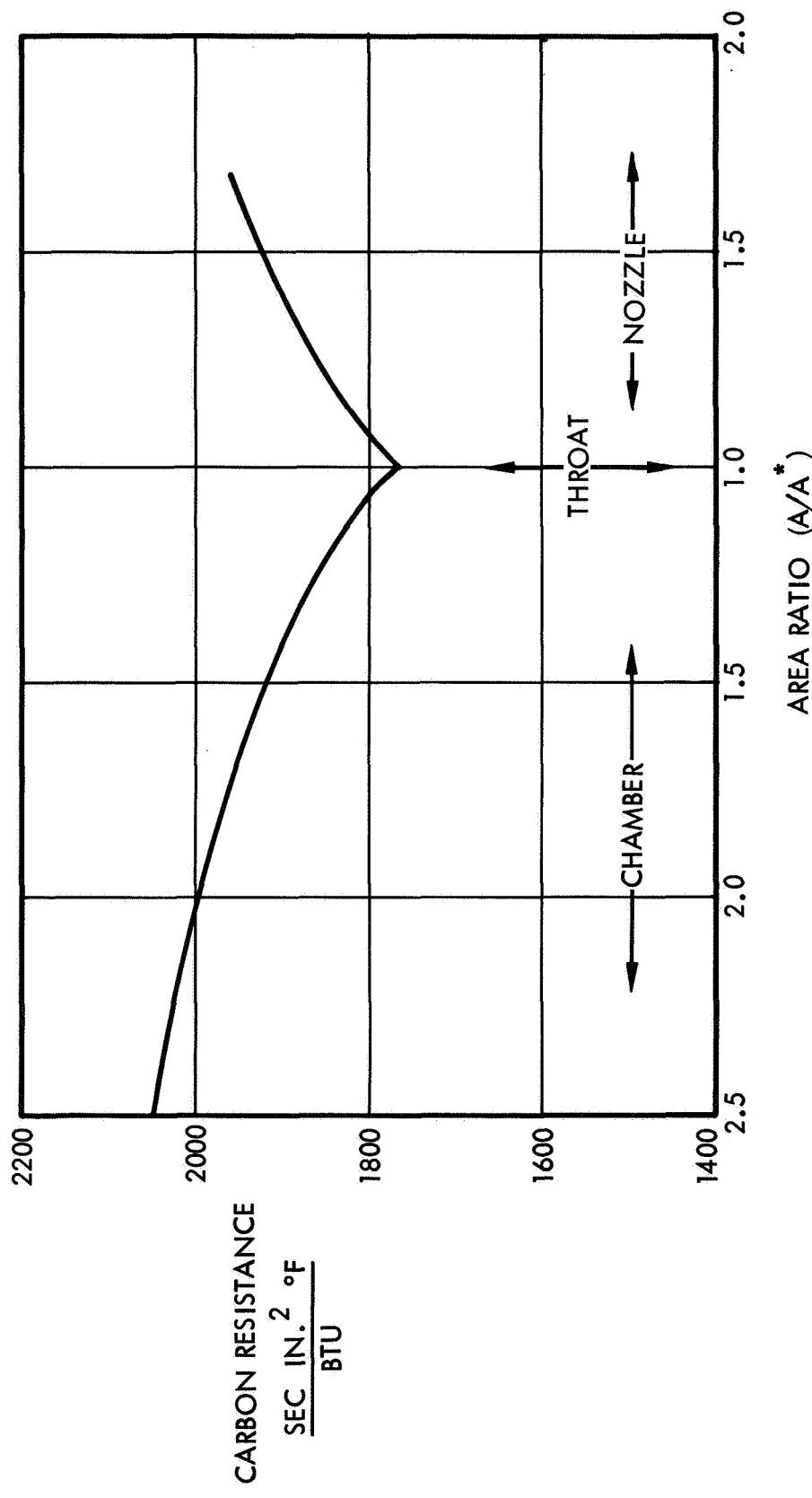


Figure A-6. Carbon Resistance as a Function of Area Ratio

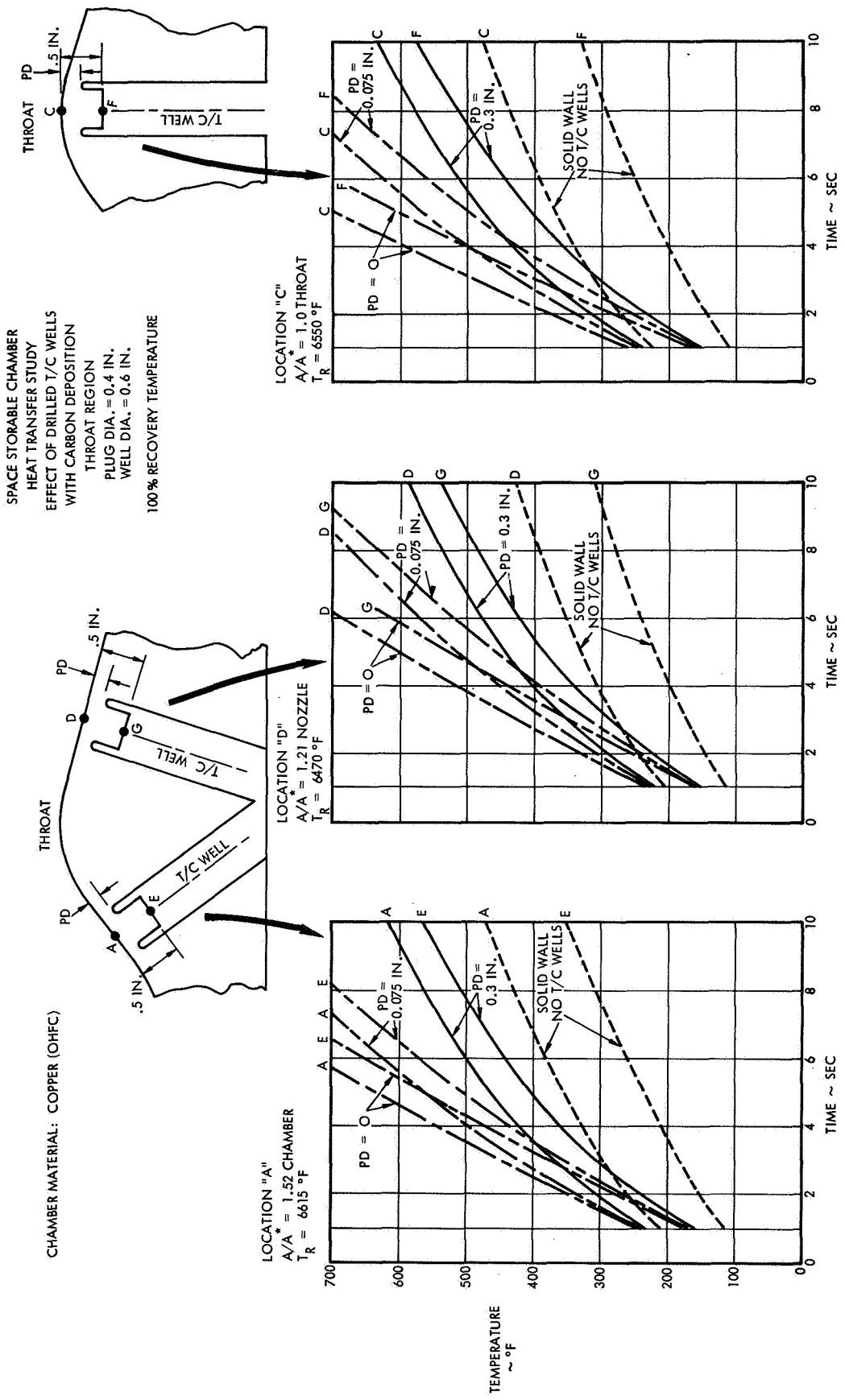


Figure A-7. Variations of Transient Temperature Profiles

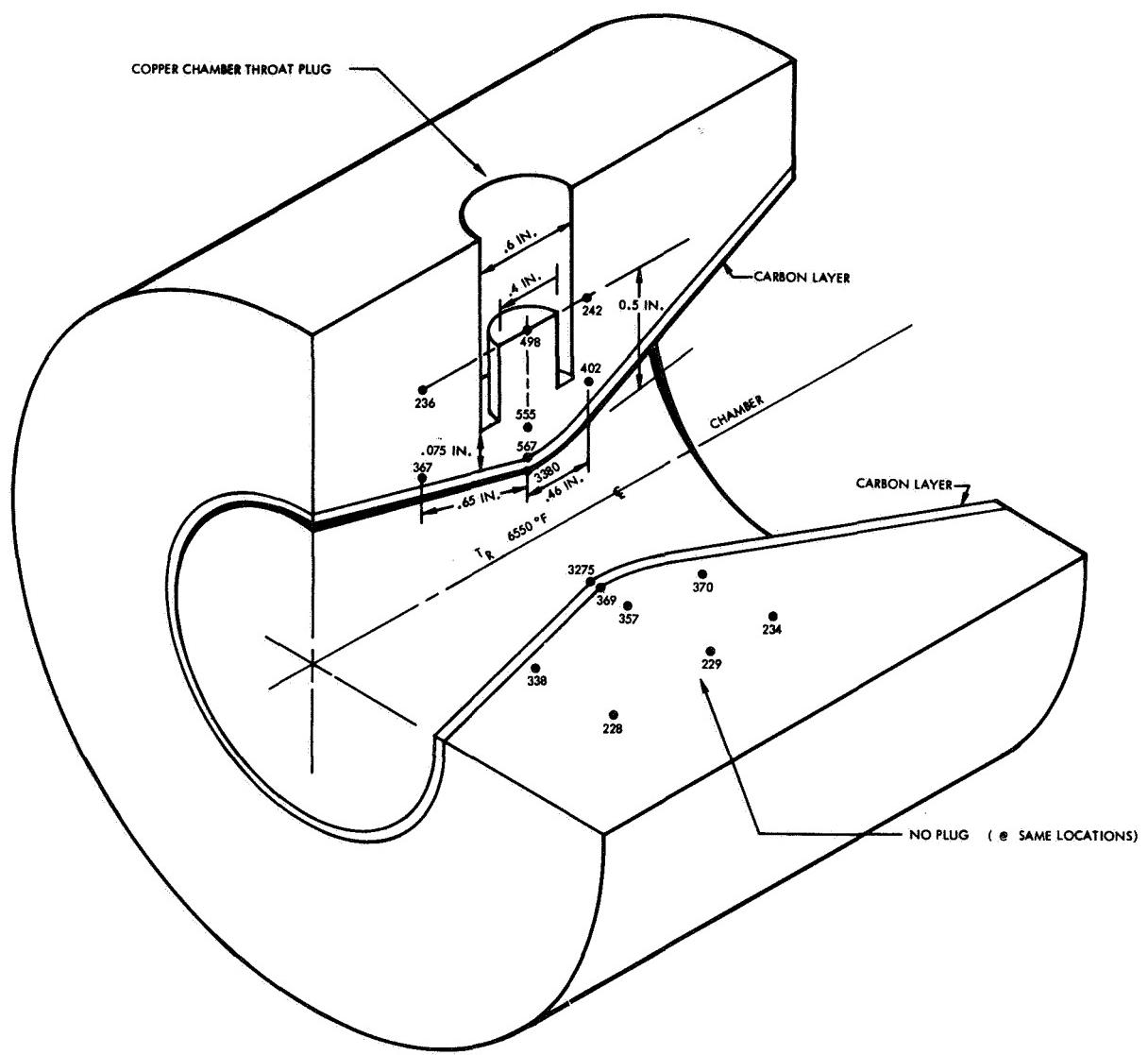


Figure A-8. Temperature Distribution Around a Throat Plug After 5 Seconds

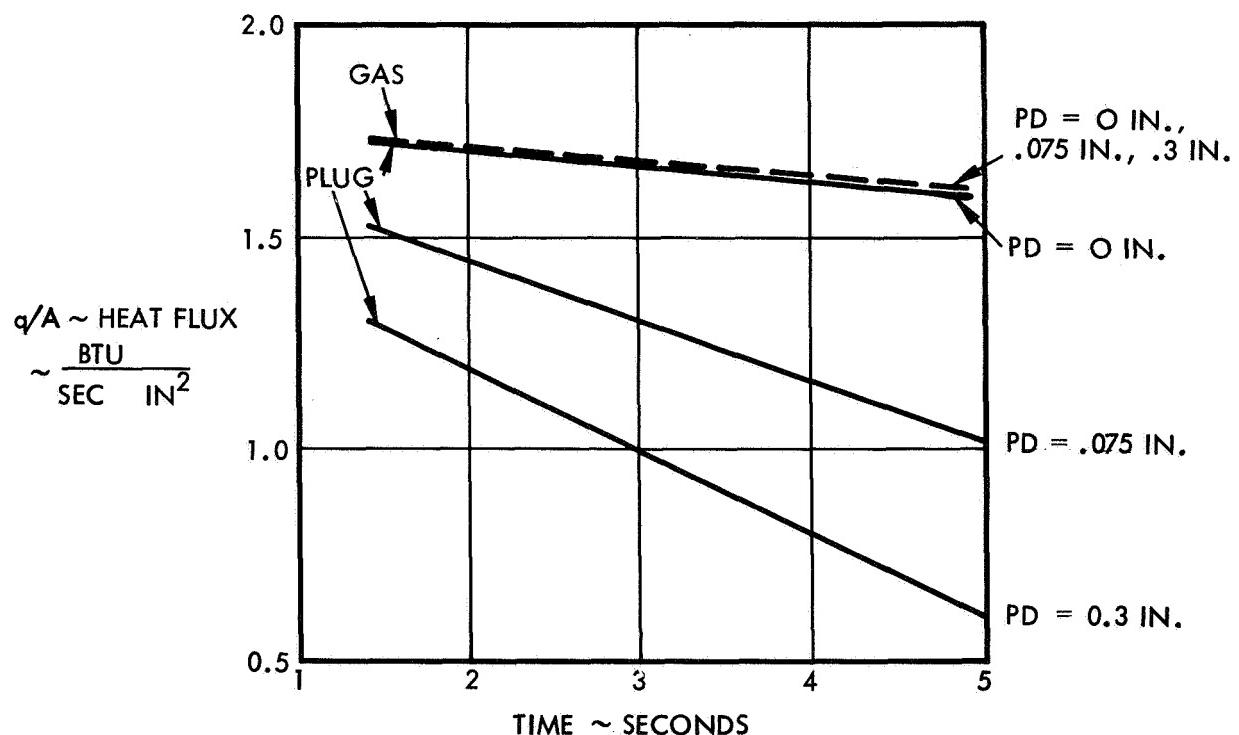
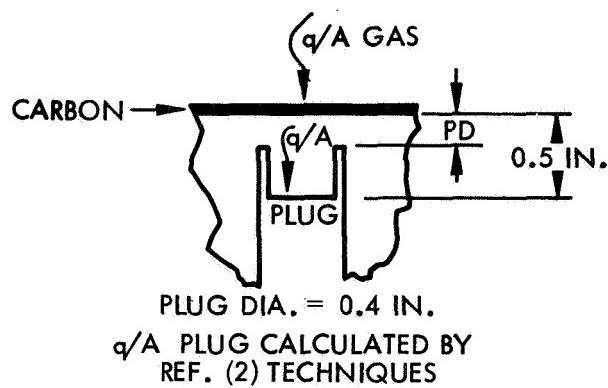


Figure A-9. Heat Flux as a Function of Time for Calorimetric Plug

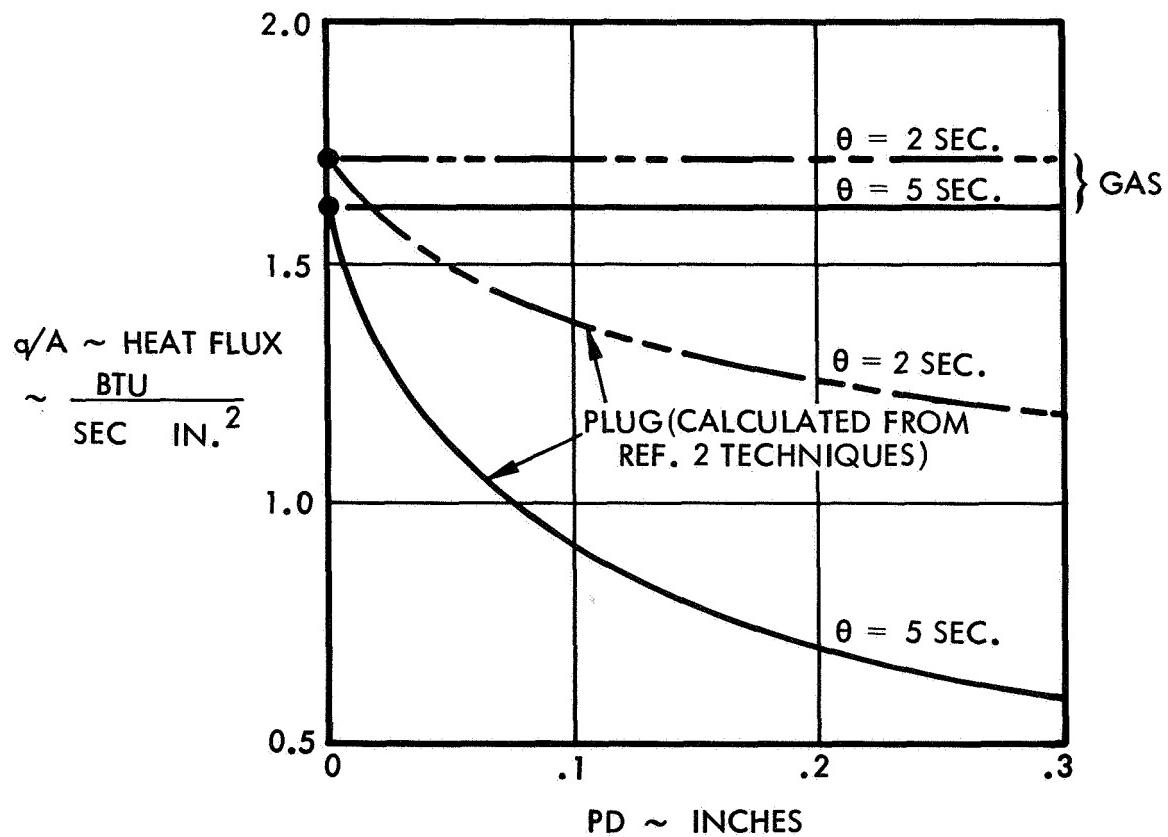
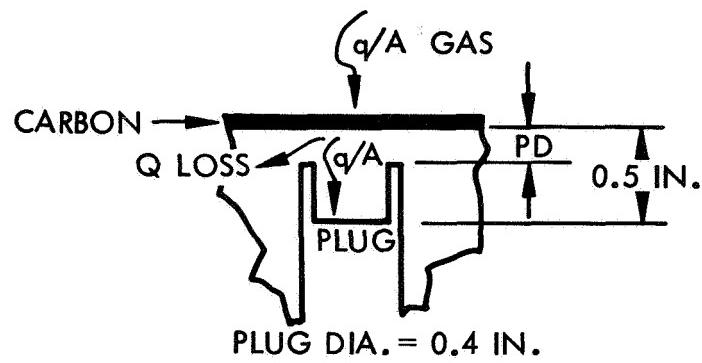
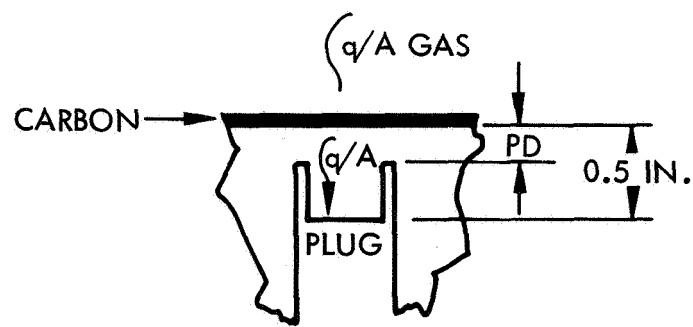


Figure A-10. Heat Flux as a Function of Calorimetric Plug Web Thickness



$\theta$  - TRANSIENT RUN TIME  
PLUG DIA. = 0.4 IN.

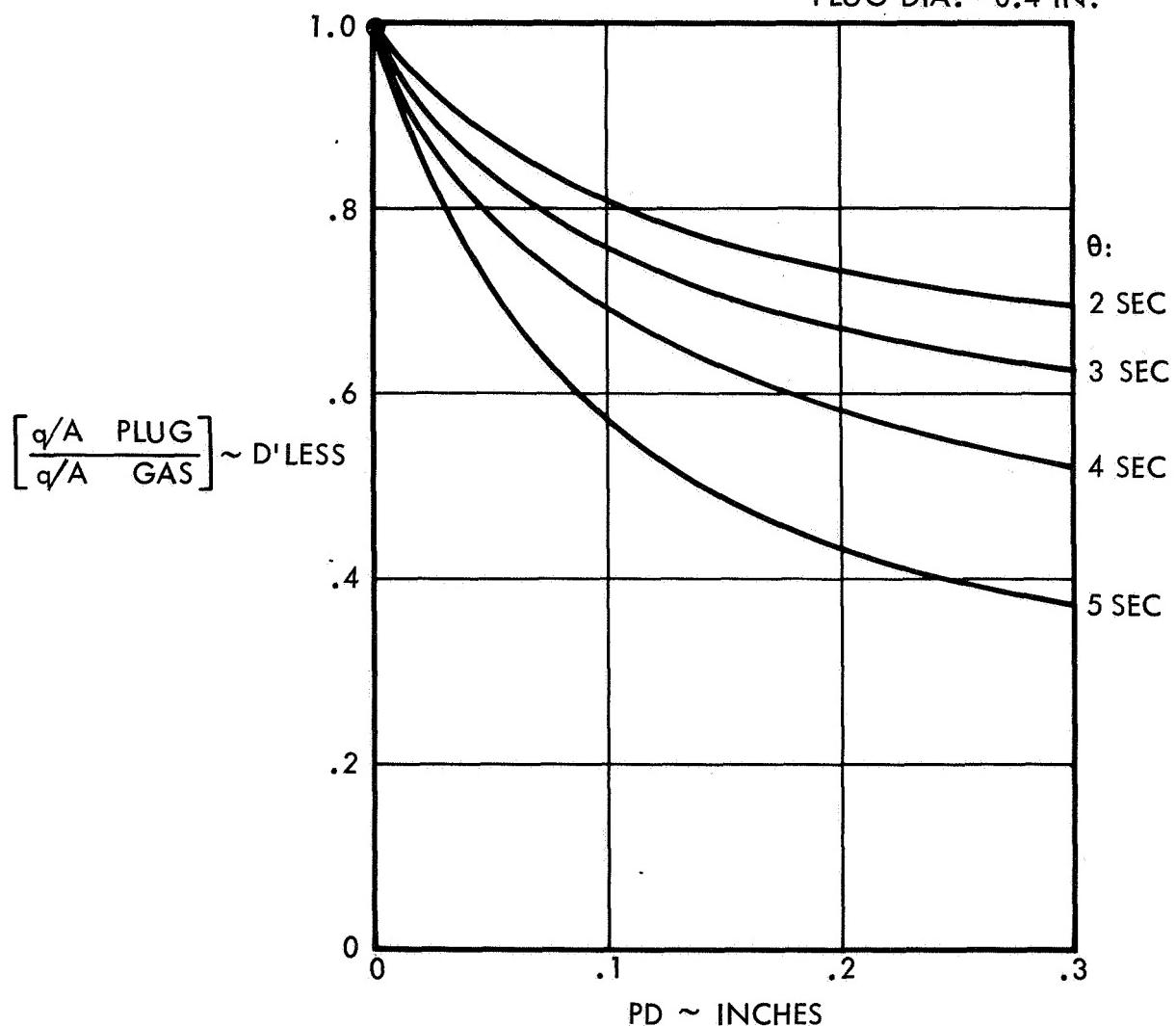


Figure A-11. Ratio of Measured Heat Flux to Gas Side Input as a Function of Calorimetric Plug Web Thickness

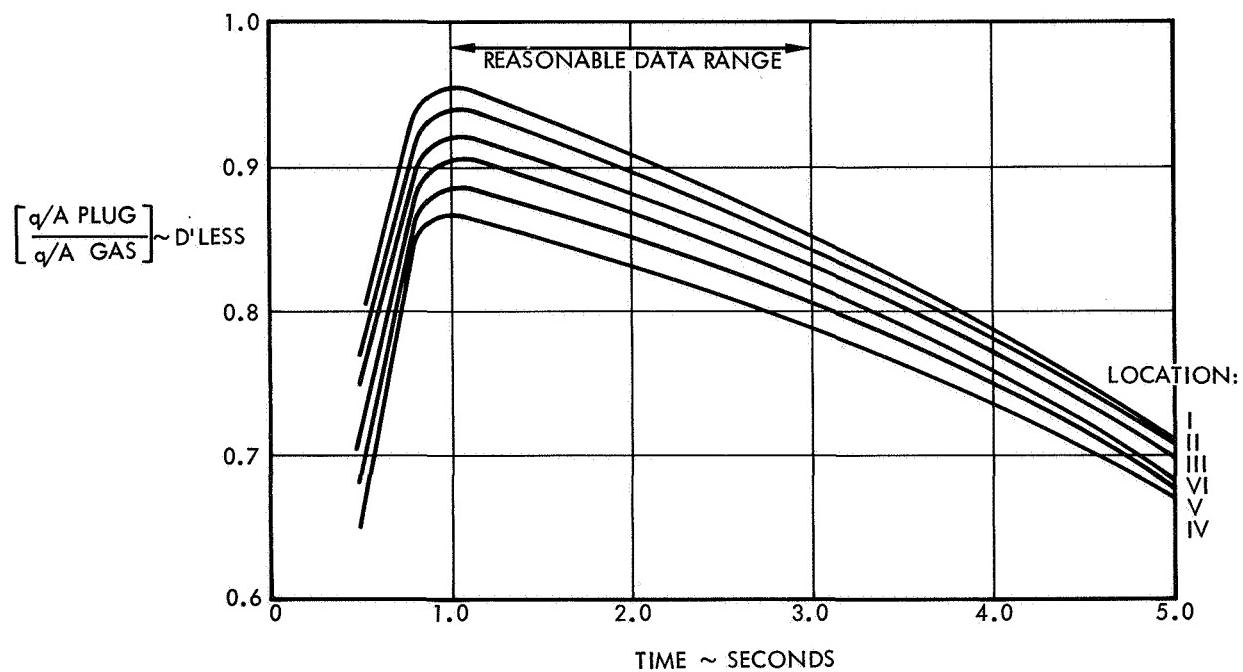
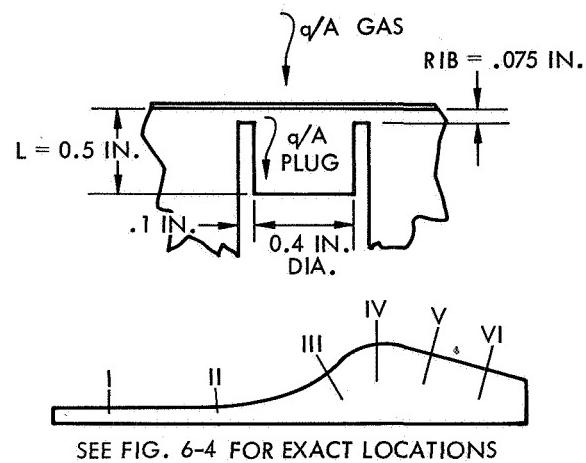


Figure A-12. Heat Flux Correction Curves for all Calorimetric Plugs

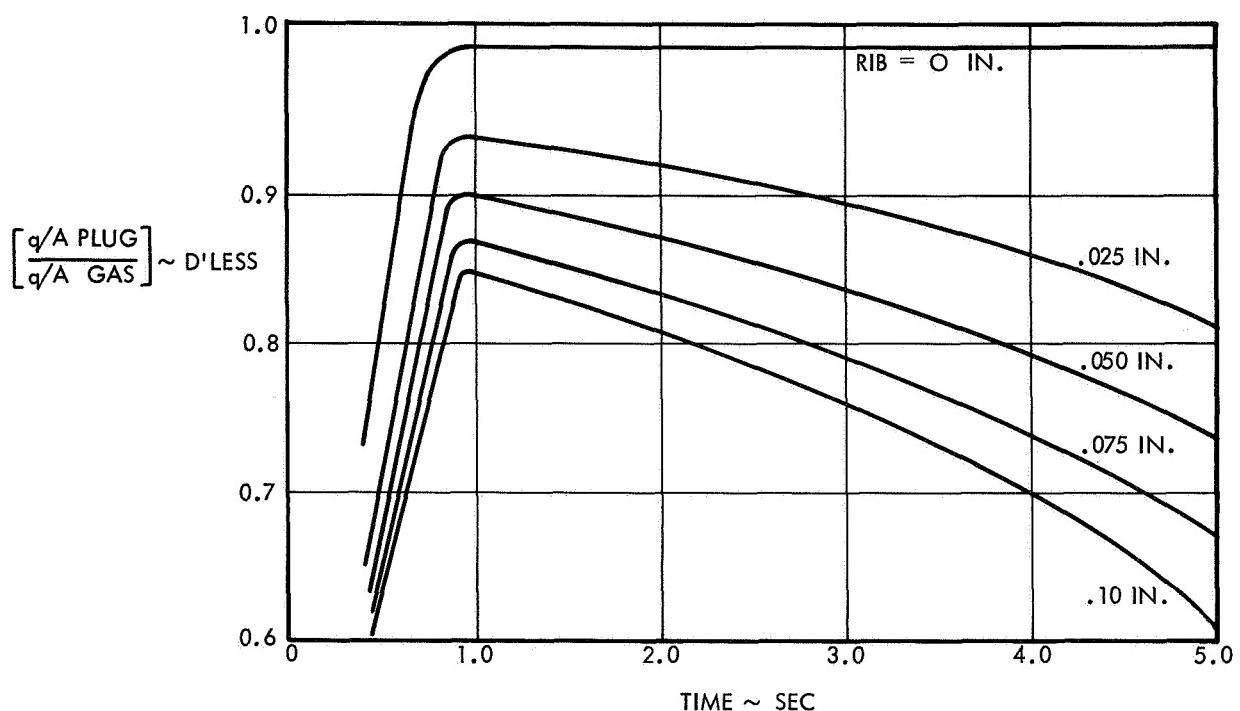
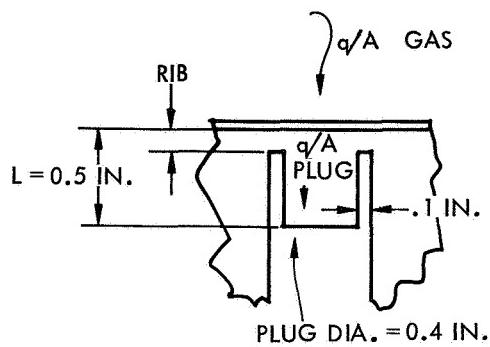


Figure A-13. Calorimetric Plug Rib Thickness as a Function of Heat Flux Correction Factor

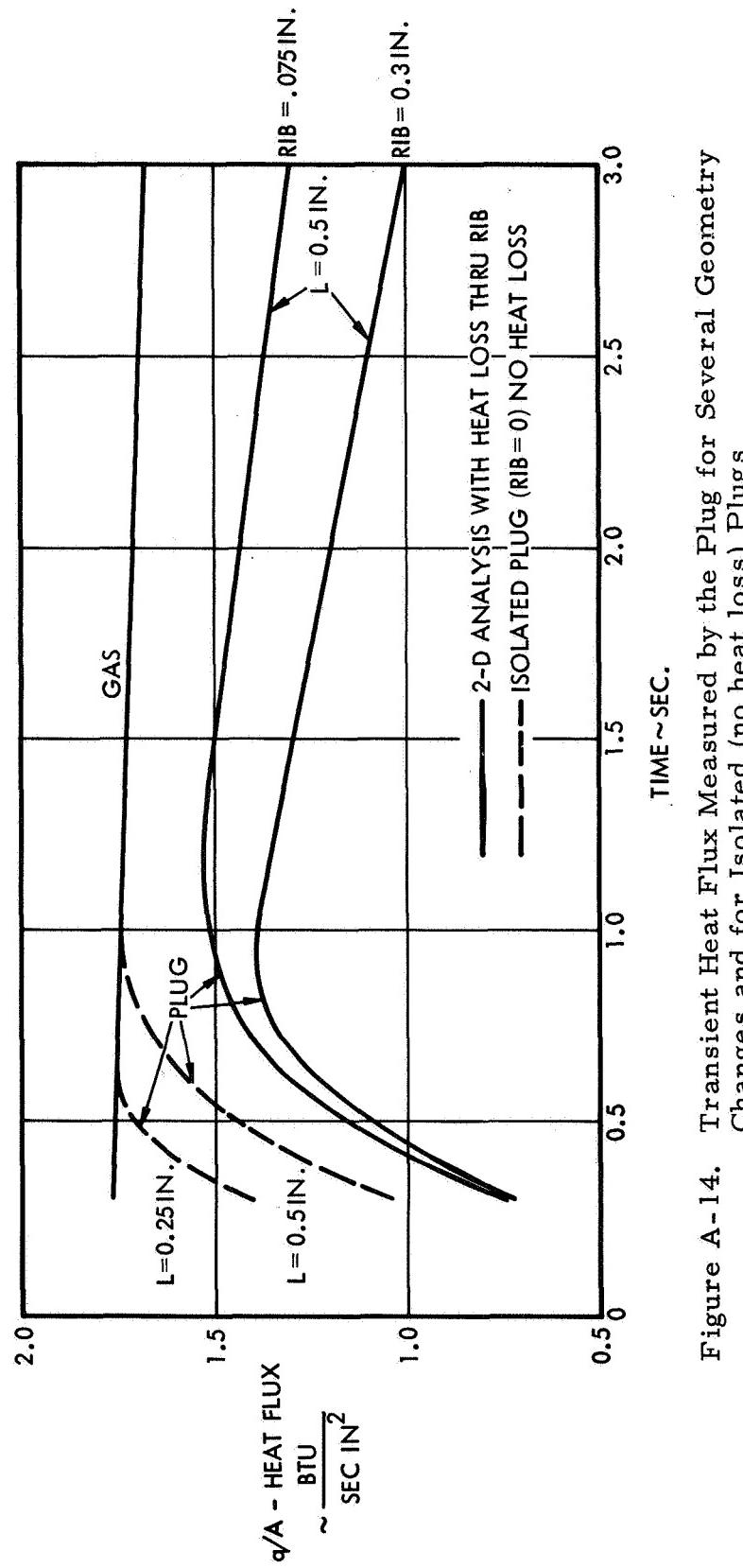
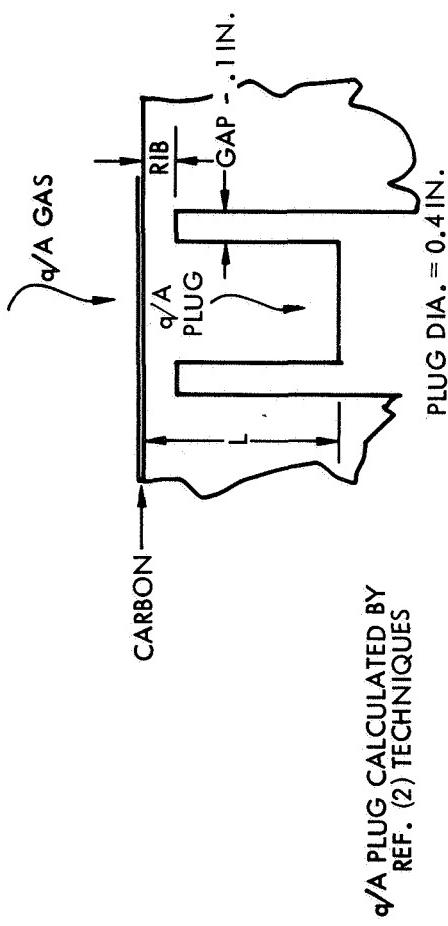


Figure A-14. Transient Heat Flux Measured by the Plug for Several Geometry Changes and for Isolated (no heat loss) Plugs

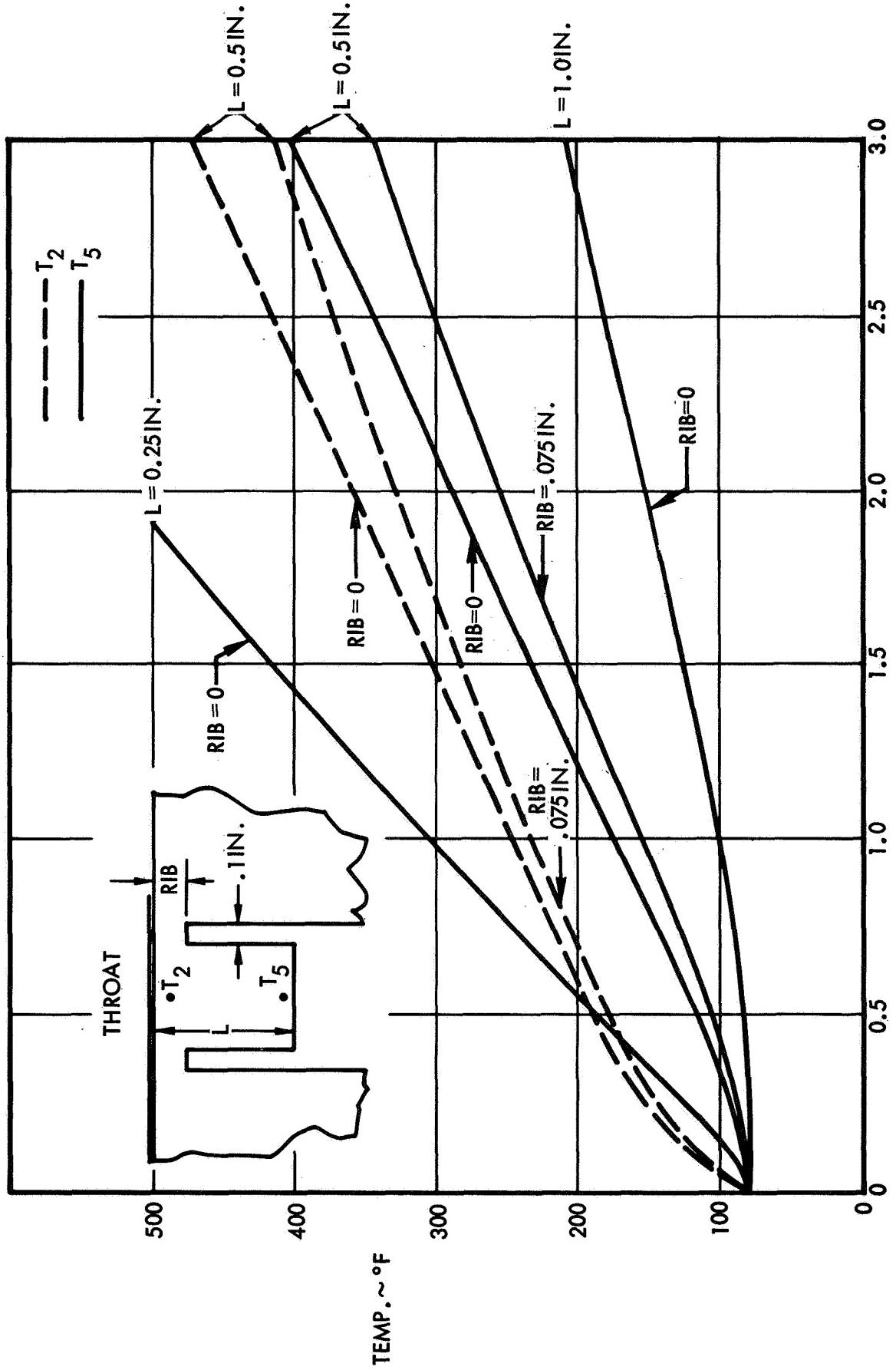


Figure A-15. Plug Base and Plug Cold Side Transient Temperatures for Several Geometry Changes and Isolated Plugs

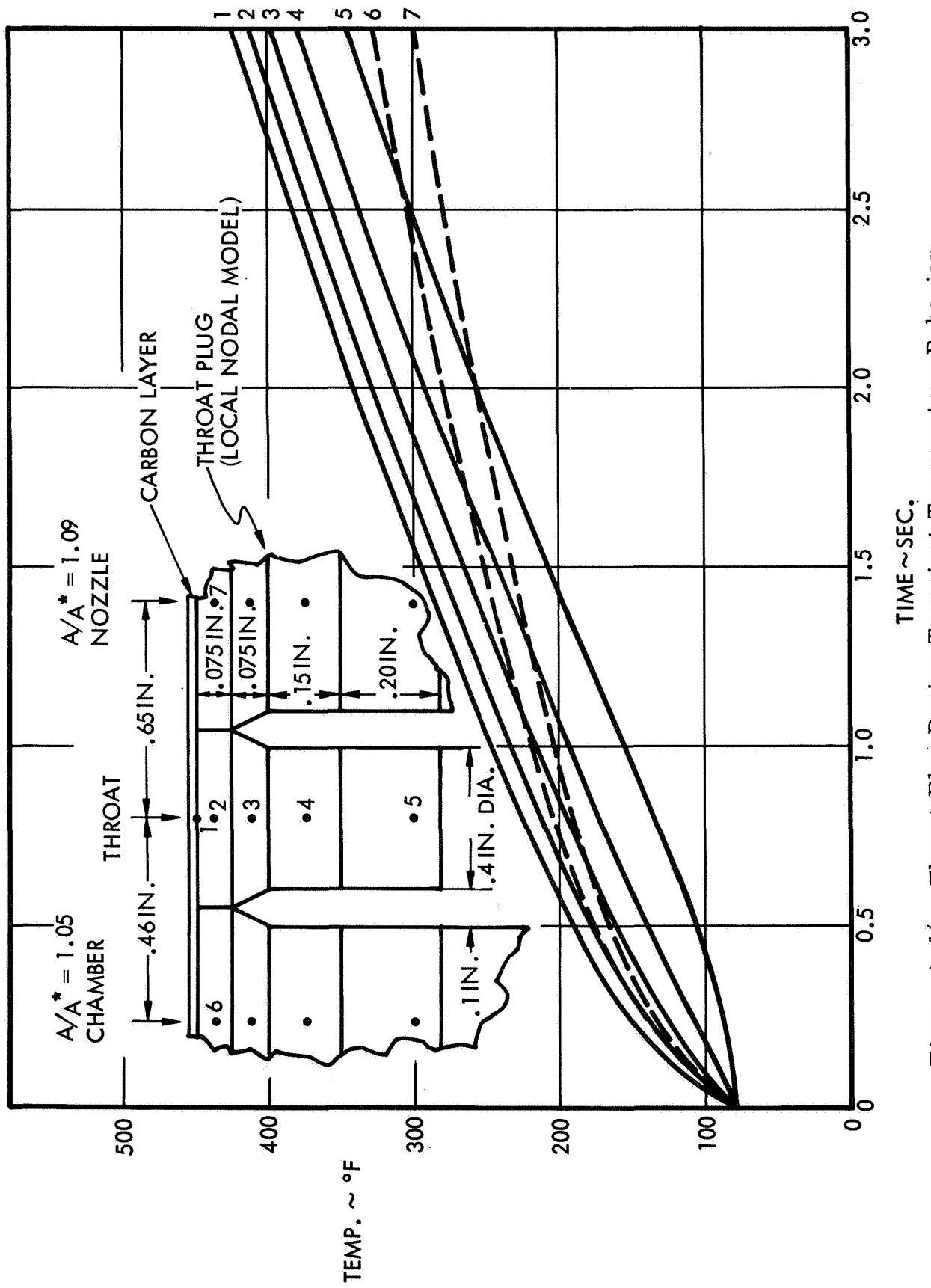


Figure A-16. Throat Plug Design Transient Temperature Behavior

## APPENDIX B

### CALCULATION OF CHARACTERISTIC VELOCITY EFFICIENCY

The index of injector performance used in the experimental program was the corrected characteristic velocity,  $C^*$ , efficiency. This parameter was calculated by two independent methods, one based on measurement of chamber pressure and the other on measurement of thrust. Details of the computational procedures and of the applied corrections are given in the following sections. The procedures and nomenclature format are essentially those developed in NASA sponsored programs at Rocketdyne.

#### 1. CHAMBER PRESSURE TECHNIQUE

Characteristic velocity efficiency based on chamber pressure is defined by:

$$\eta_{C^*} = \frac{(P_c)_o (A_t)_{\text{eff}} g_c}{(\dot{w}_T) (C^*)_{\text{theo}}} \quad (\text{B-1})$$

where

$(P_c)_o$  = stagnation pressure at the throat

$(A_t)_{\text{eff}}$  = effective thermodynamic throat area

$g_c$  = conversion factor ( $32.174 \text{ lbm-ft/lbf-sec}^2$ )

$\dot{w}_T$  = total propellant weight flow rate

$(C^*)_{\text{theo}}$  = theoretical characteristic velocity based on shifting equilibrium

Values calculated from Equation (B-1) are referred to as "corrected"  $C^*$  efficiencies, because the factors involved are obtained by application of suitable influence factor corrections to measured parameters. Stagnation pressure at the throat is obtained from measured static pressure at start of nozzle convergence by assumption of isentropic expansion; effective throat area is estimated from measured geometric area by allowing for geometrical radius changes during firing and for nonunity discharge coefficient; and chamber pressure is corrected to allow for energy losses

from combustion gases to the chamber wall by heat transfer and friction. Equation (B-2) may therefore be written as:

$$\eta_{\dot{C}^*} = \frac{P_c A_t g_c f_p f_{TR} f_{DIS} f_{FR} f_{HL} f_{KE}}{(\dot{w}_o + \dot{w}_f) (\dot{C}^*)_{theo}} \quad (B-2)$$

where

$P_c$  = measured static pressure at start of nozzle convergence, psia

$A_t$  = measured geometric throat area, in<sup>2</sup>

$g_c$  = conversion factor (32.174 lbm-ft/lbf-sec<sup>2</sup>)

$\dot{w}_o$  = oxidizer weight flow rate, lb/sec

$\dot{w}_f$  = fuel weight flow rate, lb/sec

$(\dot{C}^*)_{theo}$  = theoretical C\* based on shifting equilibrium calculations, ft/sec

$f_p$  = influence factor correcting observed static pressure to throat stagnation pressure

$f_{TR}$  = influence factor correcting for change in throat radius during firing

$f_{DIS}$  = influence factor correcting throat area for effective discharge coefficient

$f_{FR}$  = influence factor correcting measured chamber pressure for frictional drag of combustion gases at chamber wall

$f_{HL}$  = influence factor correcting measured chamber pressure for heat losses from combustion gases to chamber wall

$f_{KE}$  = influence factor correcting C\* values to account for finite chemical reaction rates

Methods of estimation of the various correction factors are described in the following paragraphs.

### 1.1 Pressure Influence Factor

Measured static pressure at start of nozzle convergence is converted to stagnation pressure at the throat by assumption of effectively no combustion in the nozzle and application of the isentropic flow equations,

with contraction ratio ( $A_c/A_t$ ) and shifting-equilibrium specific heat ratios ( $\gamma$ ). Frozen-equilibrium specific heat ratios usually make the influence correction factor about 1/2 percent larger. Hence, the value employed with shifting-equilibrium is the more conservative. The correction for this program and selected contraction ratios are given in Figure B-1.

### 1.2 Throat Radius Influence Factor ( $f_{TR}$ )

Temperature gradients produced in the solid metal nozzle wall result in thermal stresses which affect throat radius, with the result that the geometric throat diameter ambient measurement is not the same as that which exists during firing.

For the types of nozzles considered here, thermal penetration of the nozzle wall at the initiation of firing is small with respect to the wall thickness, hence the outer wall diameter is unchanged. The inner wall material will therefore expand toward the center, resulting in a decrease in throat diameter. As heat penetrates throughout the nozzle wall, the outer diameter will also increase, allowing outward expansion of the inner portion and consequent increase in throat diameter. Therefore, throat diameter during firing is a function of time, as well as of the physical properties of the throat material and the temperature and pressure of the combustion gases.

The actual computation is based upon integration of transient thermal stress equations for a hollow cylinder. A relatively simple expression results by assuming parabolic temperature distribution.

#### 1.2.1 Thermal Effects

Since performance is influenced also by throat area changes, attention should be directed primarily to this zone of the thruster. With monomaterial construction, the throat effects can be analyzed with reasonable accuracy. It can be shown that throat shrinkage and expansion effects for such nozzles can be estimated from the following for parabolic temperature distributions:

$$dr = \alpha \left[ \frac{1+\nu}{1-\nu} \right] \frac{T_i - T_o}{(R_o - R_i)^2} \left[ \frac{R_o^2 R_i}{2} - \frac{2}{3} R_o R_i^2 + \frac{R_i^3}{4} - \frac{R_o^4}{12 R_i} \right] \quad (B-3)$$

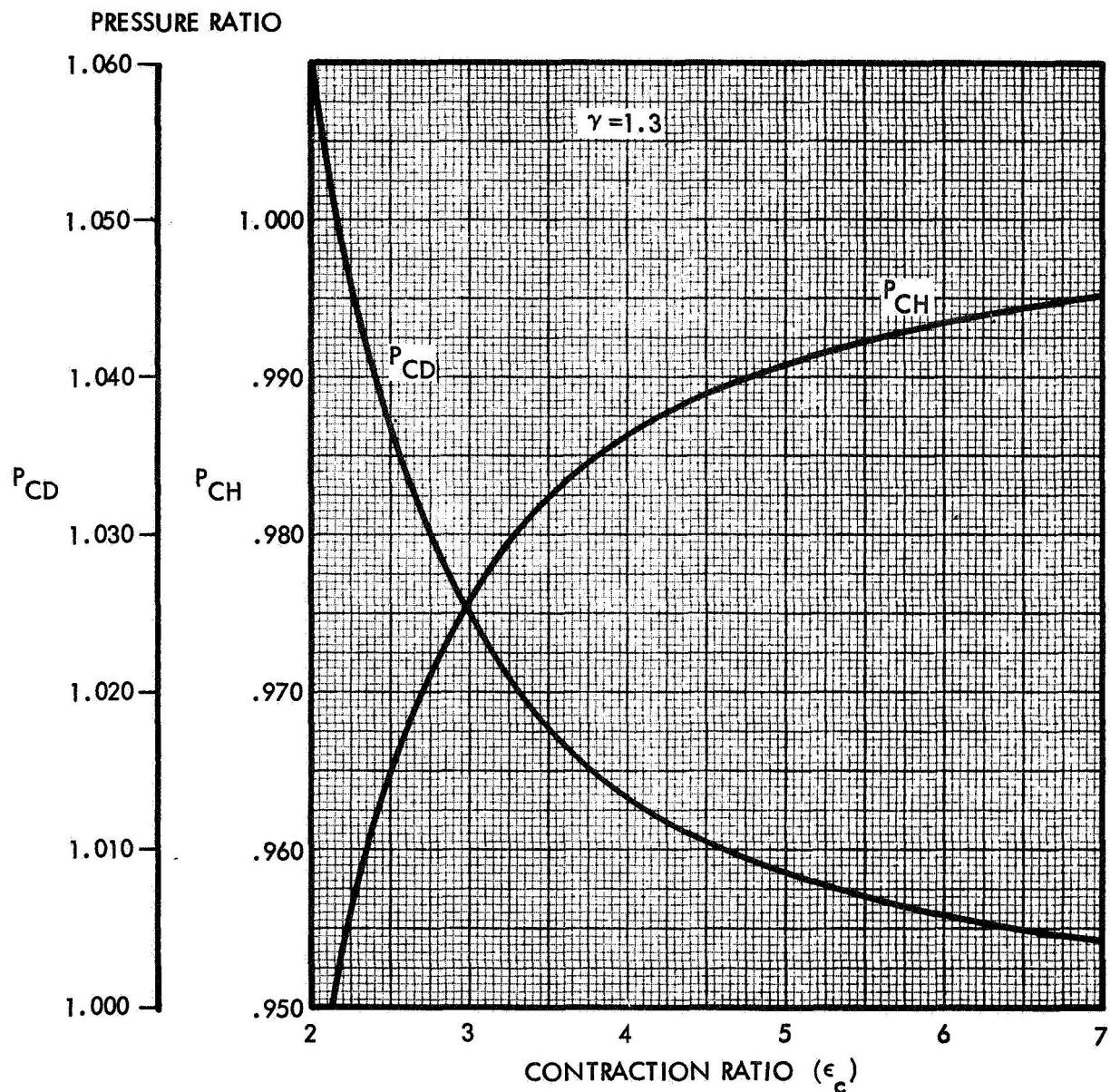


Figure B-1. Momentum Correction

where

$R_i$  = inner wall radius

$R_o$  = outer wall radius

$\alpha$  = coefficient of linear expansion of wall material

$\nu$  = Poisson's ratio of wall material

$T_i$  = temperature of inner wall

$T_o$  = temperature of outer wall

The temperature distribution is given by

$$T = a + br + cr^2 \quad (B-4)$$

and is estimated by the method of Reference B-1. The throat shrinkage effects manifest themselves at the initiation of firing. For long steady-state firings, the throat size may actually increase, depending upon the temperature distribution and resultant stresses. Plastic as well as elastic deformations are readily included, as well as gas pressure effects.

### 1.3 Throat Discharge Coefficient Influence Factor ( $f_{DIS}$ )

The discharge coefficient is defined as the ratio of actual flow rate through the throat to the theoretical maximum, based on geometric throat area and ideal, uniform, one-dimensional flow with no boundary layer. The discharge influence coefficient may be estimated in two ways: one based on calculations made from a theoretical, inviscid flow model of combustion products, and the other based on a correlation of results obtained in various experimental study results of air flow through nozzles of similar geometry.

#### 1.3.1 Theoretical Model

Total mass flow rate is given by

$$\dot{m} = \int_0^A \rho V dA \quad (B-5)$$

where

$\rho$  = gas density  
 $V$  = gas velocity  
 $A$  = cross-sectional area

Theoretical maximum flow rate at the throat is

$$\dot{m}_{\max} = \int_0^{A_t} \rho * V * dA \quad (B-6)$$

where

$A_t$  = geometric area of the throat  
 $\rho^*$  = sonic gas density  
 $V^*$  = sonic gas velocity

For ideal, uniform, parallel flow, Equation (B-6) becomes

$$\dot{m}_{\max} = \rho^* V^* A_t \quad (B-7)$$

The discharge coefficient is then

$$C_D = \frac{\dot{m}}{\dot{m}_{\max}} = \int_0^A \left( \frac{\rho}{\rho^*} \right) \left( \frac{V}{V^*} \right) \left( \frac{dA}{A_t} \right) \quad (B-8)$$

### 1.3.2 Empirical Value

Experimental conical nozzle discharge coefficients obtained with air by various investigators are plotted in Figure B-2 against the indicated geometric parameter. Data sources also are listed in Figure B-2.

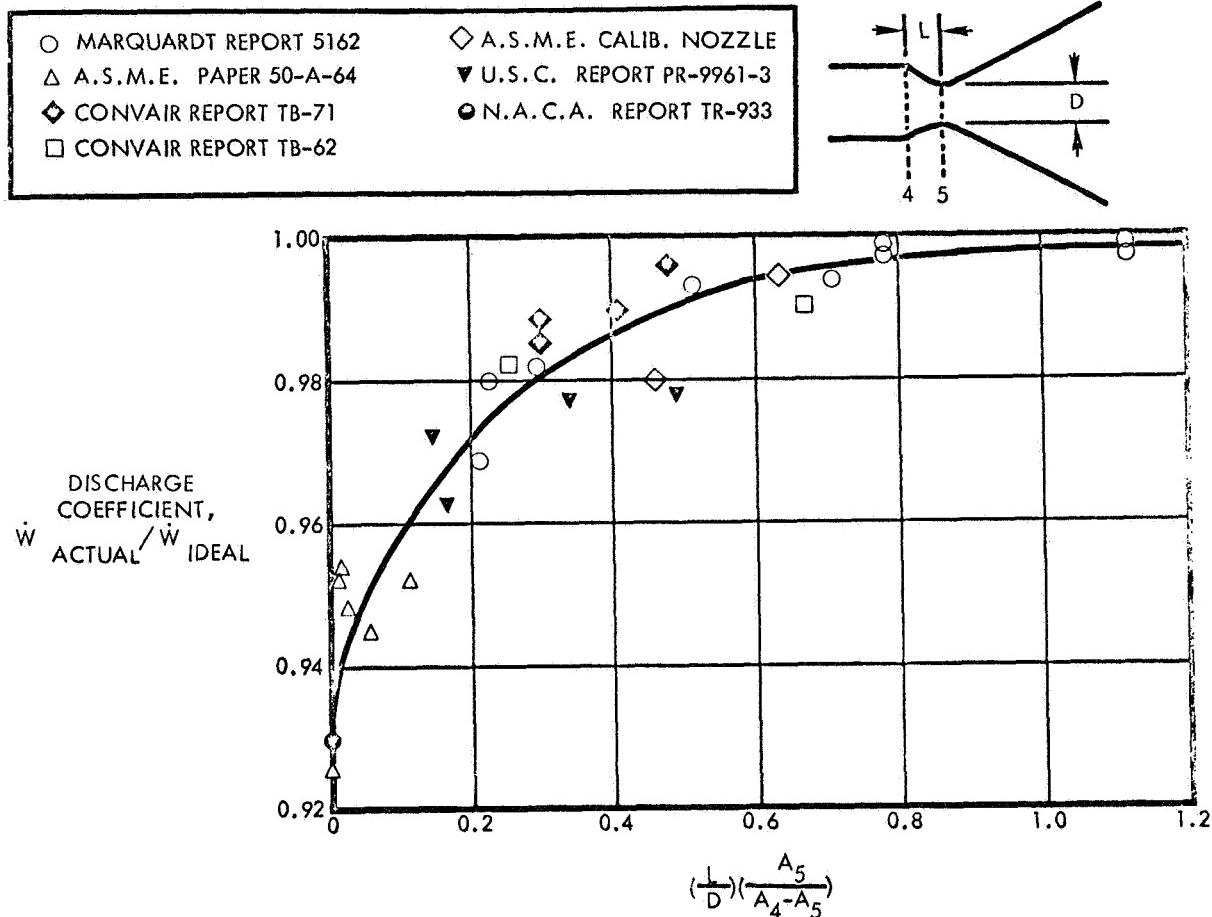


Figure B-2. Discharge Coefficient as Function of Nozzle Dimensions  
 $(A_4 = \text{cross-sectional area of chamber}, A_5 = \text{cross-sectional area of throat})$ . Data taken from indicated references, for cold flows with air

The values obtained by both methods are found to be in excellent agreement.

#### 1.4 Frictional Drag Influence Factor ( $f_{FR}$ )

Calculations of  $C^*$  based on chamber pressure are concerned with chamber phenomena up to the nozzle throat. Drag forces to this point are small enough to be considered negligible, so that the factor  $f_{FR}$  may be taken to be unit  $\mu$ .

## 1.5 Energy Loss Influence Factor ( $f_{HL}$ )

Chamber pressure and thrust are decreased by heat transfer from the combustion gases to the walls of a thrust chamber. This enthalpy loss is substantially reduced in ablative chambers and is effectively recovered in a regeneratively cooled chamber.

The effect on  $C^*$  of enthalpy loss by heat transfer can be estimated from a loss of chamber enthalpy. This is determined from a two station energy balance, one at the start of the nozzle convergence and the other at the throat which:

$$\frac{1}{2} V_c^2 + H_c = \frac{1}{2} V_t^2 + H_t + \dot{Q}_{conv} \quad (B-9)$$

where

$V_c$  = gas velocity at chamber exit

$V_t$  = gas velocity at nozzle throat

$H_c$  = gas enthalpy at chamber exit

$H_t$  = gas enthalpy at nozzle throat

$\ddot{Q}_{conv}$  = heat loss in nozzle convergence

Velocity at the throat is given by:

$$V_t = \left[ V_c^2 + 2(H_c - H_t - \dot{Q}_{conv}) \right]^{1/2} \quad (B-10)$$

With negligible nozzle inlet velocity

$$V_t = \left[ 2(H_c - H_t - \dot{Q}_{conv}) \right]^{1/2} \quad (B-11)$$

Logarithmic differentiation of Equation (B-11) gives

$$\frac{dV_t}{V_t} = 1/2 \frac{d(H_c - H_t - \dot{Q}_{conv})}{(H_c - H_t - \dot{Q}_{conv})} = 1/2 \left( \frac{dH_c - dH_t}{H_c - H_t - \dot{Q}_{conv}} \right) \quad (B-12)$$

Substitution of enthalpy definition into Equation (B-12) gives:

$$\frac{dV_t}{V_t} = 1/2 \left( \frac{c_{pc} dT_c - c_{pt} dT_t}{H_c - H_t - \dot{Q}_{conv}} \right) \quad (B-13)$$

With constant  $C_p$  between the two stations,

$$\frac{dV_t}{V_t} = 1/2 \left( \frac{c_p dT_c}{H_c - H_t - \dot{Q}_{conv}} \right) \left( 1 - \frac{dT_t}{dT_c} \right) \quad (B-14)$$

If the specific heat ratio,  $\gamma$ , is assumed constant,

$$\frac{dT_t}{dT_c} = \frac{T_t}{T_c} \quad (B-15)$$

Substituting Equation (B-15) into Equation (B-14), replacing differentials by incrementals, and noting that  $C^*$  is proportional to gas velocity at the throat gives:

$$\frac{\Delta V_t}{V_t} = \frac{\Delta C^*}{C^*} = 1/2 \left( \frac{c_p \Delta T_c}{H_c - H_t - \dot{Q}_{conv}} \right) \left( 1 - \frac{\Delta T_t}{T_c} \right) \quad (B-16)$$

Total heat loss to the chamber walls, in Btu per pound of propellant, is obtained by summation of observed heat fluxes over the appropriate areas:

$$\text{Heat loss} = \frac{\sum (q/A) A}{\dot{w}_T} \quad (B-17)$$

where

$q/A$  = experimentally observed heat flux

$A$  = area applicable to each  $q/A$  value

$\dot{w}_T$  = total propellant flow rate

If this heat loss is equated to the change in enthalpy of the gas in the combustion chamber,  $c_p \Delta T_c$ , then substitution in Equation (B-16) gives

$$\frac{\Delta C^*}{C} = 1/2 \left[ \frac{\sum(q/A)A}{\dot{w}_T} \right] \left[ \frac{1 - (T_t/T_c)}{H_c - H_t - \dot{Q}_{conv}} \right] \quad (B-18)$$

The applicable influence factor is

$$f_{HL} = 1 + \frac{\Delta C^*}{C^*} = 1 + 1/2 \left[ \frac{\sum(q/A)A}{\dot{w}_t} \right] \left[ \frac{1 - (T_t/T_c)}{H_c - H_t - \dot{Q}_{conv}} \right] \quad (B-19)$$

An alternate expression can be obtained from the basic  $C^*$  definition

$$C^* = \sqrt{\frac{RT_c}{\Gamma}} \quad (B-20)$$

Logarithmic differentiation of this yields

$$\frac{dc^*}{c^*} = \frac{1}{2} \frac{dT_c}{T_c} \quad (B-21)$$

Substituting incrementals from differentials in Equation (B-21) gives

$$\frac{\Delta c^*}{c^*} = \frac{1}{2} \frac{\Delta T_c}{T_c} \quad (B-22)$$

Equating  $\Delta T_c$  with the heat loss from Equation (B-17) results in the following

$$\frac{\Delta c^*}{c^*} = \frac{1}{2} \left[ \frac{\sum(q/A)A}{\dot{w}_t} \right] \left[ \frac{1}{c_p T_c} \right] \quad (B-23)$$

The applicable influence factor is

$$f_{HL} = 1 + \frac{1}{2} \left[ \frac{\sum(q/A)A}{\dot{w}_t} \right] \left[ \frac{1}{c_p T_c} \right] \quad (B-24)$$

where

$c_p$  = specific heat at constant pressure

Although derived independently it can be shown that these two expressions, Equations (B-19) and (B-24), are nearly equivalent.

### 1.6 Influence Factor for Chemical Kinetics (f<sub>KE</sub>)

The effect of finite chemical reaction rates is to produce a C\* less than the corresponding theoretical equilibrium values. A TRW Systems Group developed one-dimension nonequilibrium reacting gas computer program was employed with reaction rate constants selected for the propellant system. The fluid mechanical and chemical equations were integrated from the inlet section by an implicit technique. It was determined that the effect of nonequilibrium chemistry produced a C\* loss of 0.2 percent compared to the shifting equilibrium limits.

## 2. CALCULATIONS BASED ON THRUST

The alternate determination of C\* efficiency is based on thrust:

$$\eta_{C^*} = \frac{F_{vac} g_c}{(C_F)_{vac} \dot{w}_T C^*_{theo}} \quad (B-25)$$

where

$F_{vac}$  = measured thrust corrected to vacuum conditions by  
the equation:  $F_{vac} = F + P_a A_e$

$F$  = measured thrust, lbf

$P_a$  = ambient pressure, psia

$A_e$  = area of nozzle exit, in<sup>2</sup>

$g_c$  = conversion factor ( $32.174 \text{ lbm-ft/lbf-sec}^2$ )

$(C_F)_{vac}$  = theoretical shifting thrust coefficient (vacuum)

$\dot{w}_T$  = total propellant flow rate,  $\text{lbm/sec}$

$C^*_{\text{theo}}$  = theoretical shifting-equilibrium characteristic velocity,  $\text{ft/sec}$

Values of vacuum thrust are obtained by applying corrections to sea-level measurements. With these values, which include allowances for all important departures from ideality, theoretical thrust coefficients may be used for calculation of  $C^*$ .  $C_F$  efficiency is taken as 100 percent if there is no combustion in the nozzle, if chemical equilibrium is maintained in the nozzle expansion process, and if energy losses from the combustion gases are accounted for.

Applicable influence factors for measured thrust are specified in the following equation:

$$\eta_{C^*} = \frac{(F + P_a A_e) g_c \phi_{FR} \phi_{DIV} \phi_{HL} \phi_{KE}}{(C_F)_{\text{theo}} (\dot{w}_o + \dot{w}_f) (C^*)_{\text{theo}}} \quad (B-26)$$

where

$F$  = measured thrust, lbf

$P_a$  = ambient pressure, psia

$A_e$  = area of nozzle exit,  $\text{in}^2$

$g_c$  = conversion factor ( $32.174 \text{ lbm-ft/lbf-sec}^2$ )

$(C_F)_{\text{theo}}$  = theoretical shifting thrust coefficient (vacuum)

$\dot{w}_o$  = oxidizer weight flow rate,  $\text{lbm/sec}$

$\dot{w}_f$  = fuel weight flow rate,  $\text{lbm/sec}$

$(C^*)_{\text{theo}}$  = theoretical shifting equilibrium characteristic velocity,  $\text{ft/sec}$

$\phi_{FR}$  = influence for frictional losses

$\phi_{DIV}$  = influence factor for nozzle divergence

$\phi_{HL}$  = influence factor for heat losses to chamber and nozzle walls

$\phi_{KE}$  = influence factor correcting  $C^*$  and  $C_F$  values to account for finite chemical reaction rates

The influence factors in Equation (B-26) are applied to vacuum thrust ( $F + P_a A_e$ ) instead of to measured site thrust ( $F$ ) because, for convenience, the factors are readily calculated as changes in efficiency based on theoretical vacuum parameters. The total influence factor is then of the form  $\Delta F/F_{vac}$ .

Implicit in the use of theoretical  $C_F$  values are corrections to geometric throat area and to measured static chamber pressure at start of nozzle convergence. Therefore, calculation of corrected  $C^*$  efficiency from thrust measurement includes all the previously described corrections plus an additional one to account for nonparallel nozzle exit flow. However, because  $(C_F)_{theo}$  is essentially independent of small changes to chamber pressure and contraction ratio which are involved in corrections to  $P_c$  and  $A_t$ , these corrections are of no practical significance in calculation of  $C^*$  from thrust measurements.

## 2.1 Influence Factor for Frictional Drag ( $\phi_{FR}$ )

This factor corrects for energy losses caused by viscous drag forces on the thrust chamber walls. Its magnitude is estimated by a boundary layer analysis utilizing the integral momentum equation for turbulent flow, which accounts for boundary layer effects from the injector to the nozzle exit by suitable description of the boundary layer profile and local skin friction coefficient. A computer program is used to carry out a numerical integration of the equation, including effects of pressure gradient, heat transfer, and surface roughness. The program requires a potential nozzle flow solution obtained from variable-property, axisymmetric method of characteristics calculation of the flow field outside the boundary layer; corresponding properties for the subsonic combustion chamber flow field are also calculated.

## 2.2 Influence Factor for Nozzle Divergence ( $\phi_{DIV}$ )

The one-dimensional theoretical performance calculations assume that flow at the nozzle exit is uniform and parallel to the nozzle axis. The influence factor,  $\phi_{DIV}$ , allows for nozzle divergence (i.e., for nonaxial flow) and for nonuniformity across the nozzle exit plane. It is calculated by a computer program which utilizes the axisymmetric method of characteristics for a variable-property gas. Computation begins with a transonic input near Mach 1, providing a characteristic line for use in the analysis of the supersonic portion of the nozzle. The resulting pressures are integrated over the given geometry to give the geometric efficiency.

## 2.3 Influence Factor for Heat Loss ( $\phi_{HL}$ )

To obtain the heat loss influence factor from measured thrust the approach is identical to that taken previously from the pressure measurement, except that the nozzle losses must also be included. With constant specific heat and gamma from start of nozzle convergence to exit, Equation (B-22) becomes

$$\phi_{HL} = 1 + \frac{1}{2} \left[ \frac{\sum \left( \frac{Q}{A} \right) A}{\dot{w}_T} \right] \left[ \frac{1 - T_e / T_c}{H_c - H_e - Q_{nozzle}} \right] \quad (B-27)$$

when "e" corresponds to the exit condition, and the summation occurs over the entire combustion.

An alternate can also be derived as in Equation (B-24). This equation becomes

$$\phi_{HL} = 1 + \frac{1}{2} \left[ \frac{(q/A)A}{\dot{w}_T} \right] \left[ \frac{1}{c_p T_e} \right] \quad (B-28)$$

## 2.4 Influence Factor for Chemical Kinetics ( $\phi_{KE}$ )

The effect of finite chemical reaction rates is to produce  $C^*$  and  $C_F$  less than the corresponding theoretical equilibrium values. A TRW Systems Group developed one-dimensional nonequilibrium reacting gas computer program was employed with reaction rate constants selected for the FLOX methane-ethane blend propellant system. The fluid

mechanical and chemical equations were integrated from the inlet section by an implicit technique. It was determined that the effect of nonequilibrium chemistry produced a  $C^*$  loss of ~0.6 percent and a  $C_F$  loss of ~0.89 percent compared to the shifting equilibrium limits.

### 3. SAMPLE COMPUTATION WITH EXPERIMENTAL DATA

Presented here is a sample calculation for a selected test to illustrate the above methods. The physical properties and theoretical data utilized in the program are given in Appendix C. The descriptions of the computer programs used in the performance computations are given in Appendix D. The selected run is 120 of Table 5-3.

#### 3.1 Influence Factor Evaluation

The influence factors,  $f_i$  and  $\phi_j$ , of Equations (B-2) and (B-26) are summarized here for test 120.

##### 3.1.1 Momentum

The momentum correction is a standard correction to either combustion head end or start of convergence static pressures to compute an indicated nozzle stagnation pressure. This correction is a function of contraction ratio and gas gamma ratio only. The correction factor for this program and selected contraction ratios are given in Figure B-1. For test 120 the start of convergence static pressure was

$$P_{CD} = 93.2 \text{ psia}$$

Using Figure B-1, the momentum correction gives the stagnation pressure as

$$P_o = 96.7 \text{ psia}$$

The other pertinent data for subsequent calculations are:

$$\dot{W}_T = 12.4 \text{ lb/sec}$$

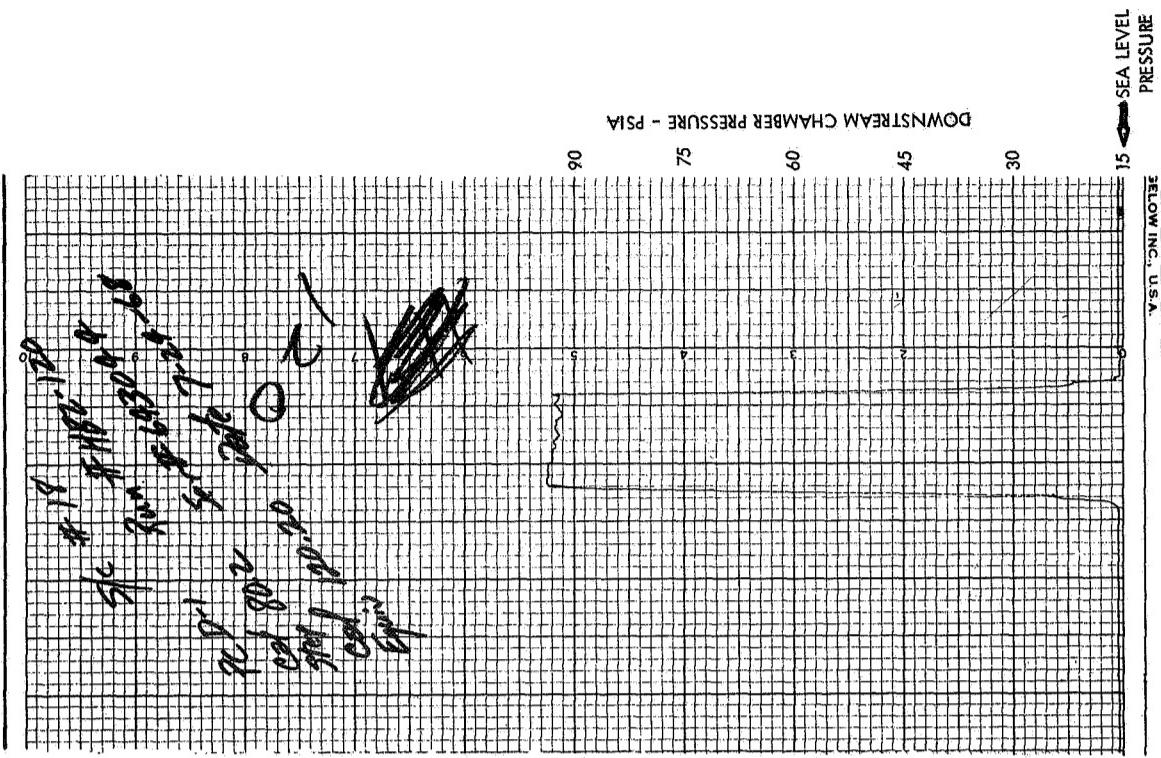
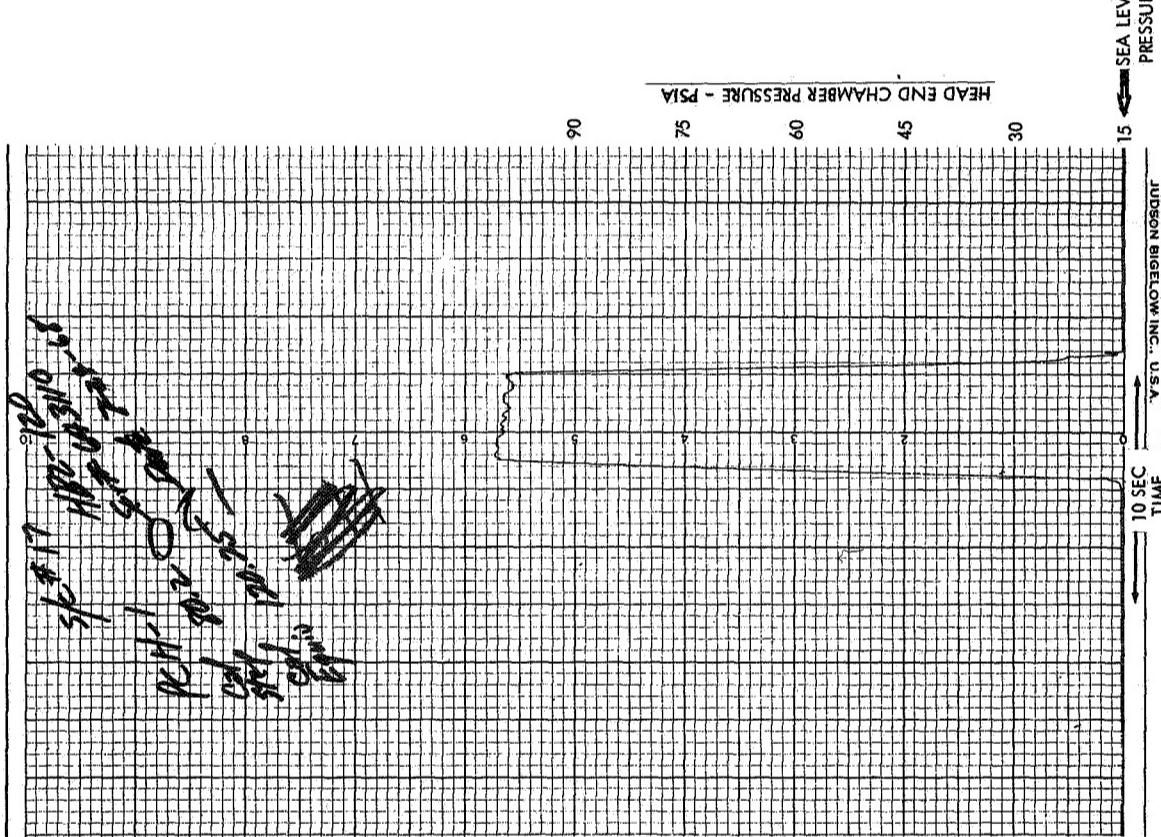
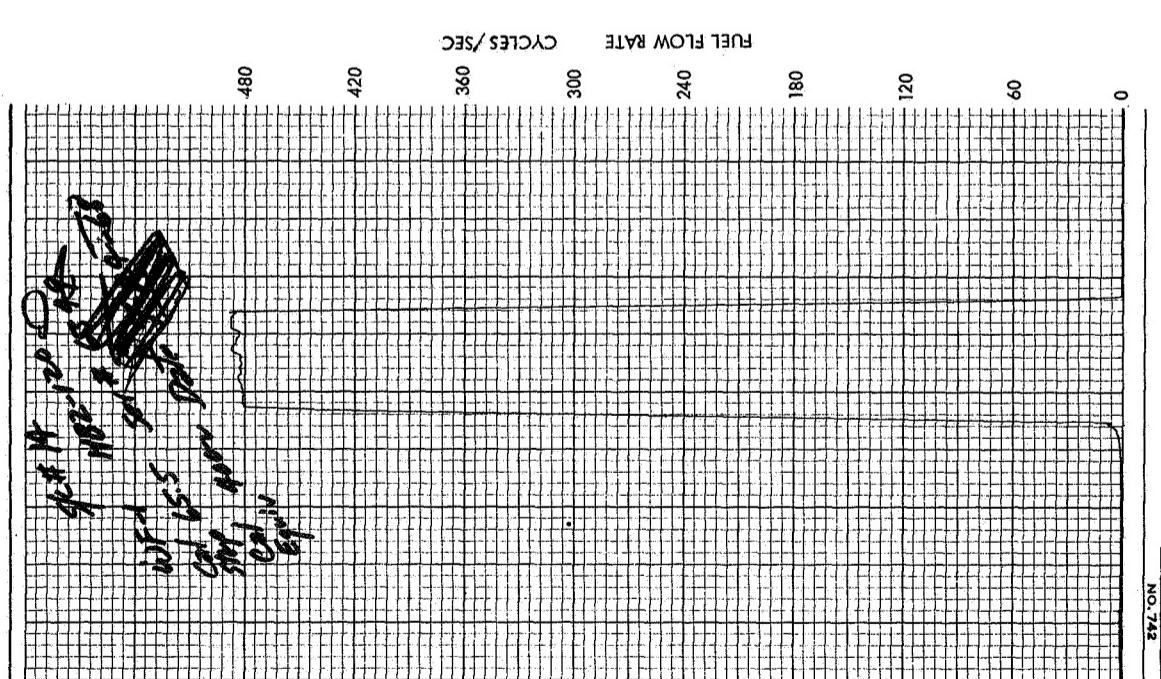
$$MR = 4.8$$

$$F = 2728 \text{ lbf}$$

See Figures B-3 and B-4 for strip chart and digital data for this test.



Paket - 1



Part - 2

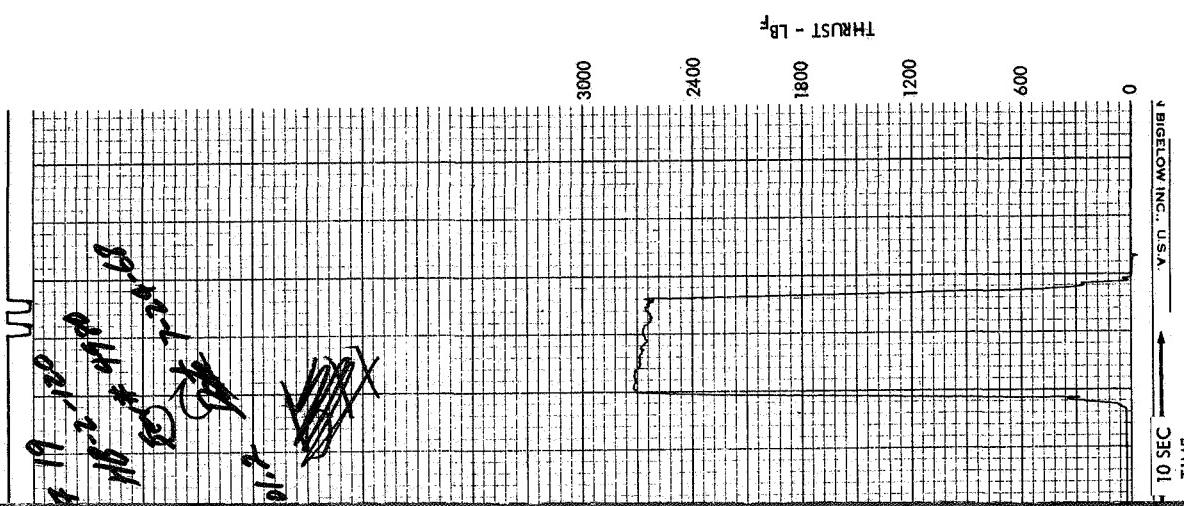


Figure B-3. Strip Chart Data for Test 120



**VRW SYSTEMS**

FILE 7 RECORD 20 SIZE 512

HEPIS H2 RUN 120 TAPE 429U JULY 24, 1964

SEC	1198	3-K FLOX	WF	WT	PTD	CN*	ETA-C*	MR	THRUST UNCORRECT	TIME
PCD	NS	LBM/SEC	LAM/SEC	LHM/SEC		ET/SEC				
14.470	0	0	0	0	15.005	-11.000	-1.0000			
14.470	0	0	0	0	15.005	-11.600	-7.6666			
14.470	0	0	0	0	15.005	-11.600	-5.0000			
14.467	0	0	0	0	15.003	-11.354	-2.5000			
14.469	0	0	0	0	15.004	-11.356	0			
14.323	0	0	0	0	14.853	-11.600	.25000			
14.370	0	0	0	0	15.005	-11.600	.25000			
14.420	0	0	0	0	15.005	-12.030	.75000			
14.482	46293	0	46293	0	27443	0	1.0000			
18.218	9.9034	1.5046	11.406	18.692	1400.9	0	6.5814	-16.017	1.0000	
33.598	10.083	2.0549	12.134	34.844	2425.2	0	4.9855	-54.282	1.2500	
89.798	10.069	2.1151	12.164	93.120	9495.3	9376.1	4.7501	2049.4	1.7500	
92.467	10.276	2.1413	12.419	95.869	0531.7	9462.7	4.7999	2091.0	2.0000	
92.723	10.216	2.1406	12.352	95.154	0552.6	9549.4	4.7726	2177.1	2.4000	
91.974	10.281	2.1023	12.364	95.377	6515.5	9426.9	4.8890	2659.9	2.5000	
92.089	10.237	2.1301	12.362	95.496	6532.5	9463.6	4.8056	2636.2	2.7500	
92.695	10.351	2.1332	12.484	96.125	6543.9	9429.0	4.8525	2655.3	3.0000	
92.764	10.305	2.1426	12.447	96.217	0559.2	9471.9	4.8069	2678.6	3.2500	
92.589	10.316	2.1406	12.418	95.994	0559.4	9460.6	4.7524	2697.7	3.5000	
92.524	10.351	2.1694	12.521	95.947	0482.6	9395.7	4.7713	664.9	3.7500	
93.229	10.253	2.1486	12.402	96.678	6594.4	9556.7	4.7717	2717.4	4.0000	
93.304	10.306	2.1436	12.482	96.756	6573.5	9520.6	4.8053	2765.6	4.2500	
93.374	10.315	2.1633	12.479	96.828	6564.3	9511.2	4.7633	2686.3	4.5000	
93.233	10.316	2.1782	12.494	96.683	0546.1	9491.6	4.7362	2659.4	4.7500	
93.980	10.274	2.1670	12.441	97.456	6626.9	9607.0	4.7411	2737.6	5.0000	
94.053	10.346	2.1265	12.543	97.740	6592.3	9553.3	4.7646	2696.7	5.2500	
94.000	10.310	2.1690	12.479	97.495	6608.4	9576.6	4.7534	2760.9	5.5000	
94.144	10.256	2.1612	12.417	97.628	6651.1	9541.3	4.7489	2699.8	5.7500	
36.863	4.8305	1.2332	6.0636	40.304	3622.5	0	3.9174	1.0530	6.0000	
23.921	1.0965	4.6199	1.2586	24.506	10673	0	0.7643	380.90	6.4000	
16.726	1.7356	4.10200	1.6378	17.345	7964.1	0	17.017	69.020	6.5000	
14.531	0	0	0	15.069	0	0	0.4954	6.7500	6.7500	
14.464	0	0	0	15.000	0	0	3.7424	7.0000	PEAK	

Figure B-4. Digital Data for Test 1120

### 3.1.2 Friction Factors

The friction effects are computed through the use of the Blasius flat plate approximation for the local skin coefficient and integrating the local shear forces

$$F_f = \int \frac{c_f \rho V^2}{2 g} dA$$

$$\text{where } c_f = 0.0296 / (R_{e_x})^{0.2}$$

The viscosity is computed at a local mean film temperature

$$\bar{T} = T_w + T_R$$

where  $T_R$  = the local recovery temperature

As described in the section on the heat transfer results, the indicated  $T_R$  values are on the order of  $3500^\circ$  to  $4000^\circ R$ . The wall temperature was taken as  $1500^\circ R$ . Integration was carried out in the numerical programming by considering three sections: (1) combustion chamber cylinder, (2) convergence section, and (3) nozzle from the throat to exit. The computed force results are:

$$\text{Cylinder } F_f = 4.03 \text{ lbf}$$

$$\text{Convergence } F_f = 2.04 \text{ lbf}$$

$$\text{Divergence } F_f = 3.16 \text{ lbf}$$

A first order approximation can now be made to obtain the correction for stagnation pressure through the approximation

$$\begin{aligned} \frac{P'_o}{P_o} &= \frac{P_c A_t + \int \tau_c dA_{wc} - \int \tau_{conv} dA_{conv}}{P_o A_t} \\ &= 1 + \frac{F_c - F_{conv}}{P_c A_t} \end{aligned}$$

The computed correction on  $P_c$  is 1.003

The  $\phi_f$  for thrust is straight forward and is

$$\phi_f \approx \frac{(F_{vac})_{calc} + \sum \tau \cos i A_i}{F_{vac\ calc}}$$

### 3.1.3 Throat Radius Effects

Using Equation (B-3) the throat radius change is computed at a  $T_w$  of 500°F.

$$dr = \frac{10}{10^6} \left[ \frac{1 + 0.33}{1 - 0.33} \right] \frac{[171 - (-1.51)]}{[5.4 - 2.8]}^2$$
$$\left[ \frac{(5.4)^2 \cdot 2.8}{2} - \frac{2(5.4)(2.8)^2}{3} - \frac{(5.4)^4}{(12)(2.8)} \right]$$
$$= -0.0064$$

The influence factor is readily determined in terms of area change

$$\phi_{TR} = \frac{R^2}{R^2 - 2(R)dr + dr^2}$$

The computed factor is

$$\phi_{TR} = 0.997$$

### 3.1.4 Throat Discharge Coefficient

From Figure B-2  $\phi_{Dis}$  is taken as

$$\phi_{Dis} = .995$$

### 3.1.5 Kinetic Effects

The kinetic effects were computed and presented in Figure C-9 for this program. Since there is a finite expansion effect it must be recognized that in computing  $C^*$  values from either  $P_c$  or F measurements, kinetic effects must include this expansion. This factor was not utilized here in the performance reduction because of its lack of previous use; however, its value is

$$\phi_{KE} = 1.002$$

### 3.1.6 Energy Loss

The heat loss effect on the  $P_c$  computation technique is easily accomplished when the Q/A axial distributions are known. In this case

$$f_{HLP_c} = 1 + \frac{1}{2} \left( \frac{840}{12.4} \right) \left[ \frac{1 - \frac{3571}{4141}}{918 - 471 - 68} \right]$$
$$= 1.013$$

For the thrust measurement

$$\phi_{HLF} = 1 + \frac{1}{2} \left( \frac{956}{12.4} \right) \left[ \frac{1 - \frac{2349}{4141}}{1852 - 471 - 141} \right]$$
$$= 1.014$$

### 3.1.7 Total Corrections

The total product correction for the  $P_c$  computation is

$$f_{Pc} = 1.008$$

which for the F computational technique is

$$f_F = 1.035$$

### 3.1.8 C\* Calculation

The substituted quantities for the C\* computation based on the two techniques are summarized below:

$$\eta_{C^*P_c} = \frac{P_o \quad A \quad g \quad f_f \quad f_{TR} \quad f_{Dis} \quad f_{HLPC}}{\dot{\omega}_t \quad C^*_{Theo}}$$

$$= \frac{(96.7) (26.3) (32.2) (1.003) (0.997) (0.995) (1.008)}{(12.4) (6932)}$$

$$= 0.961$$

$$\eta_{C^*F} = \frac{F_{mea} \quad A_e P_a \quad g \quad \phi_f \quad \phi_{Div} \quad \phi_{HLF}}{C_F \quad \dot{\omega}_t \quad C^*_{theo}}$$

$$= \frac{(2728 + 710) (32.2) (1.004) (1.017) (1.014)}{(1.4) (12.4) (6932)}$$

$$= 0.952$$

## APPENDIX C

### PHYSICAL PROPERTY AND THEORETICAL PERFORMANCE SUMMARY

#### 1. PHYSICAL PROPERTY DATA

The physical property data of the propellants used in this program are summarized here. Curve fits of property data for computer program calculations were accomplished on NASA contract "Space Storable Thrustor Investigation," NAS 3-11184.

The fuel property summary is given in Table C-1. The 55/45 blend was used throughout the program.

The nominal 80 percent FLOX blend property data are given in Table C-2.

The LPG liquid density-temperature curve fit is given in Figure C-1. The density curves for the FLOX blends were derived from the pure component data and are given in Figure C-2.

The vapor pressure curves are given in Figures C-3 and C-4 for both the fuel and oxidizer.

#### 2. THEORETICAL PERFORMANCE

The theoretical combustion performance computations were provided by NASA LeRC and cross-checked with the TRW performance program for consistency. The  $C^*$  values were found to be identical based upon inputs at the saturation temperatures of the propellants. The equilibrium  $C^*$  results are given in Figure C-5 for various  $F_2/O_2$  ratios and the fuel blend fixed at 55 percent methane/45 percent ethane. Also given at the nominal 80 percent optimum mixture ratio line are selected calculated points for other  $F_2/O_2$  ratios. Figure C-6 gives equilibrium  $C^*$  values at a fixed O/F ratio of 5.2 as a function of variable  $F_2/O_2$  ratios. Vacuum specific impulse data at a fixed O/F ratio are given in Figure C-7. Tabulated  $C^*$  data are given in Table C-3 for computational purposes.

Tabulated thrust coefficient data for the nozzle used in this program are given in Table C-4 as a function of  $F_2/O_2$  variation.

Kinetic effects were evaluated through use of the TRW Exact Program which has been adopted for standard use by the ICRPG. Both kinetic  $C^*$  and  $C_F$  factors were computed for this program with varying throat radii. The resultant  $C^*$  correction multiplying factors are given in Figure C-8.

### 3. HEAT TRANSFER INPUT DATA

Figure C-9 gives equilibrium species results as a function of mixture ratio. As such it indicates where carbon deposition can be expected to occur.

Figure C-10 gives the results of the expected thermal resistances to heat transfer. The gas side is based on a Bartz type calculation. The carbon data are based upon Pratt and Whitney data from previous FLOX/LPG efforts.

Figure C-11 presents the Mach number correction on the local recovery temperature, assuming the usual Prandtl number dependence.

Table C-1. Fuel Property Summary\*

Property	LPG Fuel		
	Methane	Ethane	55% Methane 45% Ethane
Chemical Formula	CH <sub>4</sub>	C <sub>2</sub> H <sub>6</sub>	---
Molecular Weight	16.042	30.068	22.42
Normal Freezing Point, °R	163.2	161.9	133.0
Normal Boiling Point, °R	200.8	331.7	209.0
Liquid Density at NBP lb/ft <sup>3</sup>	26.48	34.15	30.40
Liquid Density at 140°R, lb/ft <sup>3</sup>	---	---	35.28
Critical Temperature, °R	343.4	549.8	---
Critical Pressure, psia	673	708	---
Critical Volume, ft <sup>3</sup> /lb	0.0989	0.0789	---
H <sub>vaporization</sub> at NBP, Btu/lb	219.22	210.41	---
H <sub>fusion</sub> , Btu/lb	25.25	40.88	---
Viscosity at NBP, lb/ft-sec	7.0x10 <sup>-5</sup>	1.2x10 <sup>-4</sup>	---
Thermal Conductivity at NBP Btu/ft-hr-°R	0.1075	.088	---
Specific Heat at NBP, Btu/lb-°R	0.81	0.57	.70

\*The Matheson Co., Inc., East Rutherford, New Jersey.

Table C-2. Oxidizer Property Summary\*

Property	Oxidizer		
	Fluorine	Oxygen	80% FLOX
Chemical Formula	F <sub>2</sub>	O <sub>2</sub>	---
Molecular Weight	38.00	32.00	---
Normal Freezing Point, °R	96.372	97.833	---
Normal Boiling Point, °R	153.036	162.302	154.5
Liquid Density at NBP, lb/ft <sup>3</sup>	93.96	71.27	89.42
Liquid Density at 140°R, lb/ft <sup>3</sup>	96.7	75	92.36
Critical Temperature, °R	259.128	277.848	---
Critical Pressure, psia	808.	730.	---
Critical Volume, ft <sup>3</sup> /lb	0.0398	0.03725	---
H <sub>vaporization</sub> at NBP, Btu/lb	71.514	91.627	---
H <sub>fusion</sub> at NBP, Btu/lb	5.778	5.979	---
Vapor Pressure at 140°R, psia	5.6	3.1	---
Viscosity at NBP, lb/ft-sec	.000165	.000128	---
Thermal Conductivity at NBP, Btu/ft-hr-°R	.0915	.0852	---
Specific Heat at NBP, Btu/lb-°R	.367	.405	.374

\*The Matheson Co., Inc., East Rutherford, New Jersey.

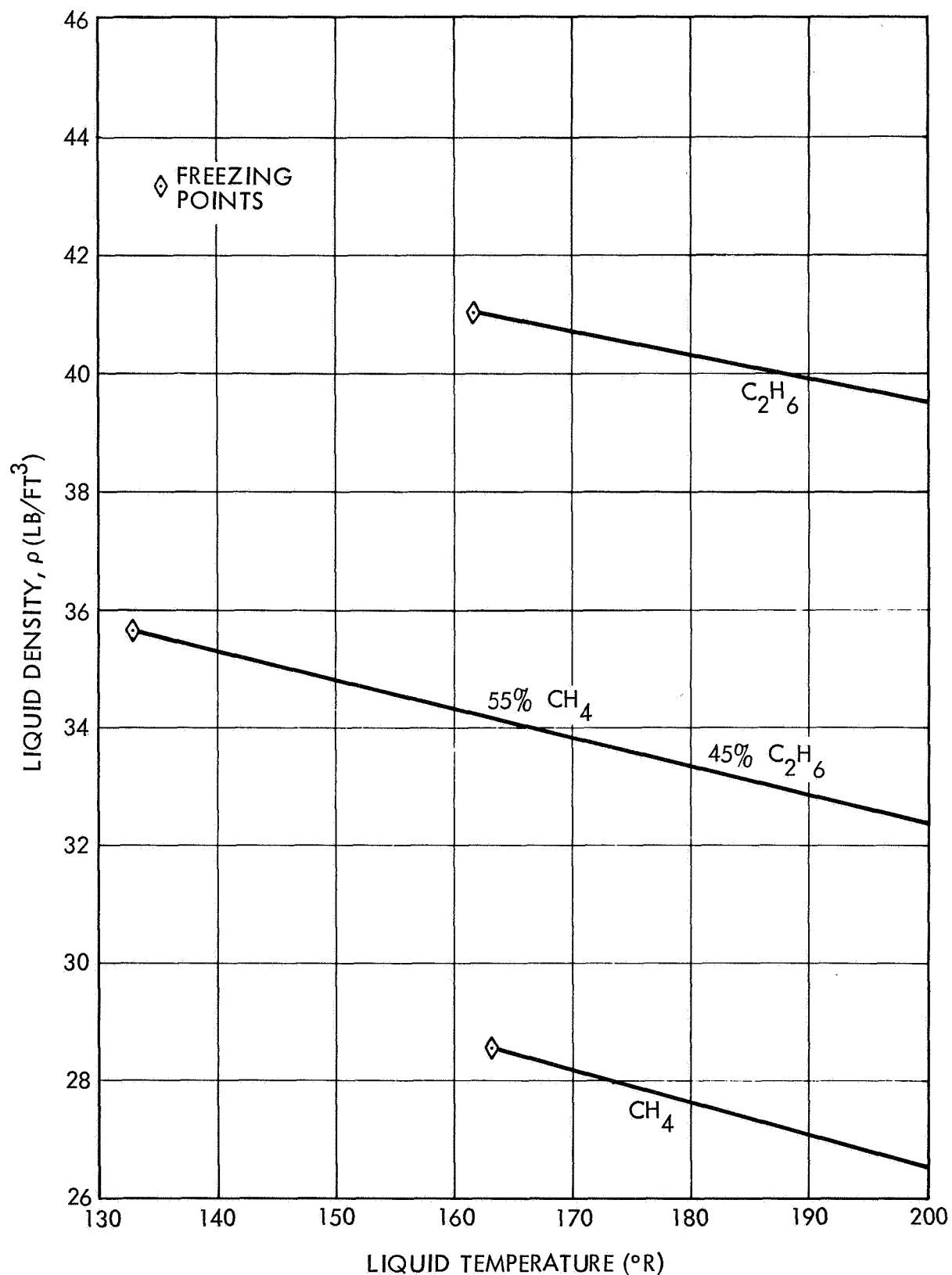


Figure C-1. LPG Liquid Density Versus Temperature

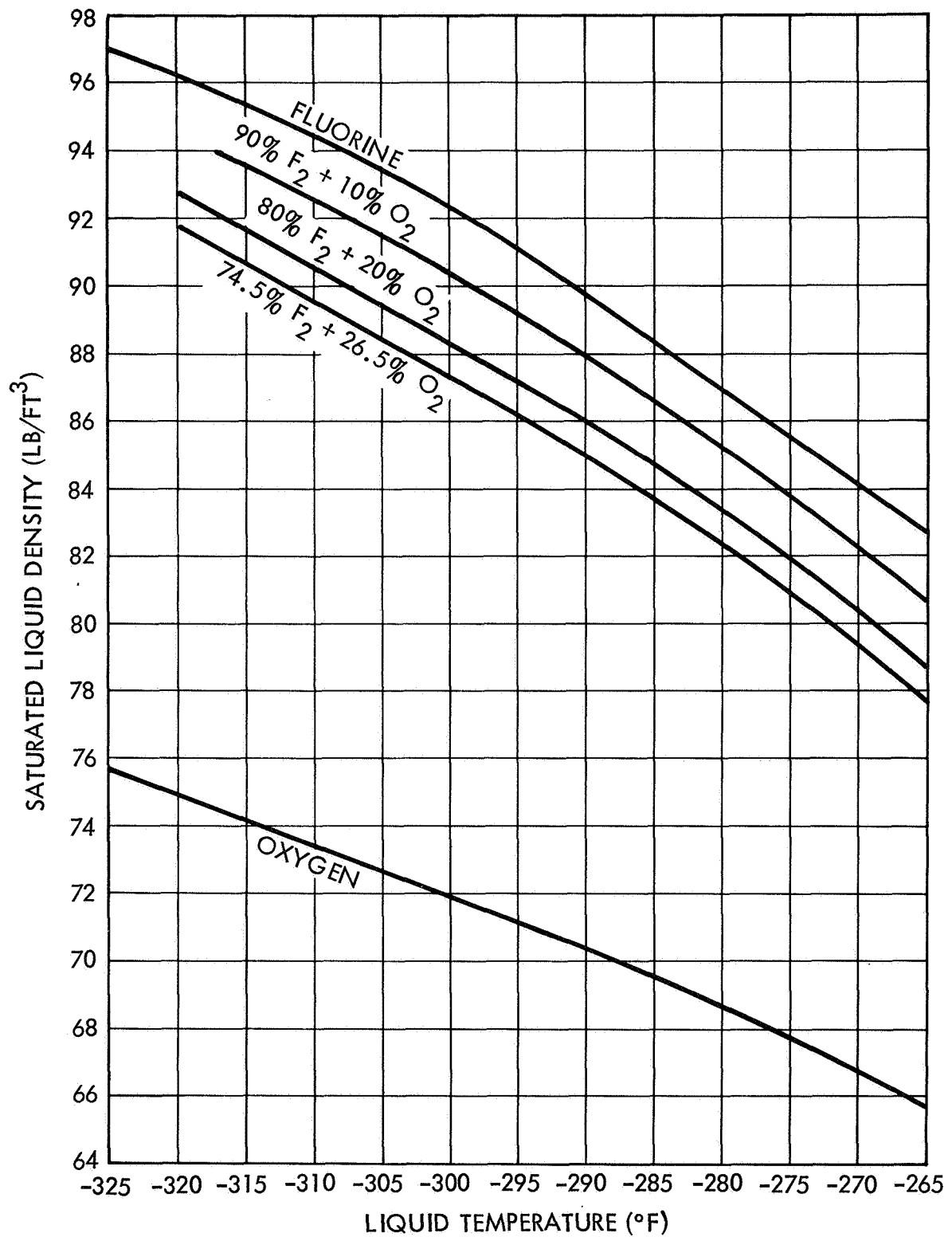


Figure C-2. Oxidizer Density Versus Temperature

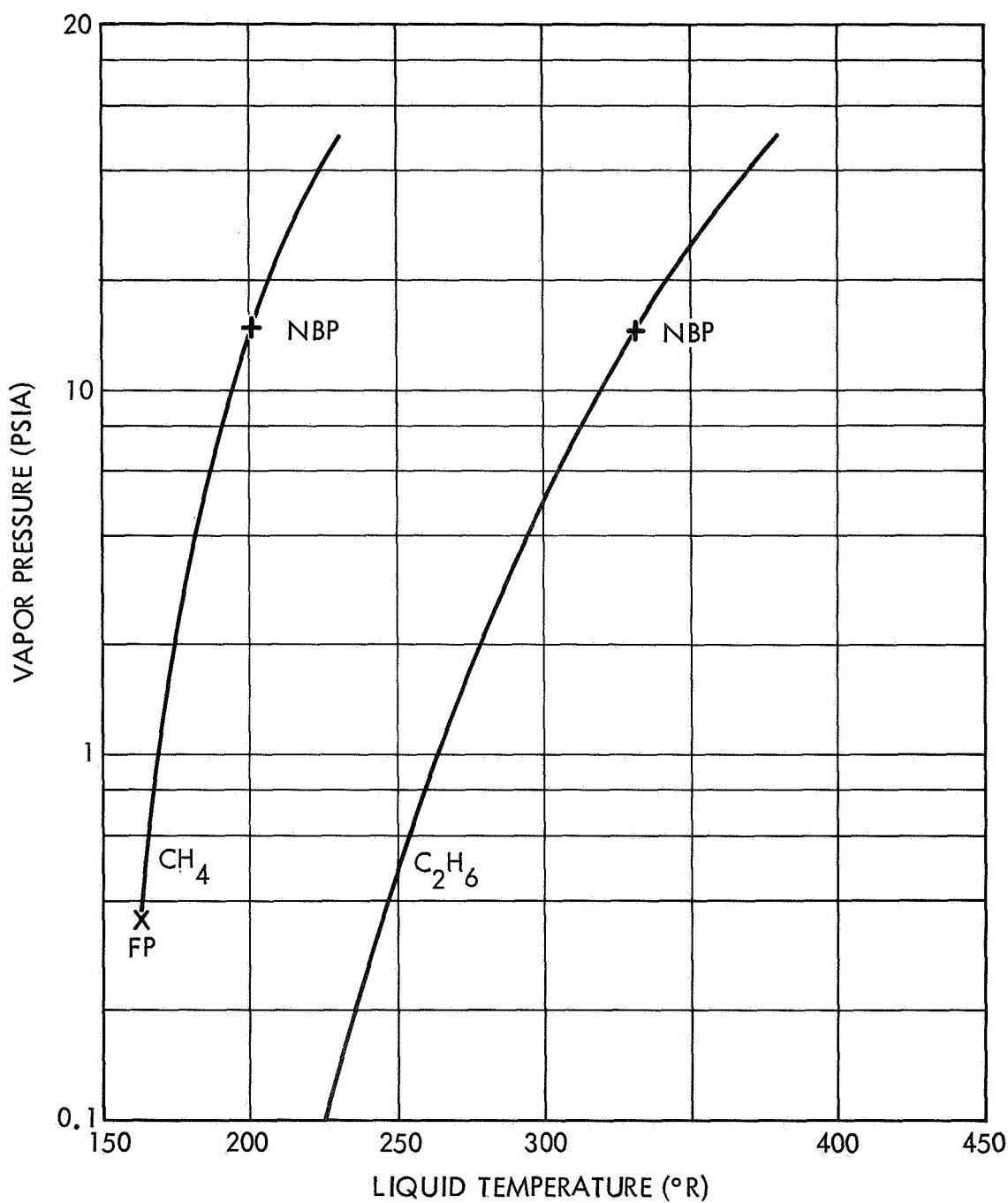


Figure C-3. Fuel Vapor Pressure

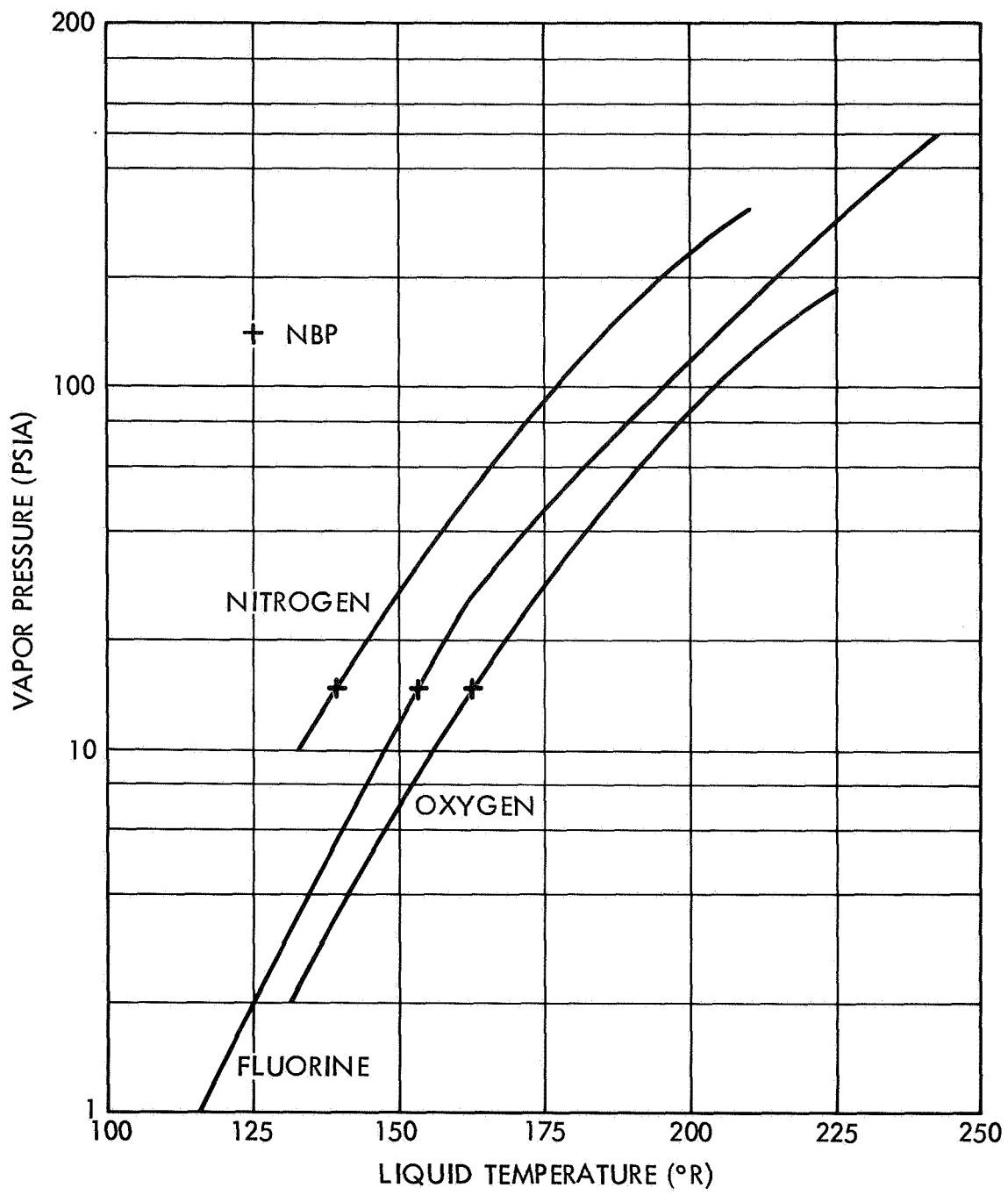


Figure C-4. Oxidizer Vapor Pressure

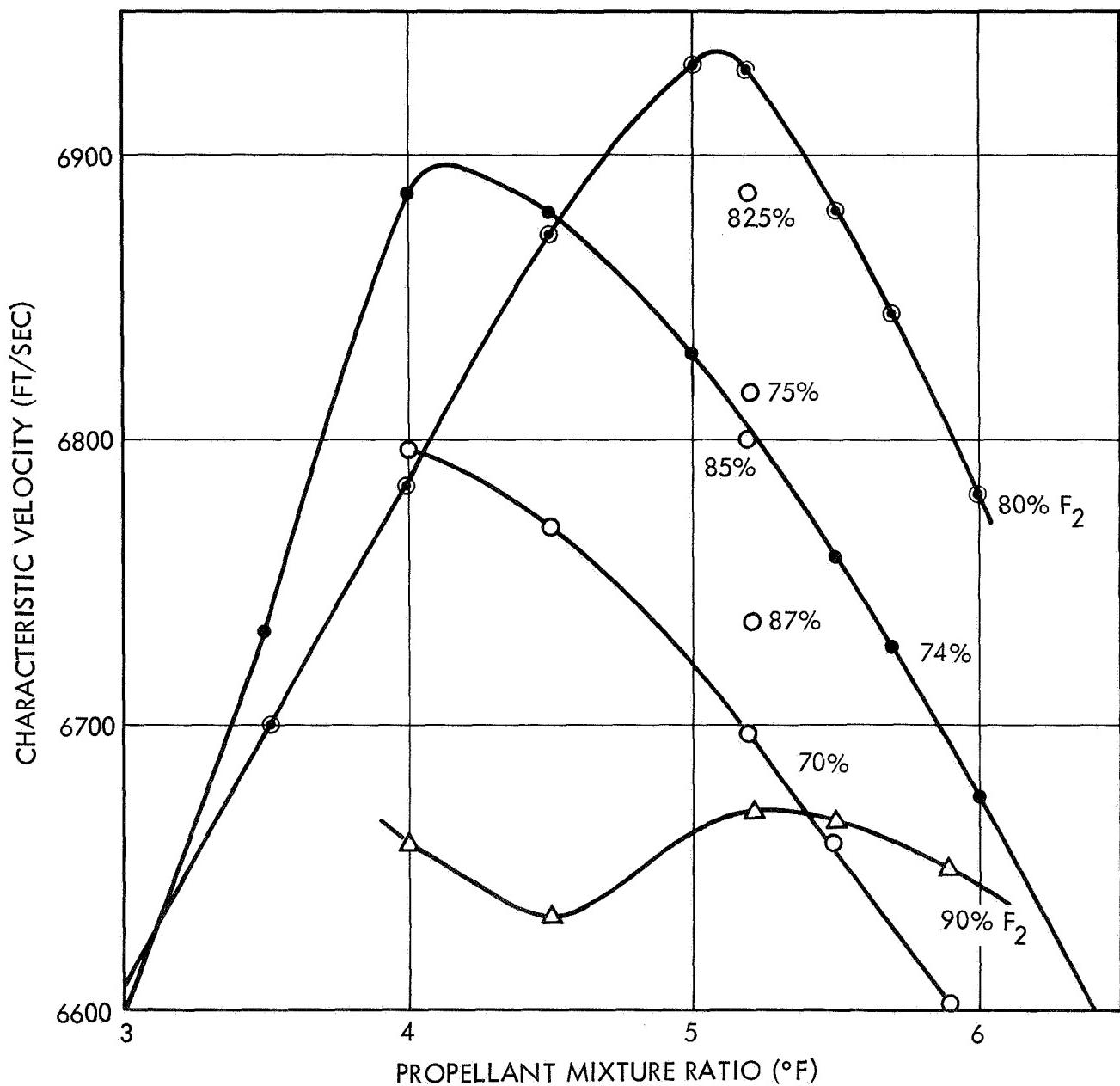


Figure C-5. Equilibrium C\* Efficiency as a Function of MR for Various Contractions of F<sub>2</sub> with 55% Methane - 45% Ethane

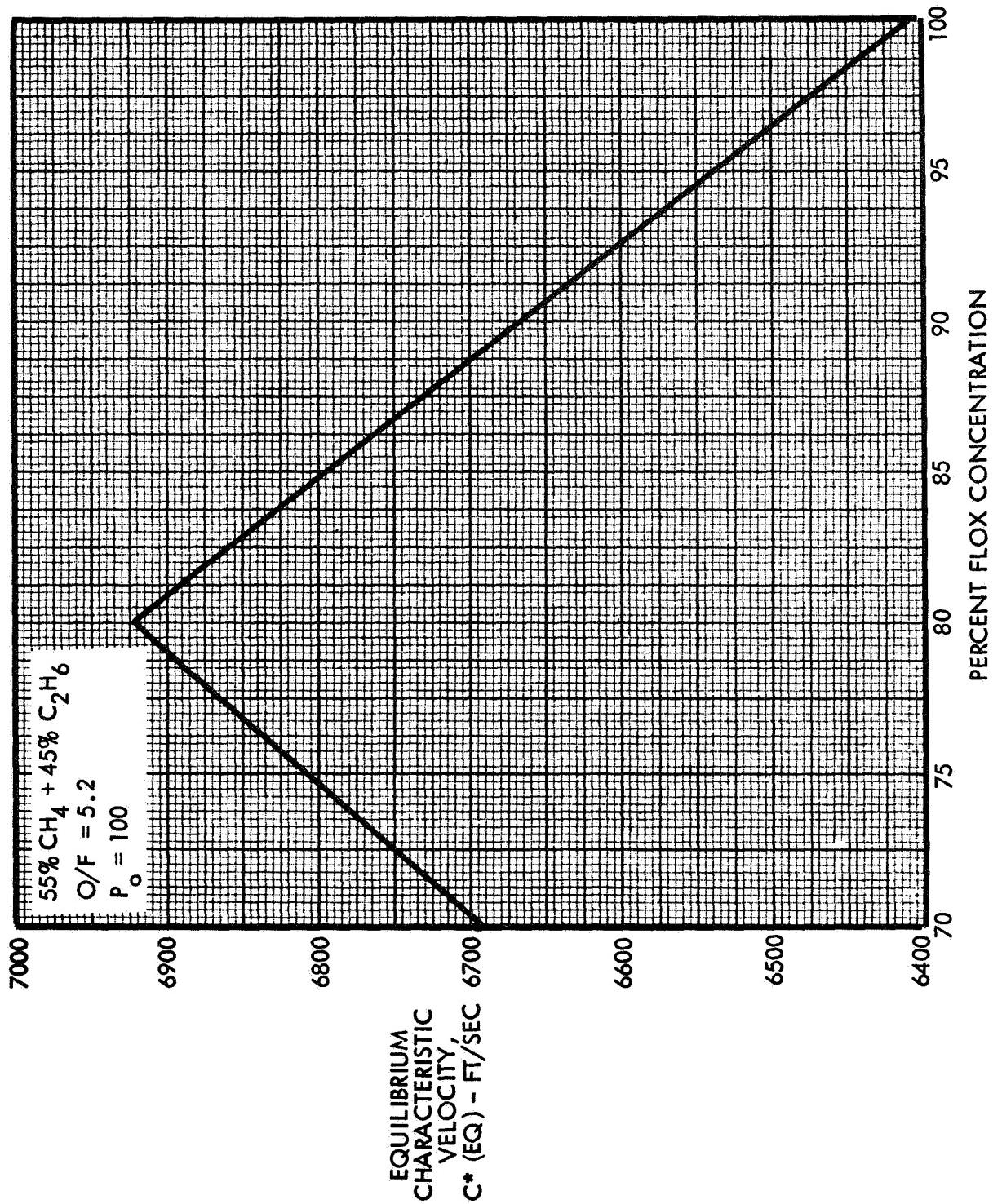


Figure C-6.  $C^*$  as a Function of  $\text{F}_2$  Concentration

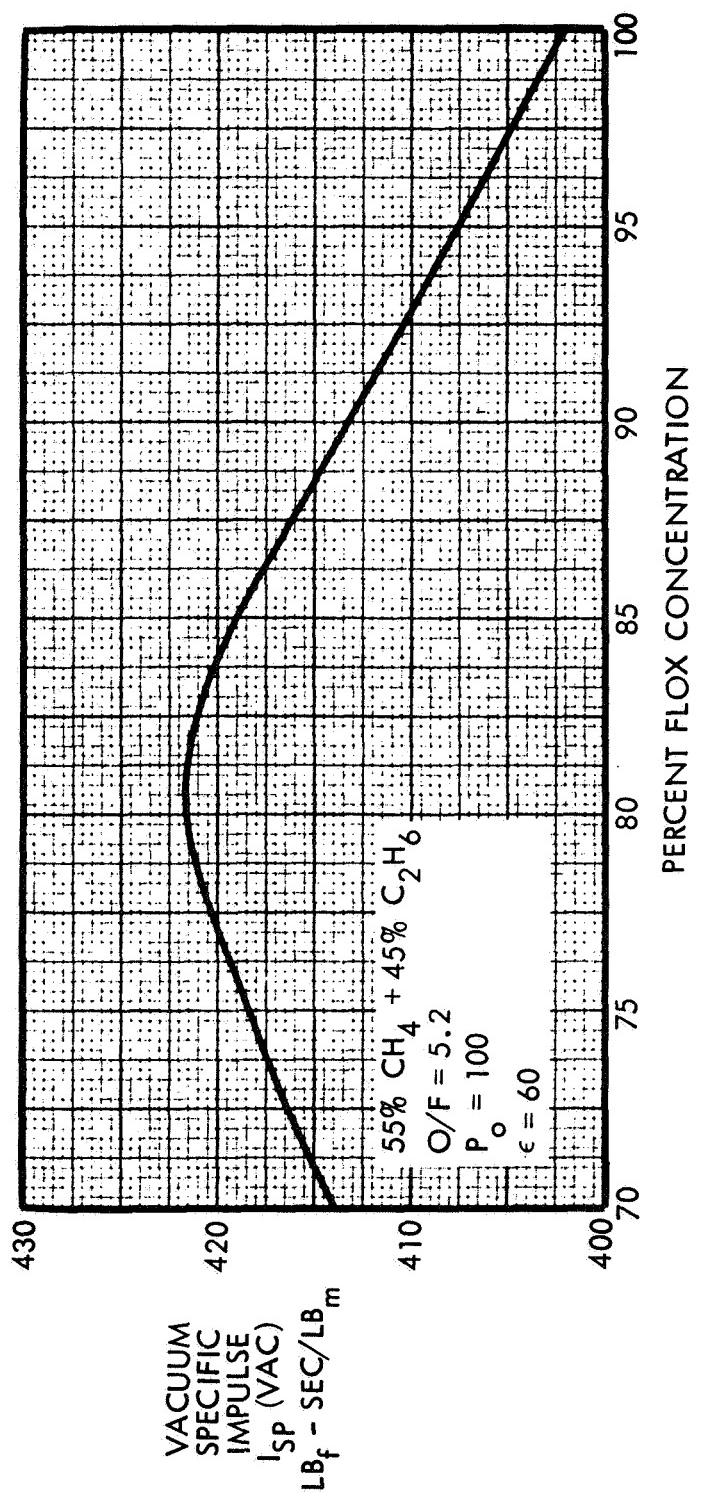


Figure C-7.  $I_{sp}$  as a Function of  $F_2$  Concentration

Table C-3. Equilibrium Performance as a Function  
of Fluorine Concentration

% FLOX/55% CH<sub>4</sub> + 45% C<sub>2</sub>H<sub>6</sub>

O/F = 5.2 P<sub>O</sub> = 100 psia

% FLOX	$\frac{T_O}{^{\circ}R}$	$\frac{C^*}{fps}$	$\epsilon = 60$		$\epsilon (1.84)$	
			$\frac{I_{sp} (vac)}{sec}$	C <sub>F</sub> (vac)	C <sub>F</sub> (sl)	C <sub>F</sub> (vac)
70	7176.	6697.	414.0	1.9888	1.1771	1.4482
75	7356.	6816.	418.3	1.9744	1.1766	1.4475
80	7542.	6931.	421.8	1.9578	1.1765	1.4476
82.5	7489.	6869.	421.2	1.9728	1.1766	1.4486
85	7445.	6802.	419.0	1.9819	1.1767	1.4492
87.5	7408.	6737.	416.4	1.9888	1.1768	1.4497
90	7373.	6669.	413.5	1.9949	1.1770	1.4502
100	7267.	6413.	402.3	2.0183	1.1782	1.4560

Table C-4. Equilibrium C\* as a Function of Chamber Pressure  
and Mixture Ratio

80% F<sub>2</sub> + 20% O<sub>2</sub>/55% CH<sub>4</sub> + 45% C<sub>2</sub>H<sub>6</sub>

MIXTURE RATIO	NOZZLE STAGNATION PRESSURE, psia						CHARACTERISTIC VELOCITY, ft/sec
	50	75	100	125	150	200	
2.0	6247	6257	6263	6268	6272	6277	6283
3.0	6569	6591	6606	6617	6626	6639	6655
3.5	6664	6684	6699	6705	6711	6720	6739
4.0	6720	6756	6780	6800	6815	6839	6872
4.5	6811	6849	6875	6896	6913	6939	6974
5.0	6861	6902	6931	6953	6972	7000	7039
5.2	6860	6902	6931	6954	6972	7001	7041
5.5	6808	6850	6879	6904	6922	6951	6991
5.9	6734	6775	6803	6825	6843	6871	6910
6.0	6715	6755	6783	6805	6822	6850	6888
7.0	6496	6530	6553	6571	6585	6607	6638
							6659

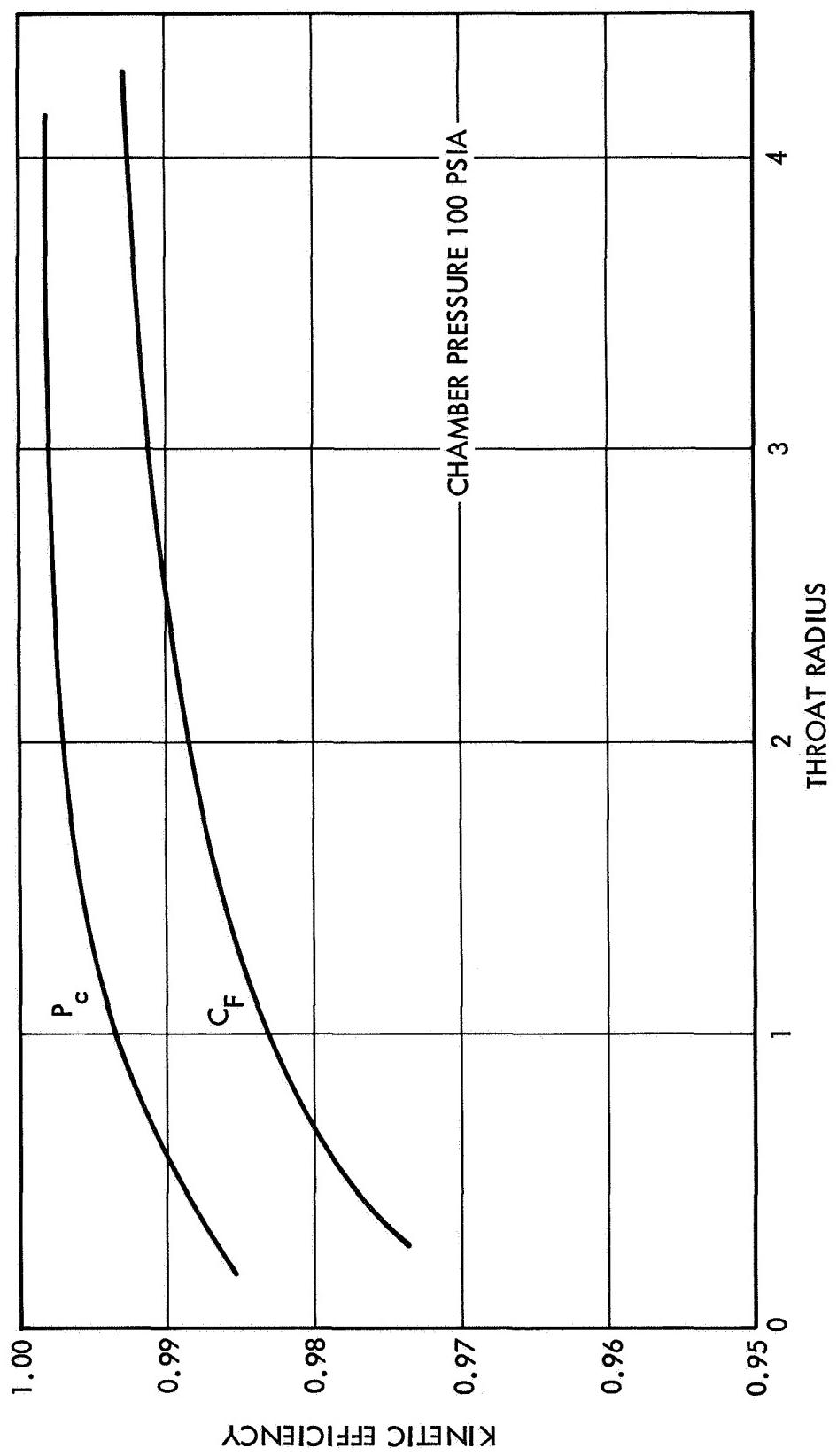


Figure C-8. Kinetic Efficiency as a Function of Chamber Throat Radii

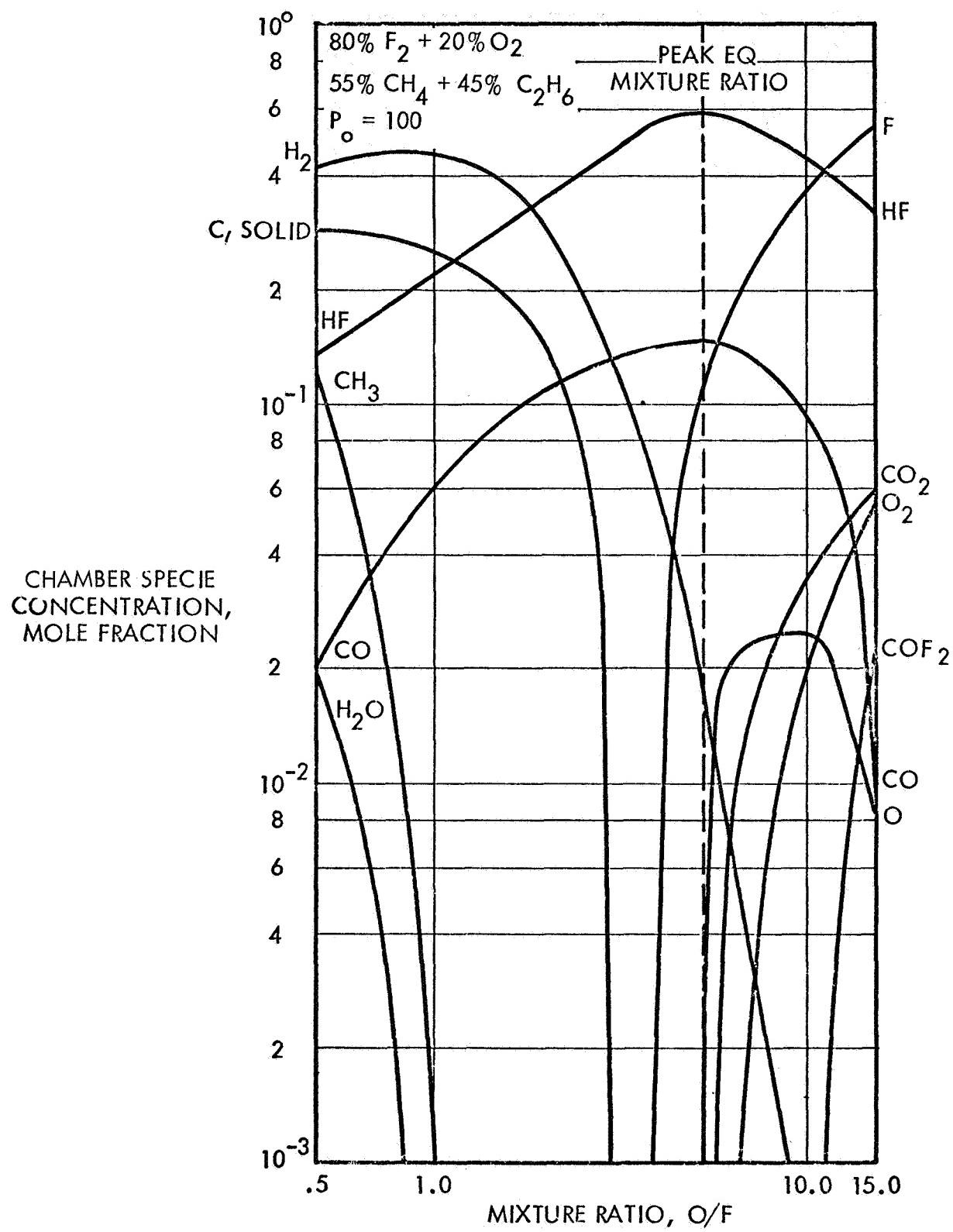


Figure C-9. Equilibrium Species as a Function of MR

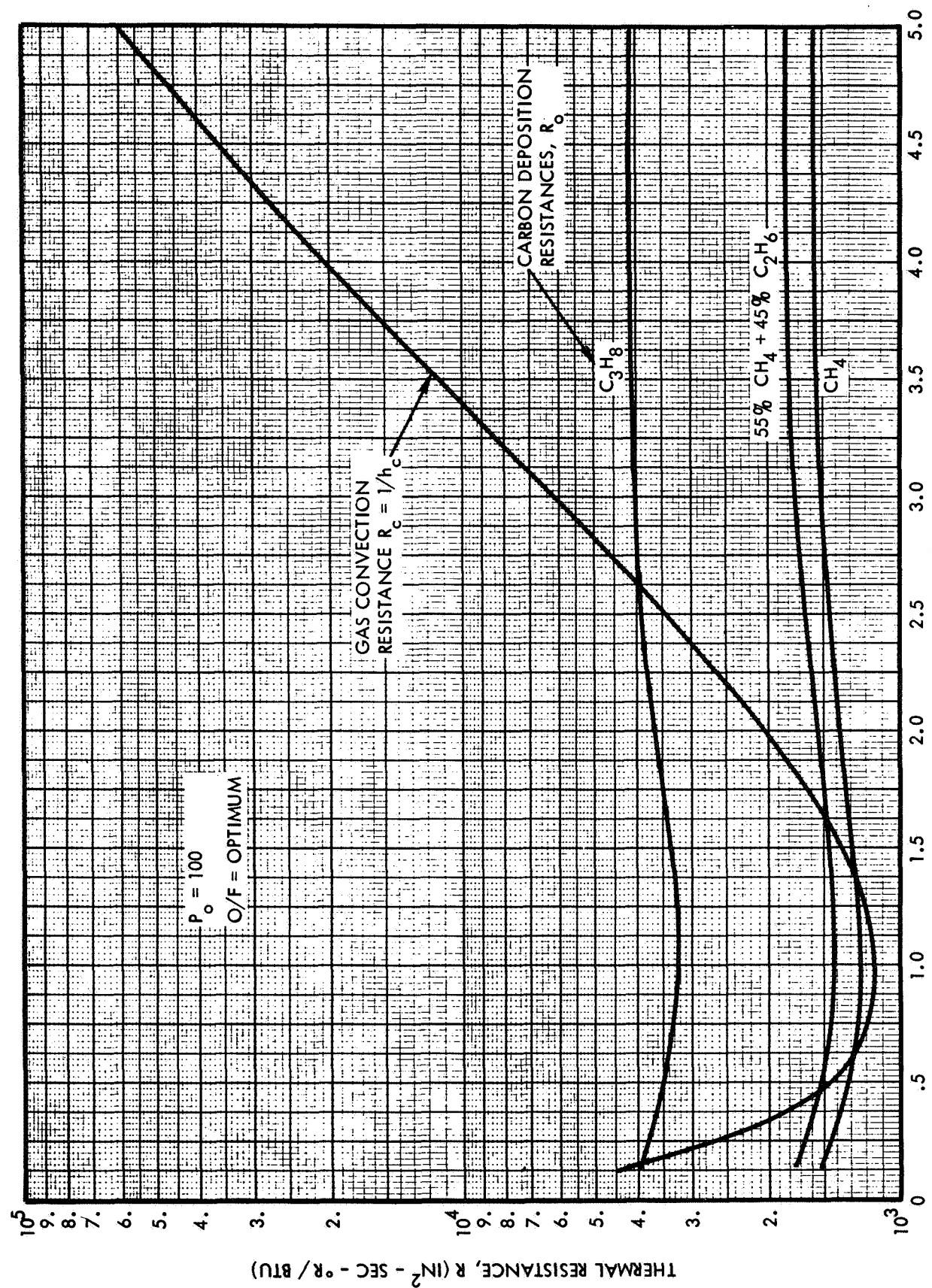


Figure C-10. Thermal Resistance as a Function of Local Wall Mach Number

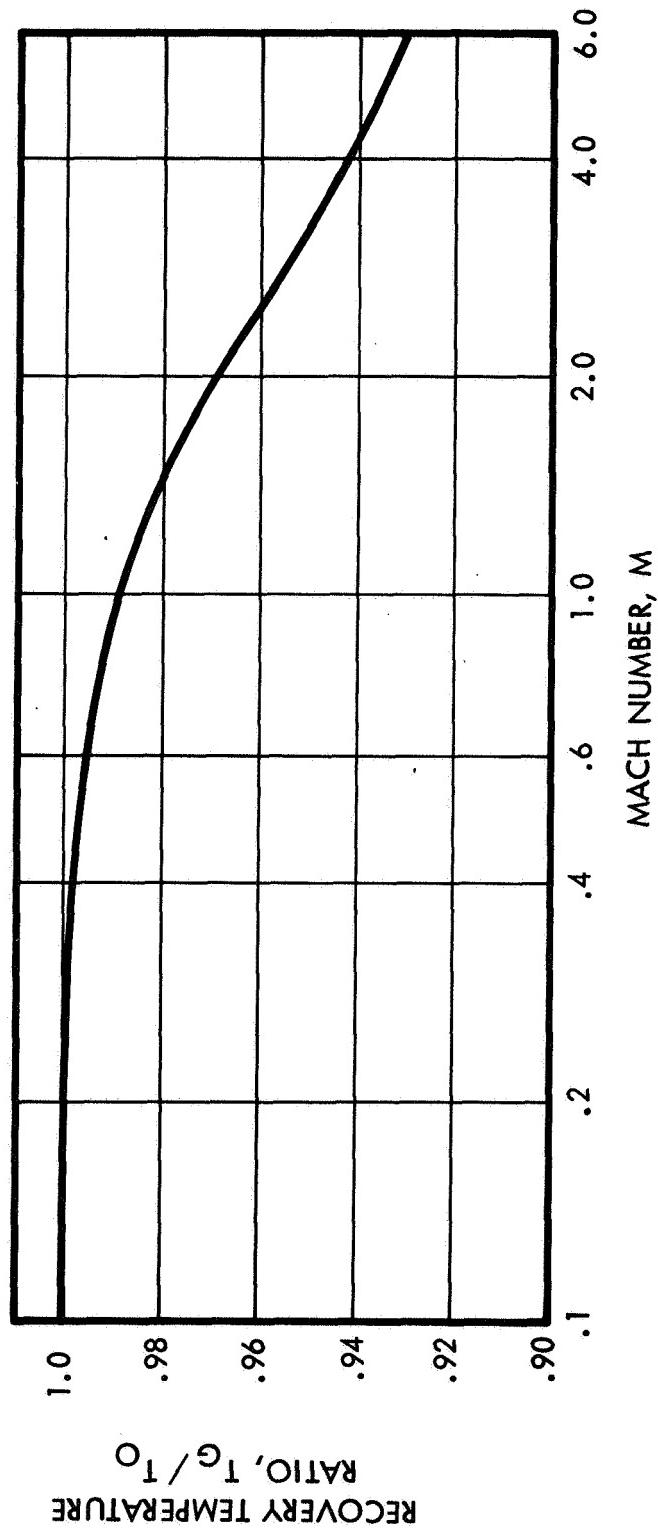


Figure C-11. Thermal Resistance as a Function of Local Wall Mach Number

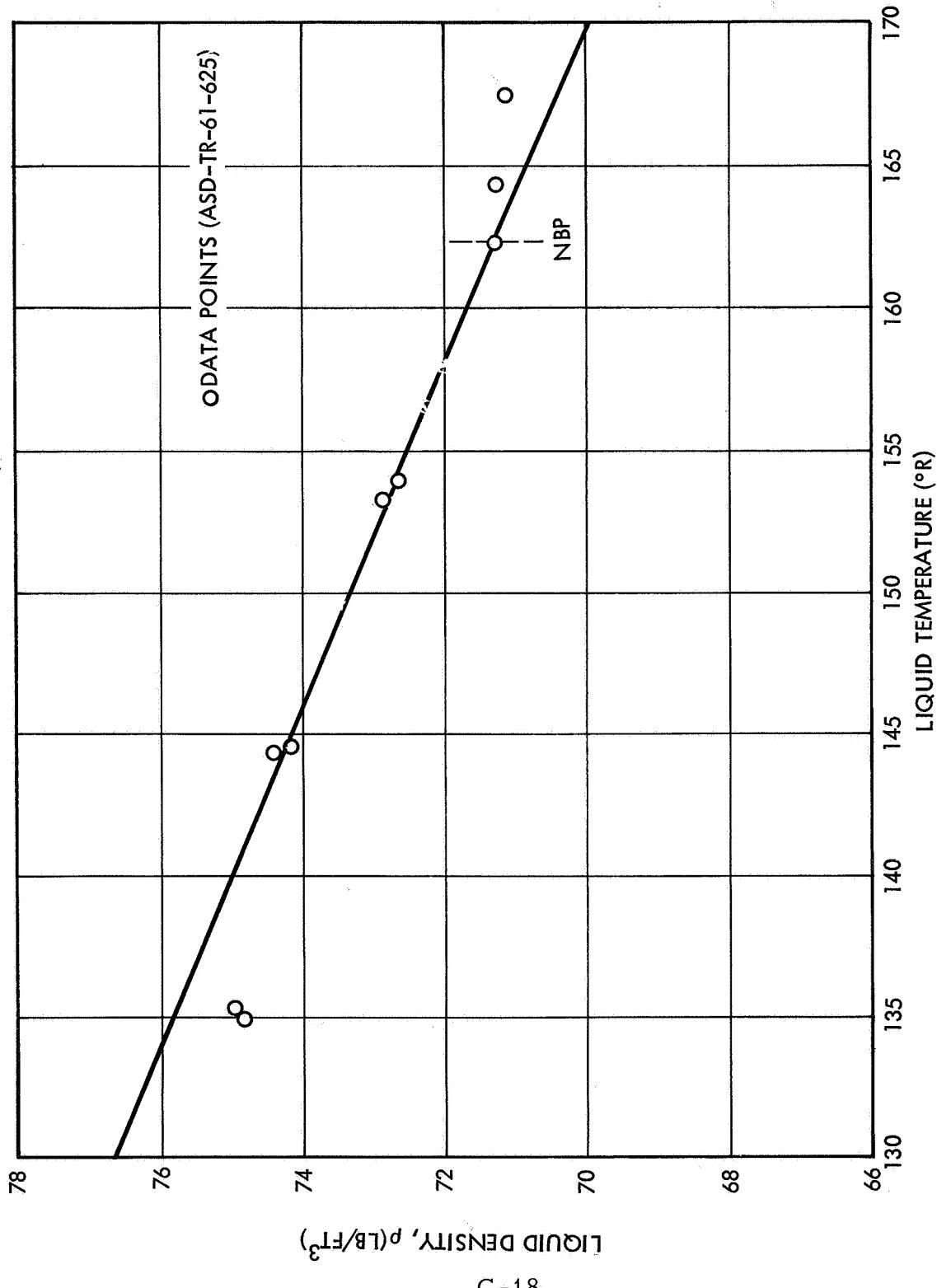


Figure C-12. Oxygen Liquid Density Versus Temperature

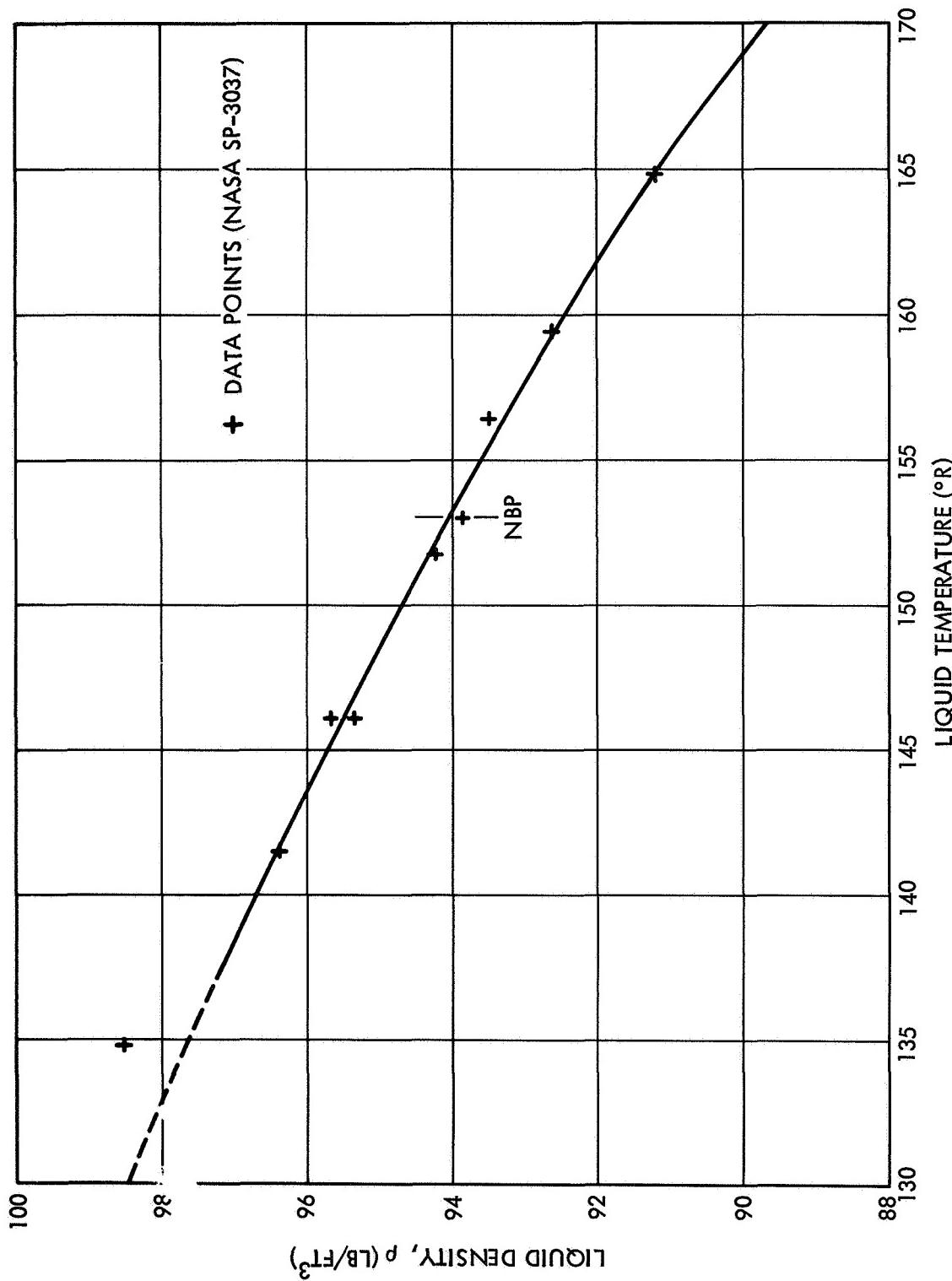


Figure C-13. Fluorine Liquid Density Versus Temperature

## APPENDIX D

### COMPUTER PROGRAMS

The following computer programs were used to facilitate analysis in the Space Storable Propellant Performance Contract.

#### 1. ROCKET CHEMISTRY PROGRAM

The generalized equilibrium chemistry program solves a wide range of thermodynamic problems requiring only the composition and two of the following system properties to be specified: pressure, volume, temperature, enthalpy, entropy, or internal energy. The program calculates composition, either from a pair of compounds with a specified weight mixture ratio, or from a series of compounds and their respective weight percents. In addition to the usual pure condensed phases, it is possible to submit a series of ideal chemical solutions composed of selected combinations of the condensed phases; the program will determine whether or not these solutions are formed by the reaction. The possible reaction products are obtained by searching a prepared master inventory tape containing entropy and enthalpy curve fit coefficients for all elements and compounds of interest. Nongaseous phases and ionized species are treated as distinct and separate compounds. The program initially assumes an ideal all-gas system. The equilibrium gas pressures of all possible gaseous species are calculated. Using these partial pressures as initial estimates, nongaseous phases and solutions are then considered. Upon convergence of the calculations, the program eliminates all but the actual gases, condensed phases, and ideal solutions present at equilibrium. Rocket performance is computed for isentropic sonic flow through a throat by specifying exit pressures, temperatures, or area ratios. Chemical reactions only, or chemical reactions and phase changes, may be stopped at any point in the expansion. Equilibrium or frozen composition, thermodynamic parameters, and the usual rocket parameters are given in the program output.

## 2. ONE-DIMENSIONAL, ONE-PHASE EXACT KINETIC COMPUTER PROGRAM

TRW Systems has developed under contract to the National Aeronautics and Space Administration Manned Spacecraft Center (Contract NAS 9-4358), a One-Dimensional, One-Phase (1D, 1P) Reacting Gas Nonequilibrium Performance Program. The computer program calculates the inviscid one-dimensional equilibrium, frozen and non-equilibrium nozzle expansion of propellant exhaust mixtures containing the six elements: carbon, hydrogen, oxygen, nitrogen, fluorine, and chlorine.

The computer program considers all significant gaseous species present in the exhaust mixtures of propellants containing these elements and all gas phase chemical reactions which can occur between the exhaust products. In order to reduce the computation times per case to a minimum, the program utilizes a second-order implicit integration method. This integration method has reduced the computation time, per case, several orders of magnitude compared to the computation time required when utilizing standard explicit integration methods such as fourth order Runge-Kutta or Adams-Moulton methods.

The throat size is determined for each combination of propellant system and mixture ratio through use of the given chamber pressure, thrust level, and the value of the one-dimensional thrust coefficient,  $C_F$ , computed by the rocket chemistry program. The reverse reaction rate constant,  $k_r = AT^{-n}e^{-B/T}$ , is employed in the Kinetics Program and forms a portion of the input data to the computer program. It is usually input in chemist's units; i. e.,  $\text{cm}^3$ , gm,  $^\circ\text{K}$ , sec, and is converted internally into units consisting of  $\text{ft}^3$ , lb,  $^\circ\text{R}$ , sec.

## 3. ONE-DIMENSIONAL, TWO-PHASE KINETIC COMPUTER PROGRAM

TRW Systems has also developed, under contract to the National Aeronautics and Space Administration Manned Spacecraft Center (Contract NAS 9-4358), a One-Dimensional, Two-Phase (1D, 2P) Reacting Gas Nonequilibrium Performance Program. This program calculates the inviscid one-dimensional equilibrium, frozen and nonequilibrium nozzle expansion of propellant exhaust mixtures containing the six elements: carbon, hydrogen, oxygen, nitrogen, fluorine and chlorine; and one metal

element, either aluminum, beryllium, boron, or lithium. Energy and momentum transfer is considered between the two phases but interphase mass transfer is not considered.

In all 79 species related by 763 reactions are handled with a maximum of 46 species and 380 reactions for the boron metal element. In addition, provision is made for eight condensed species with a maximum of four condensed species at any time. Furthermore, the condensed phase can be allocated to one (or more) size group.

All the species and reactions of importance to the proposed program can be accommodated by the TRW Systems developed one-phase and/or two-phase kinetics programs.

#### 4. VISCOUS EFFECTS COMPUTER PROGRAM

The method of Bartz for computing boundary-layer thicknesses, skin-friction, and heat flux in axisymmetric nozzles has been revised and programmed for digital computer solution. The method solves, simultaneously, the integral momentum and energy equations for thin axisymmetric boundary layers. Boundary-layer shape parameters are approximated from one-seventh power profiles of velocity and stagnation temperature; and skin-friction coefficient and Stanton number are evaluated as functions of boundary-layer thickness from the best available semiempirical relations.

This program either employs a given wall Mach number distribution as generated by, for example, the two-dimensional kinetics computer program, or can generate internally a one-dimensional Mach number distribution as a function of local area ratio and (constant)  $\gamma$ , the ratio of specific heats. In addition, the program requires a wall temperature,  $T_w$ , distribution. This distribution can be produced, by an iterative procedure, from a thermal analysis of the nozzle. A constant wall temperature may be assumed in lieu of such data.

The program computes the local parameters: convective heat transfer coefficient ( $h_g$ ), heat flux ( $q/A$ ), where  $A$  is the nozzle surface area, skin-friction coefficient ( $C_f$ ), boundary-layer thickness ( $\delta$ ), displacement thickness ( $\delta^*$ ) and momentum thickness ( $\theta$ ). The total heat rejection load,  $\dot{q}$ , is found from numerical integration of  $\dot{q}/A$  versus  $A$ .

## 5. BASIC ONE-DIMENSIONAL HEAT TRANSFER PROGRAM

This program, designated 84040 on TRW's IBM 7070, computes the change in temperature of each of a number of points (called nodes) in a slab of material, at specified intervals of time, during which the slab is to be heated and/or cooled. The heating and cooling is accomplished by convection and radiation, at the slab boundaries. The program is general enough so that it can handle heat transfer through both flat plate and cylindrical sections, regardless of size, thickness, and material layer composition. Most commonly, the program is used to simulate rocket engine firing duty cycles.

Preparation of input for this program requires the following:

- a) Convective heat transfer coefficients on the inside and outside surfaces
- b) Inside and outside adiabatic wall temperatures
- c) Initial temperatures of the node points
- d) Thermal conductivities and diffusivities of the materials in the slab
- e) Thickness of the material layers

The output consists of temperature profiles in the slab at specified time intervals.

## 6. THREE-DIMENSIONAL PROGRAM

This is a high-speed digital program for transient problems involving all nodes or combinations of nodes of heat transfer (i. e., convection, conduction, and radiation). This program can be used for any thermal problem whose finite difference equation is analogous to the differential equation for a lumped RC electrical network and can, therefore, be visualized as an electrical circuit.

The number of connecting flux paths to any node is arbitrary. This program can handle as many as 250 node points and capacitance with approximately 800 resistances.

Four valuable features are incorporated into this program:

- a) Variable thermal properties are simulated when a table showing values of each property versus temperature is entered in the input.
- b) Any node can be held at a constant temperature for a period of time and thus simulate phase transition.
- c) Erosion rate schedule is entered in the input in the form of a table.
- d) A cathode follower is used for the purpose of transferring a temperature from one node in the network to another with zero transfer of energy.

## 7. GAS PROPERTIES COMPUTER PROGRAM

This program is used to rapidly determine the following:

- a) Nozzle thrust coefficient as a function of pressure ratio
- b) Nozzle area ratio as a function of pressure ratio
- c) Nozzle area ratio as a function of Mach number
- d) Ratio of local to critical temperature as a function of Mach number
- e) Ratio of isentropic temperature drop to inlet temperature as a function of pressure ratio

The range of values covered for each of the basic parameters is:

Mach number: 1 - 10

Pressure ratio:  $3.5 - 10^4$

Ratio of specific heats: 1.1 - 1.67

The effect of the ratio of specific heats is included in all the plots.

## APPENDIX E

### TEST FACILITIES AND EQUIPMENT

All testing was done at the TRW rocket test facility at Capistrano, California, Figure E-1. The test facility is equipped for a broad spectrum of research, design, development, and testing of propulsion systems. The 2700-acre facility, Figure E-1, was constructed to take maximum advantage of an ideal rolling hill terrain which provides natural buffer zones for the testing of rocket engines fueled with highly reactive and energetic storable and cryogenic propellants.

The facility has four major test stand complexes:

- Vertical Engine Test Stand (VETS)
- Propulsion Integration Test Stand (PITS)
- High Altitude Test Stand (HATS)
- High Energy Propulsion Test Stand (HEPTS)

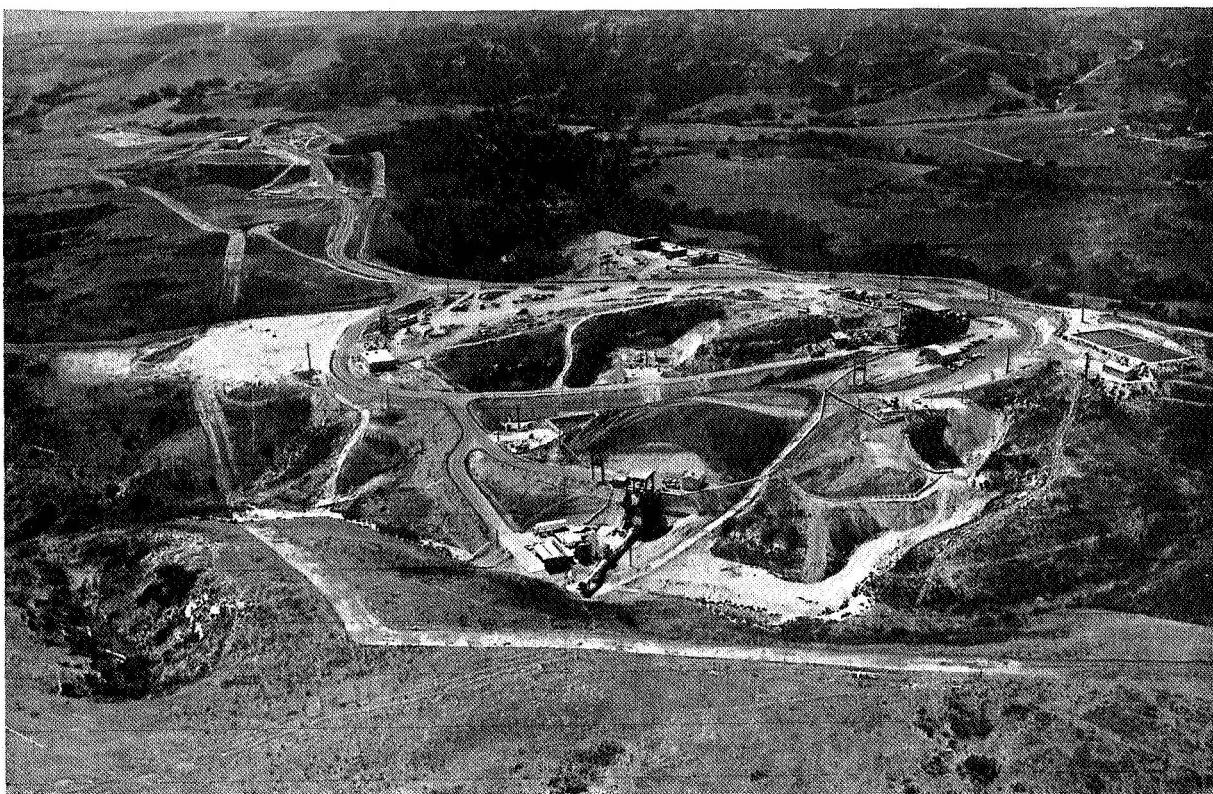


Figure E-1. Capistrano Test Site

These stands provide a total of 12 rocket engine test positions, 5 of which are used for simulated high-altitude (up to and in excess of 100,000 feet) test conditions. Engines ranging from 1/2 to 200,000 pounds of thrust can be tested on these stands.

High Energy Propellant Test Stand (HEPTS) (Figure E-2), is designed to test propulsion systems which utilize energetic fuels and oxidizers, e.g., liquid oxygen and hydrogen, fluorines, chlorintri-fluoride, chlorine pentafluoride, and noncryogenic propellants such as various hydrazine combinations and nitrogen tetroxide. Work of this contract was conducted at this test stand, in particular the B-2 test position.

Fire protection and coolant water for the six test stands at HEPTS are supplied by a gravity water feed boost pump with a capacity of 300 gpm, and an operating head pressure of 800 feet. Site water for the stands and steam generation plant is supplied by a site water supply boost pump with a capacity of 55 gpm, and an operating head pressure of 200 feet. Water utilized at the stand, after circulation, is accumulated in an 8000-gallon catch basin and then pumped back to the upper reservoir for recycling.

For the fluorine test facility, very high standards of materials selection, cleaning passivation, and leak detection are followed. The handling of fluorine, both liquid and gaseous, is accomplished remotely from the facility control room. All operations are carried out using remotely operated valves except for the transfer from delivery vehicles which are equipped with manual valves.

Data acquisition from rocket engines tested at the HEPTS is derived with the use of 500 twin-conductor shielded cables emanating from six test positions for data transmission to the HEPTS Control and Data Acquisition Center. Three hundred data lines are available for the storables propellant test stands (stands A-1, A-2, A-3, and A-4) and 200 data lines for the cryogenic propellant test stands (stands B-1, B-2, and B-2A). The HEPTS control center building also has four engine valve control consoles — one for sea-level stands A-1 and A-2, one for altitude test chambers A-3 and A-4, and one console each for the cryogenic propellant test stands B-1, B-2, and B-2A.

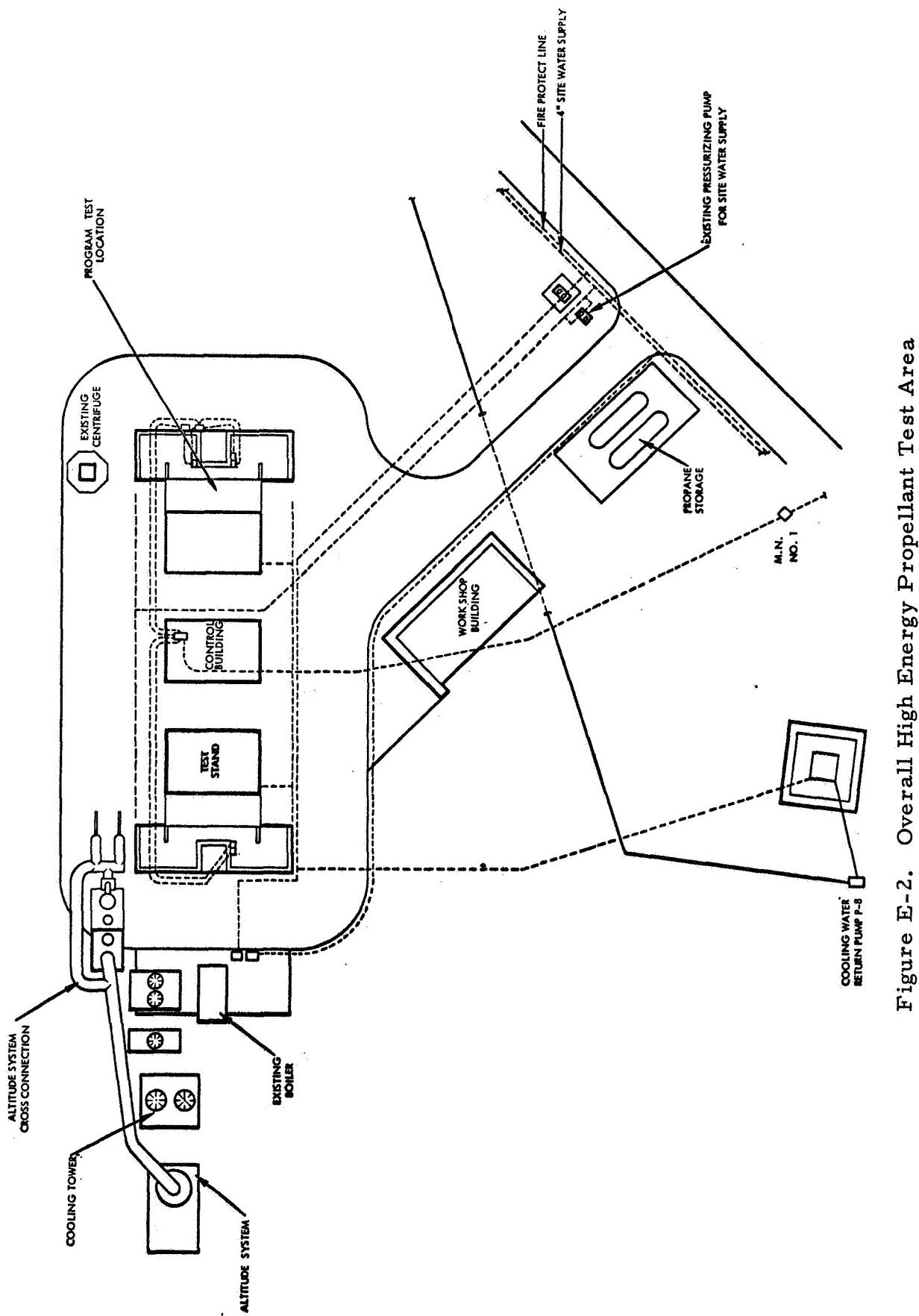


Figure E-2. Overall High Energy Propellant Test Area

The HEPTS control center is constructed of reinforced concrete, with all load-bearing elements buttressed by high-tensile strength structural steel. This 3000-square-foot building is designed to withstand a blast overpressure condition of 2 psi, or 300 lb/sq ft.

A SDS 925 computer is located in the main control center. The computer is presently programmed to provide post-test computation of most of the important rocket engine performance parameters using the prerecorded tape from the digital tape recorders. It also provides reduction to engineering units of all parameters recorded on the digital tape. Programs available provide real-time computation capability. Primary output devices for the computer are a 120 character, 10 line-per-second line printer, and an 8-channel digital-to-analog converter.

All test firings were conducted on the B-2 vertical firing thrust mount test position at HEPTS. This thrust mount can handle engines up to 10,000 pounds thrust.

Liquid methane/ethane fuel blend is supplied from a 100-gallon cryogenic storage tank. This tank is rated for 1000 psi run pressure. The fuel is pressurized by its own pressurization system using gaseous helium. Helium is stored in a TRW-owned helium trailer. The tank is cooled by liquid nitrogen from a 100,000-gallon liquid nitrogen storage tank located directly behind the B-2 test position.

The fuel is plumbed to the test stand (see Figure E-3) through liquid nitrogen jacketed feed lines up to the fire control valves. All of the valves in the system are rated for cryogenic service and are cooled with liquid nitrogen. Down stream of the fire valves the liquid nitrogen is plumbed directly into the propellant feed line to provide prerun coolant to the engine. Purges are done with gaseous nitrogen.

The FLOX is plumbed to the test stand in a manner similar to that of the fuel above. The FLOX is kept in a triple jacketed cryogenic 150-gallon storage tank.

The fuel (55 percent methane - 45 percent ethane) is purchased in "K" bottles in a preblended form. The fuel is transferred to the storage

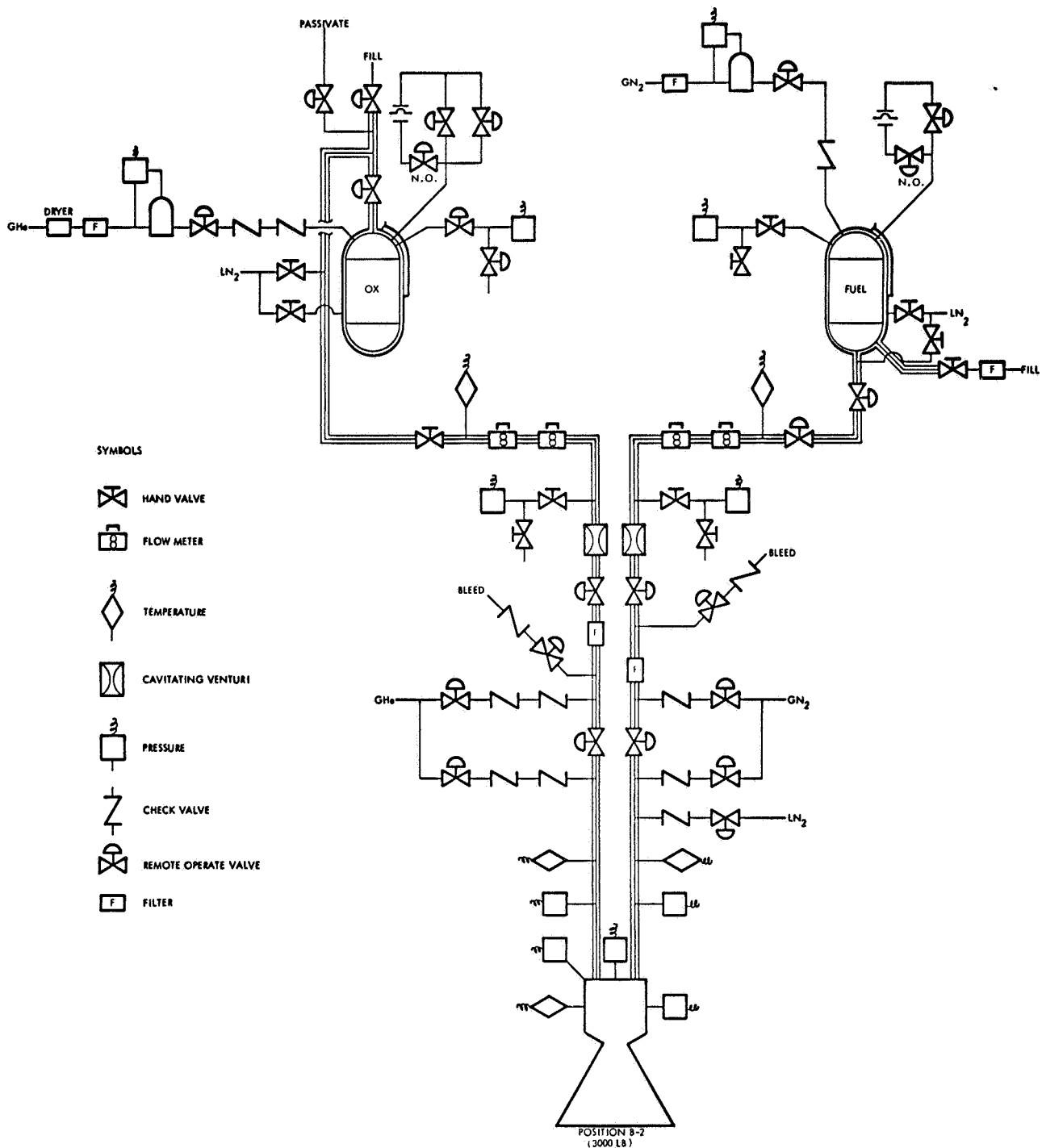


Figure E-3. Schematic Diagram of HEPTS Test Stand Position B-2

tank by liquefying the gas as it passes to the tank. The "K" bottle is weighed before and after use as a matter of record and to assure complete removal of the fuel.

The FLOX blend is mixed at the TRW test facility. The mixing operation is done by accurate measurement of the fluorine added to the FLOX storage tank and then adding the proper amount of oxygen to the FLOX tank to obtain the desired FLOX mixture. The fluorine measurements are done by an isotope level gage on the storage tank. This gage is very sensitive and when properly calibrated should give readings to within 1/2 inch. The quantity of fluorine is determined from these measurements and the known dimensions of the tank. The oxygen is kept in a small dewar and is weighed as it is passed to the FLOX tank.

The FLOX is periodically sampled and analyzed to determine the fluorine and oxygen concentrations. The FLOX samples are obtained by trapping liquid FLOX in a sample bottle. To prevent fractional distillation of the FLOX it is passed through the sample system until a liquid feather is obtained. The remote valves at the cylinder are closed, trapping the FLOX. The liquid FLOX is then allowed to gasify and is taken to the site chemistry laboratory where it is analyzed by the mercury absorption technique. In this method the FLOX is allowed to completely react with mercury. Sufficient mercury is in the test container to react with all of the fluorine in the test container. The result is gaseous oxygen, the amount of which is measured by the pressure and temperature in a known volume. An infrared spectrophotometric analysis is also made to determine the amounts of impurities (HF, CO<sub>2</sub>, CF<sub>4</sub>, and SiF<sub>4</sub>) in the sample.

## APPENDIX F

### DATA ACQUISITION SYSTEM ACCURACY AND METHODS

The purpose of this appendix is to show the reliability of the experimental measurements which are used to determine the performance efficiency. This is done by determining the errors inherent in the data acquisition processes and in the calculation process. Estimations can then be made of the range in which reasonably true values of the measured or calculated parameters will lie.

The error of a measurement is the probability limit within which the measured value will lie in relation to actual value of the parameter. An error analysis is conducted to determine this probability limit. To do this, the uncertainty in the individual measuring transducers and the systems associated with the transducers must be determined. In addition to these uncertainties, the various combinations of redundant transducers or multiple measurements to determine a given parameter must be considered. Finally, all of these probable errors will enter into combinations of multiple parameters to determine engine performance.

The scope of probable errors outlined above may be narrowed down to two basic types: source and random errors. Source errors are related to a particular system and the personnel working on the experiment. They are caused by experimental techniques and calibration procedures. Usually source errors are not estimated by statistical variations because they are unique to each experiment and variable with the personnel. Source errors, however, can be minimized by careful calibration techniques and procedures and by the use of good calibration standards. Requirements for consistency and traceability and careful examination of experimental data add to the reliability of the data. It is assumed that source errors can be eliminated by carefully conducting the experiment.

Random errors arise from unpredictable and otherwise unknown variations in the test setup. These errors are assumed to follow a normal statistical distribution. Therefore, the error analysis presented here is concerned only with the random errors of the experimental system in which a statistical analysis may be applied.

Basically, there are two methods for determining the data acquisition system measurement uncertainties. The first, the Root Sum Square Method (RSS), is obtained by calibrating each component of the data acquisition system (e.g., measuring element, recorder, etc.) and then determining the RSS value of the component uncertainties including those of the calibration equipment. The other, referred to as "end-to-end," is one in which a known stimulus is applied to the measuring instrument and the resulting reduced output is compared with the stimulus. The RSS value of the discrepancy of the output and input, and the uncertainty of the stimulus (i.e., traceability to NBS) will include all component errors. Both methods are employed at TRW Systems and therefore, as indicated in Table F-1, the acquisition accuracies are presented in terms of the total uncertainties which include traceability to National Bureau of Standards, measurement element, and acquisition system.

Typical total data acquisition system accuracies at TRW Systems of the critical firing test parameters are summarized in Table F-1. The data presented enumerate the comparative uncertainties of three data acquisition systems: (1) digital tape, (2) strip chart, and (3) oscillograph. The accuracy values are  $3\sigma$  values and are traceable to the NBS.

For testing at CTS, primary engine performance data are recorded on magnetic tapes of the digital data acquisition system. This system is employed to obtain high accuracy data and has a total sampling capability of 10,000 samples per second with a resolution of 0.1 percent. Transient data for obtaining startup and shutdown time and overshoot are recorded on oscillographs and on the digital tapes.

For all engine testing, configuration data are tabulated on special forms for permanent storage. Flowmeter calibration data are acquired on strip charts, oscillographs, and on hand-tabulated forms. All of these records are permanent, and they are stored throughout the program. Transducer and load cell calibration data are recorded on hand-tabulated forms to provide permanent records for storage.

Figures F-1 and F-2 show schematically the acquisition, processing, and distribution of the test data and the calibration information.

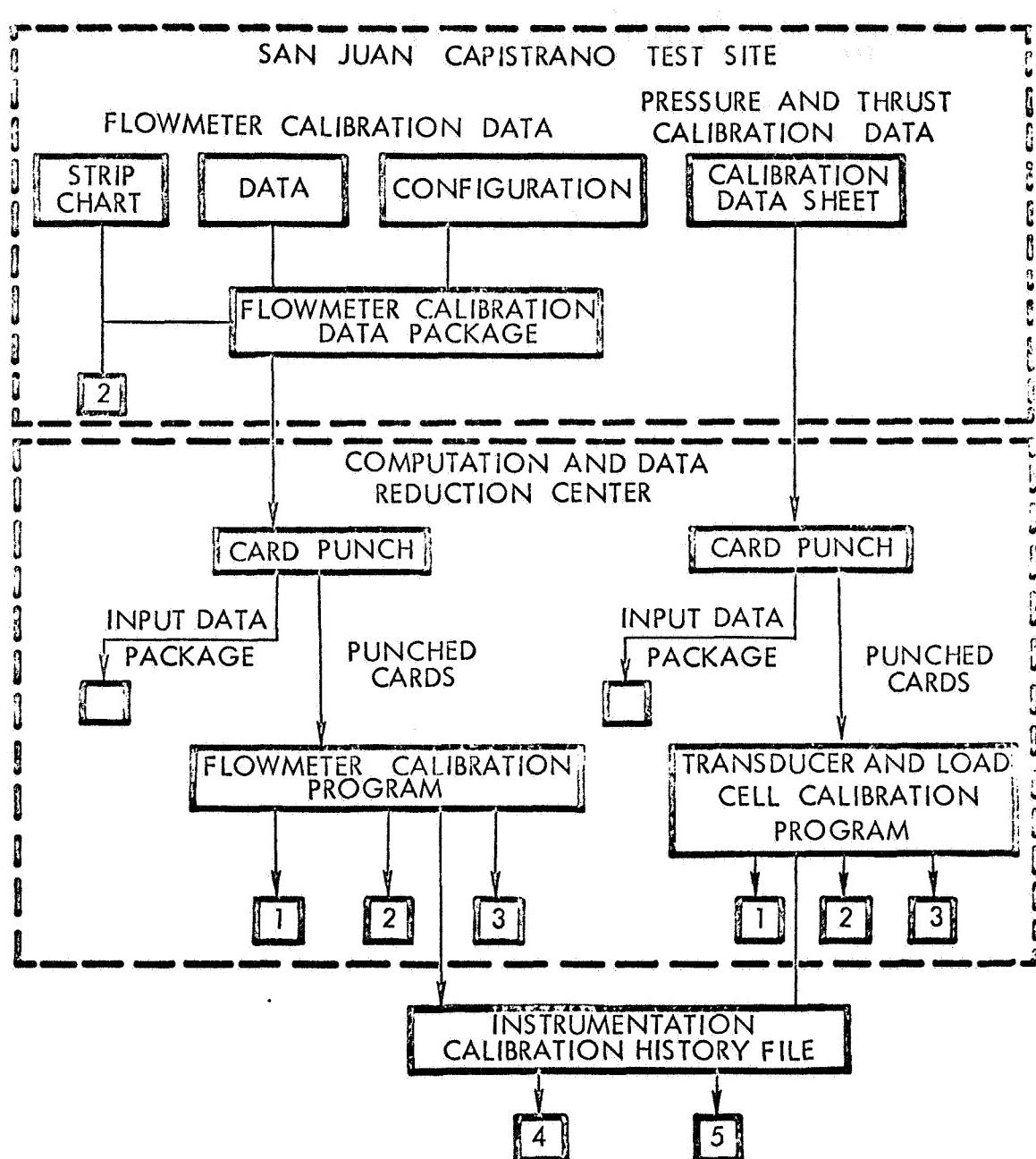
Table F-1. Data Acquisition System Accuracy

Measurement Description	Symbol	Range	Data Acquisition System Accuracy		
			Digital % FS 3 $\sigma$	Oscillograph % FS 3 $\sigma$	Strip Chart % FS 3 $\sigma$
Propellant Tank Pressure	P <sub>PTU</sub>	0 to 500 psia	0.7	2.0	2.0
Propellant Injection Pressure	P <sub>IF</sub>	0 to 500 psia	0.7	2.0	2.0
Chamber Pressure	P <sub>CD</sub>	0 to 200 psia	0.7	2.0	2.0
Capsule Pressure	P <sub>CAP</sub>	0 to 1.0 psi	5.0	5.0	5.0
Engine Temperature	T <sub>ENG</sub>	0 to 2000°F	2.0	3.0	3.0
Propellant Tank Temperature	T <sub>PTU</sub>	-300°F to 200°F	1.0	2.0	2.0
Propellant Temperature	T <sub>F</sub>	-300°F to 130°F	1.0	2.0	2.0
Fuel Propellant Flow rate	W <sub>F</sub>	0 to 60 gpm	0.5	0.5	2.0
Thrust	F	0 to 5000 lbf	1.0	2.0	2.0

## 5. DATA REDUCTION METHODS

Immediately following each test, a quick-look reduction is made to determine engine steady-state performance. This reduction is made using either strip chart data and digital data to calculate the primary propulsion parameters, e.g., engine I<sub>sp</sub> and C\*, injector pressure drops, propellant flow rate, and chamber temperatures. The quick-look digital data are reduced by using the CTS on-site computer. This computer provides the capability of developing highly accurate performance and operating data immediately after the test. As required, a quick-look reduction is made using oscillograph data to evaluate primary engine transient performance parameters, e.g., startup time, shutdown time, total impulse, and specific impulse.

Flowmeter calibration data are processed using an existing data reduction program, and the derived calibration relations for each flowmeter are published and updated as new calibrations are made. Transducer and load cell calibration data are processed using an existing program which gives a least-squares curve fit to the calibration data.



**LEGEND:**

- 1** DISTRIBUTION TO TASK ENGINEER
- 2** DISTRIBUTION TO PROJECT STORAGE
- 3** DISTRIBUTION TO PROJECT OFFICE

Figure F-1. CTS Calibration Data Flow Schematic

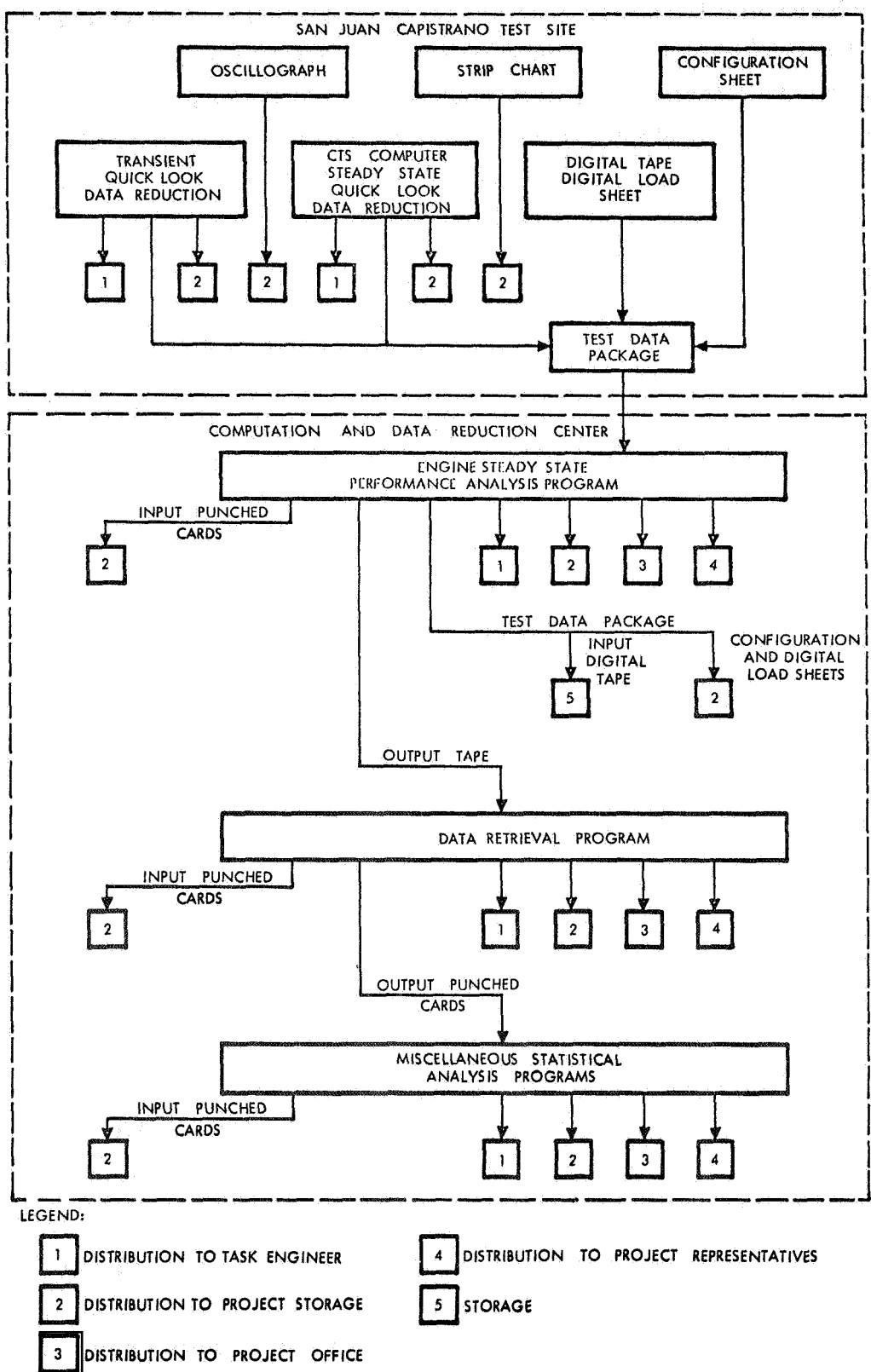


Figure F-2. Schematic Diagram, Engine Test Data Flow

These calibration data are maintained in a historical file for each transducer and load cell. New calibrations are incorporated into use with the performance analysis programs. All calibration data from instruments affecting engine performance are maintained by a central group so that complete calibration histories are readily available for all of this instrumentation; this information is made available upon request.

The majority of the steady-state performance test data are processed using the engine Steady-State Performance Analysis Computer Program. This program provides a complete reduction using current calibrations for measured test data and to calculate salient propulsion parameters, e.g.,  $C^*$ ,  $I_{sp}$ , and  $C_F$ , for test conditions. This reduction is made using weighted average values for any parameters that are measured redundantly, e.g., propellant flow rates, chamber pressures, and thrust. In addition, channel-to-channel variations in each redundantly measured parameter are automatically determined to provide a ready indication of instrumentation precision for each test. The previously discussed influence correction factors are entered directly into the program.

The system operating parameters of temperature and pressure are acquired and reduced in a manner identical to that of the static engine test data. The capability to obtain data by all three acquisition modes is maintained. In most tests, however, the acquisition mode is dictated by the required accuracy of the engine static test data.

The output from the engine steady-state performance analysis program is an input to the existing Data Retrieval Program for storage of the test results. The output data are directly read onto tapes where they are stored and updated with new data to provide a complete file of all steady-state data for the program. At any time, all or selective portions of the data may be retrieved in the form of tabular listings and/or punched cards.

The retrieved data on punched cards, along with other data from transient testing of calibrations, may be input to existing statistical analysis programs, e.g., analysis of variance and multilinear regression. Data analysis is carried out on a continuing basis to (1) determine

performance, (2) define confidence limits on performance, and (3) evaluate effects of hardware changes on performance. In addition, studies may be made to carry out instrumentation and calibration error analyses to establish accuracy and quality of the overall data acquisition system.

The instrumentation setup utilized during this experimental program employed redundant primary transducers on all critical performance parameters. Examination of these experimental data indicated the basic measurement accuracies obtained were in very close agreement with the values shown in Table F-1. The  $3\sigma$  performance data accuracy estimated, based on these data and on estimated throat area  $3\sigma$  error of  $\pm 0.1\%$ , is  $\pm 0.5\%$ .

## APPENDIX G

### FINAL REPORT DISTRIBUTION LIST (NASA CR-72486)

#### "SPACE STORABLE PROPELLANT PERFORMANCE"

NAS3-11200

	<u>Copies</u>
National Aeronautics and Space Administration Lewis Research Center 21000 Brookpark Road Cleveland, Ohio 44135	
Attention: Contracting Officer, MS 500-313	1
Liquid Rocket Technology Branch, MS 500-209	8
Technical Report Control Office, MS 5-5	1
Technology Utilization Office, MS 3-16	1
AFSC Liaison Office, MS 4-1	2
Library	2
C. Aukerman, MS 500-204	1
Office of Reliability & Quality Assurance, MS 500-203	1
J. Winters, MS 500-204	1
E. W. Conrad, MS 500-204	1
H. H. Valentine, MS 501-2	1
National Aeronautics and Space Administration Washington, D. C. 20546	
Attention: Code MT	1
RPX	2
RPL	2
SV	1
Scientific and Technical Information Facility P. O. Box 33 College Park, Maryland 20740	
Attention: NASA Representative	6
Code CRT	

	<u>Copies</u>
National Aeronautics and Space Administration Ames Research Center Moffett Field, California 94035	
Attention: Library	1
C. A. Syvertson	1
 National Aeronautics and Space Administration Flight Research Center P. O. Box 273 Edwards, California 93523	
Attention: Library	1
 National Aeronautics and Space Administration Goddard Space Flight Center Greenbelt, Maryland 20771	
Attention: Library	1
 National Aeronautics and Space Administration John F. Kennedy Space Center Cocoa Beach, Florida 32931	
Attention: Library	1
 National Aeronautics and Space Administration Langley Research Center Langley Station Hampton, Virginia 23365	
Attention: Library	1
 National Aeronautics and Space Administration Manned Spacecraft Center Houston, Texas 77001	
Attention: Library	1
 National Aeronautics and Space Administration George C. Marshall Space Flight Center Huntsville, Alabama 35812	
Attention: Library	1
Keith Chandler, R-P&VE-PA	1
 Jet Propulsion Laboratory 4800 Oak Grove Drive Pasadena, California 91103	
Attention: Library	1
W. Powell	1
 Office of the Director of Defense Research & Engineering Washington, D. C. 20301	
Attention: Office of Asst. Dir. (Chem. Technology)	1

	<u>Copies</u>
Defense Documentation Center Cameron Station Alexandria, Virginia 22314	1
RTD (RTNP) Bolling Air Force Base Washington, D. C. 20332	1
Arnold Engineering Development Center Air Force Systems Command Tullahoma, Tennessee 37389 Attention: AEOIM	1
Advanced Research Projects Agency Washington, D. C. 20525 Attention: D. E. Mock	1
Aeronautical Systems Division Air Force Systems Command Wright-Patterson Air Force Base Dayton, Ohio Attention: D. L. Schmidt, Code ASRCNC-2	1
Air Force Missile Test Center Patrick Air Force Base, Florida Attention: L. J. Ullian	1
Air Force Systems Command (SCLT/Capt. S. W. Bowen) Andrews Air Force Base Washington, D. C. 20332	1
Air Force Rocket Propulsion Laboratory (RPR) Edwards, California 93523	1
Air Force Rocket Propulsion Laboratory (RPM) Edwards, California 93523	1
Air Force FTC (FTAT-2) Edwards Air Force Base, California 93523 Attention: Mr. Donald Ross	1
Air Force Office of Scientific Research Washington, D. C. 20333 Attention: SREP, Dr. J. F. Masi	1
Office of Research Analyses (OAR) Holloman Air Force Base, New Mexico 88330 Attention: RRRD Maj. R. E. Brocken, Code MDGRT	1

	<u>Copies</u>
U. S. Air Force Washington, D. C. 20525 Attention: Col. C. K. Stambaugh, Code AFRST	1
Commanding Officer U. S. Army Research Office (Durham) Box CM, Duke Station Durham, North Carolina 27706	1
U. S. Army Missile Command Redstone Scientific Information Center Redstone Arsenal, Alabama 35808 Attention: Chief, Document Section Dr. W. Wharton	1
Bureau of Naval Weapons Department of the Navy Washington, D. C. Attention: J. Kay, Code RTMS-41	1
Commander U. S. Naval Missile Center Point Mugu, California 93041 Attention: Technical Library	1
Commander U. S. Naval Weapons Center China Lake, California 93557 Attention: Code 45 Code 753 W. F. Thorm, Code 4562	1 1 1
Commanding Officer Office of Naval Research 1030 E. Green Street Pasadena, California 91101	1
Director Naval Research Branch Office Washington, D. C. 20390 Attention: H. W. Carhart	1
Picatinny Arsenal Dover, New Jersey Attention: I. Forsten, Chief Liquid Propulsion Laboratory	1

	<u>Copies</u>
U. S. Atomic Energy Commission Technical Information Services Box 62 Oak Ridge, Tennessee Attention: A. P. Huber, Code ORGDP Box P	1
Air Force Aero Propulsion Laboratory Research & Technology Division Air Force Systems Command United States Air Force Wright-Patterson AFB, Ohio 45433 Attention: APRP (C. M. Donaldson)	1
Aerojet-General Corporation P. O. Box 296 Azusa, California 91703 Attention: Librarian	1
Aerojet-General Corporation 11711 South Woodruff Avenue Downey, California 90241 Attention: F. M. West, Chief Librarian	1
Aerojet-General Corporation P. O. Box 1947 Sacramento, California 95809 Attention: Technical Library 2484-2015A Dr. C. M. Beighley D. T. Bedsole	1 1 1
Aeronutronic Division of Philco Corporation Ford Road Newport Beach, California 92600 Attention: Dr. L. H. Linder, Manager Technical Library 2484-2015A	1 1
Aeroprojects, Incorporated 310 East Rosedale Avenue West Chester, Pennsylvania 19380 Attention: C. D. McKinney	1
Aerospace Corporation P. O. Box 95085 Los Angeles, California 90045 Attention: J. G. Wilder, MS-2293 Library-Documents	1 1

	<u>Copies</u>
Arthur D. Little, Inc. Acorn Park Cambridge 40, Massachusetts Attention: A. C. Tobey	1
Astropower, Laboratory McDonnell-Douglas Astronautics Co. 2800 Campus Drive Newport Beach, California Attention: Dr. George Moe Director, Research	1
Astrosystems, Incorporated 1275 Bloomfield Avenue Caldwell Township, New Jersey Attention: A. Mendenhall	1
ARO, Incorporated Arnold Engineering Development Center Arnold AF Station, Tennessee 37389 Attention: Dr. B. H. Goethert Chief Scientist	1
Susquehanna Corporation Atlantic Research Corporation Shirley Highway & Edsall Road Alexandria, Virginia 22314 Attention: A. Scurlock Security Office for Library	1
Battelle Memorial Institute 505 King Avenue Columbus, Ohio 43201 Attention: Report Library, Room 6A	1
Beech Aircraft Corporation Boulder Facility Box 631 Boulder, Colorado Attention: J. H. Rodgers	1
Bell Aerosystems, Inc. Box 1 Buffalo, New York 14205 Attention: T. Reinhardt W. M. Smith F. Herud	1 1 1
Bendix Systems Division Bendix Corporation Ann Arbor, Michigan Attention: John M. Bureger	1

	<u>Copies</u>
The Boeing Company Aero Space Division P. O. Box 3707 Seattle, Washington 98124 Attention: Ruth E. Peerenboom (1190) J. D. Alexander	1 1
Chemical Propulsion Information Agency Applied Physics Laboratory 8621 Georgia Avenue Silver Spring, Maryland 20910	1
Chrysler Corporation Missile Division Warren, Michigan Attention: John Gates	1
Chrysler Corporation Space Division New Orleans, Louisiana Attention: Librarian	1
Curtiss-Wright Corporation Wright Aeronautical Division Woodridge, New Jersey Attention: G. Kelley	1
University of Denver Denver Research Institute P. O. Box 10127 Denver, Colorado 80210 Attention: Security Office	1
McDonnell-Douglas Corporation Missiles & Space Systems Division 3000 Ocean Park Blvd. Santa Monica, California 90405 Attention: J. L. Waisman R. W. Hallet G. W. Burge P. Klevatt	1 1 1 1
Fairchild Stratos Corporation Aircraft Missiles Division Hagerstown, Maryland Attention: Library	1
General Dynamics/Convair P. O. Box 1128 San Diego, California 92112 Attention: F. Dore Library & Information Services (128-00)	1 1

	<u>Copies</u>
Convair Division General Dynamics Corporation P. O. Box 12009 San Diego, California 92112 Attention: Mr. R. Rovenger Centaur Resident Project Office	1
General Electric Company Re-Entry Systems Department P. O. Box 8555 Philadelphia, Pennsylvania 19101 Attention: F. E. Schultz	1
General Electric Company Flight Propulsion Lab. Department Cincinnati 15, Ohio Attention: D. Suichu	1
Grumman Aircraft Engineering Corporation Bethpage, Long Island, New York Attention: Joseph Gavin	1
Hercules, Inc. Allegheny Ballistics Laboratory P. O. Box 210 Cumberland, Maryland 21501 Attention: Library	1
IIT Research Institute Technology Center Chicago, Illinois 60616 Attention: C. K. Hersh, Chemistry Division	1
Kidde Aero-Space Division Walter Kidde & Company, Inc. 675 Main Street Belleville 9, New Jersey Attention: R. J. Hanville, Director of Research	1
Lockheed Missiles & Space Company P. O. Box 504 Sunnyvale, California Attention: Y. C. Lee, Power Systems R&D Technical Information Center	1

	<u>Copies</u>
Lockheed-California Company 10445 Glen Oaks Blvd. Pacoima, California Attention: Library	1
Lockheed Propulsion Company P. O. Box 111 Redlands, California 92374 Attention: Miss Belle Berlad, Librarian H. L. Thackwell	1 1
Lockheed Missiles & Space Company Propulsion Engineering Division (D. 55-11) 1111 Lockheed Way Sunnyvale, California 94087	1
Marquardt Corporation 16555 Saticoy Street Box 2013 - South Annex Van Nuys, California 91404 Attention: Librarian W. D. Boardman, Jr. C. Coulbert	1 1 1
Martin-Marietta Corporation Martin Division Baltimore 3, Maryland Attention: John Calathes (3214) Library	1 1
McDonnell Aircraft Corporation P. O. Box 6101 Lambert Field, Missouri Attention: R. A. Herzmark	1
North American Rockwell Space & Information Systems Division 12214 Lakewood Boulevard Downey, California 90242 Attention: Technical Information Center, D/096-722 (AJ01) H. Storms	1 1
Northrop Space Laboratories 1001 East Broadway Hawthorne, California Attention: Dr. William Howard	1
Purdue University Lafayette, Indiana 47907 Attention: Technical Librarian	1

	<u>Copies</u>
Radio Corporation of America Astro-Electronics Division Defense Electronic Products Princeton, New Jersey Attention: S. Fairweather	1
Republic Aviation Corporation Farmingdale, Long Island New York Attention: Dr. William O'Donnell	1
Rocket Research Corporation Willow Road at 116th Street Redmond, Washington 98052	1
Rocketdyne Division of North American Rockwell 6633 Canoga Avenue Canoga Park, California 91304 Attention: Library, Department 596-306	1
Rohm and Haas Company Redstone Arsenal Research Division Huntsville, Alabama 35808 Attention: Librarian	1
Space-General Corporation 777 Flower Street Glendale, California Attention: C. E. Roth	1
Stanford Research Institute 333 Ravenswood Avenue Menlo Park, California 94025 Attention: Thor Smith	1
Texaco Experiment, Incorporated P. O. Box 3407 Richmond, Virginia 23202 Attention: E. B. Monteath Librarian	1
Thiokol Chemical Corporation Alpha Division, Huntsville Plant Huntsville, Alabama 35800 Attention: Technical Director	1
Thiokol Chemical Corporation Reaction Motors Division Denville, New Jersey 07834 Attention: Librarian	1

	<u>Copies</u>
Thiokol Chemical Corporation Redstone Division Huntsville, Alabama Attention: John Goodloe	1
TRW Systems Group One Space Park Redondo Beach, California 90278 Attention: G. W. Elverum Tech. Lib. Doc. Acquisitions	1
TRW, Inc. TAPCO Division 23555 Euclid Avenue Cleveland, Ohio 44117 Attention: P. T. Angell	1
Union Carbide Corporation Nuclear Division ORGDP Records Department P.O. Box P Oak Ridge, Tennessee 37830 Attention: A. P. Huber, Superintendent Technical Division - ORGDP	1
United Aircraft Corporation Corporation Library 400 Main Street East Hartford, Connecticut 06118 Attention: Dr. David Rix Erle Martin	1
United Aircraft Corporation Pratt & Whitney Division Florida Research & Development Center P. O. Box 2691 West Palm Beach, Florida 33402 Attention: R. J. Coar Library T. E. Bailey	1 1 1
United Aircraft Corporation United Technology Center P. O. Box 358 Sunnyvale, California 94088 Attention: Librarian	1
Vought Astronautics Box 5907 Dallas 22, Texas Attention: Warren C. Trent	1

## REFERENCES

1. S. Nukiyama and Y. Tanasawa, "Experiments on the Atomization of Liquids in an Air Stream, Reports 1 to 6, Canada National Research Council Translations No. II-575 from Transactions of the Society of Mechanical Engineers (Japan), Vol. 4, 5, 6, 1938-40.
2. R. Ingebo, "Drop-Size Distributions for Impinging-Jet Breakup in Airstreams Simulating the Velocity Conditions in Rocket Combustors," NACA TN 4222, March 1958.
3. P. Weiber, "Calculated Temperature Histories of Vaporizing Droplets to Critical Points," Journal of AIAA, Vol. 1, No. 12, 1963.
4. G. Morrell, "Rate of Liquid Jet Breakup by a Transverse Shock Wave," NASA TND-1728, May 1963.
5. G. Elverum and P. Staudhammer, "The Effect of Rapid Liquid Phase Reactions on Injector Design and Combustion in Rocket Motors," Progress Report No. 30-4, Jet Propulsion Laboratory, August 25, 1959.
6. J. Rupe, "An Experimental Correlation of the Non-Reactive Properties of Injection Schemes and Combustion Effects in a Liquid Propellant Rocket Engine," JPL TR 32-255, July 15, 1965.
7. R. J. Priem and M. F. Heidmann, "Propellant Vaporization as a Design Criterion for Rocket Engine Combustion Chambers," NASA TR R-69, 1960.
8. G. Elverum and P. Staudhammer, "The Effect of Rapid Liquid Phase Reactions on Injector Design and Combustion in Rocket Motors," Progress Report No. 30-4, Jet Propulsion Laboratory, August 25, 1959.
9. P. Nelson and W. Stevens, "Size Distribution of Droplets from Centrifugal Spray Nozzles," AIChE Journal, Vol. 7, 1961.
10. B. Johnson, "An Experimental Investigation of the Effects of Combustion on the Mixing of Highly Reactive Liquid Propellants," Technical Report No. 32-689, Jet Propulsion Laboratory, July 15, 1965.
- B-1. "Performance Characteristics of Compound A/Hydrazine Propellant Combination," Technical Documentary Report No. TR-65-107, Vol. 1, May 1965.